UNIVERSIDAD
DE GRANADA

DOCTORAL THESIS

Characterization and Measurement of Communication Channels in the mmWave Band

---

Author:
Alejandro Ramírez Arroyo

Thesis supervisors:
Dr. Juan F. Valenzuela Valdés
Dr. Pablo Padilla de la Torre

Department of Signal Theory, Telematics and Communications
University of Granada
Programa de Doctorado en Tecnologías de la Información y la Comunicación

Granada, October, 2023

Editor: Universidad de Granada. Tesis Doctorales
Autor: Alejandro Ramírez Arroyo
ISBN: 978-84-1195-096-1
URI: https://hdl.handle.net/10481/85720

"Hacerse mayor es más fácil de lo que pensamos cuando aún lo vemos lejos. Nos hacemos viejos viendo pasar trenes solo de ida desde nuestra propia estación, y el tiempo nos enseña que cada vez quedan menos opciones, que en cada cana muere una oportunidad, que el mundo cambia a una velocidad que nos va superando. Sin embargo, uno tiene menos miedo y menos prisa, porque sabiendo que podríamos subir al tren que queremos, hemos encontrado el rincón ideal."

David Sainz

Preface

This is a collection of articles / article-based thesis submitted in fulfillment of the requirements requested by the University of Granada (Spain) to obtain the International PhD degree in the Doctoral Programme in Information and Communications Technologies. Prof. Juan F. Valenzuela Valdés and Prof. Pablo Padilla de la Torre have supervised the research presented in this document. The research results have been mainly developed at the University of Granada.

The development of this thesis has been mainly supported by the Spanish Ministry of Universities through the predoctoral grant FPU19/01251.

Acknowledgements

Cuatro años después de comenzar en esto del mundo de la investigación, me encuentro sentado ante estos agradecimientos, los cuales son las últimas páginas de mi tesis doctoral. Ingenuo de mí, hace cuatro años pensaría que estoy ante el final del camino. Sin ir más lejos, estos cuatro años me han enseñado que este no es más que el comienzo. Es por ello que, me gustaría aprovechar las siguientes palabras para agradecer la confianza depositada en mí por toda la gente que ha hecho posible esta tesis, tanto a nivel profesional, como a nivel personal. A pesar de que este trabajo lleve mi nombre, jamás hubiese sido posible sin vosotros. Solamente me queda deciros, ¡Gracias!

En primer lugar, me gustaría acordarme de mis directores de tesis, Juan Francisco y Pablo. Juanfra, gracias por confiar en mí cuando te pedí que me tutorizases a distancia y aquello todavía no se estilaba. Pablo, gracias por la ayuda desinteresada abriéndome las puertas de tu despacho cuando un servidor no sabía qué asignaturas escoger al irse a estudiar al extranjero. Probablemente, ambas acciones que en aquel momento no consideré especialmente relevantes, son las que hicieron que a día de hoy esté aquí. La calidad humana con la que habéis gestionado un grupo con tal crecimiento en los últimos años es entrañable. Espero que sigáis muchos años al pie del cañón, porque sois el pilar principal para que esto funcione. Ha sido un placer, es un placer, y será un placer trabajar a vuestro lado.

Gracias a todos los componentes del grupo SWAT, por hacer del ambiente laboral un lugar desenfadado al que ir con una sonrisa en la cara: Carlos, Cleo, Carmelo, Nacho, Salva, Migue, Mario, Andrés, Juane, Marcos, Ginés. En especial, gracias a Antonio por haber sido prácticamente mi tercer director en la sombra. Para no ser lo tuyo, creo que después de varios años le has acabado cogiendo el gusto a la propagación. Gracias por transmitirme tal nivel de rigurosidad por la ciencia, cuando comencé no sabía que que existía tal arte detrás de la notación y las figuras. Unos años más tarde, también estoy en esa rueda. Para lo demás, siempre nos quedará echarnos algo. Gracias a Ángel, por haber estado ahí siempre dispuesto a echar una mano, especialmente en los inicios, siempre difíciles. Espero haberme podido contagiar aunque sea un poco de tu pasión por la ciencia. Un placer haber descubierto gracias a ti que el IEEE Xplore puede ser tu periódico de confianza todas las mañanas.

Me gustaría mencionar a aquellos que hicieron posible mi estancia en Aalborg, en especial a Melisa, Nacho y Troels. Gracias por confiar en mí para trabajar con vosotros y ofrecerme vuestra disponibilidad siempre que lo necesitase. Desde el punto de vista profesional, mi estancia fue excepcional pudiendo aprender de toda vuestra experiencia. Desde el punto de vista personal, querría agradecer a todos los amigos que me llevé de allí, haciendo que una experiencia a priori desafiante, como es una estancia profesional en el extranjero, acabase convirtiéndose en una experiencia vital. Mención especial para aquel sofá que me salvó de dormir en la calle en una bonita noche de verano danesa.

Gracias a los chavales del pueblo, Alexis y Álvaro. Me alegra saber que los tres chavales que entraron en aquel piso como primera experiencia fuera de casa, han acabado encontrando su camino. Y me alegra aún más saber después de tantos años que si necesito algo, ahí estaréis. Ya sabéis dónde encontrarme.

No puedo olvidarme de mi familia. En particular, de mi hermano Alberto, mi padre Domingo, y mi madre Pura. Alberto, gracias por haber actuado como hermano mayor tantos años. El hermano pequeño también se hizo mayor, aquí me tienes para lo que necesites. Domingo, gracias por el apoyo, los valores y la enseñanza que me han permitido llegar a esta etapa de mi vida. Pura, gracias por la ayuda, el amor y la paciencia que me han hecho crecer sabiendo en lo que quiero convertirme, una buena persona. Os quiero agradecer que, aún cuando las cosas no estaban bien, conseguisteis lo más difícil, que aquel niño creciera ajeno a los problemas que conlleva la vida adulta. Siempre os estaré infinitamente agradecido. A pesar de los kilómetros que nos separan, todos los días me acuerdo de vosotros.

Por último, quiero agradecer a mi pareja Mari Ángeles por estos ocho años de amor incondicional a mi lado. Sé que en ocasiones el camino no ha sido fácil, pero siempre has tenido la virtud de afrontar los problemas con una sonrisa en la cara. Gracias por sacarle el lado positivo a la vida y tener el coraje de seguirme allá donde vaya. Probablemente siempre te quedará el gusanillo de hacer una tesis, pero quiero que sepas que esto es tanto tuyo como mío. Espero que te sigas llevando por muchos años tu premio por ser la mejor persona que me aguanta.

A Luna y Rufo, gracias por haber estado siempre a mi lado,
por hacerme mejor persona. Siempre estaréis en mi recuerdo.

"Cuando te das cuenta de que ya no eres lo que eras,
pero sigues en la brecha y eso es lo que queda."

Soukin

Abstract

5G wireless technology promises to change society as we know it. This new technology enhances the user experience by increasing the network data rate and the number of concurrent users, and reducing latency and power consumption. To ensure all these improvements, there is a technological leap where all layers of the network are involved. From a physical layer perspective, the main innovation is the frequency increase towards the millimeter wave band, also known as the mmWave band. To date, communication systems have been based on the sub-6 GHz spectrum, which is currently saturated due to the limited bandwidth. To address this issue, the research community is focusing on the feasibility of the mmWave band (30 GHz - 300 GHz) for commercial communications applications, since this band offers great advantages, such as large spectrum availability. However, there are also several technological challenges associated with millimeter waves, such as higher attenuation losses and the paradigm shift in propagation mechanisms compared to the sub-6 GHz band. In order to meet the necessary requirements of this band, it is therefore essential to perform a detailed study and characterization of the propagation channel involved in the communication.

In this thesis, the main contribution is focused on the characterization and measurement of communication channels in the mmWave band. To this end, it proposes the study of the physical layer of the communication channel from different perspectives, such as *optimization, simulation, emulation, classification, characterization* and *measurement*. Four main contributions can therefore be identified.

First, the use of optimization algorithms based on evolutionary algorithms has been proposed to optimize key performance indicators in a simulated network deployment. The simulation of propagation channels through simulators and channel modeling simplifies the complexity of the analysis compared to costly measurement campaigns, making it a suitable solution in the early stages of network development. Optimizing network parameters from a simulator thus provides a first approximation to the requirements of a real communication network. By optimizing the transmit power in the radiating elements of the network, it is possible to simultaneously improve several network parameters at multiple layers of such network.

Second, channel emulation and identification techniques have been developed for the emulation and classification of propagation channels. On the one hand, channel emulation, based on the reconstruction of target channels in the laboratory, is an intermediate solution between theoretical simulators and complex measurement campaigns. The recreation of scenarios with specific characteristics is useful for testing devices under specific operating conditions and for analyzing the communication channel. This thesis contemplates the time-gating technique as a postprocessing method for channel emulation. On the other hand, scenario identification is crucial to understanding the environments in which communications take place and deciding how they should be conducted. In this thesis, dimensionality reduction techniques are considered as a classification strategy for several propagation scenarios. Both channel emulation and scenario classification techniques have been validated through measurements in controlled environments.

Third, the knowledge of the channel response with respect to an incident wave is essential for establishing communication on a link. Therefore, it is necessary to characterize the spatial and temporal profiles of the communication channel by determining the direction-of-arrival and time-of-arrival of the channel multipath components. For this reason, this thesis develops techniques based on the joint estimation of the direction-of-arrival and time-of-arrival based on frequency invariant beamformers, which are robust to the large bandwidths employed in the mmWave band. In particular, two different techniques have been proposed, one based on elliptical arrays for 2D characterization, and the other based on toric arrays for 3D characterization.

Finally, the thesis concludes with the presentation of a measurement campaign in an industrial environment under operational conditions. The characterization of the propagation channel based on simulations and channel emulation is complemented and validated by measurement campaigns in the final stages of the development of a communication network. These industrial environments have become particularly relevant due to industrial processes automation in factories. However, these environments are particularly challenging due to their time-varying and high-density nature, leading to the high probability of link blockage. Therefore, this thesis examines the radio propagation conditions in such environments and analyses how network management techniques provide coverage in these challenging scenarios.

Keywords: anechoic chamber, beam management, channel emulation, characterization, classification, dimensionality reduction, Direction-of-Arrival, frequency invariant beamformer, heterogeneous networks, industrial scenario, measurement, mmWaves, optimization, radio propagation, reverberation chamber, spectral efficiency, time-gating, Time-of-Arrival.

Resumen

La tecnología de telefonía móvil 5G promete cambiar la sociedad tal y como la conocemos. Esta nueva tecnología mejora la experiencia del usuario al aumentar la velocidad de datos de la red y el número de usuarios simultáneos, a la vez que se reducen la latencia y el consumo de energía. Para garantizar todas estas mejoras, se produce un salto tecnológico en el que intervienen todas las capas de la red. Desde el punto de vista de la capa física, la principal innovación es el aumento de frecuencia hacia la banda de ondas milimétricas. Hasta la fecha, los sistemas de comunicaciones se han basado en el espectro sub-6 GHz, que actualmente está saturado debido a su ancho de banda limitado. Para solucionar este problema, se está estudiando la viabilidad de la banda de ondas milimétricas (30 GHz - 300 GHz) para aplicaciones de comunicaciones comerciales, ya que esta banda ofrece grandes ventajas, como una gran disponibilidad de espectro. Sin embargo, también existen varios retos tecnológicos asociados a las ondas milimétricas, como unas mayores pérdidas por atenuación y el cambio de paradigma en los mecanismos de propagación en comparación con la banda sub-6 GHz. Por tanto, para cumplir los requisitos necesarios de esta banda, es esencial realizar un estudio y una caracterización detallados del canal de propagación implicado en la comunicación.

En esta tesis, la principal contribución se centra en la caracterización y medida de canales de comunicaciones en la banda de ondas milimétricas. Para ello, se plantea el estudio de la capa física del canal de comunicaciones desde diferentes perspectivas, como la *optimización, simulación, emulación, clasificación, caracterización* y *medida.* Por tanto, se pueden identificar cuatro contribuciones principales.

En primer lugar, se propone el uso de algoritmos de optimización basados en algoritmos evolutivos para optimizar los indicadores clave de rendimiento en un despliegue de red simulado. La simulación de canales de propagación mediante simuladores y modelado de canal simplifica la complejidad del análisis en comparación con las costosas campañas de medida, lo que la convierte en una solución adecuada en las primeras fases de desarrollo y despliegue de una red. La optimización de los parámetros de red desde un simulador proporciona así una primera aproximación a los requisitos de una red de comunicaciones real. Al optimizar la potencia de transmisión en los elementos radiantes de la red, es posible mejorar simultáneamente varios de sus parámetros de rendimiento en múltiples capas.

En segundo lugar, se han desarrollado técnicas de emulación e identificación de canal para la emulación y clasificación de canales de propagación. Por un lado, la emulación de canal, basada en la reconstrucción de canales objetivo en el laboratorio, es una solución intermedia entre los simuladores teóricos y las complejas campañas de medida. La recreación de escenarios con características específicas es útil para la prueba de dispositivos en condiciones específicas de funcionamiento y para analizar el canal de comunicaciones. Esta tesis concibe la técnica de *time-gating* como un método de postprocesado para la emulación de canales. Por otro lado, la identificación de escenarios es crucial para comprender los entornos en los que tienen lugar las comunicaciones y decidir cómo deben establecerse. En esta tesis se plantea el uso de técnicas de reducción de la dimensionalidad como estrategia de clasificación de varios escenarios de propagación. Tanto las técnicas de emulación de canal como las de clasificación de escenarios se han validado mediante medidas en entornos controlados.

En tercer lugar, el conocimiento del canal de propagación es esencial para establecer la comunicación en un enlace. Por tanto, es necesario caracterizar los perfiles espaciales y temporales del canal de comunicaciones determinando la dirección de llegada (DoA) y el tiempo de llegada (ToA) de las componentes multitrayecto del canal. Por este motivo, en esta tesis se desarrollan técnicas basadas en la estimación conjunta de la DoA y el ToA mediante *beamformers* invariantes en frecuencia, que son robustos a los amplios anchos de banda empleados en la banda de ondas milimétricas. En particular, se han propuesto dos técnicas diferentes, una basada en *arrays* elípticos para caracterización 2D y la otra basada en matrices tóricas para la caracterización 3D.

Finalmente, la tesis concluye con la presentación de una campaña de medidas en un entorno industrial en condiciones operativas. La caracterización del canal de propagación basada en simulaciones y en la emulación del canal se complementa y valida mediante campañas de medida en las etapas finales del desarrollo de una red de comunicaciones. Estos entornos industriales han cobrado especial relevancia debido a la automatización de los procesos industriales en las fábricas. Sin embargo, estos entornos son particularmente complejos debido a su naturaleza variable en el tiempo y su elevada densidad, lo que conlleva una alta probabilidad de bloqueo de los enlaces. Por lo tanto, esta tesis analiza las condiciones de propagación radioeléctrica en dichos entornos y analiza cómo las técnicas de gestión de red proporcionan cobertura en estos desafiantes escenarios.

Palabras clave: cámara anecoica, gestión de haz, emulación de canal, caracterización, clasificación, reducción de dimensionalidad, dirección de llegada, *beamformer* invariante en frecuencia, red heterogénea, escenario industrial, medida, mmWaves, optimización, radiopropagación, cámara reverberante, eficiencia espectral, *time-gating*, tiempo de llegada.

Contents

Acronyms

1G First Generation.

3GPP 3rd Generation Partnership Project.

4G Fourth Generation.

5G Fifth Generation.

6G Sixth Generation.

AC Anechoic Chamber.

AI Artificial Intelligence.

AMR Autonomous Mobile Robot.

AoA Azimuth-of-Arrival.

BS Base Station.

CDF Cumulative Distribution Function.

CEA Concentric Elliptical Array.

CFR Channel Frequency Response.

CIR Channel Impulse Response.

CoMP Coordinated MultiPoint.

D-MIMO Distributed MIMO.

DAS Delay-and-Sum.

DFT Discrete Fourier Transform.

DL Deep Learning.

DNN Deep Neural Network.

DoA Direction-of-Arrival.

DoD Direction-of-Departure.

DR Dimensionality Reduction.

EE Energy efficiency.

eMBB enhanced Mobile BroadBand.

EoA Elevation-of-Arrival.

ESPRIT Estimation of Signal Parameters Via Rotational Invariance Techniques.

FFT Fast Fourier Transform.

FIB Frequency Invariant Beamformer.

FR1 Frequency Range 1.

FR2 Frequency Range 2.

GA Genetic Algorithm.

GMM Gaussian Mixture Model.

HetNet Heterogeneous Network.

ICT Information and Communication Technology.

IDFT Inverse Discrete Fourier Transform.

IFFT Inverse Fast Fourier Transform.

IIoT Industrial Internet of Things.

InF Indoor Factory.

IoT Internet of Things.

ITU International Telecommunication Union.

k-NN k-Nearest Neighbors.

KPCA Kernel PCA.

KPI Key Performance Indicator.

LDA Linear Discriminant Analysis.

LoS Line-of-Sight.

M2M Machine-to-Machine.

MIMO Multiple-Input Multiple-Output.

MISO Multiple-Input Single-Output.

ML Machine Learning.

mMTC Massive Machine Type Communications.

mmWave millimeter wave.

MPC Multi-Path Component.

MUSIC MUltiple SIgnal Classification.

MVDR Minimum Variance Distortionless Response.

NB Naive Bayes.

NLoS Non Line-of-Sight.

NMSE Normalized Mean Square Error.

NSGA-II Non-Dominated Sorting Genetic Algorithm II.

OFDM Orthogonal Frequency-Division Multiplexing.

OTA Over-the-Air.

PAP Power Angular Profile.

PCA Principal Component Analysis.

PDF Probability Density Function.

PDP Power Delay Profile.

PG Path Gain.

PL Path Loss.

PRB Physical Resource Block.

PSO Particle Swarm Optimization.

RC Reverberation Chamber.

RF Radio Frequency.

RMa Rural Macrocell.

RMSE Root Mean Square Error.

RSRP Reference Signal Received Power.

RWP Random Waypoint Model.

RX Receiver.

SAGE Space-Alternating Generalized Expectation-maximization.

SIMO Single-Input Multiple-Output.

SINR Signal-to-Interference-plus-Noise Ratio.

SISO Single-Input Single-Output.

SMPSO Speed-constrained Multi-objective PSO.

SNOI Signal-not-of-Interest.

SNR Signal-to-Noise Ratio.

SOI Signal-of-Interest.

SSB Synchronization Signal Block.

SVM Support Vector Machines.

t-SNE t-distributed Stochastic Neighbor Embedding.

ToA Time-of-Arrival.

TX Transmitter.

UAV Unmanned Aerial Vehicle.

UCA Uniform Circular Array.

UCCA Uniform Concentric Circular Array.

UMa Urban Macrocell.

UMAP Uniform Manifold Approximation and Projection.

UMi Urban Microcell.

URLLC Ultra Reliable Low Latency Communication.

UWB Ultra-Wide Band.

VAE Variational AutoEncoder.

VNA Vector Network Analyzer.

Chapter 1

Introduction

1.1 Background and motivation

Mobile communications have changed the world. Since the late 19th and early 20th centuries, humanity has shown great interest in using electromagnetic waves as a tool for transmitting information. This was reflected in pioneering works in the theoretical framework, such as those presented by James Clerk Maxwell and Heinrich Rudolf Hertz, and in the practical framework, such as the transmission of radio waves across the Atlantic Ocean by Guillermo Marconi. Given the growing potential interest encouraged by the use of radio waves as a means of information transmission, the research carried out during the 20th century led to the implementation of the First Generation (1G) technology for mobile networks in the 1980s [1]. These primitive communications, based on voice communications through analog technology, have been evolving until the current generation, the Fifth Generation (5G) technology for cellular networks, based entirely on digital technology and data communications [2]. Currently, the 3rd Generation Partnership Project (3GPP) has proposed three use cases, namely, enhanced Mobile BroadBand (eMBB), Ultra Reliable Low Latency Communication (URLLC), and Massive Machine Type Communications (mMTC), for the deployment of 5G networks [3]. These use cases appear as a consequence of the increasingly demanding requirements of the end users deployed in the networks. The former requirements are reflected in the Key Performance Indicators (KPIs), such as data rate, spectral efficiency, energy efficiency, reliability or power consumption [4]. Simultaneously improving all these KPIs is the main technological challenge for the scientific community, in order to provide efficient communications for current (5G) and future (6G) mobile generations.

With the purpose of enhancing the KPIs, the research community is making multiple efforts from the physical layer perspective [5, 6]. Several fields of study, such as antenna design [7], channel modeling [8], Multiple-Input

Multiple-Output (MIMO) systems [9], beam management [10], or signal precoding [11], are currently involved in the development of enabling technologies. All the previous fields have a common point, they are moving towards millimeter waves (mmWaves). The millimeter wave band includes those frequencies in the range 30 - 300 GHz, whose wavelength is less than 1 cm. Until just a few years ago, millimeter waves were not taken into account for commercial deployments because they were considered technologically unfeasible. Therefore, communications have traditionally been carried out in the sub-6 GHz band [12]. However, the limited bandwidth available in the sub-6 GHz band and studies carried out in the last decade have turned the mmWave band into an opportunity for further technological development of communication systems [13, 14, 15, 16, 17]. Although the millimeter wave band has been proposed as a technological solution since the last century [18, 19, 20], it was not until just 10 years ago that first deployments in challenging scenarios demonstrated their feasibility in real communication environments. For instance, in 2013, fieldwork based on measurement campaigns was conducted in the 28 GHz and 38 GHz frequency bands in outdoor and indoor environments in Manhattan [21]. This work showed that by using high-directive antennas, it is possible to overcome the attenuation phenomena in dense environments such as Manhattan with cell radii of 200 meters. These promising results encouraged the radio propagation research community to devote all its efforts to the analysis of these frequency bands, extending this experimental work over the last decade [22, 23, 24]. Simultaneously, standardization organizations like 3GPP began to standardize the radio access technology, known as 5G New Radio (5G NR), from Release 15 onwards. Thus, a new standardized frequency band, named Frequency Range 2 (FR2), between 24.25 GHz and 71 GHz was added to the existing Frequency Range 1 (FR1) band between 410 MHz and 7125 MHz, indicating the confidence of the major telecommunications companies in millimeter waves [25, 26]. In just 10 years, commercial deployments of 5G NR networks in the millimeter wave band are starting to become a reality [27, 28].

From the perspective of radio propagation research, not only the transition to millimeter waves is a turning point, but also the propagation scenarios where communications can take place are increasing. Thus, the concept of Heterogeneous Network (HetNet) networks proposes to improve the distribution of radio resources by subdividing the network into cells of different sizes [29]. While traditional deployments have taken into account urban propagation models for macrocell sizes in the FR1 band (e.g. the Okumura-Hata model [30]), communication scenarios of different nature are emerging today, such as vehicular [31], Unmanned Aerial Vehicle (UAV) [32, 33], railway [34, 35, 36], or indoor [37, 38, 39] communications. Additionally, environments that previously did not have a dedicated infrastructure to support a communication network are now being analyzed, such as shopping malls [40, 41], factories [42, 43], or stadiums [44]. Finally, even typical macrocell scenarios based on outdoor urban communications [45, 46, 47] and outdoor rural communications [48] need to be re-examined to take into account the characteristics of these higher frequency bands.

Both the emergence of mmWaves and the development of new communication scenarios emerge as an opportunity to improve mobile communications by providing a better quality of service based on higher bandwidth, less interference, and higher spatial resolution, which involves high throughput and high reliability in the cellular network. However, these advancements also give rise to several issues, leading to new open challenges. The main challenge is directly related to the propagation characteristics of millimeter waves. The shorter wavelength at these frequencies implies a paradigm shift in propagation mechanisms. Friis transmission formula [49], which expresses the Path Loss (PL) in free space, increases quadratically with the frequency, which signifies a higher channel attenuation in the mmWave band. In addition, the signals in this band are highly susceptible to shadowing and other factors, not so relevant at sub-6 GHz, have to be taken into account. This has implications such as rain attenuation due to the wavelength having a size equivalent to raindrops [50, 51], or even atmospheric attenuation due to the presence of gas molecules in the atmosphere [52]. Thus, the presence of foliage [53, 54], human blockage [55, 56, 57] and material penetration [58] becomes major blocking sources. Finally, reflection, scattering and diffraction propagation phenomena vary with respect to the sub-6GHz band. At millimeter waves, surfaces with a roughness comparable to the wavelength will favor propagation by diffuse scattering, to the detriment of specular reflection [59, 60]. In addition, due to the short wavelength, the diffraction loss phenomena are more pronounced because the objects are large in terms of wavelength, which tends more toward blocking [61].

Given the large number of attenuation sources, it is essential to ensure the Line-of-Sight (LoS) condition in the communication channel, or to enable mechanisms to ensure an adequate signal level in the communication channel even in Non Line-of-Sight (NLoS) condition. For that purpose, the physical characterization of the propagation channel, i.e., channel modeling [8, 62, 63], is fundamental both from the temporal side, and from the spatial and angular side. On the one hand, the temporal characteristics are summarized in the Channel Impulse Response (CIR), or Power Delay Profile (PDP), which express the amplitude/power of the Multi-Path Components (MPCs) as a function of their Time-of-Arrival (ToA) [64]. From the measured PDP of a propagation channel, temporal characteristics such as delay spread, number of rays, or the ToA from each component are extracted [19, 65]. On the other hand, the spatial characteristics are outlined in the Power Angular Profile (PAP), which accounts for the received power of the MPCs in terms of the angle [66, 67]. Thus, for a 3D spatial characterization, azimuth and elevation angles must be taken into account, and features such as Direction-of-Arrival (DoA) or Direction-of-Departure (DoD) can be extracted for each of the MPCs [68, 69]. Note that the previous profiles can be combined to produce a joint angular and temporal characterization of the communication channel [64, 69, 70].

The main problem with measurement campaigns is the high cost in terms of complexity and logistics [21, 27]. To address this issue, theoretical channel models are proposed to reduce the complexity of measurement campaigns [71]. Mainly, these are divided into deterministic models, such as those proposed by ray tracing techniques [72, 73, 74, 75], and stochastic models, which are based on probabilistic models of the channel characteristics, such as Saleh-Valenzuela [76], Zwick [77] or standardized 3GPP [26, 78] models. These channel models are eventually extended to channel simulators, which efficiently calculate channel characteristics through simulations, some of the best known being QuaDRiGa [79, 80] or NYUSIM [81, 82]. Therefore, these simulators are particularly useful in the early stages of mobile network deployments.

As a trade-off solution between extensive measurement campaigns and theoretical channel models, the concept of channel emulation emerges [83, 84]. This consists of the emulation of specific channel characteristics, either of the spatial or temporal profile, from measurements taken in controlled environments such as anechoic chambers [85, 86] and reverberation chambers [87]. Thus, the complexity of the measurement process is significantly reduced. This alternative has taken on particular relevance with the development of MIMO systems, which are more complex in terms of radio analysis as they have multiple transmitters and receivers operating simultaneously [88, 89]. Therefore, validating new 5G devices with Over-the-Air test allows the radio analysis to be assessed in the laboratory. For instance, additional examples of such techniques are the emulation of target channels with Rician or Hyper-Rayleigh distributions [90, 91], or the emulation of small-scale fading effects [92].

Another main field based on the study of channel modeling to improve the characterization of the communication channel is based on Artificial Intelligence (AI), Machine Learning (ML), and Deep Learning (DL). Several AI techniques have been proposed for 5G research [93, 94], with the communication channel being one of the main areas of interest. Specifically, neural networks have been employed for satellite image processing, allowing the inference of path loss channel models in both sub-6 GHz and mmWave bands [95, 96, 97]. Another approach is based on the use of supervised learning algorithms for the classification and identification of propagation environments. Optimal classification of scenarios allows channeling models to be adapted to the specific characteristics of a given environment, thereby improving the reliability and performance of communications [98]. Several practical cases of scenario identification of different nature can be found in the literature, such as indoor [99], vehicular [100] or high-speed railways [101] scenarios.

In line with the earlier discussion regarding spatial and temporal profiles, localization using these profiles has been one of the most extensively studied fields due to its interest in channel characterization [102, 103, 104]. For that reason, multiple methods to estimate and characterize the Direction-of-Arrival in multipath channels have been developed over time [105]. Typically, these methods exploit the spatial diversity of a sensor array by using sensor signal processing theory to extract the angles of incidence of an incoming wave. Some of them, such as Delay-and-Sum (DAS) [106] and Minimum Variance Distortionless Response (MVDR) [107] techniques, are based on spatial beam scanning. Others, such as the MUltiple SIgnal Classification (MUSIC) [108] algorithm, exploit the orthogonality of the signal with respect to the noise subspace in the spatial covariance matrix. Subsequently, new approaches appeared based on matrix-shifting techniques such as Estimation of Signal Parameters Via Rotational Invariance Techniques (ESPRIT) [109], or based on expectation-maximization techniques, such as Space-Alternating Generalized Expectation-maximization (SAGE) algorithm [110, 111], which avoid an extensive search of the unknown DoAs. These methods have been widely used during the development of measurement campaigns for the optimal characterization of the spatial profile of the communication channel. In addition, both localization mechanisms and channel identification take on special relevance in the deployment of mmWave 5G networks due to the need to ensure secure, reliable and robust communication links. This is mainly due to the need to compensate for the attenuation losses at these frequencies by designing highly directional antennas. This is where the concept of beam management comes in, based on the intelligent design of mmWave system architectures to manage the Radio Frequency (RF) chains to ensure optimum link performance [10, 112, 113]. Therefore, the beam management concept deals with a number of mechanisms that are in place to facilitate this management [114]. For instance, beam sweeping provides spatial coverage of a specific region and evaluates the beam suitable for each user based on beam measurement, beam determination, and beam reporting [115, 116, 117, 118]. Additionally, as mmWaves are prone to blocking, beam recovery mechanisms are defined to recover a blocked link by identifying a candidate beam [119]. Thus, the standardization of these mechanisms, together with the development of theoretical channel models and channel characterization techniques, as well as measurement campaigns, are key to the development of future mobile communications.

This thesis is fundamentally aimed towards contributing to the characterization and measurement of communication channels in the mmWave band, to facilitate and enhance the deployment of future generation technologies for mobile communications. This thesis document is organized as follows. Chapter 1, and more specifically Section 1.1, introduces the importance of millimeter waves for 5G systems, outlining the main challenges associated with the physical layer in this mmWave band and the studies and solutions proposed based on the current state-of-the-art. Sections 1.1.1 - 1.1.6 take a closer look at some of the issues presented in Section 1.1, which will be key aspects for this thesis and will be explored in more detail in later chapters. Sections 1.2 and 1.3 propose the main objectives developed and the methodology followed throughout the thesis, respectively. Section 1.4 shows the main results obtained throughout the thesis. Chapter 2 presents the journals, which include the main contributions performed during the thesis. These are preceded by an introduction to each work. This chapter is divided into four sections. Section 2.1 illustrates the simulation of propagation channels through channel simulators and their optimization using genetic algorithms and particle swarm optimization. Section 2.2 deals with channel emulation and classification, proposing post-processing techniques and identification algorithms. Section 2.3 introduces techniques based on frequency invariant beamformers to jointly characterize DoA and ToA in communication channels. Section 2.4 presents a measurement campaign performed in an industrial scenario under operational conditions for a 5G NR network, focusing on beam management procedures. Finally, Chapter 3 summarizes the main contributions developed and outlines potential future research lines based on the work of the present thesis.

1.1.1 Anechoic and Reverberation Chambers

Anechoic Chambers (ACs) and Reverberation Chambers (RCs) have been widely used in the antenna and propagation research community over time [120, 121, 122]. As previously pointed out, these facilities are suitable for Over-the-Air tests, measuring antennas, or electromagnetic compatibility tests. Basically, the first ones are enclosed environments, covered with absorbers to prevent any reflection of the waves from any surface. Therefore, it is possible to emulate an environment equivalent to free space propagation in an indoor scenario. Thus, the Line-of-Sight of the propagation channel between a Transmitter (TX) - Receiver (RX) link can be analyzed [123]. Based on this premise, several techniques have been developed for Over-the-Air testing in these environments, ranging from antenna measurements [124] to capacity and diversity assessment in MIMO systems [125, 126]. On the other hand, reverberation chambers are cavities whose walls are completely covered with conductive material. Unlike anechoic chambers, these environments favor multipath components, which make the LoS and NLoS components to be present in the TX-RX link. Generally, reverberation chambers are equipped with stirrers that randomize the multipath environment, i.e. the temporal and spatial profiles. Thus, the samples are independent of each other generating a stochastic approximation [127, 128]. In addition, the electromagnetic response of the chamber can be tuned by modifying the stirrer location and adding loads to the chamber. This allows a wide range of studies to be carried out in these environments in terms of the chamber setting, such as emulation of channel model distributions [90, 91, 129], antenna measurements [130, 131, 132], K-factor estimation [133], MIMO measurements [134] or coherence bandwidth distribution [135]. In summary, both types of chambers are excellent approaches for studying the communication channel under specific conditions defined by a given setting. In this thesis, these controlled scenarios take on particular importance in Chapters 2.2 and 2.3, where they are used to emulate communication channels that allow us to validate the proposed techniques.

1.1.2 Optimization algorithms

An optimization algorithm is simply an algorithm whose objective is to find the best element from a set of available elements in order to optimize a specific criterion or a fitness function. If the set of elements is not large enough, an extensive search is sufficient to find the optimal element. However, as the complexity of the problem increases, either through an increase in the number of variables or a large solution space, finding the optimum is no longer trivial. In addition, the criterion or fitness function to be met can be based on multiple objectives simultaneously, giving rise to what is known as multi-objective optimization [136]. As a result, a field of study has been elaborated around the development of optimization algorithms for solving general-purpose problems [137, 138]. Two main families of algorithms can be highlighted, the Genetic Algorithms (GAs) and the Particle Swarm Optimization (PSO). The genetic algorithms are techniques inspired by the process of natural evolution. These exploit genetic evolution techniques such as cellular crossover or cellular mutation to converge a set of solutions to a heuristic optimum solution [139, 140]. To do this, from an initial random population of individuals, the best candidates are selected according to the chosen fitness function. These candidates are mixed using the crossover mechanism, thus generating new individuals in the population. Finally, small changes are randomly made to some individuals using a mutation operator [141]. This adjustment prevents the population from being trapped in a local maximum or minimum of the solution space. Repeating this process iteratively over several iterations results in the convergence of the individuals in the population toward a heuristic solution. A widely extended example of this type of algorithms is NSGA-II [142]. Particle swarm optimization is based on the natural principles of the movement of animals, such as the flight of a bird flock. It uses the interaction between the particles in the swarm to converge on a solution [143, 144]. Applied to the field of optimization, a set of initial particles is distributed in the search space. Based on the fitness function, these particles move through the solution space at different speeds and accelerations according to the local fitness evaluation, but also to the best fitness evaluation, i.e., the best known location in the search space [145]. Iteratively, these swarms of particles eventually converge on heuristic solutions by exploring and exploiting the search space. These techniques have been successfully applied to the electromagnetic field [146] with algorithms such as SMPSO [147]. In this thesis, both families of algorithms are exploited in order to search for the optimal parameters of a 5G network deployment by combining prior principles and channel model simulators. These aspects are explored in detail in Chapter 2.1.

1.1.3 Time-Gating Technique

Time-gating is a post-processing technique that can be used for signal processing purposes. Specifically, this method modifies the time response of a given signal. In order to do this, the signal is windowed within the temporal region of interest using a windowing function, e.g., rectangular, Hamming, or Hann windows. Therefore, the temporal profile of interest can be analyzed in depth. This technique is well known in the field of signal processing and has been successfully used in real applications such as imaging for objects identification [148], or cancer cell analysis for near-field scanning microwave microscopy [149, 150]. Particularized to propagation channel applications, this method applied over electromagnetic signals modifies the channel impulse response in the time domain. Note that this technique can be properly applied when the time resolution of the signal is sufficient to distinguish different multipath components. Therefore, mmWave band is feasible for the application of time-gating due to the large bandwidth available [151]. In the antenna field, this method has been proposed to remove non-desired components in antenna radiation pattern measurements in anechoic chambers [152] and highly reflective environments [153]. These measurements are suitable even in purely reverberation chambers through windowing the LoS component [154]. By isolating this component from NLoS reflections, the channel impulse response of the equivalent free space channel is emulated, i.e. the equivalent response that would be acquired in an anechoic chamber is achieved. In this way, the advantages of this method can be further extended. Not only does temporal windowing allow for the isolation of a specific component, but also the shifting and replication of these windows increase the degrees of freedom of the propagation channel. These properties can be exploited in channel emulation to generate new emulated communication channels, a topic thoroughly discussed in Chapter 2.2 of this thesis.

1.1.4 Machine Learning and Dimensionality Reduction

As previously stated, machine learning approaches have been proposed for solving problems related to the propagation field. Within ML algorithms, two main branches can be distinguished. The first of these branches encompasses supervised learning algorithms, which, based on a set of labeled training observations, can learn to identify data distributions in order to distinguish new observations [155]. This class of algorithms has been used to solve propagation channel classification problems [98, 99, 100, 101], with some classical supervised learning algorithms being k-Nearest Neighbors (k-NN) [156], decision trees [157], Naive Bayes (NB) [158], Linear Discriminant Analysis (LDA) [159] or Support Vector Machines (SVM) [160]. However, these algorithms are subject to a specific number of classes that must be known in advance. To solve this issue, the paradigm of unsupervised learning algorithms appears. This type of algorithm works on an unlabelled dataset. This means that there is no a priori knowledge in the input [161]. Therefore, these techniques attempt to identify patterns and properties inherent to the dataset, generating data structures based on feature extraction [162]. Within these algorithms, there is a subset called Dimensionality Reduction (DR) algorithms. These convert a high-dimensional space into a low-dimensional space while preserving the information of the original dataset [163]. Thus, this dimensionality reduction can reveal information by the cluster analysis in the low-dimensional space. One of the classic examples of DR algorithms is Principal Component Analysis (PCA) [164]. This technique consists of transforming the original coordinate system into a new lower-dimensional coordinate system which is a linear combination of the original. This transformation is achieved by maximizing the variance of the data for each coordinate. A more complex case is proposed by t-distributed Stochastic Neighbor Embedding (t-SNE) [165]. This algorithm performs non-linear transformations on a dataset to generate a low-dimensional space. Specifically, the algorithm models the distances in the original space as a set of probabilities between observations and generates the low-dimensional space in such a way that these probabilities are preserved also for the observations in the new space. Additionally, the algorithm can be tuned by using hyperparameters, in order to adjust the data visualization [166]. Applied over communication channels, an accurate classification can facilitate channel modeling approaches, which are fundamental for the development of future mobile deployments. In Chapter 2.2, these methods are studied as a technique to visually identify and classify several communication channels.

1.1.5 Frequency Invariant Beamformers for DoA and ToA characterization

Previously introduced in the background and motivation, the DoA and ToA estimation algorithms are essential for the characterization of the spatial and temporal profiles of the propagation channel. However, the solutions previously proposed are generally valid for narrowband approximations [106, 107, 108, 109, 110, 111], meaning they are applicable to signals with limited bandwidth. This approach is not valid for the 5G paradigm, where bandwidth is expected to scale up significantly to take advantage of Ultra-Wide Band (UWB) technology [167]. For this reason, it is necessary to analyze signal processing solutions based on wideband channels [168]. One of the alternatives for these channels is the one devised by Frequency Invariant Beamformers (FIBs). As the name suggests, they have a frequency-invariant response, allowing them to operate over large bandwidths [169, 170]. Although FIBs were initially proposed to be implemented using linear arrays, there was a quick convergence towards circular arrays due to the full angular coverage in the spatial profile, and their uniform response around the angular axis [171]. Thus, methods for joint estimation of DoA and ToA with uniform circular arrays have been developed over time [172, 173, 174]. These methods take advantage of the spatial distribution of the elements along the array to model the phase distribution at each element in terms of the DoA and ToA. Through the use of FIBs and basis function expansions, it is possible to make the spatial and temporal components of the channel independent, performing an independent analysis of each multipath component in both profiles. Measurement campaigns have validated the good performance of these algorithms in multipath environments [175], with the possibility of extending them to new geometries such as concentric circular arrays [176]. In this thesis, an in-depth analysis of the performance of these methods is carried out in order to propose new geometries that generalize the techniques already proposed in the state-of-the-art. This study is presented in Chapter 2.3.

1.1.6 Radiopropagation in industrial environments

Communications in industrial environments have attracted particular interest in the last decade [177, 178]. This interest stems from the desire to automate industrial processes [179]. From a communications point of view, the use of wireless technology will allow the elimination of wiring in production lines, increasing the flexibility and reconfiguration of the agents involved in the factories. However, this wireless communication must be highly robust and reliable. This is the reason why the integration of 5G networks is emerging as a candidate solution [180]. However, from a propagation perspective, there are several challenges due to the unique nature of these scenarios [181] and several studies and measurement campaigns have been performed in order to characterize these factories and industrial environments [182, 183, 184, 185]. Naturally, as it has been generally the case with any propagation channel, these studies have eventually moved to the mmWave band [42, 43, 186]. In particular, compared to other indoor environments, factories possess high ceilings and a large amount of metal equipment, such as machinery or industrial ventilation ducts. In addition, these environments tend to be divided into different halls depending on the work being carried out. These characteristics make the environment prone to heavy multipath propagation. Furthermore, they are also considered to be time-varying channels due to the influence of obstacles such as robots or humans that are constantly moving. This makes the channel susceptible to fading due to LoS blocking, which can be critical for the reliability of the network. In response to these issues, the beam management procedures previously addressed are crucial for optimal resource management of the mobile agents involved in the communications [10, 112, 114]. Based on these techniques, it is possible to design a smart robust network with respect to time-varying channels and capable of providing highly reliable communications. Chapter 2.4 deals with the addressed issues and presents a measurement campaign performed in an FR2 5G network, which deeply analyzes the physical layer of the communication channel. Additionally, a focus on beam management procedures is proposed to assess the feasibility of these techniques under operational conditions.

1.2 Objectives

As detailed in the previous Section, this thesis deals with the study of the propagation channel in the mmWave band, since this topic is fundamental for the development of mobile communications. The analysis of the propagation channel is of special relevance as it is the physical source in which communications take place. From this perspective, the present work proposes the following objectives to be fulfilled:

- ***Simulation* and *optimization* of propagation channels.** Simulation of communication channels is fundamental in the development of early stages of network deployment. At the same time, the optimization of network parameters allows an efficient deployment of radio resources. This issue is addressed in Chapter 2.1 on the basis of a multilayer network optimization.

- ***Emulation* and *classification* of communication channels.** Due to the constantly increasing number of propagation channels where communications can take place, a proper classification of these channels is essential. Likewise, channel emulation emerges as an opportunity to efficiently recreate these channels in controlled environments. Chapter 2.2 analyzes these issues using post-processing and Machine Learning techniques through channels acquired in controlled scenarios.

- ***Characterization* based on DoA and ToA estimation.** The determination of Direction-of-Arrival and Time-of-Arrival in multipath environments facilitates the design of a communications system due to the crucial importance of knowing these parameters. Chapter 2.3 proposes and develops methods for the characterization of both parameters based on arrays with multiple geometries.

- ***Measurements* of communication channels.** The validation of the theoretical channel models is carried out on the basis of measurement campaigns in operational conditions. Chapter 2.4 presents the validation of an industrial scenario in the FR2 band based on measurement campaigns in factories.

In summary, the present thesis aims to shed light on, and contribute to the development of future mobile communications through the study and analysis of the propagation channel in the mmWave wave band from multiple approaches and points of view.

1.3 Research Methodology

In order to satisfactorily meet the challenges previously proposed, the following research methodology has been conducted. First, there has been a thorough review of the state-of-the-art in the early stages of the development of the thesis. This state-of-the-art review has mainly addressed the following three topics: (i) Characteristics of controlled environments such as anechoic and reverberant chambers, (ii) Measurement techniques and equipment, and (iii) Post-processing methods and propagation channel characterization. After this review of the state-of-the-art, which has also been carried out methodically throughout the thesis, the whole process of data analysis process and programming tasks has been performed with *MatLab software*. This programming language and computing environment has been used for signal post-processing (e.g., Time-Gating technique), and the development of characterization methods (e.g., Frequency Invariant Beamformers) and propagation channel classification (e.g. Machine Learning techniques such as t-Distributed Stochastic Neighbor Embedding). Regarding the simulation and optimization of the propagation channel, in specific cases with a high computational cost, the Spanish Supercomputing Network has been employed through the Picasso node.

From the *hardware* and measurement perspective, fieldwork has been mainly carried out in two locations: the facilities of the SWAT research group of the University of Granada (UGR), Spain, and the 5G Smart Production Lab of Aalborg University (AAU), Denmark. In the SWAT research group facilities, a Vector Network Analyzer (VNA) has been employed. Specifically, Rohde & Schwarz ZVA67 model, which measures the scattering parameters and can operate up to 67 GHz. As radiating elements, standardized gain horns fed with waveguide-to-coaxial transitions have been used. This equipment has been used in the infrastructure consisting of a semi-anechoic and semi-reverberant chamber equipped with automatic positioning systems for the radiating elements. This fact has allowed to conduct several measurements in controlled scenarios, which have been part of the focus of analysis in this thesis. In the 5G Smart Production Lab facilities, the radio scanner Rohde & Schwarz TSME6 is employed. This equipment is mounted on the top of an Autonomous Mobile Robot (AMR), which is designed to self-navigate the facilities. Thus, this equipment allows and facilitates the process of generating coverage maps in a propagation scenario, being able to subsequently process and analyze the measurements through *MatLab*.

The combination of the acquisition of measurements by means of the *hardware* elements previously introduced, together with the post-processing analysis and methods proposed and implemented through the *software* tools, has made it possible to perform and obtain the results shown in this thesis.

1.4 Thesis Results

This is the list of **publications** in renowned **journals** that support the results achieved in this thesis:

- [J1] **A. Ramírez-Arroyo**, P. H. Zapata-Cano, Á. Palomares-Caballero, J. Carmona-Murillo, F. Luna-Valero and J. F. Valenzuela-Valdés, “Multilayer Network Optimization for 5G & 6G,” *IEEE Access*, vol. 8, pp. 204295-204308, 2020.
- [J2] **A. Ramírez-Arroyo**, J. C. González-Macías, J. J. Rico-Palomo, J. Carmona-Murillo, and A. Martínez-González, “On the Spectral Efficiency for Distributed Massive MIMO Systems,” *Applied Sciences*, vol. 11, no. 22, p. 10926, 2021.
- [J3] **A. Ramírez-Arroyo**, A. Alex-Amor, C. García-García, Á. Palomares-Caballero, P. Padilla and J. F. Valenzuela-Valdés, “Time-Gating Technique for Recreating Complex Scenarios in 5G Systems,” *IEEE Access*, vol. 8, pp. 183583-183595, 2020.
- [J4] **A. Ramírez-Arroyo**, L. García, A. Alex-Amor and J. F. Valenzuela-Valdés, “Artificial Intelligence and Dimensionality Reduction: Tools for Approaching Future Communications,” *IEEE Open Journal of the Communications Society*, vol. 3, pp. 475-492, 2022.
- [J5] **A. Ramírez-Arroyo**, A. Alex-Amor, P. Padilla and J. F. Valenzuela-Valdés, “Joint Direction-of-Arrival and Time-of-Arrival Estimation with Ultra-wideband Elliptical Arrays,” *IEEE Transactions on Wireless Communications*, 2023.

In addition, the following two **papers** are included as results of the thesis and are currently under review in peer-reviewed journals:

- [J6] **A. Ramírez-Arroyo**, A. Alex-Amor, R. Medina, P. Padilla and J. F. Valenzuela-Valdés, “Joint Ultra-wideband Characterization of

Azimuth, Elevation and Time of Arrival with Toric Arrays," submitted to *IEEE Transactions on Wireless Communications*, 2023.

- [J7] **A. Ramírez-Arroyo**, M. López, I. Rodríguez, T. B. Sørensen, S. Caporal del Barrio, P. Padilla, J. F. Valenzuela-Valdés and P. Mogensen, "FR2 5G Networks for Industrial Scenarios: An Experimental Characterization and Beam Management Procedures in Operational Conditions," submitted to *IEEE Transactions on Vehicular Technology*, 2023.

Other related **papers** that have been generated along the development of this thesis but have not been included:

- [J8] F. Delgado-Ferro, **A. Ramírez-Arroyo**, J. Navarro-Ortiz and J. F. Valenzuela-Valdés, "ML-based 5G Network Performance Analysis in a Semi-Anechoic and Semi-Reverberation Chamber," submitted to *IEEE Wireless Communications*, 2023.
- [J9] J. E. Galeote-Cazorla, **A. Ramírez-Arroyo**, F. J. López-Martínez and J. F. Valenzuela-Valdés, "Empirical Validation of a Class of Ray-Based Fading Models," submitted to *IEEE Transactions on Wireless Communications*, 2023.

Other related **conferences** that have been generated along the development of this thesis but have not been included:

- [C1] **A. Ramírez-Arroyo**, A. Alex-Amor, C. García-García, Á. Palomares-Caballero, P. Padilla and J. F. Valenzuela-Valdés, "Time-Gating Technique to Emulate New Scenarios," in *2021 15th European Conference on Antennas and Propagation (EuCAP)*, Dusseldorf, Germany, pp. 1-5, 2021.
- [C2] **A. Ramírez-Arroyo**, L. García, A. Alex-Amor and J. F. Valenzuela-Valdés, "An Introduction to Dimensionality Reduction for Propagation Measurements," in *2022 16th European Conference on Antennas and Propagation (EuCAP)*, Madrid, Spain, pp. 1-5, 2022.
- [C3] **A. Ramírez-Arroyo**, A. Alex-Amor, P. Padilla and J. F. Valenzuela-Valdés, "Wideband Elliptical Arrays for DoA and ToA Estimation in Multipath Environments," in *2023 17th European Conference on Antennas and Propagation (EuCAP)*, Florence, Italy, pp. 1-5, 2023.
- [C4] **A. Ramírez-Arroyo**, M. López, I. Rodríguez, T. B. Sørensen, S. Caporal del Barrio, P. Padilla, J. F. Valenzuela-Valdés and P. Mogensen, "A Study of FR2 Radio Propagation with Focus on Mobility Management in an Industrial Scenario," in *2023 17th European Conference on Antennas and Propagation (EuCAP)*, Florence, Italy, pp. 1-5, 2023.

The work carried out during the thesis has led to the grant of a **project** for young researchers, in which the Ph.D. candidate is the PI:

- Project Title: "Estudio de la estimación conjunta de *Direction-of-Arrival* (DoA) y *Time-of-Arrival* (ToA) para geometrías genéricas en el rango de ondas milimétricas", Ref.: PPJIB2022-05, Funding Entity: Universidad de Granada (UGR), 01/01/2023-31/12/2023, PI: **Alejandro Ramírez Arroyo**. Received Funding: 1.500,00€

During the realization of the thesis, the following **international stay** has been carried out in research centers of recognized prestige:

- Research stay for 3 months at Department of Electronic Systems, Aalborg University (AAU), Aalborg, Denmark, in 2022.

In addition, the PhD candidate's academic training has been complemented by the following **international courses**:

- European School of Antennas and Propagation (ESoA) course entitled "Mobile Radio Propagation for 5G and Beyond", and organized by Prof. Claude Oestges, University of Louvain (UCLouvain), Louvain-La-Neuve, Belgium, 2022.
- European School of Antennas and Propagation (ESoA) course entitled "Short Range Radio Propagation: Theory, Models and Applications", and organized by Prof. Vittorio Degli Esposti, University of Bologna (UniBo), Cesenatico, Italy, 2023.

Chapter 2

Publications

The research results obtained during the development of this thesis are presented in this chapter. For that purpose, the publications related with these results are included and the main results and contributions are summarized throughout this chapter in each publication. In total, 7 works are presented, 5 of which correspond to JCR indexed journals, and 2 of them are works that have been submitted to journals and are being reviewed. These works have been organized in four sections: (i) Network Optimization over simulated Communication Channels, (ii) Emulation and Classification of Propagation Channels, (iii) Characterization of Ultra-Wide Band Propagation Channels, and (iv) Measurement Campaigns at mmWave frequencies. Thus, these four sections cover the main issues related to propagation channels which have been analyzed throughout the thesis, namely, *optimization, simulation, emulation, classification, characterization* and *measurement.* In addition, each paper provides information on the journals in which they have been published and their quality indexes.

2.1 Network Optimization over simulated Communication Channels

2.1.1 Multilayer Network Optimization for 5G & 6G

This work presents the optimization of a channel model simulator based on multi-objective optimization in several layers, namely, the radio and network layers. Through the use of GAs and PSO, the search for optimal power allocation for the network deployment is performed. The optimal deployment of a telecommunications network is closely linked to the KPIs. Optimizing some of them, such as channel capacity, energy consumption, signaling costs, or energy efficiency, maximizes the deployment performance. In addition, a channel simulator based on heterogeneous networks with different cell sizes (macrocells, microcells and picocells) and propagation models (Urban Macrocell, Urban Microcell and Rural Macrocell) is considered. Optimization results confirm the possibility of improving multiple KPIs simultaneously from different layers of the network.

THIS IS THE PUBLISHED VERSION OF THE PAPER:

A. Ramírez-Arroyo, P. H. Zapata-Cano, Á. Palomares-Caballero, J. Carmona-Murillo, F. Luna-Valero and J. F. Valenzuela-Valdés, "Multilayer Network Optimization for 5G & 6G," *IEEE Access*, vol. 8, pp. 204295-204308, 2020.

- Journal Impact Factor (JIF) in JCR 2020: 3.367
- Category: COMPUTER SCIENCE, INFORMATION SYSTEMS. JIF Rank: 65/161 (Q2).
- Category: ENGINEERING, ELECTRICAL & ELECTRONIC. JIF Rank: 94/273 (Q2).
- Category: TELECOMMUNICATIONS. JIF Rank: 36/91 (Q2).

Disclaimer:
This work has been published in IEEE Access.
DOI: 10.1109/ACCESS.2020.3036744

IEEE Access
Multidisciplinary | Rapid Review | Open Access Journal

Received October 17, 2020, accepted October 31, 2020, date of publication November 9, 2020, date of current version November 19, 2020.

Digital Object Identifier 10.1109/ACCESS.2020.3036744

Multilayer Network Optimization for 5G & 6G

ALEJANDRO RAMÍREZ-ARROYO[1], **PABLO H. ZAPATA-CANO**[1],
ÁNGEL PALOMARES-CABALLERO[1], **JAVIER CARMONA-MURILLO**[2], **(Member, IEEE),**
FRANCISCO LUNA-VALERO[3], **(Associate Member, IEEE), AND JUAN F. VALENZUELA-VALDÉS**[1]
[1]Department of Signal Theory, Telematics and Communications, CITIC, Universidad de Granada, 18014 Granada, Spain
[2]Department of Computing and Telematics Engineering, Universidad de Extremadura, 06006 Badajoz, Spain
[3]Department of Languages and Computer Science, Universidad de Málaga, 29016 Málaga, Spain

Corresponding author: Alejandro Ramírez-Arroyo (alera@ugr.es)

This work was supported in part by the projects of the Spanish National Program of Research, Development, Innovation, under Grant TIN2016-75097-P, Grant RTI2018-102002-A-I00, and Grant EQC2018-004988-P, in part by the Junta de Andalucía under Project B-TIC-402-UGR18, in part by the European Regional Development Fund and Junta de Extremadura under Project IB18003, and in part by the Predoctoral Grant FPU19/01251 and Grant FPU18/01965.

ABSTRACT Mobile communications are growing and the number of users is constantly increasing at an accelerated rate, as well as the demand for the services they request. In the last few years, many efforts have focused on the design and deployment of the new fifth generation (5G) cellular networks. However, novel highly demanding applications, which are already emerging, need to go beyond 5G in order to meet the requirements in terms of network performance. But, at the same time, as the Earth does not allow us to increase the carbon footprint anymore, the energy consumption of the communication networks has to be critically taken into consideration. A multi-objective approach for addressing all these issues is therefore required. This work develops a cellular network framework that allows the evaluation of different system parameters over dynamic traffic patterns, as well as optimizing the different conflicting objectives simultaneously. The novelty relies on that the optimization process integrates key performance indicators from different layers of the network, namely the radio and the network layers, aiming at reaching solutions that account for the power consumption of the base stations, the total capacity provided to mobile users and also the signaling cost generated by handovers. Moreover, new metrics are needed to evaluate different solutions. Starting from the well-known energy efficiency merit factor (bits/Joule), three new merit factors are proposed to classify the network performance since they take into account several network parameters at the same time. These indicators show us the ideal working point that can be used to plan the point of operation of the network. These operation points are a medium-high power and capacity load and a low signaling load.

INDEX TERMS 5G networks, optimization, heterogeneous networks, energy efficiency.

I. INTRODUCTION

In 2019, the monthly mobile traffic reached 38 Exabytes, while this figure is estimated to be 160 Exabytes by 2025, at a 30 percent compound annual growth rate. On the other hand, the number of devices connected to the Internet will triple the world population by 2022, when there will be 3.6 devices per user compared to 2.4 devices per user in 2017 [1], [2]. This growth is due to the emergence of new applications on the Internet, such online video games, vehicular communications, tactile Internet, remote surgery, virtual reality (VR) and augmented reality (AR), which do not only require large bandwidths, but also challenging requirements such as a massive number of connections and ultra-low and reliable latency [3]–[5]. In order to meet these requirements, both public and private initiatives started to develop the new generation of mobile networks, the fifth or 5G, almost a decade ago. The design principles of this new technology were aimed at reaching 100x data rates, end-to-end delay below 1ms, 99.999% reliability, etc. Among them, given the current carbon footprint of the ICT industry [6], [7], these challenging operating requirements have to be achieved by saving 90% of the energy consumption. Three main target scenarios have been standardized in the Release 15 of

The associate editor coordinating the review of this manuscript and approving it for publication was Javed Iqbal.

the 3GPP consortium [8], namely, enhanced mobile broadband (eMBB), for providing the users with higher data rates than LTE, massive machine-type communications (mMTCs), for enabling a massive number of device connections, and, finally, ultra-reliable low-latency communications (uRLLC), aimed at low latency transmissions for small amounts of data with ultra-high reliability. Despite these predefined 5G scenarios, applications such as the tactile Internet does have requirements that go beyond 5G, as they need both extreme high data rates and ultra-reliable low latency. Therefore, the next generation networks (6G) will necessarily encompass new scenarios that combine the features of eMBB and uRLLC in order to provide services to the newly envisioned applications [9], [10].

Our working hypothesis is that a multi-layer optimization will be required to satisfy these demands, as it is proposed here. Indeed, this work targets these latter scenarios using a novel approach that jointly optimizes not only several performance criteria from both the radio and the network layer, but also considering energy efficiency issues [11]. From the radio interface, we have considered the capacity the network provides to the users, and the power consumption of the base stations (BSs). And, from the network layer, the number of bits used for signaling when a handover occurs due to the user mobility, as it is strongly correlated to the latency [12] required for uRLLC scenarios. To the best of our knowledge, these optimization objectives, which accounts for two complementary planes of the network, are yet rarely considered together. An accurate modeling of a heterogeneous network has been used, taking into consideration 5G enabling technologies [13] such as mmWave [14], massive MIMO [15], [16] and network densification [17].

The optimization of different layers of the network and energy at the same time is seldom reported in the literature. Several previous works related to the physical layer are, for example, the work of Zhang *et al.* [18]. They have proposed a joint power allocation, mode selection, and channel assignment scheme for optimizing energy efficiency in D2D (Device-to-Device) communications. Liu *et al.* [19] have performed two-dimensional optimization on traffic data rate and green energy generation on HetNets. Fletscher *et al.* [20], [21] have proposed several methods to optimize user allocation and energy efficiency simultaneously. Rengarajan *et al.* [22] and Di Renzo *et al.* [23] propose novelty models for the optimization of energy efficiency at the physical layer. On the other hand, works related to the network layer are, for example, the work of Keshavarzian *et al.* [24]. They have introduced several algorithms to minimize the energy consumption taking into account the mobility-aware capability. Muñoz *et al.* [25] optimize load balancing and handover costs in the network layer. Also, Xu *et al.* [5] address the handover problem in ultra-dense heterogeneous networks, focusing on a single-layer optimization where they can decrease the delay in the network. Since the problem is addressed from a single-layer perspective, the authors obtain slightly lower data rates than their reference model.

In this article, several multi-objective optimization problems have been formulated, tackling separately all pairwise combination of the capacity, signaling and power consumption objectives, plus a three-objective approach that considers them all simultaneously. The problems have been addressed by using Pareto-based multi-objective metaheuristics that compute a set of trade-off solutions to the problem, thus providing the decision maker (the network designer) with compromise network configurations.

The structure of this article is as follows. Section II presents the configuration of the system, detailing the different models used to compute the parameters and association strategies for assigning users to the base stations. In Section III, the optimization and network configuration are shown. Section IV analyzes the results obtained in the optimization. Finally, Section V provides the reader with the main conclusions drawn in this work and the future lines that remain open for future research.

II. SYSTEM MODEL

This section first describes the modeling of the target scenario, including both the base stations and the users of the network. Then, it details the formulation of the problem objectives, such as, capacity, power consumption, and signaling overhead. An availability indicator is also used to measure the demand satisfaction of the users in a given amount of time. Finally, the UE-BS association policy is included. The inputs and outputs of all models are combined to generate a comprehensive model based on the physical and network layers. This comprehensive model allows the realization of a multilayer optimization in Sections III and IV.

A. CONFIGURATION

The scenario comprises a working area of dimensions 500×500 m^2, where the BSs are distributed according to a uniform random distribution that is independent on each of the axes. These BSs are characterized into three possible cell types according to their size and operating frequency (macro, micro or femto). Their specifications are shown in Table 1. UEs are also randomly distributed around the terrain, but they move using a Random Waypoint Model (RWP), where their location, velocity and acceleration change over time. A graphical example of cell types and UEs movements in a scenario is illustrated in Fig. 1. According to the MIMO framework used, UEs may be equipped with two, three and four antennas, modelling low, medium and high demanding users, respectively.

As a traffic model between the UE and the BS, we assume that the session arrival follows a Poisson process with mean rate $\lambda = 0.2$. We also assume that the duration of a typical session is exponentially distributed with mean $\mu = 10$ s. In this scenario, BSs are connected to an access network where the routers offer IPv6 connectivity between mobile users and the rest of the deployed network.

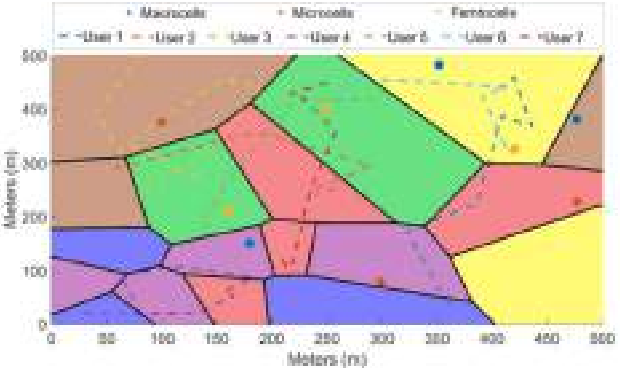

FIGURE 1. **UEs and BSs in different propagation scenarios. Purple "UMA LOS", Blue "UMA NLOS" Green "UMi LOS", Red "UMi NLOS" Brown "RMa LOS" and Yellow "RMa NLOS".**

TABLE 1. **Specifications of the Base Stations.**

	Macrocell	Microcell	Femtocell
Frequency (GHz)	2	5	28
Bandwidth (MHz)	10	25	140
Max Power (dBm)	46	25	20
Height (m)	25	10	6
BSs antennas	5	20	100

B. CAPACITY MODEL

First of all, the calculation of the power received (P_{RX}) by each user at each time t must be performed.

$$P_{RX}\,[\mathrm{dBm}] = P_{TX}\,[dBm] + G\,[dB] + L_{PATHLOSS}[dB] \quad (1)$$

where P_{RX} and P_{TX} are the received and transmitted power, respectively, G is the sum of the gains of the transmitting and receiving antennas, and $L_{PATHLOSS}$ are the signal losses due to the transmission path that depend on the region where the signal is transmitted, as shown in Fig. 1. $L_{PATHLOSS}$ is computed as:

$$L_{PATHLOSS}\,[dB] = L_{SPACE}\,[dB] + L_{SHADOWFADING}\,[dB] \quad (2)$$

where L_{SPACE} are the signal losses due to the distance between UE and BS, decaying following an attenuation exponent n. $L_{SHADOWFADING}$ is the variation in $L_{PATHLOSS}$ due to multiple variables such as multipath propagation, the distribution of which follows a log-normal distribution. This distribution is given by an expected value μ and standard deviation σ that depend on the transmission models depicted below. Mathematically, L_{SPACE} can be seen as

$$L_{SPACE}\,[dB] = 20log_{10}\left(\frac{4\pi d_0}{\lambda}\right) + n10log_{10}\left(\frac{d}{d_0}\right) \quad (3)$$

where the first term computes the signal losses in free space until reference distance d_0 for a specific wavelength λ, and the second term considers how the signal decays at a distance d depending on the region with an attenuation exponent n.

Three transmission models are used in the experiment, UMi (Urban Microcells), UMa (Urban Macrocells) and RMa (Rural Macrocells) [26]–[28]. Fig. 1 shows how the terrain is divided according to different transmission models randomly. Each transmission model has also two possible cases, LOS (Line-Of-Sight) and NLOS (Non-Line-Of-Sight). They are assigned randomly to each region, making NLOS to appear more frequently in urban models, whereas LOS does in rural scenarios. The combination of models and cases results in six scenarios characterized by the attenuation exponent n, the expected value μ and the standard deviation σ.

Finally, the signal to interference plus noise ratio (SINR) has been calculated as follows:

$$SINR_k = \frac{P_{rx,j,k}(mW)}{\left(\sum_{\substack{n=1\\ n\neq j}}^{M} P_{rx,n,k}\,(mW)\right) + P_{N_0}(mW)} \quad (4)$$

where $P_{rx,j,k}$ is the power received by user k from BS_j and $\sum_{\substack{n=1\\ n\neq j}}^{M} P_{rx,n,k}$ is the total power received by user k from all the base stations M that work at the same frequency excepting BS_j, i.e., the interference. Finally, P_{N_0} is the noise power given by:

$$P_{N_0}\,[dBm] = -174 + 10\log_{10}\left(BW_j(MHz)\right) \quad (5)$$

where BW_j is the bandwidth available by the BS_j in MHz.

Once the SINR is obtained, the capacity of the channel can be calculated. The main aim when using MIMO is to improve the spectral efficiency by increasing the number of transmitters and receivers, resulting in better transmission conditions compared to a SISO system. This MIMO model is commonly used for studies of different nature, such as channel estimation [29], radiation pattern studies [30], or MIMO channel efficiency evaluations [31]. The capacity is computed for each time instant t due to the UEs movement. Eq. (6) is used for MIMO systems [29]–[32].

$$C_{k,j,t}\left(\frac{bits}{s}\right) = \frac{BW_{j,t}}{N_{j,t}}\log_2\left|I_j + \frac{SINR_{k,t}}{No.Rx_k} * H * H^H\right| \quad (6)$$

where $BW_{j,t}/N_{j,t}$ is the total bandwidth available to the user, and the $\log_2$ calculates the spectral efficiency in bits/s/Hz, where I_j is an identity matrix whose dimension is the number of transmitter antennas by BS_j and H is the channel matrix, which is generated randomly by using a complex normal distribution. The channel matrix dimensions are given by the number of antennas from users (rows) and base stations (columns).

C. POWER CONSUMPTION MODEL

One of the objectives of the optimization problem is the reduction of energy cost. Therefore, energy efficiency (EE) is an important parameter to define [33]. This indicator becomes fundamental in the deployment of new mobile generations due to the requirements of 90% reduction of power consumption. Nowadays, energy efficiency is a parameter to be taken into account in any new deployment [34], [35]. We have considered an EE indicator that shows the performance in bits per Joule, that is, the number of bits of information that can be reliably transmitted through the communication channel per energy unit. It can be defined as:

$$EE\left(\frac{bits}{Joule}\right) = \frac{DataRate(bits/s)}{PowerConsumption(W)} \tag{7}$$

One of the main motivations for including EE issue is the fact that the theoretical limits of both the transmission data rates and the minimum latency are known: the Shannon limit and the speed of light, respectively. However, there is no known limit of the maximum energy efficiency that can be obtained in a network. In addition, Section IV will show how energy efficiency is a major distinguishing criterion to characterize the results.

Regarding the power consumption model, it takes into account both the consumption between UE and BS and the consumption between BS and the router in the access network. The power consumption of a BS, denoted as P_{bc}, can be expressed in the Aggregated Power Consumption Model [36] as:

$$P_{bc} = \alpha P + \beta + \delta S + \rho \tag{8}$$

where P represents the transmitted or radiated power of each BS and S is the data rate. The coefficient α denotes the power transmission efficiency due to an RF amplifier and supply losses, β represents the power dissipated due to signal processing, and δ is a constant denoting dynamic power consumption per data unit. These terms differ for different BS types defining a differential consumption model [37].

Detailing this model further, it can be seen that the power consumption can be therefore divided into three types. On the one hand, αP, the power consumption proportional to the transmission that depends directly on the power transmitted by the BS. On the other hand, δS, the power consumption proportional to the capacity that depends exclusively on the demand required by the user since it is directly linked to the data traffic. Finally, β and ρ represent fixed consumption terms.

Taking all this into consideration, the total power consumption in the system can be calculated as follows:

$$P_{Total} = \sum\nolimits_{i=1}^{BS} M_i P_{bc} + P_{Backhaul} \tag{9}$$

where the first term is the sum of the powers of all base stations multiplied by the number of transmitting antennas corresponding to each base station, and $P_{Backhaul}$ represents the energy consumed by the backhaul. This latter has to be included to sum up the power consumption required to carry the signaling information from one region to another through the access network.

D. SIGNALING MODEL

To achieve an efficient service provisioning and a better usage of the network resources, 5G networks require to address issues not only in the radio and data link environment, but also in the layer 3 management protocols. Mobility management mechanisms allow reachability and maintain ongoing communication during roaming of mobile users in different networks. One of the key aspects in the performance of these protocols is related to the signaling, especially in densified networks, where high-speed mobile nodes experience frequent handovers with a high signaling load due to the short cell radius [38], [39].

Thus, for optimal system design, it is necessary to accurately model the impact of the mobility in other network parameters. In this work, we measure the impact of the mobility management on radio and link metrics. In current centralized solutions, the mobility management relies on an IP mobility anchor node, which is the network agent that tracks the network connection point of a user as the user moves. Whenever the user changes their point of attachment to the network, the user registers with this agent through signaling messages informing of its current location. As a result of this signaling exchange, the Mobile Node (MN) acquires a new IP address in this foreign network.

In mobility management protocols [40], [41], this anchor node is the centralized part of the system since it is on the critical path of both signaling and data for mobile users. Regarding the signaling, a mobility management protocol requires that an MN sends a location update to its mobility anchor whenever it moves from one subnet to another. This location registration is required even though the MN does not communicate with others while moving. The signaling cost associated with location updates may become very significant as the number of MNs increases.

Moreover, this cost depends on the size in bytes of the signaling messages (s_u) and the number of hops between the MN and the mobility anchor ($h_{MN-anchor}$) in every handover process during the time interval that the MN communication remains active. Thus, we refer to the aggregate signaling cost of registration update for a session as C_s and it is expressed as:

$$C_s = s_u h_{MN-anchor} N_h \tag{10}$$

where N_h is the number of handovers that cause a layer 3 handover.

E. AVAILABILITY MODEL

Availability is defined as the probability of a user demand to be fulfilled at a given time. This parameter turns out to be of vital importance because in many occasions the total capacity provided is not sufficient to meet the user requirements. This fact will depend on whether his demand is satisfied by the capacity, so availability in the model is computed as

$$Availability_k = P\{C_k \geq D_k\} \tag{11}$$

where C_k is the capacity for the user k and D_k are the demands from the user k. Total availability in the system is computed as an average of every user present in the scenario.

$$Availability_{Total} = \frac{\sum_{i=1}^{k} Availability_k}{N} \tag{12}$$

F. BS-UE ASSIGNMENT

Two policies for pairing UEs and BSs have been devised, being they two aimed at maximizing SINR. Other criteria could have been used, such as minimizing the distance or maximizing the power received between UE and BS. However, the maximization of the SINR is the one usually applied in actual network deployments. The two strategies are:

- Planning 1: the UE is paired with the BS that provides the highest SINR out of all those available in the scenario, regardless its type.
- Planning 2: the aim is to avoid continuous handovers between BSs. As so, it pairs the UE with the BS that provides the highest SINR among all those available in the scenario, but only when the change leads to an improvement in the SINR above a certain threshold.

III. MULTILAYER NETWORK OPTIMIZATION

A. NETWORK CONFIGURATIONS

Two different configurations have been devised. A light setting with 20 UEs and 5 BSs, and a heavy one with 50 UEs and 20 BSs, respectively. From now on, the first configuration will be mentioned as light configuration, and the second one as heavy configuration. These configurations distribute the propagation models randomly as shown in Fig. 1. Moreover, the type of UEs and BSs are also uniformly distributed.

B. OPTIMIZATION PROBLEM

This section clearly states the optimization problem addressed in this work. First, the decision variables that define the problem are the transmitted powers of the BSs, which fully impacts all the optimization objectives defined in the previous section. Indeed, it clearly determines the power consumption of the network (eq. (9)). As it also directly changes the SINR, because it modifies the power received by the users (eq. (4)) and, hence, the data rates provided by the network (eq. (6)) and the cell limits, inducing a different number of handovers, thus modifying the signaling cost. Moreover, the availability changes if the data rates changes. As it can be seen, updating the transmission power of just one single base station may provoke changes in the values of all the objectives.

Given the problem difficulty, with a severe epistasis among the decision variables, and the potential large scale of the instances of the ultradense deployments, we have relied on metaheuristics [42] as optimization tools. More concretely, evolutionary multi-objective algorithms (MOEAs) have been used [43] because, on the one hand, they can approximate the Pareto front of a problem in one single run and, on the other hand, as randomized black-box optimizers, they can address optimization problems with nonlinear, non-differentiable or noisy objective functions. The objectives to be optimized are those shown in Section II, namely, capacity, power consumption, signaling cost and availability.

In this way, the optimization problem is mathematically formulated as follows: Let B be the set of the deployed Base Stations (BTSs). A solution to the presented problem is then a real-valued vector, $s \in (0, 1]^{|B|}$, where s_i indicates the transmitted power of BTS i. Thus, the four objectives functions are:

$$\begin{aligned} f_1(s) &= \min\ PowerConsumption(s) \\ f_2(s) &= \max\ Capacity(s) \\ f_3(s) &= \min\ SignalingCost(s) \\ f_4(s) &= \max\ Availability(s) \end{aligned}$$

which are grouped and combined resulting in several multi-objective optimization problems.

C. ALGORITHMS

A brief technical description of the each of the algorithms used to address the problem is provided in the following. Note that in order to measure the quality of the approximated fronts given by the algorithms, the hypervolume indicator (HV) was used, which is recognized as one of the most suitable Pareto-compliant metrics in the multi-objective community [44]. Higher values of this indicator are better.

- NSGAII: The Non-Dominated Sorting Genetic Algorithm II [45] is a genetic algorithm based on generating a new population from the original one by applying the typical genetic operators (selection, crossover, and mutation); then, the individuals in the new and old population are sorted according to their rank, and the best solutions are chosen to create a new population.
- SMPSO: SMPSO [46] is a multi-objective particle swarm optimization algorithm in which global best particles are generally the non-dominated solutions found during the particle movement and they can be exploited to guide the particle swarm to approach the entire Pareto Front.

All the two algorithms use Polynomial Mutation as mutation operator, with a probability of 0.01. In the case of NSGAII, SBXCrossover with crossover rate of 0.9 is also used.

IV. RESULTS

In order to provide the results with confidence, 30 independent runs of the MOEAs have been carried out. Also, thorough statistical procedures have been used [47] with a confidence level of 95% (p-value < 0.05). The p-value obtained for the multcompare test is 1.5229e-06. The results of this procedure have shown that all the differences are statistically significant, thus pointing out that the HV of SMPSO is statistically greater (better) than that of NSGA-II and the MatLab algorithms. The results have been analyzed in terms of the empirical attainment functions (EAF) [48] and the best aggregated front among all the non-dominated solutions found in all the 30 runs. The EAD used here is the 50%-attainment surface in the multi-objective domain that is analogous to the median value in the single-objective one.

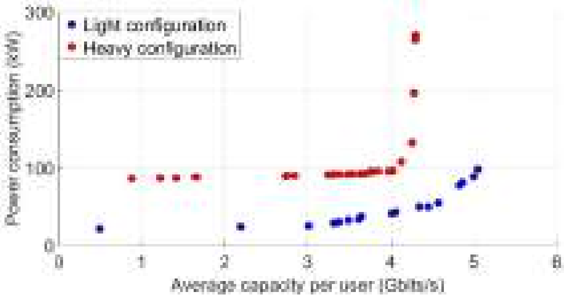

FIGURE 2. Pareto front of the average capacity per user against power consumption. Results obtained for planning 1 in both heavy and light configurations.

A. JOINT OPTIMIZATION OF CAPACITY AND POWER CONSUMPTION

The first experiment carried out considers two objectives: the capacity per user and the power consumption. The results show the average over time of the capacity for every UE. Similarly, they show the power consumption for every BS. Both light and heavy configurations have been considered. The assignment UE-BS selected is planning 1.

Fig. 2 shows the average capacity that a user can reach for the lowest power consumption that can provide that capacity. It can be concluded that heavier configurations need to use larger amounts of power to fulfill the user data rates demanded by each user. This behavior can be explained from two points of view. On the one hand, the number of UEs is larger in the heavy configuration. Therefore, the number of BSs has to be larger to obtain the same capacity per user, and the transmitted power will be larger for a larger number of BS. On the other hand, the more UEs and BSs, the more interference is generated in the system for the same scenario, which implies difficulties to provide the same service.

The benefits of having such an approximated Pareto front is that the decision maker can easily choose whether s/he desires to lose the capacity to save power, or conversely to provide the maximum possible capacity at the expense of power savings. One of the ways to find the balance between these two parameters can be obtained representing the relationship among themselves, the energy efficiency, as it can be observed in Fig. 3. This illustrates EE in the capacity range. The horizontal axis is the same as in Fig. 2, so that the vertical axis is scaled by normalizing it with respect to the horizontal axis and thus obtaining the EE. Therefore, the maximum point in terms of EE for both light and heavy strategies could be considered as an optimal operation point.

Fig. 3 shows how the most efficient points are those with an average capacity of around 3 Gbps for the light configuration and 4 Gbps for the heavy configuration. In addition, it can be clearly seen how the light configurations work better than the heavy configurations. Finally, it shows the differences in efficiency are greater in the light configurations.

From this point on, only light configuration has been used (in this section and in the others as well). The solutions with higher energy consumption have also been limited. As it can be seen in Fig. 3 the energy efficiency falls drastically at these points and we are not interested in working on these points.

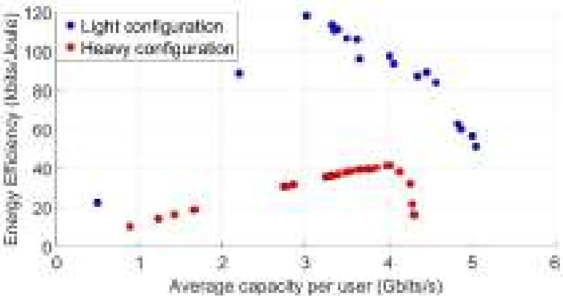

FIGURE 3. Energy efficiency of the Pareto front of the average capacity per user against power consumption. Results obtained for planning 1 in both heavy and light configurations.

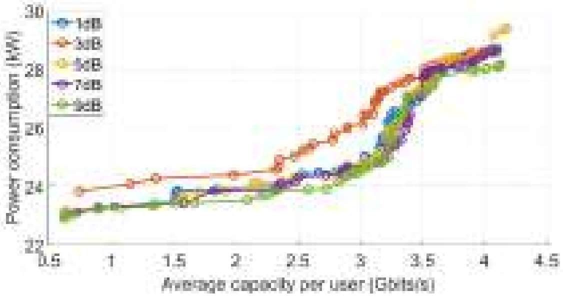

FIGURE 4. Pareto front of the average capacity per user against power consumption for several fixed thresholds. Results obtained for planning 2 in the light configuration. Best aggregated value.

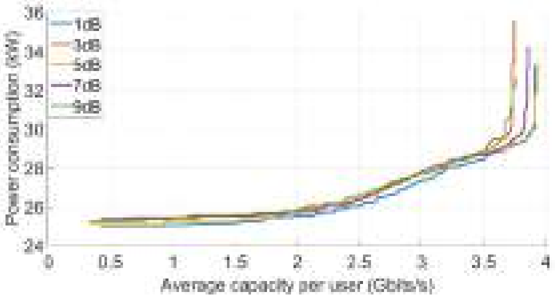

FIGURE 5. Pareto front of the average capacity per user against power consumption for several fixed thresholds. Results obtained for planning 2 in the light configuration. Average.

Now, the planning strategy (BS-UE assignment) is changed to evaluate its impact. The optimization is done separately with 5 different threshold values (1, 3, 5, 7 and 9 dB). The approximated Pareto fronts for the fixed threshold values are shown in Figs. 4 and 5. The results represent the best aggregated non-dominated solutions of the 30 runs of each threshold case in Fig. 4, whereas the attainment functions are depicted in Fig 5. Looking at Fig. 4, the results show similar results for the different thresholds, except for 3 dB (orange line), which is slightly worse. Despite the range between 3.2 and 3.5 Gbits/s, the best approximated front is when the threshold is equal to 9 dB. However, when moving to the average fronts in Fig. 5, the differences among thresholds

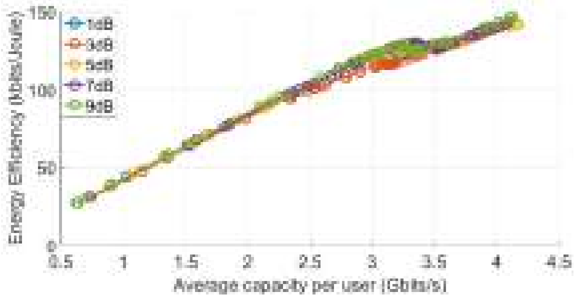

FIGURE 6. Energy efficiency of the Pareto front of the average capacity per user against power consumption for several fixed thresholds. Results obtained for planning 2 in the light configuration.

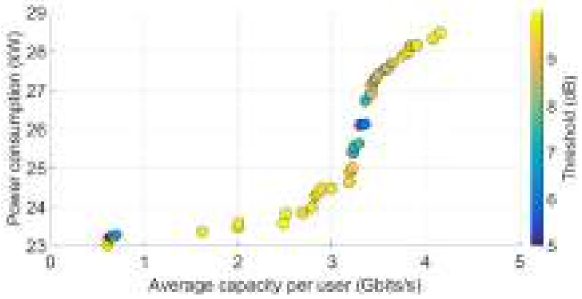

FIGURE 7. Pareto front of the average capacity per user against power consumption when the threshold is optimized. Results obtained for planning 2 in the light configuration.

diminish. In this figure, the blue line that represents a threshold of 1 dB is slightly better. This indicates that the algorithm can more easily find solutions with that threshold since average optimal results are achieved by the lowest threshold. In contrast with Fig. 4 where the best Pareto front results are found with a threshold of 9 dB. This fact indicates the need for a high computing workload to approach the average results towards the best aggregated values.

As it is explained in Section II.C, the merit factor accepted by the scientific community, EE (bits/Joule), eases the comparison of different solutions of a given approximation to Pareto front. In order to obtain the maximum limit of the energy efficiency, the values have been obtained from the aggregated Pareto fronts (see Fig. 4). Thus, Fig. 6 illustrates the energy efficiency for several thresholds, which are very similar among them. The only remarkable difference appears, again, in the central part of the graph, between 3 to 3.5 Gbits/s, where it seems that the slope decreases and the orange line (3 dB) is clearly below.

To obtain more information about the effects of the threshold on the network parameters, a new experiment has been conducted, but now including a threshold parameter as a decision variable to be optimized. The results obtained in this case are illustrated in Figs. 7 and Fig 8.

Fig. 7 depicts the approximated Pareto front when the threshold is taken into consideration. It also displays a color scale on the right part of the plot to show the threshold value computed by the algorithm for each of the non-dominated solutions reached. It can be observed that all these solutions have always obtained thresholds above 5 dB. A second interesting finding arises when the capacity is roughly 3.2 Gbits/s, where a sharp increase in the power consumption occurs. This is a very valuable information for the network designer (decision maker) as s/he can significantly reduce the energy consumption of the network, penalizing minimally its capacity. As it can be seen, at this point the algorithm tries different values for the threshold around 7 dB, without finding a better performance in terms of capacity without increasing power consumption. At a first glance, if only Fig. 7 is considered, it may seem reasonable to work at operating points below 3 Gbps. However, observing the energy efficiency in Fig. 8, the true fact is that the solutions near 4 Gbits/s do have the higher energy efficiency. This is due to the fact that the increase in energy consumption is counteracted by the rapid increase in capacity, so that in terms of efficiency, the increase in capacity is bearable at the expense of the additional transmission power required. It is also important to note from Fig. 8 that in the zone where the algorithm does not find suitable solutions (3 to 3.5 Gbits/s approximately) the trend of energy efficiency changes showing that best efficiencies are in accordance with Fig. 7.

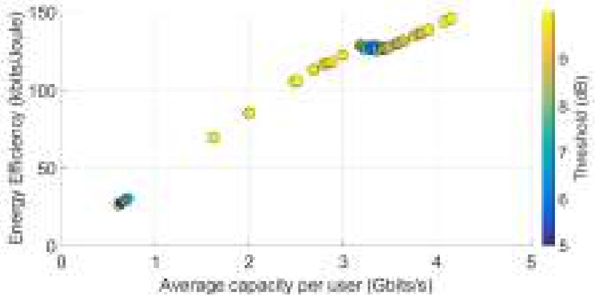

FIGURE 8. Energy efficiency of the Pareto front of the average capacity per user against power consumption when the threshold is optimized. Results obtained for planning 2 in the light configuration.

B. JOINT OPTIMIZATION OF SIGNALING COST AND CAPACITY

The second experimentation is the joint optimization of data rates and signaling cost. As explained above, signaling cost is the accumulative layer 3 mobility signaling overhead for supporting mobility service for a user. This metric is directly proportional to the number of hops between the mobility anchor and the user and also to the total number of handovers. Therefore, the reduction of this cost implies an overall reduction in the handover latency. Therefore, the aim of this second experiment is to target a possible 6G scenario where ultra-low latency and very high transmission data rates are required.

In a similar way to the previous section, the variables to be optimized are the transmitted power at the base station and the optimization is performed for fixed thresholds. Fig. 9 shows the aggregated front of the non-dominated solutions reached in the 30 independent runs. It can be seen that higher thresholds obtain the approximated fronts that converge the most. It has to be clarified that, a zero signaling cost indicates that

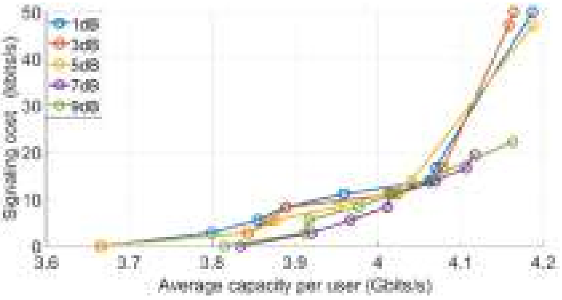

FIGURE 9. Pareto front of the average capacity per user against signaling cost for several fixed thresholds. Results obtained for planning 2 in the light configuration. Best aggregated value.

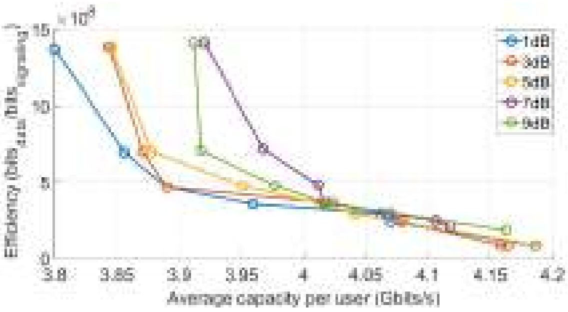

FIGURE 10. Efficiency ($bits_{data}/bits_{signaling}$) of the Pareto front of the average capacity per user against signaling cost for several fixed thresholds. Results obtained for planning 2 in the light configuration.

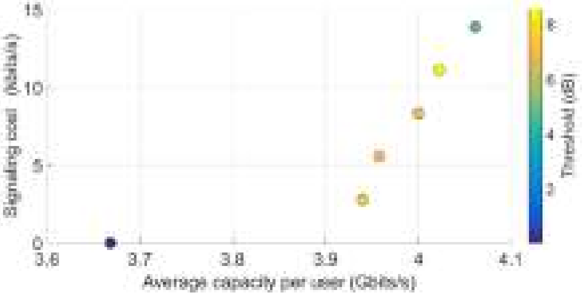

FIGURE 11. Pareto front of the average capacity per user against signaling cost when the threshold is optimized. Results obtained for planning 2 in the light configuration.

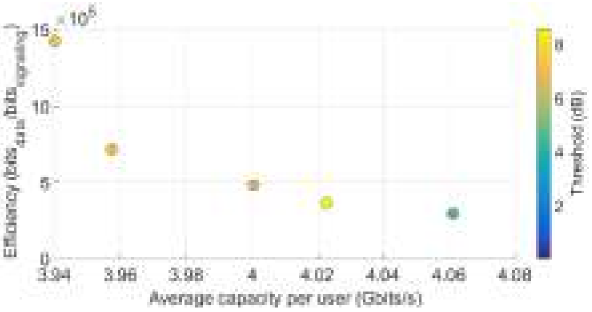

FIGURE 12. Efficiency ($bits_{data}/bits_{signaling}$) of the Pareto front of the average capacity per user against signaling cost when the threshold is optimized. Results obtained for planning 2 in the light configuration.

the user remains in the same cell throughout the simulation, sacrificing capacity at the cost of decreasing latency. In order to further analyse the information enclosed in the approximated fronts, similar to the merit factor shown previously (EE), this work proposes for the first time, and to the best of our knowledge, a merit factor that provides the ratio of data sent for each signaling bit used (if no signaling is generated because no handover occurs, the metric remains undefined).

Fig. 10 shows the results, which indicates that lower capacities obtain higher efficiencies in terms of signaling bits sent through the network per data bit. It can be therefore concluded that it is more interesting to work at operation points with low signaling. From the results, it can be seen that a high threshold is required to obtain the highest values in our merit factor (green and purple lines) since they obtain same merit factor for larger capacities.

In a similar way to the previous section, an optimization with a threshold as the variable is done. Figs. 11 and 12 show capacity-signaling cost optimization when the threshold value is a decision variable for the best aggregated value in order to see the maximum performance of the network. Similar to Fig. 9, Fig. 11 reveals that the higher capacity incurs the higher signaling cost. This is explained by the fact that to obtain maximum capacity, the user has to be constantly moving between those BSs that provide the best SINR, which incurs in signaling cost, and therefore, higher latencies. Moreover, paths followed by the signaling traffic are fixed. For that reason, it is not possible to find a large number of solutions in the Pareto front.

To conclude this section, it can be said that high thresholds produce better results than low thresholds. It should also be noted that the cost of signaling vary much more strongly than the capacities in relative terms. Finally, it is more convenient to work in the area of low signaling as it is shown in Fig. 12.

C. JOINT OPTIMIZATION OF SIGNALING COST AND POWER CONSUMPTION

In this section, a power consumption-signaling cost optimization is carried out following the methodology of the previous ones. Figs. 13 and 14 show the best aggregate and average value of the 30 simulations respectively. In these figures, it can be seen how the high threshold values (green and

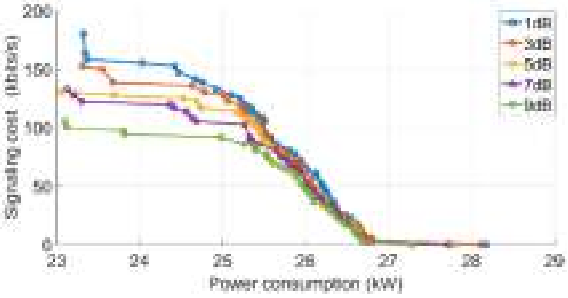

FIGURE 13. Pareto front of the power consumption against signaling cost for several fixed thresholds. Results obtained for planning 2 in the light configuration. Best aggregated value.

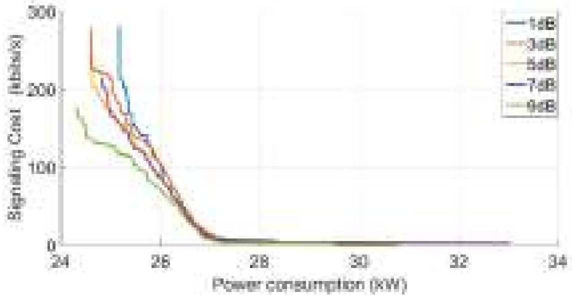

FIGURE 14. Pareto front of the power consumption against signaling cost for several fixed thresholds. Results obtained for planning 2 in the light configuration. Average.

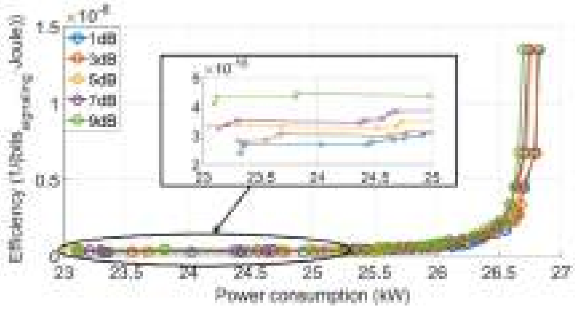

FIGURE 15. Efficiency ($1/(bits_{signaling} \cdot Joule)$) of the Pareto front of the power consumption against signaling cost for several fixed thresholds. Results obtained for planning 2 in the light configuration.

purple) work much better. Furthermore, the differences are much more pronounced for lower power consumption values. The higher power consumption incurs in lower signaling cost. The increase in the transmitted power by BSs decreases the number of handovers since the users tend to stay connected to the same BS.

In a similar way to the previous sections, a new merit factor that can compare the different points on the Pareto front is proposed. This new merit factor is the inverse of the watts consumed multiplied by the signaling cost. This merit factor will indicate the joint cost of the signaling and the power consumption and it will show the best operation points. Thus, Fig. 15 shows this new merit factor. In line with the previous figures, the best values of the new merit factor are obtained for the higher thresholds. This trend is shown across the entire range of power consumption. It can be seen how the most efficient working points are for the highest power consumed.

To follow the same structure as in the previous sections, optimization is carried out with the threshold as another decision variable in the optimization. The results are shown in Figs. 16 and 17. Fig. 16 presents the best Pareto front and Fig. 17 presents the merit factor. The results show how in the extremes of power consumption, the algorithm always chooses very high values for the threshold. This is in line with Figs. 13 and 14 where it can be seen that the differences between the different thresholds are greater at the extremes.

D. TRI-OBJECTIVE OPTIMIZATION PROBLEM

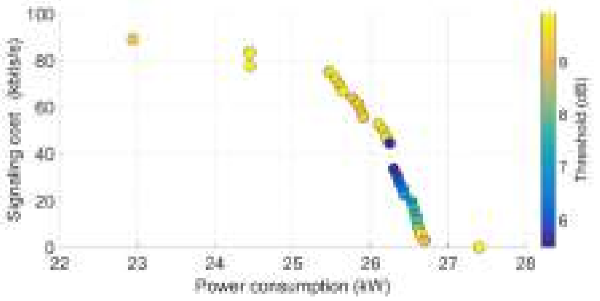

FIGURE 16. Pareto front of the power consumption against signaling cost when the threshold is optimized. Results obtained for planning 2 in the light configuration.

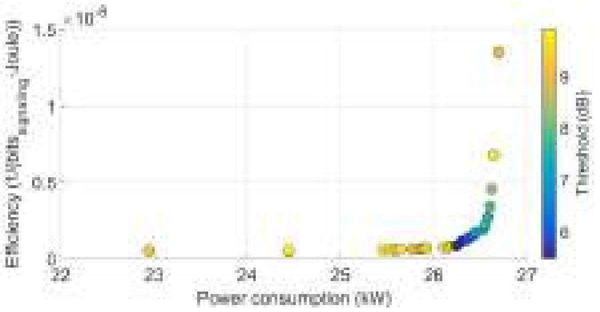

FIGURE 17. Efficiency ($1/(bits_{signaling} \cdot Joule)$) of the Pareto front of the power consumption against signaling cost when the threshold is optimized. Results obtained for planning 2 in the light configuration.

From the previous sections, it can be seen how when comparing data rates and power consumption, the best operation points are for high data rates. However, when comparing signaling cost and data rates, the optimum operation points are at low data rate points. Therefore, these operation points are contradictory and a joint optimization of the three factors is necessary in order to draw conclusions. Therefore, a combination of the three previous optimizations is made, where a surface is obtained as Pareto front as it is a three-dimensional optimization. Fig. 18 depicts this optimization and three trends can be distinguished. Signaling is minimized for low capacities and high power consumptions. Capacity is maximized for high power consumptions and high signaling. Power consumption is minimized for low capacities and high signaling.

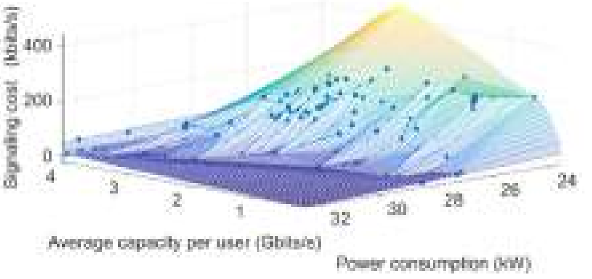

FIGURE 18. Pareto front of average capacity per user against power consumption against signaling cost. Results obtained for planning 1 in the light configuration.

Finally, a merit factor that takes into account the three network parameters simultaneously (data rates, power

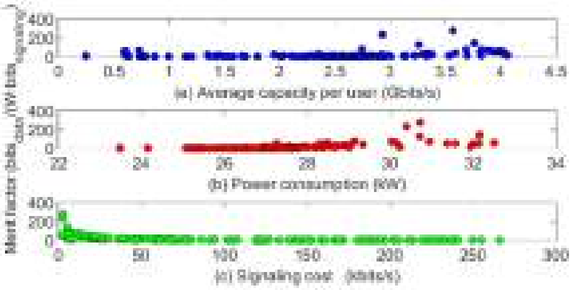

FIGURE 19. Merit factor ($bits_{data}/(W \cdot bits_{signaling})$) as a function of: (a) data rate, (b) power consumption and, (c) signaling cost.

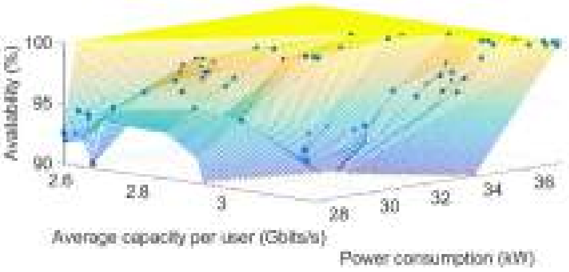

FIGURE 20. Pareto front of average capacity per user against power consumption against availability. Results obtained for planning 1 in the light configuration.

consumption and signaling cost) is proposed. This merit factor is calculated by dividing the data bits by the power consumed and the signaling bits. It reveals how many data bits can be sent with a watt of power and one bit of signaling. Fig. 19 shows this new merit factor as a function of average capacity in Fig. 19(a), as a function of power in Fig. 19(b) and as a function of signaling in Fig. 19(c). In these figures, it can be seen that the highest efficiencies of this merit factor are given for medium-high capacity and power values (around 3.5 Gbits/s and 30 to 31 kW). Also, in accordance with the previous sections, the best operations points are those found for low signalization values.

In addition, Fig. 20 shows a three-dimensional optimization that involves capacity, power consumption and availability. Taking into account availability is another key factor since the user should have coverage in order to satisfy his requirements. Total availability is obtained for high power consumptions where higher SINRs are able to improve the capacity, and therefore the data rate.

E. NSGAII AND SMPSO TRI-OBJECTIVE OPTIMIZATION PROBLEM

The previous section shows the study of the objectives with the default algorithm used by MatLab. Going further as explained in Section III, this study is performed with two additional algorithms, NSGAII and SMPSO. These allow us to go deeper into the tri-objective optimization case and extend results depending on the algorithm used. Ten iterations have been performed for each algorithm. The figures shown throughout this section show a representative description of the set of all the iterations.

Following the idea proposed in Fig. 18, a representation of the three-dimensional Pareto front is drawn in Fig. 21 for each of the three algorithms applied. On the one hand, the front of NSGAII differs slightly from the original MatLab front. On the other hand, the front proposed by SMPSO is quite different from the two previous ones.

In order to study these results further, the objectives are divided into three two-dimensional planes presented in Fig. 22. The first column, which draws the signaling as a colour scale, shows that NSGAII and SMPSO achieve better results than MatLab. NSGAII finds a space of solutions with lower energy consumption (objectives are shifted downwards) and less signaling (colder colors). In SMPSO it is remarkable that a set of low signaling cost objectives is found. They minimize energy consumption and signaling cost in exchange for lower average capacity per user. This set of objectives at the bottom left would be the example of a conservative deployment. The second column represents the power consumption as a colour scale. NSGAII gets colder colours since it is the algorithm with the best solutions in terms of energy saving. SMPSO concentrates the objectives in high

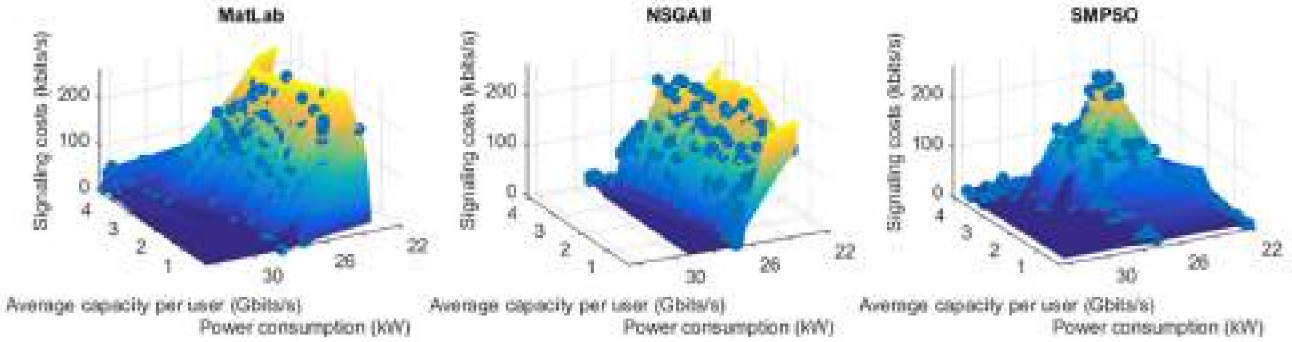

FIGURE 21. Pareto fronts of average capacity per user against power consumption against signaling costs. Optimization algorithms are default in MatLab, NSGAII and SMPSO. Results obtained for planning 1 in the light configuration.

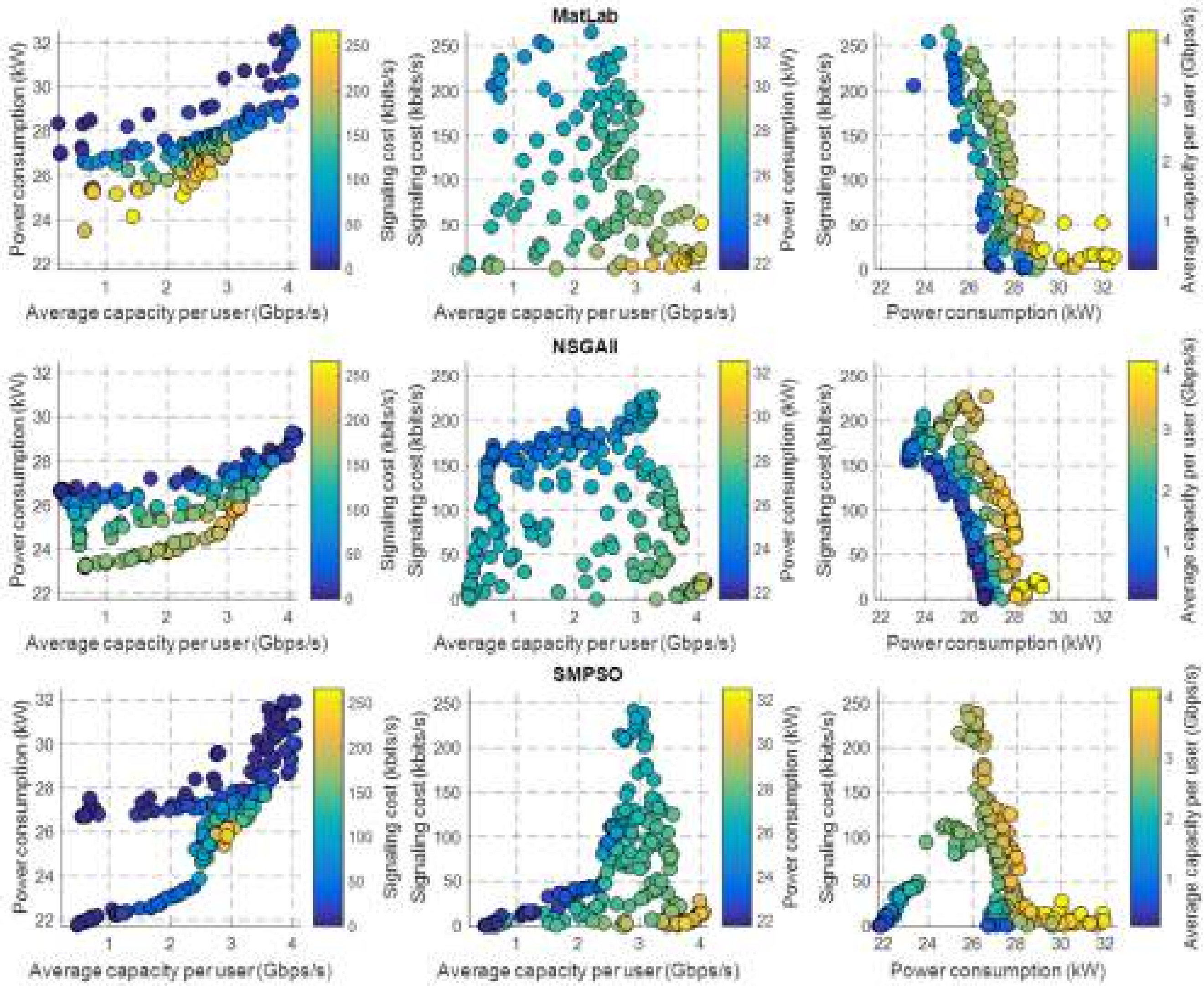

FIGURE 22. **Two-dimensional representation of the Pareto fronts. First, second and third rows represent MatLab, NSGAII and SMPSO algorithms respectively. First, second and third column represent signaling costs, power consumption and average capacity per user as a colour scale.**

TABLE 2. **Hypervolume Comparison.**

	MatLab	NSGAII	SMPSO
Hypervolume	0.39259	0.48809	0.61668

capacity areas except for a small section corresponding to the conservative case explained above.

Finally, the third column draws the power average capacity per user as a colour scale. By the same reasoning as above, NSGAII objectives are shifted to the left, corresponding to more energy efficient areas for similar capacities and signaling. SMPSO explores a new area at the bottom left corresponding to the conservative case.

The previous analysis of the Fig. 22 can be completed with another analysis using performance metrics such as hypervolume. Table 2 shows the average hypervolume for all iterations of each algorithm.

In terms of hypervolume, the best algorithm is SMPSO, followed by NSGAII in second place, and finally MatLab. The explanation is similar to that given in Fig. 22. On the one hand, NSGAII improves on MatLab with decreases in power consumption. On the other hand, SMPSO explores Pareto front areas that are not analyzed in the two previous algorithms. This case allows a more complete view of the Pareto front, which maximizes the hypervolume.

F. BASELINE COMPARISON

The hypervolume indicator shows the best Pareto fronts in a very compact way. However, it does not allow to see the improvement from the starting point. A visual comparison with the baseline can be made. The baseline used for the study consists on the average capacity per user, signaling cost and power consumption objectives when all BSs are operating at maximum power. This operation point provides the following results: 2.51 Gbps (average capacity per user),

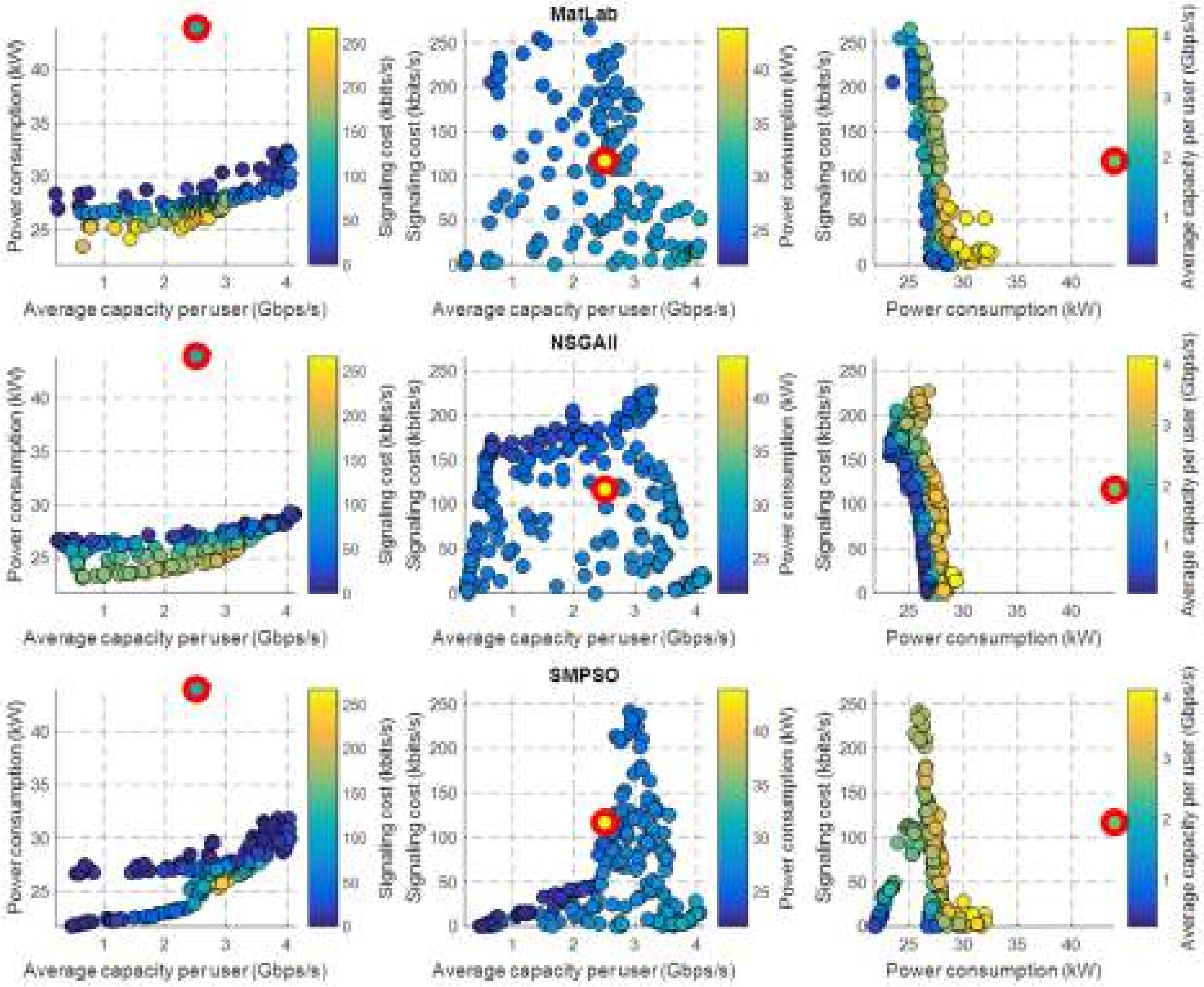

FIGURE 23. **Baseline in the two-dimensional representation of the Pareto fronts. First, second and third rows represent MatLab, NSGAII and SMPSO algorithms respectively. First, second and third column represent signaling costs, power consumption and average capacity per user as a colour scale.**

43.9 kW (power consumption) and 116.5 kbps (signaling cost). Fig. 23 shows the operating point of the baseline on the Pareto fronts obtained for the three algorithms. In the first column it is clear that the power consumed in the deployment is improved, going from 43.9 kW to values in the range of 23 kW to 33 kW. The second column shows that the baseline obtains intermediate values in terms of signaling and capacity. However, the yellow color of the baseline indicates that the power consumed to obtain these capacities and signaling is much higher than the rest of the objectives on the fronts. Finally, the third column shows a performance similar to the first one, where the power consumed is much higher than the Pareto front.

V. CONCLUSION

In this work, we have presented a multilayer network optimization that optimizes some performance criteria. The comprehensive model, based on the physical and network layers, allows the multilayer optimization where all objectives are improved simultaneously. UEs capacity and BSs power consumption from the network layer are optimized. UEs signaling bits due to handovers in the network from the data link layer are also considered in the optimization. These optimizations are reflected in Pareto fronts, which show a set of non-dominated solutions to the problem. They keep a trade-off that provides the network designer with a set of optimal settings for the network deployment. In order to decide a certain configuration, the calculation of efficiency parameters, such as energy efficiency, has also been carried out, showing the optimum operating point for the network. To go deeper into finding the optimal working point, three new merit factors have been proposed that take into account different parameters of the network.

The analysis of the merits factors shows the optimal operation points. These points can be useful for the telecommunication companies in order to allow new services with high performance in all parameters. Therefore, the new merits factors play a fundamental role in finding the balance between the different criteria assessed. Pareto fronts have been obtained from three different optimization algorithms. The comparison with the baseline shows that these Pareto fronts are able to improve multiple objectives simultaneously. The hypervolume analysis indicates that SMPSO presents the best objectives on the Pareto front.

As a future direction, D2D communications and multi-access edge computing (MEC) could improve the performance indicators since these technologies decrease the signaling costs and power consumption on the scenario due to the cooperation among close users. Moreover, the statistical multiplexing could increase the benefits of the optimization by coordinating several streams simultaneously. Although this technique slightly increases signaling traffic in the network, this is offset by the potential resource savings in terms of spectrum allocation.

5G and 6G aim to substantially improve all these QoS metrics simultaneously. To this end, this study has easily illustrated the trade-off between these performance indicators reached by three multi-objective optimization algorithms.

REFERENCES

[1] Ericsson. (2019). *Ericsson Mobility Report November 2019*. [Online]. Available: https://www.ericsson.com/4acd7e/assets/local/mobility-report/documents/2019/emr-november-2019.pdf

[2] Cisco. (2020). *Cisco Annual Internet Report (2018-2023)*. [Online]. Available: https://www.cisco.com/c/en/us/solutions/collateral/executive-perspectives/annual-internet-report/white-paper-c11-741490.html

[3] E. Steinbach, M. Strese, M. Eid, X. Liu, A. Bhardwaj, Q. Liu, M. Al-Ja'Afreh, T. Mahmoodi, R. Hassen, A. El Saddik, and O. Holland, "Haptic codecs for the tactile Internet," *Proc. IEEE*, vol. 107, no. 2, pp. 447–470, Feb. 2019.

[4] Z. Xiang, F. Gabriel, E. Urbano, G. T. Nguyen, M. Reisslein, and F. H. P. Fitzek, "Reducing latency in virtual machines: Enabling tactile Internet for human-machine co-working," *IEEE J. Sel. Areas Commun.*, vol. 37, no. 5, pp. 1098–1116, May 2019.

[5] X. Xu, X. Tang, Z. Sun, X. Tao, and P. Zhang, "Delay-oriented cross-tier handover optimization in ultra-dense heterogeneous networks," *IEEE Access*, vol. 7, pp. 21769–21776, 2019.

[6] A. Gorbenko, O. Tarasyuk, A.-L. Kor, and V. Kharchenko, "Green economics: A roadmap to sustainable ICT development," in *Proc. IEEE 9th Int. Conf. Dependable Syst., Services Technol. (DESSERT)*, Kiev, Ukraine, May 2018, pp. 561–567.

[7] M. M. Martino, G. Mutani, M. M. Pastorelli, and M. R. Miceli, "Smart energy users: ICT instruments for the consumer awareness," in *Proc. IEEE Int. Telecommun. Energy Conf. (INTELEC)*, Osaka, Japan, Oct. 2015, pp. 1–6.

[8] *Summary of Rel-15 Work Items*, document TR 21.915, 3GPP, 2018.

[9] V. Wong, R. Schober, D. W. K. Ng, and L. Wang, *Key Technologies for 5G Wireless Systems*. Cambridge, U.K.: Cambridge Univ. Press, 2017.

[10] X. Chen, D. Wing Kwan Ng, W. Yu, E. G. Larsson, N. Al-Dhahir, and R. Schober, "Massive access for 5G and beyond," 2020, *arXiv:2002.03491*. [Online]. Available: http://arxiv.org/abs/2002.03491

[11] T. Han and N. Ansari, "A traffic load balancing framework for software-defined radio access networks powered by hybrid energy sources," *IEEE/ACM Trans. Netw.*, vol. 24, no. 2, pp. 1038–1051, Apr. 2016.

[12] J. Heinonen, P. Korja, T. Partti, H. Flinck, and P. Poyhonen, "Mobility management enhancements for 5G low latency services," in *Proc. IEEE Int. Conf. Commun. Workshops (ICC)*, Kuala Lumpur, Malaysia, May 2016, pp. 68–73.

[13] D. Lopez-Perez, M. Ding, H. Claussen, and A. H. Jafari, "Towards 1 Gbps/UE in cellular systems: Understanding ultra-dense small cell deployments," *IEEE Commun. Surveys Tuts.*, vol. 17, no. 4, pp. 2078–2101, 4th Quart., 2015.

[14] Z. Pi and F. Khan, "An introduction to millimeter-wave mobile broadband systems," *IEEE Commun. Mag.*, vol. 49, no. 6, pp. 101–107, Jun. 2011.

[15] E. G. Larsson and L. Van Der Perre, "Massive MIMO for 5G," *IEEE 5G Tech Focus*, vol. 1, no. 11, pp. 1–4, Mar. 2017.

[16] T. L. Marzetta, "Massive MIMO: An introduction," *Bell Labs Tech. J.*, vol. 20, pp. 11–22, Mar. 2015.

[17] X. Ge, S. Tu, G. Mao, T. Han, and C. X. Wang, "5G ultra-dense cellular networks," *IEEE Trans. Wireless Commun.*, vol. 23, no. 1, pp. 72–79, Feb. 2016.

[18] R. Zhang, C. Qi, Y. Li, Y. Ruan, C.-X. Wang, and H. Zhang, "Towards energy-efficient underlaid device-to-device communications: A joint resource management approach," *IEEE Access*, vol. 7, pp. 31385–31396, 2019.

[19] D. Liu, Y. Chen, K. K. Chai, T. Zhang, and M. Elkashlan, "Two-dimensional optimization on user association and green energy allocation for HetNets with hybrid energy sources," *IEEE Trans. Commun.*, vol. 63, no. 11, pp. 4111–4124, Nov. 2015.

[20] L. A. Fletscher, J. M. Maestre, and C. V. Peroni, "Coalitional planning for energy efficiency of HetNets powered by hybrid energy sources," *IEEE Trans. Veh. Technol.*, vol. 67, no. 7, pp. 6573–6584, Jul. 2018.

[21] L. A. Fletscher, J. Barreiro-Gomez, C. Ocampo-Martinez, C. V. Peroni, and J. M. Maestre, "Atomicity and non-anonymity in population-like games for the energy efficiency of hybrid-power HetNets," *IEEE Trans. Netw. Service Manage.*, vol. 15, no. 4, pp. 1600–1614, Dec. 2018.

[22] B. Rengarajan, G. Rizzo, and M. A. Marsan, "Energy-optimal base station density in cellular access networks with sleep modes," *Comput. Netw.*, vol. 78, pp. 152–163, Feb. 2015.

[23] M. Di Renzo, A. Zappone, T. T. Lam, and M. Debbah, "System-level modeling and optimization of the energy efficiency in cellular networks—A stochastic geometry framework," *IEEE Trans. Wireless Commun.*, vol. 17, no. 4, pp. 2539–2556, Apr. 2018.

[24] I. Keshavarzian, Z. Zeinalpour-Yazdi, and A. Tadaion, "Energy-efficient mobility-aware caching algorithms for clustered small cells in ultra-dense networks," *IEEE Trans. Veh. Technol.*, vol. 68, no. 7, pp. 6833–6846, Jul. 2019.

[25] P. Munoz, R. Barco, and S. Fortes, "Conflict resolution between load balancing and handover optimization in LTE networks," *IEEE Commun. Lett.*, vol. 18, no. 10, pp. 1795–1798, Oct. 2014.

[26] K. Haneda *et al.*, "Indoor 5G 3GPP-like channel models for office and shopping mall environments," in *Proc. IEEE Int. Conf. Commun. Workshops (ICC)*, Kuala Lumpur, Malaysia, May 2016, pp. 694–699.

[27] K. Haneda *et al.*, "5G 3GPP-like channel models for outdoor urban microcellular and macrocellular environments," in *Proc. IEEE 83rd Veh. Technol. Conf. (VTC Spring)*, Nanjing, China, May 2016, pp. 1–7.

[28] G. R. MacCartney and T. S. Rappaport, "Rural macrocell path loss models for millimeter wave wireless communications," *IEEE J. Sel. Areas Commun.*, vol. 35, no. 7, pp. 1663–1677, Jul. 2017.

[29] H. Jiang, D. Tang, J. Zhou, X. Xi, J. Feng, J. Dang, and L. Wu, "Approximation algorithm based channel estimation for massive MIMO antenna array systems," *IEEE Access*, vol. 7, pp. 149364–149372, 2019.

[30] J. R. Perez and R. P. Torres, "On the impact of the radiation pattern of the antenna element on MU-MIMO indoor channels," *IEEE Access*, vol. 8, pp. 25459–25467, 2020.

[31] A. Al-Wahhamy, H. Al-Rizzo, and N. E. Buris, "Efficient evaluation of massive MIMO channel capacity," *IEEE Syst. J.*, vol. 14, no. 1, pp. 614–620, Mar. 2020.

[32] T. L. Marzetta, E. G. Larsson, H. Yang, and H. Q. Ngo, *Fundamentals of Massive MIMO*. Cambridge, U.K.: Cambridge Univ. Press, 2018.

[33] E. Bjornson and E. G. Larsson, "How energy-efficient can a wireless communication system become?" in *Proc. 52nd Asilomar Conf. Signals, Syst., Comput.*, Pacific Grove, CA, USA, Oct. 2018, pp. 1252–1256.

[34] M. Masoudi *et al.*, "Green mobile networks for 5G and beyond," *IEEE Access*, vol. 7, pp. 107270–107299, 2019.

[35] Z. Dong, J. Wei, X. Chen, and P. Zheng, "Energy efficiency optimization and resource allocation of cross-layer broadband wireless communication system," *IEEE Access*, vol. 8, pp. 50740–50754, 2020.

[36] K. M. S. Huq, S. Mumtaz, J. Bachmatiuk, J. Rodriguez, X. Wang, and R. L. Aguiar, "Green HetNet CoMP: Energy efficiency analysis and optimization," *IEEE Trans. Veh. Technol.*, vol. 64, no. 10, pp. 4670–4683, Oct. 2015.

[37] G. Auer, V. Giannini, C. Desset, I. Godor, P. Skillermark, M. Olsson, M. Imran, D. Sabella, M. Gonzalez, O. Blume, and A. Fehske, "How much energy is needed to run a wireless network?" *IEEE Wireless Commun.*, vol. 18, no. 5, pp. 40–49, Oct. 2011.

[38] J. Carmona-Murillo, I. Soto, F. J. Rodríguez-Pérez, D. Cortés-Polo, and J. L. González-Sánchez, "Performance evaluation of distributed mobility management protocols: Limitations and solutions for future mobile networks," *Mobile Inf. Syst.*, vol. 2017, pp. 1–15, Feb. 2017.

[39] E. M. O. Fafolahan and S. Pierre, "A seamless mobility management protocol in 5G locator identificator split dense small cells," *IEEE Trans. Mobile Comput.*, vol. 19, no. 8, pp. 1745–1759, Aug. 2020.

[40] D. Shin, K. Yun, J. Kim, P. V. Astillo, J.-N. Kim, and I. You, "A security protocol for route optimization in DMM-based smart home IoT networks," *IEEE Access*, vol. 7, pp. 142531–142550, 2019.

[41] J. Kim, P. V. Astillo, and I. You, "DMM-SEP: Secure and efficient protocol for distributed mobility management based on 5G networks," *IEEE Access*, vol. 8, pp. 76028–76042, 2020.

[42] C. A. C. Coello, G. B. Lamont, D. A. V. Veldhuizen, *Evolutionary Algorithms for Solving Multi-Objective Problems*, 2nd ed. New York, NY, USA: Springer, 2007.

[43] C. Blum and A. Roli, "Metaheuristics in combinatorial optimization: Overview and conceptual comparison," *ACM Comput. Surv.*, vol. 35, no. 3, pp. 268–308, Sep. 2003.

[44] E. Zitzler and L. Thiele, "Multiobjective evolutionary algorithms: A comparative case study and the strength Pareto approach," *IEEE Trans. Evol. Comput.*, vol. 3, no. 4, pp. 257–271, Nov. 1999.

[45] K. Deb, A. Pratap, S. Agarwal, and T. Meyarivan, "A fast and elitist multiobjective genetic algorithm: NSGA-II," *IEEE Trans. Evol. Comput.*, vol. 6, no. 2, pp. 182–197, Apr. 2002.

[46] A. J. Nebro, J. J. Durillo, J. Garcia-Nieto, C. A. Coello Coello, F. Luna, and E. Alba, "SMPSO: A new PSO-based Metaheuristic for multi-objective optimization," in *Proc. IEEE Symp. Comput. Intell. Milti-Criteria Decis.-Making*, Nashville, TN, USA, Mar. 2009, pp. 66–73.

[47] S. García, D. Molina, M. Lozano, and F. Herrera, "A study on the use of non-parametric tests for analyzing the evolutionary algorithms' behaviour: A case study on the CEC'2005 special session on real parameter optimization," *J. Heuristics*, vol. 15, no. 6, pp. 617–644, Dec. 2009.

[48] J. Knowles, "A summary-attainment-surface plotting method for visualizing the performance of stochastic multiobjective optimizers," in *Proc. 5th Int. Conf. Intell. Syst. Design Appl. (ISDA)*, Warsaw, Poland, Sep. 2005, pp. 552–557.

ALEJANDRO RAMÍREZ-ARROYO was born in Córdoba, Spain, in 1997. He received the B.Sc. degree in telecommunication engineering from the Universidad de Granada, Spain, in 2019, where he is currently pursuing the M.Sc. degree in telecommunication engineering. His current research interests include heterogeneous networks, optimization techniques, and propagation channels and models for 5G networks.

PABLO H. ZAPATA-CANO received the B.Sc. degree in telecommunications engineering from the Universidad de Granada, Spain. He is currently a SMARTNET M.Sc. Scholar with TelecomSud Paris, where he was a recipient of an Erasmus Mundus grant. Since 2018, he has been also active in research as a Graduate Research Assistant with the Universidad de Granada, publishing several articles in international journals and conferences. His research interests include wireless communications, 5G Ultradense networks, green communications, and optimization techniques.

ÁNGEL PALOMARES-CABALLERO was born in Jaen, Spain, in 1994. He received the B.Sc. and M.Sc. degrees in telecommunication engineering from the Universidad de Granada (UGR), Spain, in 2016 and 2018, respectively. He is currently pursuing the Ph.D. degree with a national predoctoral fellowship. Since 2017, he has been with the Department of Signal Theory, Telematics and Communications, Universidad de Granada. His research interests include millimeter-wave antennas and phase shifters, gap-waveguide, structures with higher symmetries, and optimization algorithms.

JAVIER CARMONA-MURILLO (Member, IEEE) received the Ph.D. degree in computer science and communications from the University of Extremadura, Spain, in 2015. From 2005 to 2009, he was a Research and Teaching Assistant. Since 2009, he has been an Associate Professor with the Department of Computing and Telematics System Engineering, Universidad de Extremadura. During the past years, he has spent research periods with the Centre for Telecommunications Research, King's College London, U.K., and Aarhus University, Denmark. His current research interests include 5G networks, mobility management protocols, performance evaluation, and the quality of service support in future mobile networks.

FRANCISCO LUNA-VALERO (Associate Member, IEEE) received the degree in engineering and the Ph.D. degree in computer science from the University of Málaga, Spain, in 2002 and 2008, respectively. Until 2012, he was a Research Assistant with the University of Málaga. In 2012, he held a postdoctoral position the Universidad Carlos III of Madrid. In 2013, he was with the Universidad de Extremadura as an Assistant Professor. Since 2015, he has been an Associate Professor with the University of Málaga. His current research interests include the design and implementation of parallel and multi-objective meta-heuristics, and their application to solve complex problems arising in several domains, including telecommunications, finance, and structural design.

JUAN F. VALENZUELA-VALDÉS was born in Marbella, Spain. He received the degree in telecommunications engineering from the Universidad de Málaga, Spain, in 2003, and the Ph.D. degree from the Universidad Politécnica de Cartagena, Spain, in May 2008. In 2004, he joined the Department of Information Technologies and Communications, Universidad Politécnica de Cartagena. In 2007, he joined the Head of research with EMITE Ing. In 2011, he joined the Universidad de Extremadura, and in 2015, he joined the Universidad de Granada, where he is currently an Associate Professor. He was a Co-Founder of Emite Ing., a spin-off company. He also holds several national and international patents. His publication record is composed of more than 80 publications, including 40 JCR indexed articles, more than 30 contributions in international conferences and 7 book chapter. His current research interests include wireless communications and efficiency in wireless sensor networks. He has also been awarded several prizes, including a National Prize to the Best Ph.D. in mobile communications by Vodafone and the i-patentes award by the Spanish Autonomous Region of Murcia for innovation and technology transfer excellence.

2.2 Emulation and Classification of Propagation Channels

2.2.1 On the Spectral Efficiency for Distributed Massive MIMO Systems

Distributed MIMO (D-MIMO) is expected to be a disruptive technology for future mobile generations due to the multi-connectivity between the User Equipment and the Base Station. This paper analyzes the spectral efficiency of D-MIMO systems under different operating conditions. Simulations have been carried out in the sub-6 GHz band (FR1) and mmWave band (FR2). Additionally, these simulations have been complemented with measurements performed in anechoic and reverberation chamber environments in order to emulate D-MIMO systems. Properties such as power allocation, antenna spacing, and LoS vs NLoS condition have been analyzed for the optimal deployment of a D-MIMO system. Simulation results and channel emulations demonstrate that low spatially correlated and power-balanced channels take advantage of the spatial diversity of the propagation channel, thus maximizing the performance of these systems.

THIS IS THE PUBLISHED VERSION OF THE PAPER:

A. Ramírez-Arroyo, J. C. González-Macías, J. J. Rico-Palomo, J. Carmona-Murillo, and A. Martínez-González, "On the Spectral Efficiency for Distributed Massive MIMO Systems," *Applied Sciences*, vol. 11, no. 22, p. 10926, 2021.

- Journal Impact Factor (JIF) in JCR 2021: 2.838
- Category: ENGINEERING, MULTIDISCIPLINARY. JIF Rank: 39/92 (Q2).

Disclaimer:
This work has been published in Applied Sciences.
DOI: 10.3390/app112210926

applied sciences

MDPI

Article

On the Spectral Efficiency for Distributed Massive MIMO Systems

Alejandro Ramírez-Arroyo [1,*], Juan Carlos González-Macías [2], Jose J. Rico-Palomo [2], Javier Carmona-Murillo [2] and Antonio Martínez-González [3]

[1] Department of Signal Theory, Telematics and Communications, University of Granada (UGR), 18071 Granada, Spain
[2] Department of Computing and Telematics Engineering, University of Extremadura (UEx), 06006 Badajoz, Spain; jcgzlezm@unex.es (J.C.G.-M.); jjricopal@unex.es (J.J.R.-P.); jcarmur@unex.es (J.C.-M.)
[3] Department of Information and Communication Technologies, Technical University of Cartagena (UPTC), 30202 Murcia, Spain; toni.martinez@upct.es
* Correspondence: alera@ugr.es

Abstract: Distributed MIMO (D-MIMO) systems are expected to play a key role in deployments for future mobile communications. Together with massive MIMO technology, D-MIMO aims to maximize the spectral efficiency and data rate in mobile networks. This paper proposes a deep study on the spectral efficiency of D-MIMO systems for essential channel parameters, such as the channel power balance or the correlation between propagation channels. For that purpose, several propagation channels were acquired in both anechoic and reverberation chambers and were emulated using channel simulators. In addition, several frequency bands were studied, both the sub–6 GHz band and mmWave band. The results of this study revealed the high influence of channel correlation and power balance on the physical channel performance. Low-correlated and high-power balance propagation channels show better performances than high correlated and power unbalance channels in terms of spectral efficiency. Given these results, it will be fundamental to take into account the spectral efficiency of D-MIMO systems when designing criteria to establish multi-connectivity in future mobile network deployments.

Keywords: distributed MIMO systems; anechoic chamber; reverberation chamber; spectral efficiency; power balance

check for updates

Citation: Ramírez-Arroyo, A.; González-Macías, J.C.; Rico-Palomo, J.J.; Carmona-Murillo, J.; Martínez-González, A. On the Spectral Efficiency for Distributed Massive MIMO Systems. *Appl. Sci.* **2021**, *11*, 10926. https://doi.org/10.3390/app112210926

Academic Editor: John Xiupu Zhang

Received: 30 September 2021
Accepted: 17 November 2021
Published: 18 November 2021

1. Introduction

The prognosis for average user data consumption in 2026 is expected to be 35 GB/month compared with approximately 9 GB/month currently [1,2], which implies a 25% compound annual growth rate. In 2026, the most consumed user applications will continue to be based on streaming video. It is anticipated that these applications will require up to 27 GB/month per user, compared with 6 GB/month today. Applications contributing to this dramatic increase in 2026 include: (i) 1080 p full HD (1920 × 1080); (ii) full HD virtual reality (VR); and (iii) 4K UHD (3840 × 2160). Beyond 2026, more demanding video streaming applications are expected to take user traffic to new levels, such as: (i) 8K UHD (7680 × 4320); and (ii) volumetric data streaming [3]. Consequently, this prediction shows an increase of approximately 4 times in 5 years until 2026. If we linearly extrapolated this result to 2030, we obtain an increase factor of between 20 and 30 times the current traffic of the users. It is expected that the above usage cases and any future cases will require the same type of 5G key performance indicators (KPIs) including: (i) new target values (e.g., higher data rates, lower latency, higher reliability . . .); and (ii) new cut-off hybrids across the three types of user services for 5G, enhanced mobile broadband (eMBB), ultra-reliable low-latency communications (uRLLCs) and massive machine-type communications (mMTCs) [4]. Technological challenges and goals for the short (SEVO), medium (MEVO) and long (LEVO)-term evolution of 5G are shown in Figure 1.

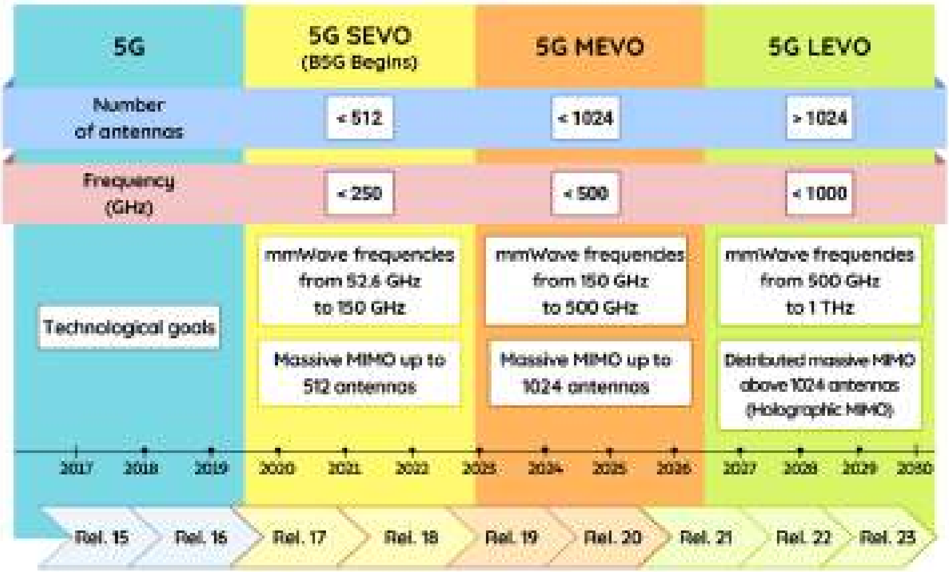

Figure 1. Evolution roadmap of the communication standards and major technological challenges for future mobile communications.

Within this framework and perspective, technological advances are mandatory to fulfill the user requirements. Thus, multiple-input multiple-output (MIMO) is fundamental for the development of mobile networks. In particular, massive MIMO technology expects to increase the transmission speed on the network by using multiple antennas at the transmitter (TX) and receiver (RX), and high frequencies, known as millimeter waves (mmWaves) [5]. However, the propagation channel for mmWaves is particularly exposed to attenuation and fading issues. Therefore, it will be necessary to connect the user equipment (UE) to several base stations (BSs) simultaneously. Systems with multiple BSs may be known as distributed MIMO (D-MIMO) systems or coordinated multipoint (CoMP) systems. CoMP term usually refers to systems where a suppression is sought through channel awareness being distributed by the backhaul network [6]. These systems will allow the multi-connectivity between BS and UE, which will require a deep study on the designing criteria on the network in order to provide an optimal network operation.

Massive MIMO and coordinated interference schemes have been proposed as solutions to mitigate high interference and thus increase spectral efficiency [7]. However, the main issue of this technique is the increased system overload in the fronthaul [8] and backhaul [9] networks. A solution for cooperation in transmissions is to find a balance for the number of coordinated cells in order to decrease the overheads [10,11]. These coordinated transmissions are typically based on three techniques: coordinated beamforming, coordinated transmissions and coordinated scheduling [12–15]. Moreover, new strategies are emerging to improve the performance of the previous techniques, such as those based on games or deep learning [16–18]. Previous work by MacCartey and Rappaport [6] demonstrate that the full knowledge of the propagation channel provides an increase in the data rate for the CoMP systems. However, it also proves that both the sharing of full CSI and BSs coordination imply a drastic increase on the backhaul overhead, as stated previously in [9]. For that reason, the interference mitigation may not be worthy in practical cases. Nevertheless, it is preferable to use multi-BS systems to increase the data rate of the network, since they avoid overheads. For this, the joint spectral efficiency of the distributed MIMO systems is sought. This study deals with the above-mentioned issues and proposes the following contributions:

- A field study on the spectral efficiency of distributed MIMO systems for the sub–6 GHz band that quantifies the losses of spectral efficiency due to power unbalance in several distributed MIMO systems working together. In this paper, channel propagation measurements are acquired in reverberation chambers to emulate different environments;
- A theoretical study is carried out in order to simulate a distributed massive MIMO system in the mmWave band. A deep analysis on the spectral efficiency is presented using the NYUSIM simulator;
- A field study is performed to emulate a distributed MIMO system in the mmWave band. A measurement campaign is performed to emulate several distributed MIMO scenarios above 30 GHz. A comparison with the power unbalance in the sub–6 GHz band is made in order to see the implementation viability of distributed MIMO scenarios for future mobile generations.

The study is organized as follows. Section 2 introduces the distributed MIMO model and the channel matrix that provides the spectral efficiency of the measured scenario. Sections 3–5 show the analysis of the D-MIMO scenarios in real deployments and simulations, and sub–6 GHz and mmWave bands. Finally, the main conclusions of the article are drawn in Section 6.

2. Distributed MIMO Model

The main goal to study the scenarios is the emulation of distributed MIMO systems by combining values from several communication channels acquired in different environments. Therefore, diverse channel matrices are combined in order to form a single matrix that symbolizes the D-MIMO channel matrix [6,19]. Each propagation environment has a certain number of transmitting (TX) and receiving (RX) antennas. TXs simulate a transmitting BS, where each BS is placed in a different location, emitting to a user equipment (UE) located in a fixed place and composed by several RXs. Mathematically, the combination of channel matrices can be depicted in Equation (1). A deep and detailed explanation on channel matrix models can be found on [20,21].

$$\boldsymbol{H} = \left[\boldsymbol{H}_1^T, \boldsymbol{H}_2^T, \ldots, \boldsymbol{H}_N^T\right]^T, \tag{1}$$

N is the total number of MIMO systems that form the D-MIMO. $\boldsymbol{H}_i$ is the channel matrix from a single MIMO whose dimension is $\mathrm{L}_i \times \mathrm{R}$. L_i and R is the number of TX and RX in the BS and UE for the i-MIMO system, respectively. Finally, $\boldsymbol{H}$ is the channel matrix of the D-MIMO with dimensions $\mathrm{L} \times \mathrm{R}$, where L is computed as $\sum_{i=1}^{N} \mathrm{L}_i$.

It is essential to emphasize that each $\boldsymbol{H}_i$, related to different MIMO systems, represents propagation channels that may differ from each other due to the unique conditions of each scenario. Therefore, the power received by the UE is expected to be different from different schemes. In this paper, a modulation of $\boldsymbol{H}_i$ is introduced to emulate the unbalance power that might occur in a D-MIMO system. In order to perform this unbalance, $\boldsymbol{H}_i$ is multiplied by a balance factor (Att) that emulates losses in the transmission due to obstacles in the propagation path or shadow fading.

$$\boldsymbol{H}_i^{Att} = Att_i \cdot \boldsymbol{H}_i\,; \qquad Att_i \geq 0 \tag{2}$$

By applying this balance factor to certain i-MIMO systems, the performance of D-MIMO systems can be analyzed when they suffer a strong power unbalance. The spectral efficiency of the system can be computed to determine the effect on the D-MIMO once the power balance is modified. This metric of the full communication channel is estimated using the following formulas [22]:

$$\boldsymbol{H}_{norm}(f_i) = \boldsymbol{H}(f_i)\left[\frac{1}{N_f}\sum_{i=1}^{N_f}||\boldsymbol{H}(f_i)||^2\right]^{-\frac{1}{2}}, \tag{3}$$

$$\eta(\text{bps/Hz}) = log_2\left|\boldsymbol{I}_L + \frac{\text{SINR}}{\text{L}}\boldsymbol{H}\boldsymbol{H}^H\right|, \tag{4}$$

where SINR is the signal-to-interference-plus-noise ratio rate, $\boldsymbol{H}$ represents the channel matrix of the D-MIMO, $\boldsymbol{I}$ is an identity matrix, and the superscript $^{(H)}$ denotes the conjugate transpose operator. First of all, $\boldsymbol{H}$ must be normalized ($\boldsymbol{H}_{norm}$) in order to take into account the frequency dependence of the communication channel in Equation (3) [23], where N_f is the number of frequency samples. Note that the number of frequency samples N_f must be chosen long enough so that no channel effect at a single frequency is unnoticed. The spectral efficiency in Equation (4) is calculated from the normalized channel frequency response $\boldsymbol{H}_{norm}$. Throughout the article, additional modifications will be added to the channel frequency response shown in Equation (3) to demonstrate the importance of effects such as power unbalance in D-MIMO systems.

A visual example of the composition of a D-MIMO system is illustrated in the Figure 2. This example shows the composition of a D-MIMO throughout several measurements acquired in a semi-anechoic and semi-reverberation chamber. As previously stated, n–MIMO systems are deployed, where the UE/RX is located in a fixed position. However, the BS/TX position is changed in order to move and point to different locations inside the chamber. This provokes the diversity of the propagation channel which is finally reflected on the channel matrix $\boldsymbol{H}$. Each one of the following sections details how the channel matrices $\boldsymbol{H}_i$ were obtained.

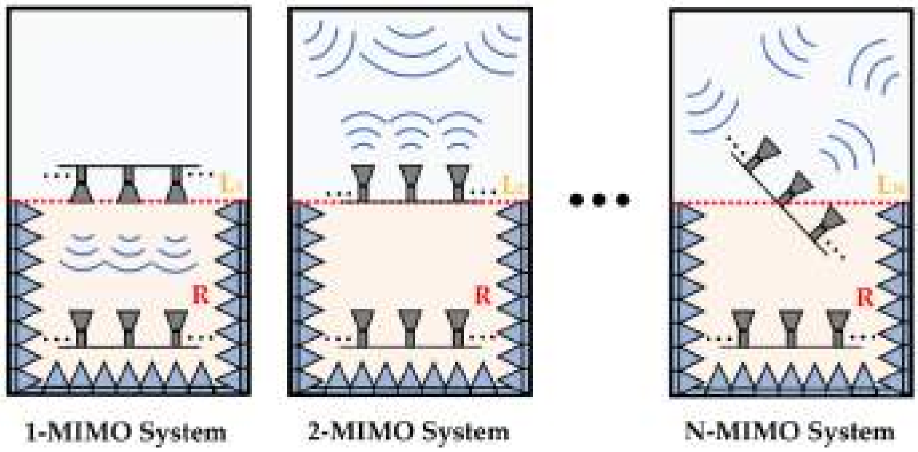

Figure 2. Scheme of a D-MIMO consisting of a set of MIMO subsystems acquired in a semi-anechoic and semi-reverberation chamber.

3. Power Unbalance on Sub–6 Ghz D-MIMO Systems

This section presents the effect of the power unbalance for a D-MIMO system composed by multiple MIMO subsystems acquired in a reverberation chamber. The first part of the section briefly describes the acquisition process of the propagation channels. The second part shows and details the results of this power unbalance. From an analytical perspective, the relevance of this section lies in understanding how the spectral efficiency can be maximized while the power allocation is minimized at the same time.

3.1. Measurement Scenario

The first subset of measurements is taken in a reverberation chamber. These measurements are characterized by the rich scattering scenario generated inside the chamber. The reflection of the waves on the shielded walls creates several multipath components (MPCs) that reach the UE in different time instants, which increase the diversity of the scenario. Seven different scenarios are measured inside the reverberation chamber, where the BS has twelve transmitter antennas and UE has three receiver antennas. In order to generate diversity on the propagation channel, two mechanical stirrers are inserted inside the reverberation chamber. Since stirrers can adopt 50 different positions, together with 201 frequency points (250 kHz frequency spacing) from 1775 GHz to 1825 GHz, 10,050 channel propagation are measured for each TX-RX pair on each scenario. The main difference between the seven scenarios is found in the load of the reverberation chamber, which is changed by introducing several absorbers in different positions. A deep explanation of the measuring process can be found in [24,25].

Once the acquisition process is carried out, seven MIMO systems are achieved and saved on seven $\boldsymbol{H}_i$. The full D-MIMO system is formed by the matrix $\boldsymbol{H} = \left[\boldsymbol{H}_1^T, \boldsymbol{H}_2^T, \ldots, \boldsymbol{H}_7^T\right]^T$ whose dimensions are 84 TX × 3 RX.

3.2. Power Balance Analysis

In order to analyze the effect of the power balance in a D-MIMO system, the balance of the measurements must be assessed. For that purpose, Table 1 shows the normalized power balance (NPB) over the maximum value for the *i*-MIMO system. Since all scenarios are normalized, it can be seen that scenario A reaches the maximum power in the receivers. As stated in [22,23], this scenario lacks absorbers, so it is logical to expect maximum received power. The higher the number of absorbers, the lower the received power due to the absorption effect.

Table 1. Normalized power balance (NPB) for the *i*-MIMO system.

	A ($\boldsymbol{H}_1$)	**B ($\boldsymbol{H}_2$)**	**C ($\boldsymbol{H}_3$)**	**D ($\boldsymbol{H}_4$)**	**E ($\boldsymbol{H}_5$)**	**F ($\boldsymbol{H}_6$)**	**G ($\boldsymbol{H}_7$)**
Power allocation	1	0.48	0.36	0.85	0.58	0.15	0.14

Once the power allocation is known, we can establish a D-MIMO system formed by the first transmitter of the scenarios from A to E and all three receivers from every scenario. This leads to a D-MIMO whose channel matrix $\boldsymbol{H}$ has the dimensions 5 TX × 3 RX. In this new $\boldsymbol{H}$, the average value of the normalized power is 0.65. Scenarios A and B are modified by applying the balance factors Att_1 and Att_2 Equation (2) to the first two rows of $\boldsymbol{H}$ to see the effect of the power balance. Figure 3a shows the spectral efficiency of the D-MIMO when it is modulated with both balance factors simultaneously. As it can be seen, the higher the Att_2 value is, the higher the spectral efficiency obtained. Since Att_2 modulates $\boldsymbol{H}_2$ (NPB $= 0.48$) and the average NPB for the full matrix $\boldsymbol{H}$ is 0.65, it is intended to obtain an Att_2 value as close as possible to 1. This fact provides an NPB in the $\boldsymbol{H}_2$ row that is the closest to the average NPB. Observing the effect of Att_1, the spectral efficiency rises from 0.01 to 0.6, where it reaches a maximum. From that value, the metric tends to decrease. Since $\boldsymbol{H}_1$ NPB is 1, the value of Att_1 that provides a NPB similar to the average NPB is 0.65. It is clearly observed that the maximum spectral efficiencies are reached for these values. In short, the D-MIMO is able to maximize its spectral efficiency when the *i*-MIMO systems tend to be balanced due to the balance factor inclusion.

In order to validate this reasoning, a second experiment was carried out. The first transmitter from the scenarios C, D, E, F and G were chosen. Therefore, a D-MIMO with channel matrix $\boldsymbol{H}$ (5 TX × 3 RX) was created. In this case, the average NPB is 0.42 and the balance factors Att_3 and Att_4 are applied to the scenarios C ($\boldsymbol{H}_3$) and D ($\boldsymbol{H}_4$), respectively. Figure 3b presents the spectral efficiency when both balance factors are included. First, the NPB in scenario C is 0.36. Therefore, larger values of Att_3 obtain a NPB closer to the average NPB of the D-MIMO. Consequently, the spectral efficiency increases as Att_3 increases. Based on the modulation of scenario D (Att_4), the NPB is 0.85. In order to maximize the spectral efficiency, the NPB must tend to values around the average NPB. This is obtained for values of Att_4 around 0.5. Note that Att_4 values above 0.5 do not increase the spectral efficiency even when it implies increasing the transmission power of scenario C. This fact is due to the power unbalance when Att_4 is too high.

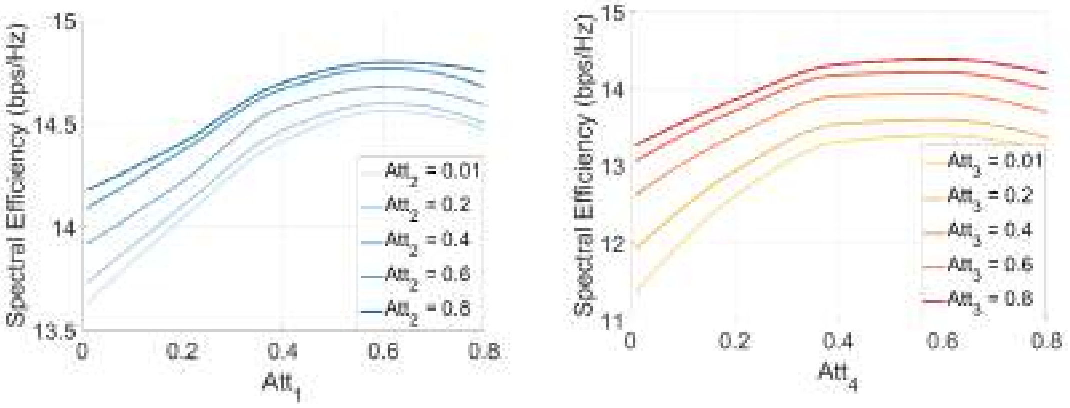

(**a**) (**b**)

Figure 3. Spectral efficiency of a D-MIMO when the power balance is modulated with two balance factors. SINR is fixed to 15 dB. The *i*-MIMO systems that form the D-MIMO are the scenarios (**a**) A (Att_1), B (Att_2), C, D, E, and (**b**) C (Att_3), D (Att_4), E, F, G.

To conclude this section, it was proven that the spectral efficiency of a D-MIMO system is directly proportional to the power balance. Therefore, the received power variance between the TX-RX pair should be reduced in order to provide satisfactory UE services.

4. Correlation and Los on Emulated D-MIMO Systems above 6 Ghz

4.1. Emulation Scenario

In this section, an analysis on the TX correlation and the effect of the line-of-sight (LoS) in D-MIMO systems is performed. For that purpose, several measurements of the propagation channel are simulated in NYUSIM [26]. NYUSIM is a mmWave simulator that has a wide variety of configuration parameters for the simulated environment. In particular, it allows to simulate scenarios for a wide frequency range and several propagation models. In this study, simulations from 10 GHz to 78 GHz are carried out for two environment models: urban macrocell (UMa) and urban microcell (UMi). Several channel matrices $\boldsymbol{H}$ were simulated for a wide range of configuration parameters. Table 2 shows the choice of simulation parameters in detail. Note that each simulation was iterated ten times in order to avoid outliers in the channel matrices $\boldsymbol{H}$. The chosen distances, antenna spacing, and frequencies ensure the UE far-field condition for all simulations shown in this section.

Table 2. NYUSIM simulation parameters.

Simulation Parameters	
Frequency	10 GHz, 28 GHz, 40 GHz and 78 GHz
Bandwidth	800 MHz
Frequency samples	1601 (500 kHz frequency spacing)
Propagation environment	Urban macrocell (UMa) and urban microcell (UMi)
Visibility	Line-of-sight (LoS) and non-line-of-sight (NLoS)
UE-BS distance	50 to 1000 m
TX antennas in the BS	200 antennas (Lineal array)
RX antennas in the UE	20 antennas (Lineal array)
TX antenna separation	$\lambda/10$, $\lambda/2$ and λ
RX antenna separation	$\lambda/10$, $\lambda/2$ and λ
EIRP	30 dBm
Iterations	10

4.2. Correlation and LoS Analysis

The first test consists of studying the TX/RX antenna spacing in the BS/UE to determine its effect on spectral efficiency. For that purpose, a D-MIMO system with 50 TX and

10 RX was created. The D-MIMO is formed by 3 BS which are 100 m, 120 m, and 140 m away from the receiver. The relative distance between BSs is set to be the largest BS-UE distance (140 m). On each BS the transmission is made with 17 TX, 17 TX, and 16 TX, respectively. The simulations are made for two environments (UMa and UMi) and three frequencies (28 GHz, 40 GHz, and 78 GHz). Since the goal is to study the TX/RX antenna spacing effect, three distances are considered for the TX/RX spacing: λ/10, λ/2, and λ. For the sake of clarity, the spacing is set to the same value on both sides of the communication. Theoretically, the closer the antennas are to each other, the lower the benefit from spatial diversity is due to the higher correlation between channels. Figure 4a,b show the results for this test. We define Θ as the difference between the Shannon theoretical limit and the spectral efficiency simulated. The Shannon theoretical limit establishes the spectral efficiency for completely decorrelated channels. Therefore, the Shannon limit cannot be exceeded and Θ provides an idea of how far the scenario is from the theoretical limit. Looking at both scenarios, UMa (Figure 4a) and UMi (Figure 4b), the UMa scenario tends to obtain similar results for all frequencies, while the UMi scenario shows differences up to 3 bps/Hz due to the frequency band. However, the main effect is induced by the TX/RX spacing. The farther apart the TX and RX are spaced in the ULA, the closer the theoretical limit of spectral efficiency is. In this case, the propagation channel looks different for the receivers and the propagation channels become independent from each other. Therefore, we can take advantage of the spatial multiplexing and the spectral efficiency to be closer to the Shannon limit. It is remarkable that curves between λ/10 and λ/2 are more separated than curves between λ/2 and λ. This fact shows that a λ/10 spacing significantly affects the channel due to the high correlation. However, spacing values above λ/2 are enough decorrelated to take advantage of the channel diversity. In absolute terms, the improvement from λ/10 to λ/2 is 13 bps/Hz (UMa) and 12 bps/Hz (UMi). Nevertheless, the improvement from λ/2 to λ is only 2 bps/Hz (UMa) and 5 bps/Hz (UMi). In conclusion, a wider spacing between BS antennas allows an increase in spectral efficiency for the user by decreasing the antenna correlation and increasing the independence of the communication channels.

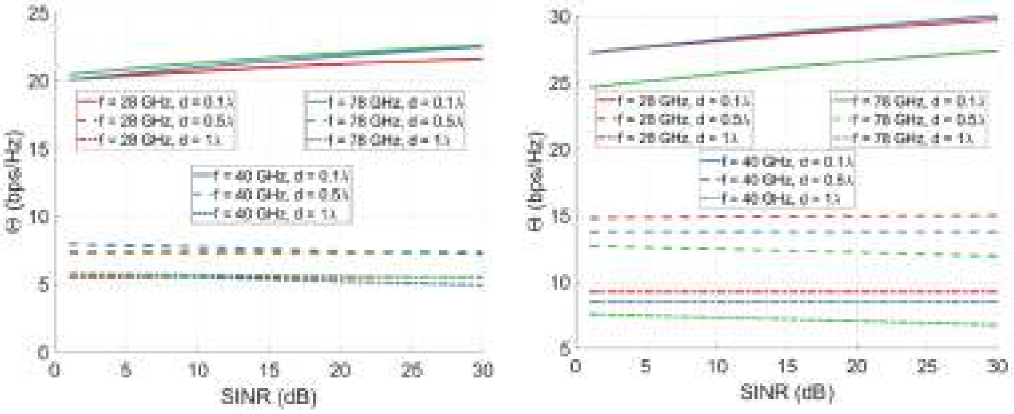

(**a**) (**b**)

Figure 4. Distance to the spectral efficiency theoretical limit for three frequencies (28 GHz, 40 GHz and 78 GHz) and three TX/RX antenna spacing (λ/10, λ/2 and λ) for several SINR values in a D-MIMO (50 × 10). (**a**) UMa scenario and (**b**) UMi scenario.

The second test studies the influence of LoS and NLoS on the communication channels of a D-MIMO system. A D-MIMO formed by 50 TX and 10 RX is analyzed, where 2 BS are considered (25 TX per BS). Both BS are moved simultaneously from 50 to 1000 m away from the UE. The relative distance between BSs is set to be the BS-UE distance. According to the previous test, the antenna spacing is set to λ/2. Two environments were tested (UMa and UMi) and two frequencies were considered (10 GHz and 28 GHz). Figure 5a,b show the spectral efficiency of both frequencies and visibility conditions in function of the distance between the UE and both BSs for the UMa and UMi scenario respectively. For the UMa and UMi environment (LoS and NLOS cases), the spectral efficiency slightly decreases over distance due to attenuation in the propagation path. This decrease is not linear. Due to fading effects, there are distances where a constructive contribution of the multipath environment implies an increase in the efficiency. Likewise, at other distances, a destructive contribution from the multipath environment decreases the efficiency. Note that the 28 GHz channel also has lower efficiency than the 10 GHz channel due to higher attenuation. However, besides all effects mentioned, the main one is the LoS/NLoS condition. For both environments, the spectral efficiency is increased by approximately 25% when the propagation path includes the Line-of-Sight. In conclusion, the network deployment for massive D-MIMO systems should ensure a spacing antenna above λ/2 and should provide the UE with LoS to maximize the spectral efficiency of the communications.

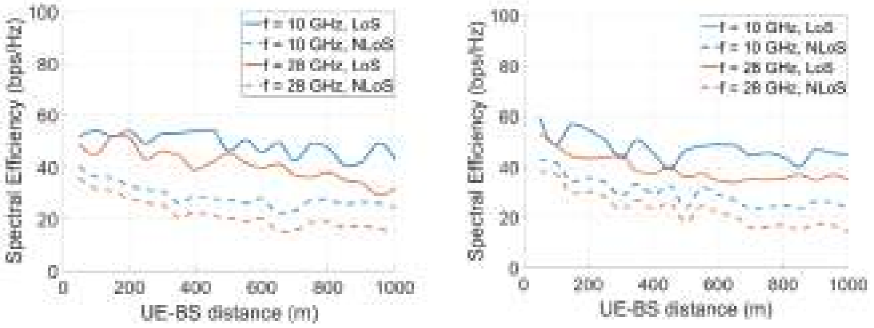

(**a**) (**b**)

Figure 5. Spectral efficiency of a D-MIMO (50 × 10) system for two frequencies (10 GHz and 28 GHz) and LoS and NLoS visibility conditions. SINR is fixed to 15 dB. (**a**) UMa scenario and (**b**) UMi scenario.

5. D-MIMO System on a Semi-Anechoic and Semi-Reverberation Chamber in the mmWave Band

5.1. Measurement Scenario

This last section is focused on the analysis of a D-MIMO system in the mmWave band acquired in a controlled scenario, such as a semi-anechoic and semi-reverberation chamber. For that purpose, two distinct scenarios are taken into account. On the one hand, the semi-anechoic part is commonly used for the characterization of radiating elements due to the absorption of any reflection in the scenario. In this case, it is used as a communication channel where the lack of reflections decreases the diversity of the scenario. Only one direct beam reaches the receiver through the LoS. Therefore, it is expected to notice a very high correlation between channel measurements. On the other hand, the semi-reverberation part implies a rich scattering environment since the metallic walls generate several propagation paths for the electromagnetic waves. In this case, any movement on the BS/UE generates a totally different propagation path, which makes the correlation between channels low. A complete and detailed description of the chamber is available in [27].

5.2. Anechoic and Reverberation Channel Analysis

Once the two types of propagation channels are known, two MIMO systems are acquired. The first one has a BS with 11 TX pointing the UE in the semi-anechoic part. The transmitters are arranged at 90° amplitude in the azimuth angle, with an angle separation between consecutive transmitters of 9°. The UE is composed by 5 RX in a 20 cm lineal array, where the separation between consecutive RX is 5 cm. The frequency range of the measurement goes from 40 GHz to 50 GHz for 101 frequency samples (100 MHz frequency spacing) and the distance on the LoS is 150 cm. The second MIMO measured is similar to the first one. The main difference lies on the BS pointing angle. In this case, the BS points directly to the metallic wall in the semi-reverberation part, which makes a NLoS scenario where the signal reaches the RX through several reflections. In this case, the shortest path from the TX to the RX is 720 cm.

Due to the peculiarities of the scenarios, several conclusions can be drawn. The anechoic channels are expected to achieve lower attenuations due to the proximity between the pair TX/RX. However, the correlation between channels will be high due to the low spatial diversity of the scenario. On other hand, the reverberation channels are expected to obtain higher attenuations due to the TX-RX distance. Nevertheless, the channels tend to be independents.

Once the previous facts were known, we created a D-MIMO system formed by both MIMO systems. A matrix channel $\boldsymbol{H} = \left[\boldsymbol{H}_1^T, \boldsymbol{H}_2^T\right]^T$ with dimensions 22 TX × 5 RX for 101 frequency samples was obtained. The normalized power balance for the submatrix $\boldsymbol{H}_1$ and $\boldsymbol{H}_2$ is 1 and 0.158, respectively. As previously stated, the anechoic channels achieve the maximum power, and the reverberation channels are attenuated in a factor 6.325 in average. Without the application of a normalization factor, reverberation channels will be masked by the anechoic channels. Therefore, as shown in Section 3, Att_1 and Att_2 factors multiply the anechoic and reverberation channels in order to modulate the D-MIMO balance power. Figure 6 shows a parametric sweep of both factors for the spectral efficiency. Att_1 moves in the range from 0 to 2 and Att_2 in the range from 0 to 5. Moreover, a black line with slope 6.325 is shown. This line represents those operating points where the D-MIMO is balanced in terms of power. On the right side of this line, the D-MIMO system is dominated by anechoic channels, while the reverberation channels prevail in the left side. The higher the prevalence of the anechoic channels, the lower the spectral efficiency due to the high correlation between these channels. As we approach the equilibrium line, the presence of the significantly less correlated reverberation channels becomes higher, which increases the efficiency. In the balanced region, the efficiency is maximized around 45 bps/Hz. On the left side, the values remain around the maximum because the reverberation channels are the predominant ones over the anechoic channels.

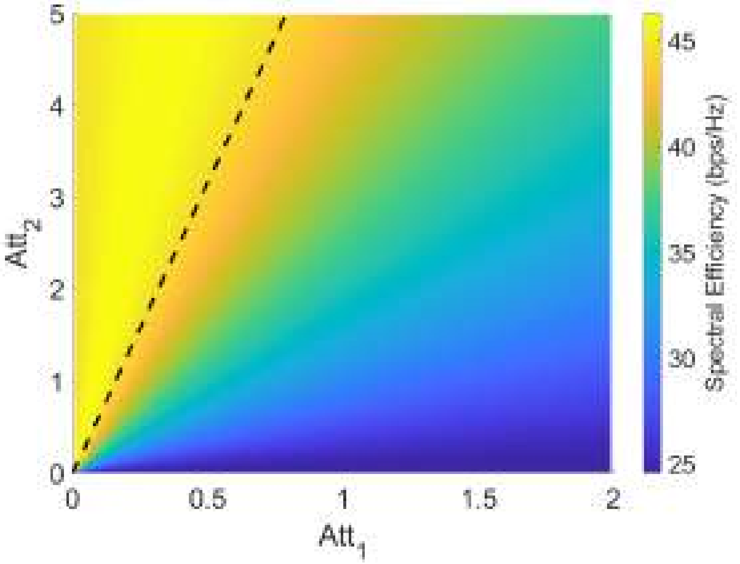

Figure 6. Spectral efficiency for a parametric sweep of Att_1 and Att_2. The black line stands for the region where both MIMO subsystems are balanced in terms of power. The SINR is fixed to 30 dB and the values are averaged over the 101 frequency samples.

Finally, to further explore this scenario, three key operating points were studied in terms of SINR. Figure 7 illustrates the spectral efficiency of the MIMO subsystem formed by the anechoic channels, the unbalanced D-MIMO and the balanced D-MIMO. The first curve takes into account only the $\boldsymbol{H}_1$ channel matrix. For 30 dB SINR, it reaches a spectral efficiency of 24.5 bps/Hz. This operating point is shown in Figure 6 for $Att_1 = 1$ and $Att_2 = 0$. If we include the reverberation channels, the unbalanced D-MIMO is formed. In this case, diversity is added to the scenario, although reverberation channels are masked due to unbalancing. The effect can be seen in the second curve, where the spectral efficiency is slightly improved. This operating point corresponds to $Att_1 = 1$ and $Att_2 = 1$, where the spectral efficiency is 30.9 bps/Hz in Figure 6. Finally, the channel power balance can improve further the scenario. This effect is shown in the third curve, where the spectral efficiency is significantly improved ($Att_1 = 0.158$ and $Att_2 = 1$). Due to this fact, values up to 45 bps/Hz are achieved. This means an improvement of 45.6% compared with the unbalanced case and 83.7% compared with the anechoic subsystem.

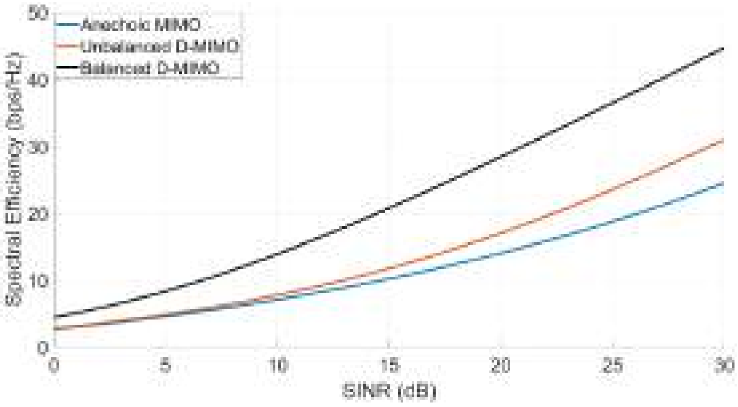

Figure 7. Spectral efficiency for the anechoic MIMO (blue line), unbalanced D-MIMO (red line) and balanced MIMO (black line). For each value of SINR, the spectral efficiency is averaged over the 101 frequency samples.

Once the previous case was studied, a second set of measurements was acquired. On the one hand, 33 TX points the UE in the semi-anechoic chamber. As in previous case, TXs are arranged at a 90° amplitude in the azimuth angle with a separation of 9° (11 locations). However, we added 11 TX 5 cm on the left and 11 TX 5 cm on the right to form a ULA. Each position includes 11 TX that varies in the azimuth angle, for a total of 33 TX. On the other hand, the UE is composed of 25 RX in a 20 cm uniform rectangular array (URA), where the separation between the consecutive RX is 5 cm in both axes. The second MIMO is similar to the first one, but pointing the semi-reverberation chamber. The distances and frequency ranges are the same as in the previous example.

After the acquisition, the D-MIMO channel matrix is formed by combining both MIMO system, whose size is 66 TX × 25 RX. The normalized power balance for the anechoic MIMO and reverberation MIMO is 1 and 0.091, respectively. This means the reverberation MIMO is even more unbalanced than in Figure 6. Specifically, reverberation channels are attenuated in an 11.042 factor compared with the anechoic channels. Figure 8A presents a sweep parameter for Att_1 and Att_2 factors, where we can extract similar conclusions as in Figure 6. Note that the black line which indicates the balance power equilibrium is shifted to the left. This is due to the larger unbalance from the reverberation chamber. The slope of this equilibrium point is 11.042. In the balance region, the spectral efficiency is maximized around 205 bps/Hz. Figure 8B shows the operation points previously illustrated in Figure 7. When the number of propagation channels increases and the power distribution is balanced, the spectral efficiency is also expected to increase. For a 30 dB SINR, the anechoic MIMO obtains 60.7 bps/Hz, the unbalanced D-MIMO gets 94.3 bps/Hz and the balance D-MIMO achieves 205.8 bps/Hz. In relative terms, the balanced D-MIMO system has an improvement of 118.3% compared with the unbalanced case and 238.9% compared with the anechoic subsystem. These results show how critical a proper assignation of the power resources is for massive D-MIMO systems.

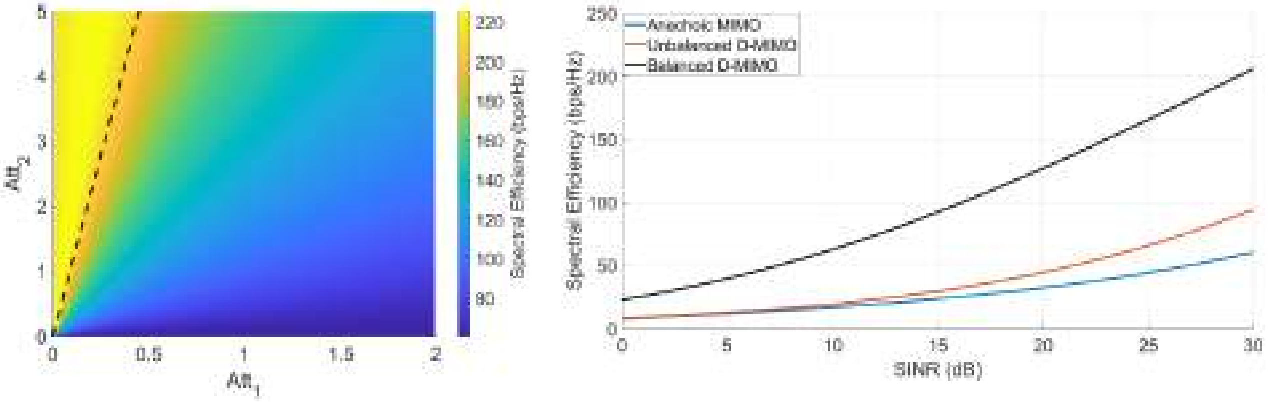

(**a**) (**b**)

Figure 8. (**a**) Spectral efficiency (D-MIMO 66 × 25) for a parametric sweep of Att_1 and Att_2 and (**b**) spectral efficiency for the anechoic MIMO (blue line), unbalanced D-MIMO (red line) and balanced MIMO (black line).

The analysis made in this section shows that decorrelation of channels in a D-MIMO, as well as channel power balance, imply the improvement of propagation channel conditions, ensuring both conditions induce optimal physical channel performance. Furthermore, by comparing both D-MIMOs, it was shown that the higher the number of propagation channels are, the more noticeable this improvement is.

6. Conclusions

In the current work, an analysis of the performance of D-MIMO systems under different conditions was carried out. Several MIMO scenarios have been proposed. On the frequency side, several bands were studied, including the sub–6 GHz and the mmWave band. On the scenario side, both simulated and real measurements were analyzed for a wide variety of environments. Rural and urban scenarios were emulated, and channels from anechoic and reverberation chambers were acquired.

The analysis of all these measurements was focused on the balance power and the correlation between propagation channels for distributed MIMO systems. These systems are expected to be fundamental in the future deployment of mobile networks due to the large number of antennas which allows high spectral efficiencies. In this study, it was found that D-MIMO provides high data rates compared with common MIMO systems. However, it is fundamental to perform an accurate deployment analysis in order to find decorrelated and balanced propagation channels in terms of power. Throughout the study, we observed how the combination of both properties takes full advantage of the benefits of the propagation channel, significantly increasing the spectral efficiency on the physical layer of the communication channels. The network operation following design criteria such as those seen in this study is fundamental for the multi-connectivity expected in D-MIMO systems. An optimal choice of such criteria showed network performances of 45.6% (22 TX × 5 RX D-MIMO) and 118.3% (66 TX × 25 RX D-MIMO) better than non-optimal cases in terms of spectral efficiency for similar D-MIMO systems but with different power allocation criteria.

Author Contributions: Conceptualization, A.R.-A. and J.C.G.-M.; methodology, A.R.-A., J.C.G.-M. and J.C.-M.; formal analysis and investigation, A.R.-A., J.C.G.-M., J.J.R.-P., J.C.-M. and A.M.-G.; writing—original draft preparation, A.R.-A., J.C.G.-M., J.J.R.-P. and A.M.-G.; writing—review and editing, A.R.-A. and J.C.G.-M. All authors have read and agreed to the published version of the manuscript.

Funding: This work was supported in part by the Spanish Government under Project PID2020-112545RB-C54, Project RTI2018-102002-A-I00 and Project TIN2016-75097-P, in part by "Junta de Andalucía" under Project B-TIC-402-UGR18, Project A-TIC-608-UGR20 and Project P18.RT.4830, in part by "Junta de Extremadura" under Project IB18003 and in part by the predoctoral grant FPU19/01251.

Data Availability Statement: Not applicable.

Acknowledgments: The authors would like to thank the constructive comments and help of Juan Valenzuela-Valdés.

Conflicts of Interest: The authors declare no conflict of interest.

References

1. Ericsson. Ericsson Mobility Report June 2021. 2021. Available online: https://www.ericsson.com/4a03c2/assets/local/mobility-report/documents/2021/june-2021-ericsson-mobility-report.pdf (accessed on 29 September 2021).
2. Cisco. Cisco Annual Internet Report (2018–2023). 2020. Available online: https://www.cisco.com/c/en/us/solutions/collateral/executiveperspectives/annual-internet-report/white-paper-c11-741490.html (accessed on 29 September 2021).
3. Han, B.; Liu, Y.; Qian, F. ViVo: Visibility-aware mobile volumetric video streaming. In Proceedings of the 26th Annual International Conference on Mobile Computing and Networking, London, UK, 21–25 September 2020; Association for Computing Machinery: New York, NY, USA, 2020; pp. 1–13.
4. Ramirez-Arroyo, A.; Zapata-Cano, P.H.; Palomares-Caballero, A.; Carmona-Murillo, J.; Luna-Valero, F.; Valenzuela-Valdes, J.F. Multilayer Network Optimization for 5G & 6G. *IEEE Access* **2020**, *8*, 204295–204308.
5. Albreem, M.A.; Juntti, M.; Shahabuddin, S. Massive MIMO Detection Techniques: A Survey. *IEEE Commun. Surv. Tutor.* **2019**, *21*, 3109–3132. [CrossRef]
6. MacCartney, G.R.; Rappaport, T.S. Millimeter-Wave Base Station Diversity for 5G Coordinated Multipoint (CoMP) Applications. *IEEE Trans. Wirel. Commun.* **2019**, *18*, 3395–3410. [CrossRef]
7. Jungnickel, V.; Manolakis, K.; Zirwas, W.; Panzner, B.; Braun, V.; Lossow, M.; Sternad, M.; Apelfröjd, R.; Svensson, T. The role of small cells, coordinated multipoint, and massive MIMO in 5G. *IEEE Commun. Mag.* **2014**, *52*, 44–51. [CrossRef]
8. Zhang, J.; Ji, Y.; Jia, S.; Li, H.; Yu, X.; Wang, X. Reconfigurable Optical Mobile Fronthaul Networks for Coordinated Multipoint Transmission and Reception in 5G. *J. Opt. Commun. Netw.* **2017**, *9*, 489–497. [CrossRef]
9. Yu, Y.-J.; Hsieh, T.-Y.; Pang, A.-C. Millimeter-Wave Backhaul Traffic Minimization for CoMP Over 5G Cellular Networks. *IEEE Trans. Veh. Technol.* **2019**, *68*, 4003–4015. [CrossRef]
10. Bassoy, S.; Farooq, H.; Imran, M.A.; Imran, A. Coordinated Multi-Point Clustering Schemes: A Survey. *IEEE Commun. Surv. Tutor.* **2017**, *19*, 743–764. [CrossRef]
11. Bassoy, S.; Imran, M.A.; Yang, S.; Tafazolli, R. A Load-Aware Clustering Model for Coordinated Transmission in Future Wireless Networks. *IEEE Access* **2019**, *7*, 92693–92708. [CrossRef]
12. Chen, S.; Zhao, T.; Chen, H.-H.; Lu, Z.; Meng, W. Performance Analysis of Downlink Coordinated Multipoint Joint Transmission in Ultra-Dense Networks. *IEEE Netw.* **2017**, *31*, 106–114. [CrossRef]
13. Schwarz, S.; Rupp, M. Exploring Coordinated Multipoint Beamforming Strategies for 5G Cellular. *IEEE Access* **2014**, *2*, 930–946. [CrossRef]
14. Marotta, A.; Cassioli, D.; Antonelli, C.; Kondepu, K.; Valcarenghi, L. Network Solutions for CoMP Coordinated Scheduling. *IEEE Access* **2019**, *7*, 176624–176633. [CrossRef]
15. Li, L.; Yang, C.; Mkiramweni, M.E.; Pang, L. Intelligent Scheduling and Power Control for Multimedia Transmission in 5G CoMP Systems: A Dynamic Bargaining Game. *IEEE J. Sel. Areas Commun.* **2019**, *37*, 1622–1631. [CrossRef]
16. Georgakopoulos, P.; Akhtar, T.; Politis, I.; Tselios, C.; Markakis, E.; Kotsopoulos, S. Coordination Multipoint Enabled Small Cells for Coalition-Game-Based Radio Resource Management. *IEEE Netw.* **2019**, *33*, 63–69. [CrossRef]
17. Mismar, F.B.; Evans, B.L. Deep Learning in Downlink Coordinated Multipoint in New Radio Heterogeneous Networks. *IEEE Wirel. Commun. Lett.* **2019**, *8*, 1040–1043. [CrossRef]
18. Song, G.; Wang, W.; Chen, D.; Jiang, T. KPI/KQI-Driven Coordinated Multipoint in 5G: Measurements, Field Trials, and Technical Solutions. *IEEE Wirel. Commun.* **2018**, *25*, 23–29. [CrossRef]
19. Park, S.; Alkhateeb, A.; Heath, W.R., Jr. Dynamic Subarrays for Hybrid Precoding in Wideband mmWave MIMO Systems. *IEEE Trans. Wirel. Commun.* **2017**, *16*, 2907–2920. [CrossRef]
20. Li, J.; Wang, D.; Zhu, P.; Wang, J.; You, X. Downlink Spectral Efficiency of Distributed Massive MIMO Systems with Linear Beamforming Under Pilot Contamination. *IEEE Trans. Veh. Technol.* **2018**, *67*, 1130–1145. [CrossRef]
21. Lv, Q.; Li, J.; Zhu, P.; You, X. Spectral Efficiency Analysis for Bidirectional Dynamic Network with Massive MIMO Under Imperfect CSI. *IEEE Access* **2018**, *6*, 43660–43671. [CrossRef]
22. Marzetta, T.L.; Larsson, E.G.; Yang, H.; Ngo, H.Q. *Fundamentals of Massive MIMO*; Cambridge University Press: Cambridge, UK, 2018.
23. Loyka, S.; Levin, G. On physically-based normalization of MIMO channel matrices. *IEEE Trans. Wirel. Commun.* **2009**, *8*, 1107–1112. [CrossRef]

24. Valenzuela-Valdes, J.; Martinez-Gonzalez, A.; Sanchez-Hernandez, D. Emulation of MIMO Nonisotropic Fading Environments with Reverberation Chambers. *IEEE Antennas Wirel. Propag. Lett.* **2008**, *7*, 325–328. [CrossRef]
25. Valenzuela-Valdes, J.; Martinez-Gonzalez, A.; Sanchez-Hernandez, D. Diversity Gain and MIMO Capacity for Nonisotropic Environments Using a Reverberation Chamber. *IEEE Antennas Wirel. Propag. Lett.* **2009**, *8*, 112–115. [CrossRef]
26. Ju, S.; Kanhere, O.; Xing, Y.; Rappaport, T.S. A Millimeter-Wave Channel Simulator NYUSIM with Spatial Consistency and Human Blockage. In Proceedings of the 2019 IEEE Global Communications Conference (GLOBECOM), Waikoloa, HI, USA, 9–13 December 2019; pp. 1–6.
27. Ramírez-Arroyo, A.; Alex-Amor, A.; García-García, C.; Palomares-Caballero, Á.; Padilla, P.; Valenzuela-Valdés, J.F. Time-Gating Technique for Recreating Complex Scenarios in 5G Systems. *IEEE Access* **2020**, *8*, 183583–183595. [CrossRef]

2.2.2 Time-Gating Technique for Recreating Complex Scenarios in 5G Systems

Due to the constant evolution of mobile communications, it is fundamental to characterize propagation conditions in a large number of scenarios. In some cases, *in situ* measurements are not feasible. In this publication, a scenario-creation strategy based on the time-gating technique is proposed. This technique can modify the propagation channel in the time domain by removing reflections, shifting multipath components, or generating new artificial reflections. Therefore, its use in anechoic and reverberation chambers is proposed. By means of a geometrical study of the scenario, it is possible to recreate multipath propagation channels by using single path components modified with the time-gating technique. According to the previous work, the recreation of low spatially correlated and power-balanced channels maximizes the spectral efficiency. This emulation technique opens up the possibility to recreate scenarios based on measurements in controlled scenarios such as anechoic and reverberation chambers.

THIS IS THE PUBLISHED VERSION OF THE PAPER:

A. Ramírez-Arroyo, A. Alex-Amor, C. García-García, Á. Palomares-Caballero, P. Padilla and J. F. Valenzuela-Valdés, “Time-Gating Technique for Recreating Complex Scenarios in 5G Systems,” *IEEE Access*, vol. 8, pp. 183583-183595, 2020.

- Journal Impact Factor (JIF) in JCR 2020: 3.367
- Category: COMPUTER SCIENCE, INFORMATION SYSTEMS. JIF Rank: 65/161 (Q2).
- Category: ENGINEERING, ELECTRICAL & ELECTRONIC. JIF Rank: 94/273 (Q2).
- Category: TELECOMMUNICATIONS. JIF Rank: 36/91 (Q2).

Disclaimer:
This work has been published in IEEE Access.
DOI: 10.1109/ACCESS.2020.3028750

IEEE Access
Multidisciplinary | Rapid Review | Open Access Journal

Received September 16, 2020, accepted September 30, 2020, date of publication October 5, 2020, date of current version October 19, 2020.
Digital Object Identifier 10.1109/ACCESS.2020.3028750

Time-Gating Technique for Recreating Complex Scenarios in 5G Systems

ALEJANDRO RAMÍREZ-ARROYO[1], **ANTONIO ALEX-AMOR**[1,2], **CARMELO GARCÍA-GARCÍA**[1], **ÁNGEL PALOMARES-CABALLERO**[1], **PABLO PADILLA**[1], AND **JUAN F. VALENZUELA-VALDÉS**[1]
[1]Department of Signal Theory, Telematics and Communications, Universidad de Granada, 18071 Granada, Spain
[2]Information Processing and Telecommunications Center, Universidad Politécnica de Madrid, 28040 Madrid, Spain
Corresponding author: Alejandro Ramírez-Arroyo (alera@ugr.es)

This work was supported in part by the Spanish Program of Research, Development and Innovation under Project TIN2016-75097-P, Project RTI2018-102002-A-I00, and Project EQC2018-004988-P; in part by the Junta de Andalucía under Project B-TIC-402-UGR18 and Project P18.RT.4830, and in part by the Predoctoral Grant FPU19/01251 and Grant FPU18/01965.

ABSTRACT This article presents a novel application of the time-gating technique to the field of propagation channel study. The time-gating technique is well known in the field of antenna measurement and it is used to eliminate reflected components in outdoor measurements or anechoic chambers. In this article, we present a new measurement configuration for shielded chambers that allows to configure different propagation scenarios. In this configuration, the chamber is covered in one part with absorbers and in the other without absorbers (in order to generate reflected components). Applying the time-gating technique, we can modify, adjust and tune the reflections that a certain propagation environment has. This yields a relative control of the propagation environment in both far field and near field regions and allows to quantify the spectral efficiency and signal correlation that MIMO systems would display operating in those propagation environments.

INDEX TERMS Anechoic chamber, impulse response, MIMO, recreate scenarios, reverberation chamber, time-gating.

I. INTRODUCTION

Advances in communication systems and technologies are having a fundamental and profound impact on people's daily lives and social activities [1], [2], leading to a continuous expansion of data traffic and the number of connections [3]. In this scenario, wireless communication systems have become one of the most powerful, dynamic and promising areas for user access to the Information and Communication Technologies (ICTs). The 3rd Generation Partnership Project (3GPP) divides the 5G program into two phases, phase 1 in the Release-15 and phase 2 in the Release-16 [4]. In the first one there is a growing support to vertical industries [5], [6]: non terrestrial networks (NTN), vehicle to all (V2X), public safety, Industrial Internet of Things (IoT) that has been boosted in the Release-16 and in the predefinition of the Release-17 [7]. Since communication needs will not be fully met by 5G networks, the International Telecommunications Union (ITU) has already set up a working group to look at the development of future networks beyond 5G (ITU-T Focus Group Technologies for Network 2030, FG NET-2030). This focus group has stated that autonomous vehicles, machine-to-machine mass communications, touch Internet and holographic communications will become a reality in the coming years and frequency bands above 100 GHz will need to be explored in order to make these communications a reality. In this context, any communication system is conditioned and limited by the propagation environment in which the communication takes place [8]. This makes it essential that the influence of the radio environment is properly studied in order to determine the conditions under which the communications take place (level of available power, maximum transmission speed, etc.), as well as the main limitations and clear risks of communication failure. On this basis, many scenarios need to be emulated, such as: Microcellular outdoor scenarios (O2O, Outdoor-to-Outdoor) [9], indoor scenarios [10] (I2I, Indoor-to-Indoor), outdoor-to-indoor scenarios [11], [12] (O2I, Outdoor-to-Indoor), or vehicular scenarios (V2X, Vehicular-to-Vehicular/Infrastructure), among others. Moreover, it will also be necessary to characterize particular scenarios, such as tunnels, factories, trains and car interior (on-car), which

The associate editor coordinating the review of this manuscript and approving it for publication was Wei Fan.

complete the environments proposed for 5G and beyond applications [13], [14]. Therefore, it is necessary to characterize the propagation conditions in a large number of scenarios.

There are many research groups performing in-situ measurements with different channel sounders at different frequencies and very different locations. As an example, three surveys of the propagation measurements can be found in [15]–[17]. However, a cheaper alternative is to reproduce such environments in the laboratory. Different alternatives have been proposed in recent years to perform Over the Air Test (OTA) measurements in the laboratory [18]–[22]. The first alternative is to perform measurements in an anechoic chamber with multiple antennas positioned in a circle that are connected to a channel emulator that reproduces the channel conditions. Another cheaper solution is based on reverberation chambers in which the configuration of the scenario is achieved by introducing different objects inside the chamber [23]. For example, in [24] the propagation environment of an oil refinery is compared to the introduction of a certain load into the chamber. In [25], [26] different scenarios are emulated with different angles of arrival and different number of multipath components (MPCs). In addition, there are specific designs to reproduce certain scenarios such as those found in [27], [28] where vehicle scenarios are reproduced. In order to refine those scenario emulations, post-processing techniques have been developed, such as changing the Rician factor [29] or selecting certain samples [30] to reproduce a specific scenario. In order to increase the number of recreated scenarios, this article proposes the use of a scenario creation strategy based on the well-known time-gating technique for measuring antennas, where different parameters such as spectral efficiency, signal correlation or power balance are analyzed. On what follows, it is shown how the time-gating technique can be used to modify the real propagation scenario allowing to remove some reflections inside a chamber, or with an appropriate signal processing, to change the time of arrival of some reflections. Furthermore, it allows to go beyond the limits of a certain measurement setup, i.e., allowing new degrees of freedom with the creation of artificial reflections.

The paper is organized as follows. Section II introduces the time-gating technique and particularizes its use to antenna measurement. Sections III and IV show the capabilities of the time-gating technique for the recreation of complex scenarios in anechoic chambers and reverberation chambers, respectively. Finally, the main conclusions of the work are drawn in Section V.

II. MEASUREMENT SET-UP AND TIME-GATING TECHNIQUE

This section describes the measurement set-up and the steps followed in the application of the time-gating technique. Afterwards, we particularize its use to the characterization of antenna radiation patterns, in order to test the capabilities of the method.

The measurements were taken in a shielded chamber with the following dimensions: $5 \times 3.5 \times 3.5$ meters. This chamber was designed to make measurements above 10 GHz, so we will have a maximum wavelength of 3 cm. Specifically, in this article measurements above 30 GHz have been made. Therefore, a maximum wavelength of 1 cm is considered, which together with an antenna diameter of 28 mm (see Section III), ensures that measurements are in the far field. This assumption is valid due to the use of virtual arrays for the considered MIMO configurations. The chamber, shown in Figs. 1 and 2, is divided into two parts. The left part resembles a traditional anechoic chamber and has been successfully used for the measurement of radiation patterns in [31]–[33]. The measurement of radiation patterns is possible because the minimum reflections caused in the reverberant chamber can be eliminated with the time-gating technique and because the level of the reflections is very low when going through an electrically long distance (large number of wavelengths), since they are reflected in some of the walls on the right. The part on the right has been left uncovered with absorbers to resemble a reverberation chamber. If we position the transmitter in the direction of the wall there will be multiple reflections that will vary depending on the direction. In this way we can approximately control the number of reflections that our measurement has. The chamber is equipped with two different positioning systems. On one side a motorized system has been installed that allows the movement of the receiving antenna in the x-axis and in the z-axis according to Fig. 3, with a movement amplitude of 2 meters in the x-axis and 1 meter in the z-axis with the aim of being able to form virtual arrays. On the other side we have a motorized table that allows us to move in 4 directions: (i) the 360° turn in roll (β) as shown in Fig. 1 (ii) the turn in azimuth (ϕ), (iii) the movement in $x2$-axis, that is in parallel with the x-axis of the other system and (iv) the movement in y-axis (Fig. 3) to move the two systems closer and further apart. Therefore, at this end it will be possible to configure virtual arrays with almost infinite possibilities. Depending on the configuration and the pointing direction, it will allow us to have a relative control of the directions of arrival and the number of clusters. From now and on, we will refer in this article to the left side as the anechoic chamber part and to the right side as the reverberant chamber part although strictly speaking they are neither an anechoic nor a reverberant chamber.

Figs. 1(a) and 1(b) show a sketch of the anechoic and reverberant chamber, respectively. Fig. 2 illustrates a panoramic view of the chamber. The transmitter can be rotated to target the anechoic zone or the reverberant zone. This transmitter can be oriented on three axes (y, ϕ, β) as Fig. 3 details. Also, the receiver has mobility in the axes x and z. Fig. 3 shows the signal processing steps associated to the time-gating technique. The frequency samples acquired in the VNA represent the channel matrix $H(f)$. The time-gating technique enables the channel matrix processing by means of controlling the impulse response of the channel $h(t)$. In a first step, $h(t)$ is obtained from $H(f)$ after applying the inverse Fourier transform (IFT). Then, the impulse response $h(t)$ is modified according to the needs of the scenario: In antenna

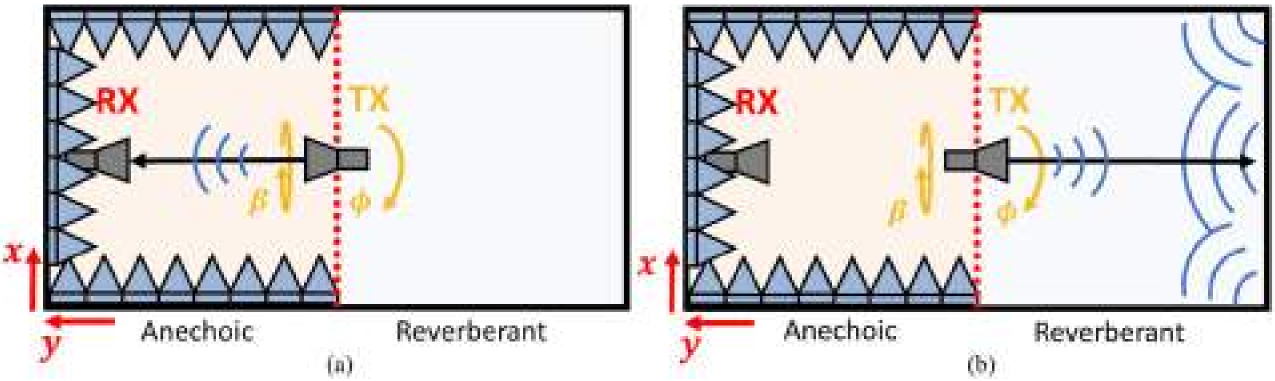

FIGURE 1. Schematics of the anechoic (a) and reverberation (b) chamber. In the anechoic chamber, the receiver is reached by LoS to the transmitter. In the reverberation chamber, the receiver is reached by multiple paths due to the multiple reflections.

FIGURE 2. Panoramic view of the chamber. The picture is taken from the bottom right of the diagrams view.

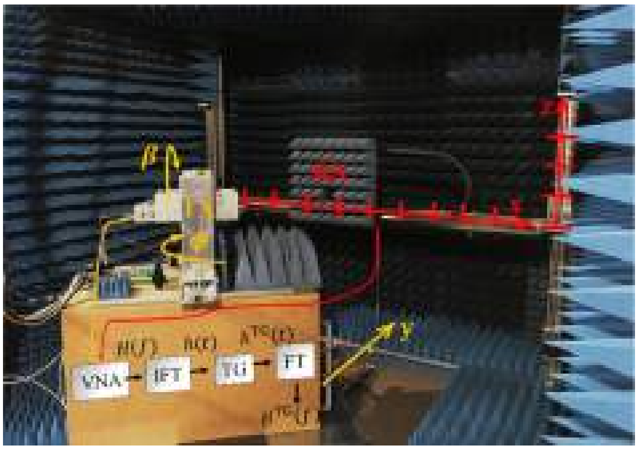

FIGURE 3. Antenna measurement scenario and signal processing steps. The transmitter (TX) antenna is able to move in roll (β) and azimuth (ϕ) angles and along the y axis. The receiver (RX) antenna is able to move along the x and z axes.

measurement, noise and reflections are removed from the radiation pattern. In propagation, we may want to amplify or create artificial reflections, in order to study their impact on the capacity of the channel. Finally, the modified channel matrix $H^{\mathrm{TG}}(f)$ is recovered from the time-gated impulse response $h^{\mathrm{TG}}(t)$ with the use of the Fourier transform (FT). This $H^{\mathrm{TG}}(f)$ is the new channel matrix that can recreate new scenarios. We are interested in applying the time-gating technique for the recreation of realistic propagation scenarios. However, time-gating has also application in antenna measurement [34], being particularly useful to improve the performance of imperfect anechoic environments. In addition, its use has recently been extended for the accurate characterization of antenna radiation patterns in reverberating enclosures [35]. In our case, it will be our test field in order to validate the time-gating method and calibrate the optimal parameters of its configuration and it is depicted in Appendix A.

III. RECREATING SCENARIOS IN ANECHOIC CHAMBERS

In this section, the potential of the time-gating technique for the recreation of MIMO scenarios inside anechoic chambers is illustrated. In this side of the chamber the environments are fully controlled and it serves us to test and validate our technique. The objective of this section is to show that with a single measurement (SISO) we can recreate several scenarios and save some resources and measurements. In Appendix B, it is described the method used to estimate the time of arrival and the amplitude of the reproduced arrays.

A. MISO SCENARIO

As an example, we will try to recreate with the use of time-gating the measurement scenario presented in Fig. 4. Four transmitting antennas are separated by 30 cm forming a linear array. The RX antenna is placed at 80 cm from the first TX antenna, TX_1. All radiating elements are standard gain horns, fed in this case with a WR22 waveguide-to-coaxial transition. The operating frequency range of the measurement covers from 32 GHz to 39 GHz.

The normalized impulse response $h(t)$ of the measured MISO (Multiple Input Single Output) scenario is illustrated in Fig. 5(a). For the sake of clarity, the peaks associated to the different TX antennas are marked in different colors. The

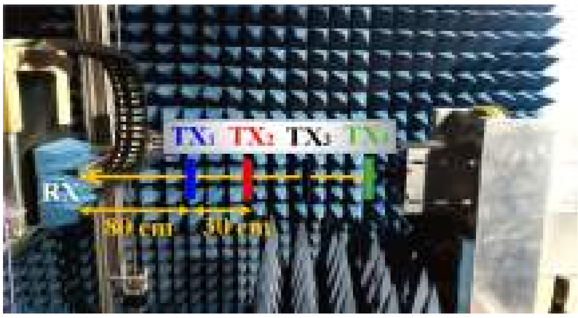

FIGURE 4. Measurement scenario for the MISO (4 × 1) system. The TX antennas are separated by 30 cm, forming a virtual linear array.

location of the peaks is related to the distance between TX and RX antennas. The first transmitting antenna (TX_1) is located at 80 cm from the RX antenna. As a consequence, the propagating signal takes 2.67 ns to reach the RX antenna. However, note that the maximum is located at 3.4 ns, taking into account the length of the waveguide-to-coaxial transitions, not included in the calibration. The separation between consecutive peaks is constant in Fig. 5(a), being approximately 1 ns, since the distance between adjacent antennas is constant too. Therefore, the impulse responses of TX_2, TX_3, and TX_4 are centered at 4.4 ns, 5.4 ns and 6.4 ns, respectively. Additionally, if reflections and noise are negligible in the measurement, the amplitude decay between consecutive peaks can be approximated by only considering free space losses. The attenuation factor *att* is estimated for each TX_i antenna as the relation between the distances of the considered TX_i antenna and the first transmitter antenna TX_1 to the RX antenna. That is, $80\text{cm}/80\text{cm} = 1$ for TX_1, $80\text{cm}/110\text{cm} = 0.73$ for TX_2, $80\text{cm}/140\text{cm} = 0.58$ for TX_3 and $80\text{cm}/170\text{cm} = 0.47$ for TX_4.

As a result, the measured impulse response of the complete MISO scenario can be reconstructed from the impulse response of an individual TX antenna. For this case, we applied the time-gating technique over TX_1 and kept the relevant information of the measurement (from 1.8 ns to 5 ns). A symmetric Hann window with a relative window size of 20% is used in the process. Then, identical but attenuated and delayed copies of TX_1 are used to recreate the impulse responses of $TX_2(att = -0.73, t_{TX_2} = 4.4 \text{ ns})$, $TX_3(att = 0.58, t_{TX_3} = 5.4 \text{ ns})$ and $TX_4(att = -0.47, t_{TX_4} = 6.4 \text{ ns})$. For TX_2 and TX_4, note that a minus sign was used in the attenuation factor since the TX antennas are separated by half a wavelength. Thus, this sign preserves the original shape of the impulse response in Fig. 5(a) by adding an additional phase of 180°. Fig. 5(b) presents the reconstructed impulse response of the MISO scenario after the time-gating technique is applied. As it is shown, the similarities between the original and reconstructed impulse response of Figs. 5(a) and 5(b) are noticeable.

In order to quantify the quality of the recreation, we will compare the spectral efficiency of the original and recreated scenarios. The spectral efficiency of a MIMO (Multiple Input Multiple Output) system is calculated according to [36]

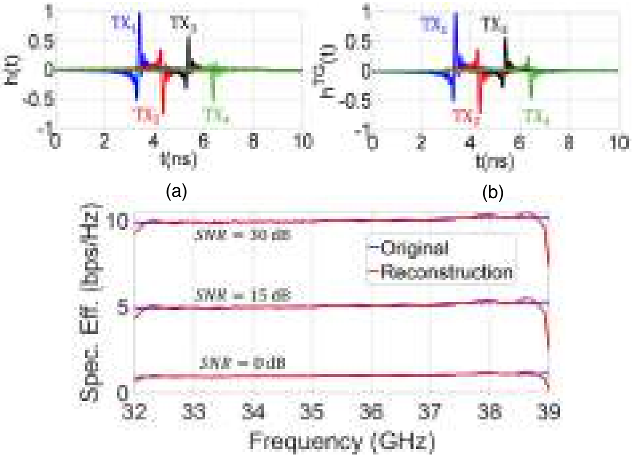

(a) (b)

(c)

FIGURE 5. Normalized impulse response of the MISO scenario: (a) original, (b) reconstructed with time-gating technique. (c) Spectral efficiency for different SNR values.

$$\eta \left[\frac{\text{bps}}{\text{Hz}}\right] = \log_2 \left| \det \left(\mathbf{I}_{N_{RX}} + \frac{SNR}{N_{TX}} \mathbf{H}^H \mathbf{H} \right) \right| \tag{1}$$

where N_{TX} is the number of transmitter antennas, N_{RX} is the number of receiver antennas, *SNR* is the signal-to-noise ratio, $\mathbf{H}$ is the channel matrix of dimensions $N_{TX} \times N_{RX}$, and the superscript ^{H} indicates the conjugate transpose. To include the frequency dependence of the channel, channel matrices $\mathbf{H}$ are normalized as detailed in [37], [38]

$$\mathbf{H}_{\text{norm}}(f_i) = \mathbf{H}(f_i) \left[\frac{1}{N_f} \sum_{i=1}^{N_f} \|\mathbf{H}(f_i)\|^2 \right]^{-1/2} \tag{2}$$

where $\|\cdot\|$ is the Frobenius norm.

Fig. 5(c) shows the spectral efficiency of the original (measured) and reconstructed scenarios for different SNR values. As it can be appreciated, there is an excellent agreement between both curves. The differences at the beginning and end of the frequency band are caused by the frequency window used in the Fourier transform. With the use of the time-gating technique, it is shown how the original MISO scenario can be recreated from the measurement of a single TX antenna, saving time and resources during the process. This technique could be of special interest for massive MIMO scenarios, due to their complexity and large number of elements required.

B. MIMO SCENARIO

Fig. 6 presents the measurement scenario of a MIMO 4 × 3 system. Four transmitter antennas are separated by 30 cm along the *y* axis and three receiver antennas are separated by 40 cm along the *x* axis. We will demonstrate that the time-gating technique can be used to recreate MIMO scenarios, simplifying and saving resources in the process. Similarly to the previous study, the measured

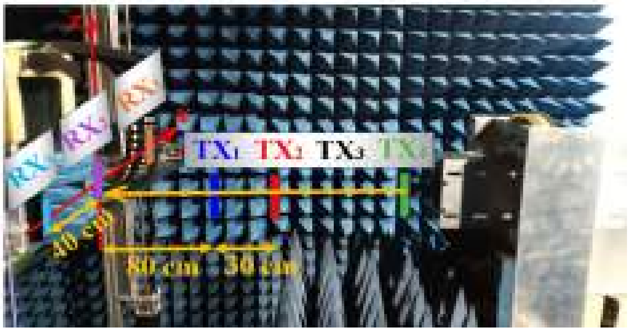

FIGURE 6. Measurement scenario for the MIMO (4 × 3) system. TX antennas are separated by 30 cm. RX antennas are separated by 40 cm.

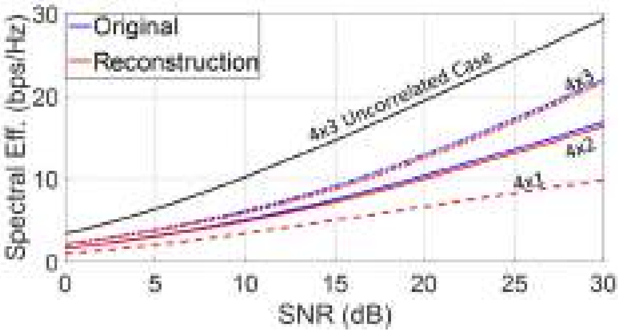

FIGURE 7. Original (blue curves), reconstructed (red curves) and theoretical limit (black curve) spectral efficiencies for different MIMO $N_{TX} \times N_{RX}$ systems when varying the number of RX antennas. For each SNR value, the spectral efficiency is averaged in the whole frequency range.

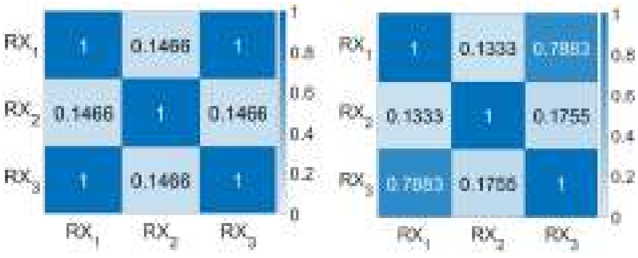

(a)

	RX_1	RX_2	RX_3
RX_1	1	0.1466	1
RX_2	0.1466	1	0.1466
RX_3	1	0.1466	1

(b)

	RX_1	RX_2	RX_3
RX_1	1	0.1333	0.7883
RX_2	0.1333	1	0.1755
RX_3	0.7883	0.1755	1

FIGURE 8. Correlation matrices of the three RX antennas for the (a) reconstructed and (b) original scenarios.

impulse response of the complete MIMO channel can be reconstructed from the impulse response of a reference SISO scenario. Thus, the channel matrix (4 × 3) is formed by attenuated and delayed copies of the reference signal, $h_{ref}(t)$. In our case, the reference TX and RX antennas from which the copies are built are TX_1 and RX_2, respectively. The attenuation factors and time delays are subsequently extracted by applying basic trigonometry and taking into account the gain drop associated to the radiation properties of the utilized horn antennas. More details are provided in Appendix B.

Fig. 7 illustrates the original and reconstructed spectral efficiency as a function of the SNR for different scenarios: MISO 4 × 1 (all TX and RX_2), MIMO 4 × 2 (all TX, RX_1 and RX_2), and MIMO 4 × 3 (all TX and all RX). In addition, the theoretical limit is shown, where a fully uncorrelated matrix is generated by using a normal Gaussian distribution. In this case, all the signals between any transmitter and receiver are completely different, which maximizes the transmitted information and consequently, the spectral efficiency. Analyzing the results, a noticeable agreement is evidenced between the measured and reconstructed scenario. As expected, the spectral efficiency increases as the SNR and the number of receivers is increased. However, note that the increase in spectral efficiency between MISO and MIMO 4 × 2 systems is greater than between MIMO 4 × 2 and MIMO 4 × 3. This fact could be linked to the high correlation [39] between the signals arriving at RX_1 and RX_3. For this reason, Fig. 8 shows the correlation matrices of the RX antennas for the configuration illustrated in Fig. 6. In the recreated scenario, the signals arriving at RX_1 and RX_3 are forced to be identical due to the symmetry of the scenario (see Appendix B). Thus, the correlation coefficients $C_{13} = C_{31}$ are exactly one in Fig. 8(a). In the original measured scenario, these coefficients are expected to be high, but different from one due to asymmetries in the radiation pattern, reflections, noise, etc. Conversely, the receivers RX_1 and RX_3 are uncorrelated with the central receiver RX_2, as the coefficients $C_{12} = C_{21}$ and $C_{23} = C_{32}$ indicate in Figs. 8(a) and 8(b).

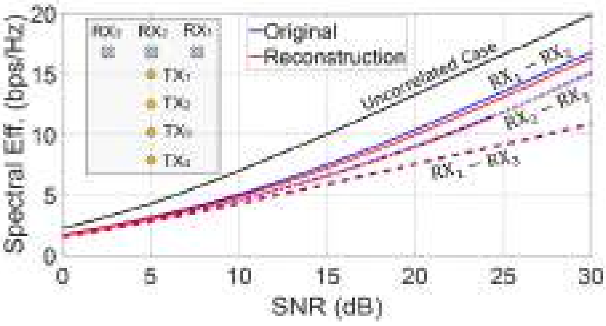

FIGURE 9. Original (blue curves), reconstructed (red curves) and theoretical limit (black curve) spectral efficiencies for every possible combinations of RX antennas in a MIMO 4 × 2 system. For each SNR value, the spectral efficiency is averaged in the whole frequency range. Solid (–), dash-dotted (–.) and dashed (––) lines correspond to $RX_1 - RX_2$, $RX_2 - RX_3$ and $RX_1 - RX_3$ pairs of RX antennas, respectively.

Fig. 9 focuses on the MIMO 4 × 2 system for every possible combination of RX antennas. The lowest spectral efficiency is obtained for RX_1 and RX_3 due to the high correlation between the receivers (see Fig. 8(b)). When the system is measured with RX_1 and RX_2, or RX_2 and RX_3, the spectral efficiency is higher than the previous case on account of the decorrelation of the signals. In fact, the spectral efficiency when $RX_1 - RX_2$ are used is slightly higher since the correlation in this case is slightly lower than in the case of $RX_2 - RX_3$.

The measurements on the MIMO 4 × 2 system can also be compared with the theoretical limit. Compared to the MIMO 4 × 3 system (see Fig. 7), the measurements in Fig. 9 are closer to the theoretical limit. This fact is explained because in the MIMO 4 × 2 system it is possible to decorrelate the signals received as explained previously. In the MIMO 4 × 3 system the correlation between RX_1 and RX_3 is always taken into account, and due to the symmetry of the system the correlation is close to one, moving the measurement away from the theoretical limit.

IV. RECREATING SCENARIOS IN REVERBERATION CHAMBERS

A. SISO SCENARIO

In this section, we show how the time-gating technique can be applied for the recreation of complex scenarios in reverberation chambers. For this case, the measurement scenario is presented in Fig. 10. A transmitter horn antenna (same one used in Section III) points at the metallic wall of the reverberation chamber. The multiple reflections inside the reverberating environment are acquired by a receiver antenna, which is aligned with the TX antenna. The frequency range of the measurement is set from 38 GHz to 39 GHz.

FIGURE 10. Measurement scenario for the SISO system inside the reverberation chamber. A transmitter antenna (TX) points at the metallic wall of the chamber and a receiver antenna (RX) acquires the multiple reflections inside it.

Fig. 11 shows the original and reconstructed signals inside the reverberation chamber. As previously done, we will use the spectral efficiency to quantify the quality of the recreation. It is remarkable that fewer reflections are observed compared to a reverberant chamber. It is due to the fact that half of the chamber is anechoic, so some of the reflections are attenuated. The reconstruction process is presented in three steps: Fig. 11(a) illustrates a comparison between the original and reconstructed scenarios when only the primary reflection R_p is considered. As it can be appreciated, the primary reflection, placed at 22 ns, contains most of the relevant information about the original scenario. It gives an average estimation of the spectral efficiency. However, secondary reflections must be also considered to completely define the scenario. Thus, identical but attenuated and delayed copies of R_p are used to recreate the secondary reflections R_{s1} and R_{s2}. In the present scenario, R_{s2} has a higher amplitude than R_{s1}. Therefore, the contribution of R_{s2} to the spectral efficiency is expected to be more significant compared to R_{s1}. Fig. 11(b) confirms this fact, showing that a good recreation of the measured scenario can be achieved by only considering the primary reflection R_p and the second secondary reflection R_{s2}. Finally, Fig. 11(c) presents the final reconstruction, which considers the primary reflection R_p and the two secondary reflections R_{s1} and R_{s2}. The inclusion of R_{s1} in the recreation adjusts some of the small details of the small measured spectral efficiency. The improvement through the addition of reflections can be quantified from the spectral efficiency normalized mean square errors (NMSEs), which for Figs. 11(a), 11(b) and 11(c) are 2.164, 1.653 and 1.506 respectively. The greater contribution of R_{s2} with respect to R_{s1} implies a greater decrease in the NMSE between Figs. 11(a) and 11(b) than between Figs. 11(b) and 11(c). The rest of the peaks observed in

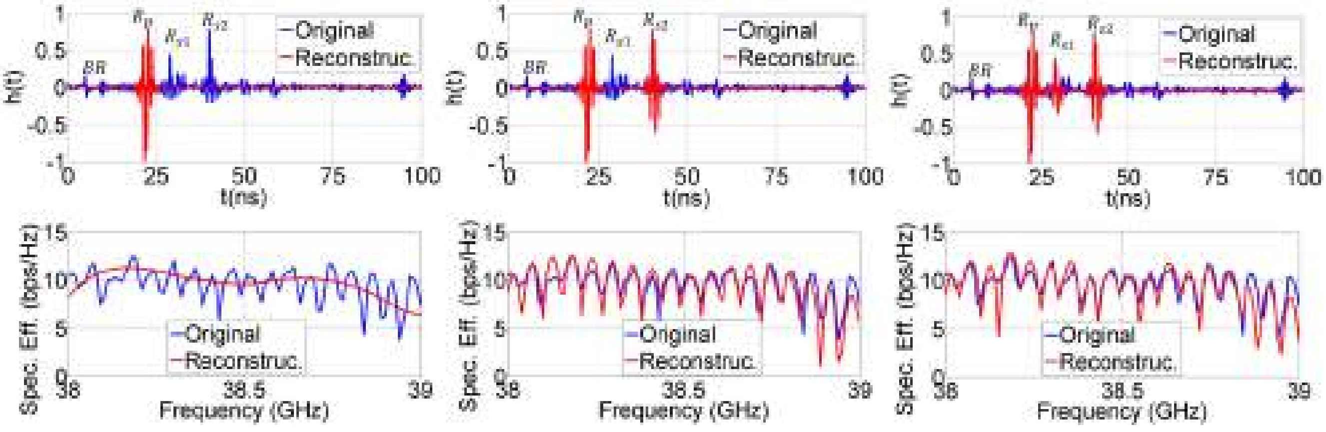

(a) (b) (c)

FIGURE 11. Original and reconstructed signals in the reverberation chamber. The reconstruction is presented in three steps, and the impulse responses and spectral efficiencies (for a $SNR = 30$dB) are provided together: (a) Only the primary reflection (R_p) is considered. (b) The primary reflection (R_p) and the second secondary reflection (R_{s2}) are considered. (c) Final reconstruction, including the primary reflection (R_p) and both secondary reflections (R_{S1},R_{S2}). Secondary reflections are identical but attenuated and delayed copies of R_p ($R_{s2} = -0.4R_p$,$R_{s2} = -0.75R_p$). *BR* refers to back radiation. The spectral efficiency NMSEs for the three reconstructions are 2.164, 1.653 and 1.506, respectively.

the measured impulse response of Fig. 11 are low-amplitude reflections that contain little information about the environment. Therefore, these peaks were excluded from the recreation for the sake of simplicity. Conversely, the origin of the two peaks observed at 5 ns and 9.5 ns is different. They appear before the primary reflection. This means that both peaks correspond to back radiation (*BR*) from the TX antenna. In addition, the amplitude level of both peaks is reduced, since the transmitter horn antenna is a directive antenna with low back-lobe level. Unlike the flat response observed in the MISO scenario of Fig. 5(c), there is a prominent ripple in the measured spectral efficiency of Fig. 11. The existence of multiple reflections in the reverberation chamber creates interference patterns that cause an increase or decrease in spectral efficiency at certain frequencies. For this reason, the reconstructed spectral efficiency is flatter when only a single reflection, R_p, is considered (see Fig. 11(a) vs Figs. 11(b) and 11(c)). In addition, the amplitude of the ripple is related to the amplitude of the secondary reflections. That is, the bigger the secondary reflections are, the bigger the ripple is.

B. MIMO SCENARIO

Once the SISO case has been studied, a more complex case is analyzed. Fig. 12 presents the measurement scenario of the MIMO 3 × 3 system located inside the reverberation chamber. Three TX antennas, oriented in azimuth angles of −45°, 0° and 45°, face the front metallic wall of the reverberation chamber. Three RX antennas, separated by 40 cm, are placed along the x axis behind the TX antennas. The frequency range of the measurement is set from 36 GHz to 39 GHz.

Fig. 13 shows the nine original and reconstructed time-domain signals for the different TX and RX antennas. Similar to previous sections, a reference signal (TX_2-RX_2) is used to replicate the different reflections observed in the chamber. The primary reflection is observed approximately at 22 ns, which fits the expected travelling time corresponding to the distance that the wave takes to hit the front wall and to be reflected back towards the receivers, approximately 6.2 meters. Finally, Fig. 14 shows the original and reconstructed spectral efficiencies as a function of the frequency and SNR. Good agreement is observed in the recreation.

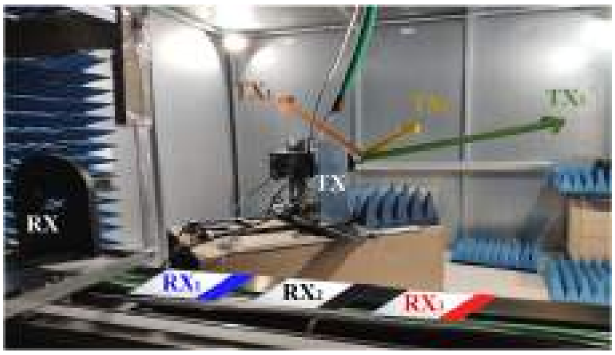

FIGURE 12. Measurement scenario for the MIMO system inside the reverberation chamber. Three transmitter antennas (TX) point at the metallic wall of the chamber and three receiver antennas (RX) acquire the multiple reflections inside it.

C. MODIFYING THE MIMO SCENARIO

The time-gating technique allows to recreate complex scenarios, but also to go beyond the limits imposed by the measurement setup. In previous sections, we saw that the phase and amplitude of an antenna array can be easily controlled and that the number of required antennas can be reduced, which is especially useful for massive MIMO systems. Inside reverberation chambers, controlling and modifying the different reflections could be of potential interest. As an example, Figs. 15(a) and 15(b) illustrate the effect of eliminating all reflections inside the chamber except the primary one, located at 22 ns in Fig. 13. Eliminating the reflections in the reverberation chamber provokes an increase in the correlation of the

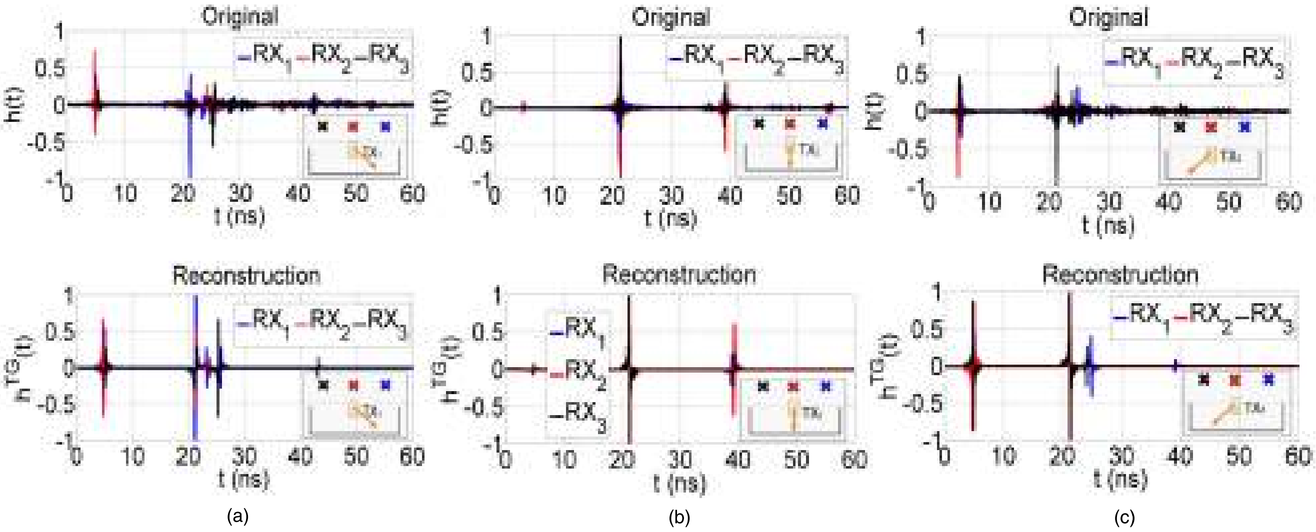

(a) (b) (c)

FIGURE 13. Original and reconstructed signals for the MIMO 3 × 3 scenario inside the reverberation chamber: (a) TX_1 (−45°), (b) TX_2 (0°), (c) TX_3 (45°).

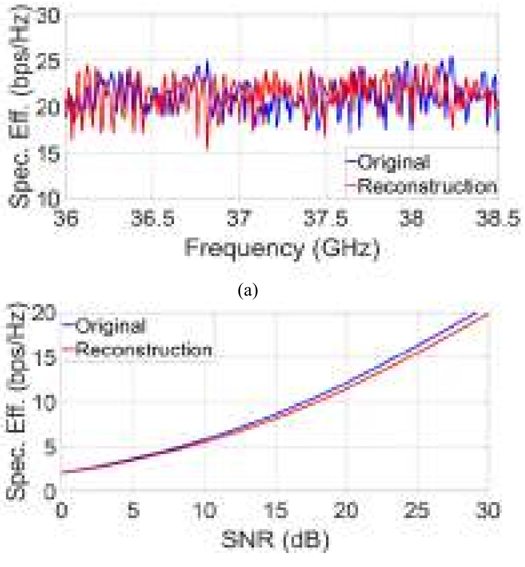

(a)

(b)

FIGURE 14. Original and reconstructed spectral efficiencies for the MIMO 3 × 3 scenario inside the reverberation chamber: (a) as a function of the frequency (SNR = 30 dB), (b) as a function of the SNR (averaged in frequency).

TABLE 1. Normalized average power values.

	RX_1	RX_2	RX_3
TX_1	1.60	1.22	1.21
TX_2	8.11	11.77	8.69
TX_3	1	1.53	1.76

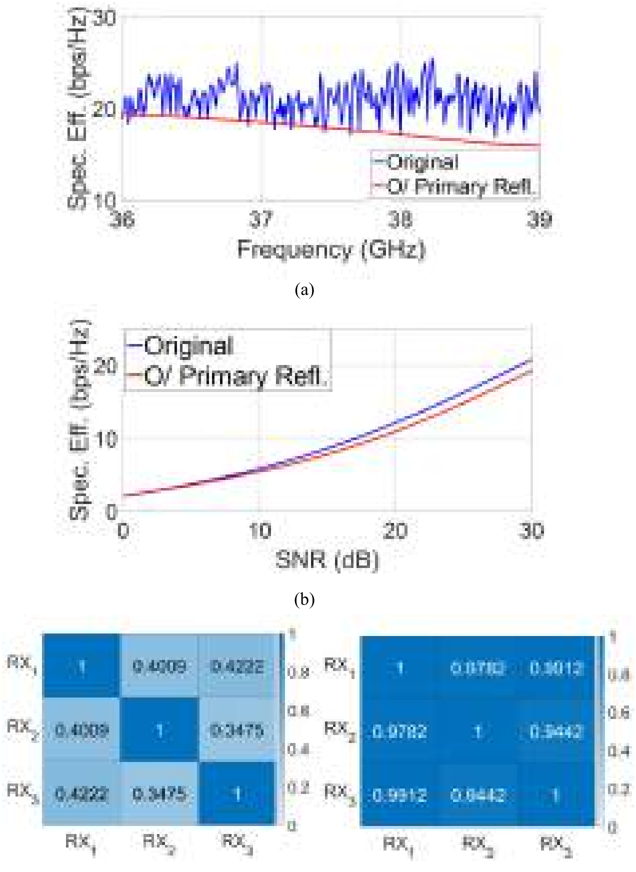

(a)

(b)

(c)

(d)

FIGURE 15. Degradation of the spectral efficiency after removing all reflections in the reverberation chamber except the primary one (red curves): (a) as a function of the frequency (SNR = 30 dB), (b) as a function of the SNR (averaged in frequency). Correlation matrices of the three TX antennas for the (c) original scenario and (d) the modified scenario where only the primary reflection (22 ns) is considered.

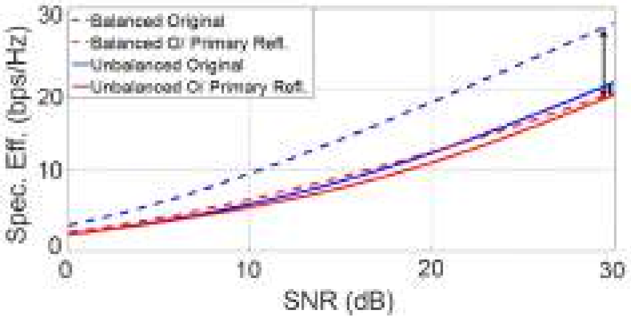

FIGURE 16. Spectral efficiency comparison for balanced and unbalanced power cases for the MIMO scenario in the reverberation chamber.

different MIMO channel, as shown in the correlation matrices of Figs. 15(c) and 15(d). As a consequence, the spectral efficiency is reduced.

The decrease in spectral efficiency due to the correlation is not as high as it might be expected, being only 1bps/Hz. Therefore, other factors such as the power balance can be decisive for the spectral efficiency curve. In order to see the effects of the power balance for each TX−RX pair in the MIMO system, Table 1 is shown. It presents the average power values of each TX−RX pair normalized to the lowest average power. Consequently, the values shown indicate the power factor in which each TX−RX pair multiplies to the worst case.

The table shows a clear trend. The pairs involving TX_2 have an average power approximately one order of magnitude higher than the other transmitters. This can be explained by the fact that TX_1 and TX_3 are oriented in azimuth angles of −45° and 45° respectively. Thus, the distance the wave travels is greater for these transmitters, as well as the number of reflections given the shape of the chamber. The normalized average power values are not exactly identical for TX_1 and TX_3 due to the fact that the reverberant environment is not perfectly symmetrical to the YZ plane. However, these receivers keep the same order of magnitude. The power unbalance causes the real behavior of the system to tend to a 1 × 3 SIMO rather than a 3 × 3 MIMO since only one transmitter radiates 77.4% of the power received by the receivers. To solve this problem, the values of each pair are scaled to create a perfectly balanced system. The results are shown in Fig. 16, where the spectral efficiency is shown for the original signal and only for the primary reflection, both in the balanced and unbalanced case. Additionally, the power balance increases the spectral efficiency both for the original signal and for primary reflection. On the other hand, when the power is balanced the effect of signal decorrelation is much greater as the curves are much more separated. Power balance does not change the correlation of the signals, so it remains as shown in Figs. 15(c) and 15(d).

V. CONCLUSION

This article presents a deep analysis of the use of the time-gating technique to the field of propagation channel. Several parameters concerning the propagation channel are analyzed, such as spectral efficiency, signal correlation and power balance. The time-gating technique is well known in the field of antenna measurement as a tool to eliminate reflected components in outdoor measurements or imperfect anechoic chambers. This technique can be applied in both far field and near field measurements. Taking advantage of its potential, a new measurement configuration for shielded chambers based on time-gating is provided. This configuration allows to configure different propagation scenarios. The proposed configuration is based on a mixed chamber that is covered in one part with absorbers (anechoic zone) and in the other without absorbers (reverberating zone) in order to generate reflected components. Applying the time-gating technique, it is possible to modify, adjust and tune the reflections that a certain propagation environment has. This yields a relative control of the propagation environment and lets to quantify the capacity that MIMO systems can display operating in those propagation environments. Furthermore, it allows to go beyond the limits of a certain measurement setup, allowing new degrees of freedom with the change of the time of arrival of some reflections or the creation of artificial reflections.

In order to show the potential of the time-gating technique for the recreation of propagation scenarios inside anechoic chambers, different configurations have been deeply studied in the frequency range between 32 GHz and 39 GHz. Therefore, MISO, MIMO and SISO scenarios are recreated either for anechoic or reverberating environments. Additionally, we explore the capability of tune the propagation scenario controlling the phase and amplitude of an antenna array along with modifying the different reflections in the scenario, which is especially useful for massive MIMO systems. The experimental results provided are of relevance and validate the use of the time-gating technique for the recreation and characterization of new propagation channels, reducing the complexity and the limitations derived from the on-site measurements of real scenarios. As a future direction, several metrics can be exploited when applying time-gating. Some of them, such as the angle and time of arrival, add new degrees of freedom, which add a wide range of possibilities to the recreation of scenarios. Thus, this technique opens the door to create a tool capable of emulating different specific environments (vehicular scenarios, trains, tunnels, etc.) in the laboratory based on measurements in the chamber.

APPENDIX A. TIME GATING VALIDATION

For the validation of the method, we set the following measurement scenario based on the configuration of the anechoic chamber shown in Fig. 3. A fixed receiver antenna is placed in front of a transmitter antenna, which is only able to move in azimuth angles (ϕ). Both radiating elements are standard gain horns with 47 mm diameter, fed with a WR-34 waveguide-to-coaxial transition. The operation frequencies of the measurement are within the range 22-27.5 GHz. The radiation pattern is measured with a R&S-ZVA67 vector network analyzer (VNA). Note that the pattern results of the UGR measuring system shown in this Appendix have been validated through an exhaustive comparison process with the measuring facilities of the Technical University of Madrid (UPM) [40].

Fig. 17 shows the normalized impulse response of the system before, $h(t)$, and after, $h^{\mathrm{TG}}(t)$, applying the time-gating technique. The time interval associated to the direct ray is highlighted in green in the figure. Outside this interval, the presence of noise and reflections provokes a further degradation in the reconstruction of the antenna radiation pattern. With the time-gating technique, the impulse response is truncated in the interval of interest and noise and reflections are eliminated. As illustrated in Fig. 17, different kinds of windows can be applied for this purpose [41].

Fig. 18 presents the radiation pattern of the horn antenna (E-plane) at 27.5 GHz before and after applying the time-gating technique. The bandwidth of the measurement is $\mathrm{B} = 5.5$ GHz, with $\mathrm{N_f} = 101$ frequency samples. Then, a symmetrical-centered time-domain ($\mathrm{t_1} = \mathrm{t_2} = \mathrm{t_{TG}}$) Hann window was used for the reconstruction of the radiation pattern. As shown in Fig. 18, the time-gating technique improves considerably the quality of the measurements after eliminating the ripple associated to noise and reflections. Furthermore, it has emphasized the presence of the first null in the radiation pattern (±38°), which was masked by reflections in the anechoic chamber. These facts potentially allow to reduce

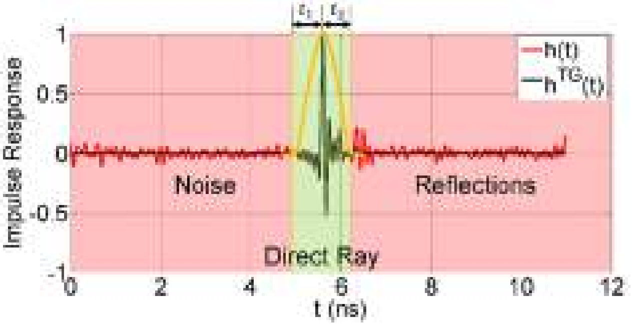

FIGURE 17. Normalized impulse response of the original $h(t)$ and time-gated $h^{TG}(t)$ signals. Time-gating is applied in the antenna measurement scenario to eliminate noise and reflections.

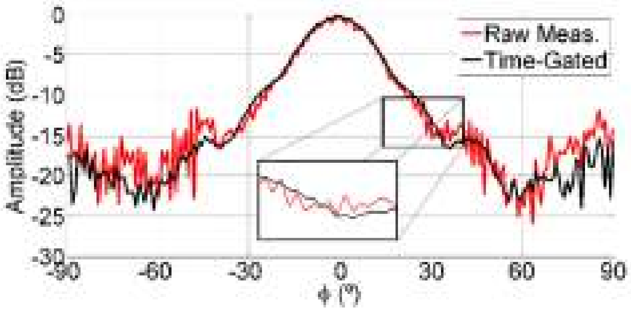

FIGURE 18. Radiation pattern of the horn antenna (E-plane) at 27.5 GHz before and after using the time-gating technique. For the time-gated measurement, a Hann window was used with $t_1 = t_2 = t_{TG} = 2.2$ ns (20%). For a fair comparison, no additional smoothening technique has been applied to the time-gated signal in a post-processing step.

the number of azimuth samples in order to speed up the measurement, while maintaining a good overall performance. We should remark that no additional smoothing process has been utilized in Fig. 17 except from the time-gating itself. As a consequence, the ripple can be further reduced if the time-gated signal is smoothed in a post-processing step (i.e., see Fig. 22).

A. EFFECT OF THE WINDOW SIZE

The window size plays a fundamental role in the time-gating technique. Narrow windows may eliminate part of the information about the direct ray contained in the impulse response. Conversely, wide windows may not completely eliminate reflections in the anechoic chamber.

Fig. 19 shows the effect of varying the window size on the radiation pattern when a symmetrical Hann window is applied. In the plot, the width of the window is referred as a percentage of the total time interval (11 ns) of the impulse response. As previously detailed, a narrow window (green curve: 1%) cuts relevant information of the impulse response, leading to the degradation of the main lobe and the loss of the first null in the radiation pattern. Conversely, a wide window (blue curve: 80%) cancels out the beneficial effect of time-gating, since most of the reflections are kept inside the window. For this measurement scenario, we determined that $t_{TG} = 20\%$ (black curve) is an optimal value.

B. EFFECT OF THE NUMBER OF FREQUENCY SAMPLES

The number of frequency samples N_f acquired from the VNA represents a trade-off between measurement time and quality of the acquisition. The higher N_f is, the longer the measurement takes, but the better the reconstruction is. From the results illustrated in Fig. 20, the optimal number of frequency samples is $N_f = 101$, which is the value assigned for the rest of the measurements. Below 51 samples (blue and red curves), the antenna pattern starts to degrade, appearing a ripple in the main lobe and losing the information of the first null. Below 13 samples (green curve), the ripple maintains and the symmetry in the main lobe is lost.

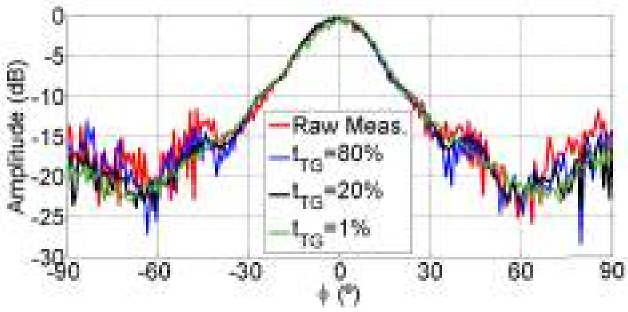

FIGURE 19. Effect of varying the window width on the radiation pattern. In the plot, $t_1 = t_2 = t_{TG}$ is referred as a percentage of the total time (11 ns).

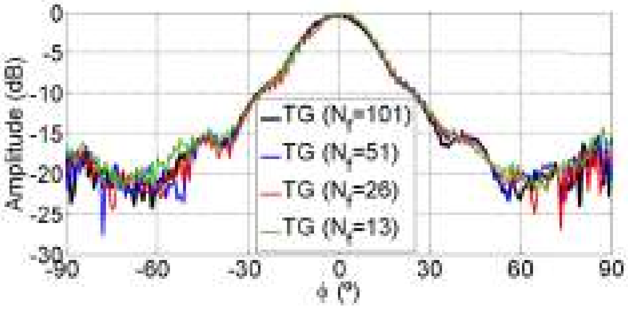

FIGURE 20. Effect of varying the number of frequency samples N_f obtained from the VNA. In all curves, a Hann window was used with $t_1 = t_2 = t_{TG} = 2.2$ ns (20%).

APPENDIX B. RECREATION OF THE MIMO SCENARIO

Fig. 21 describes in detail the recreation of the MIMO system shown in Fig. 6. As previously discussed in the text, a reference signal $h_{\text{ref}}(t)$, obtained from the measurement of a simple SISO (single input single output) scenario, is used to recreate the full MIMO system. Thus, each signal $h_{ij}(t)$ that radiates the transmitter antenna TX_i and reaches the receiver antenna RX_j is an attenuated and delayed version of the reference signal $h_{\text{ref}}(t)$. That is,

$$h_{ij}(t) = A_{ij} h_{\text{ref}}(t - t_{ij}) \tag{3}$$

where A_{ij} is the attenuation factor and t_d is the time delay. Equivalently, the problem can be formulated in the frequency domain:

$$H_{ij}(f) = A_{ij} H_{\text{ref}}(f)\, e^{-j2\pi f t_{ij}} \tag{4}$$

where $H_{\text{ref}}(f)$ is the Fourier transform of $h_{\text{ref}}(t)$.

By applying basic trigonometry, the time delay can be extracted from the location of the reference antennas. In Fig. 6, the reference antennas are TX_1 and RX_2 and their separation is $d_{\text{ref}} = 80$ cm. Thus, the time delay is calculated as

$$t_{ij} = \frac{d_{ij} - d_{\text{ref}}}{c} \tag{5}$$

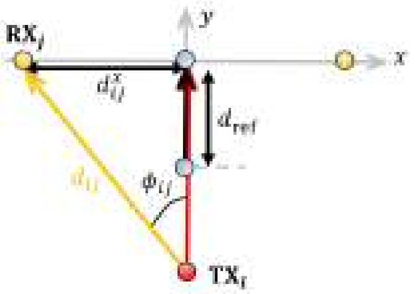

FIGURE 21. Recreation of the MIMO scenario for a pair of TX and RX antennas: TX_i and RX_j, respectively.

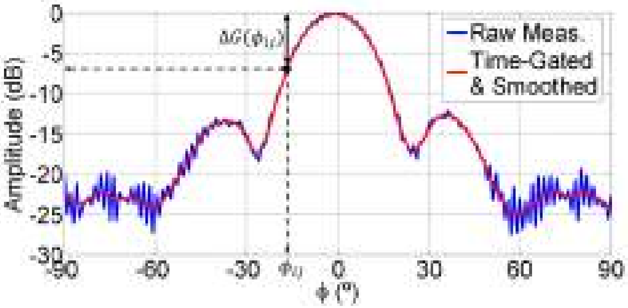

FIGURE 22. Measured and time-gated radiation pattern (E-plane) at 39 GHz of the horn antenna used in Section III. For a given azimuth angle ϕ_{ij}, the gain drop can be estimated.

TABLE 2. Attenuation factors and time delays of the MIMO 4 × 3 scenario.

	TX_1	TX_2	TX_3	TX_4
RX_1	$\begin{pmatrix}0.025\\0.31\text{ ns}\end{pmatrix}$	$\begin{pmatrix}0.056\\1.23\text{ ns}\end{pmatrix}$	$\begin{pmatrix}0.13\\2.19\text{ ns}\end{pmatrix}$	$\begin{pmatrix}0.20\\3.15\text{ ns}\end{pmatrix}$
RX_2	REF	$\begin{pmatrix}0.76\\1\text{ ns}\end{pmatrix}$	$\begin{pmatrix}0.58\\2\text{ ns}\end{pmatrix}$	$\begin{pmatrix}0.52\\3\text{ ns}\end{pmatrix}$
RX_3	$\begin{pmatrix}0.025\\0.31\text{ ns}\end{pmatrix}$	$\begin{pmatrix}0.056\\1.23\text{ ns}\end{pmatrix}$	$\begin{pmatrix}0.13\\2.19\text{ ns}\end{pmatrix}$	$\begin{pmatrix}0.20\\3.15\text{ ns}\end{pmatrix}$

where c is the speed of light in the air. The attenuation factor A_{ij} is expressed as

$$A_{ij}[\text{dB}] = 0 - 20\log\left(d_{ij}/d_{\text{ref}}\right) - \Delta G(\phi_{ij}) \tag{6}$$

A_{ij} presents two major contributions: free space loss and a gain drop $\Delta G(\phi_{ij})$ that depends on the position of RX antennas. Considering a normalized reference signal $h_{\text{ref}}(t)$, the term associated to free space loss is calculated with basic trigonometry, as shown in equation (6). The gain drop $\Delta G(\phi_{ij})$ can be estimated by looking at the radiation pattern of the utilized horn antenna, displayed in Fig. 22. Note that if TX and RX antennas are aligned along the y axis ($\phi_{ij} = 0$), the gain drop is zero.

The different attenuation factors and time delays used for the reconstruction of the MIMO 4 × 3 scenario presented in Section III.B are illustrated in Table 2. For each cell of Table 2, the attenuation factor (in linear units) is shown at the top and the time delay at the bottom. The reference is assumed to present no attenuation ($A_{12} = 1$) and no delay ($t_{12} = 0$). The incoming signals to RX_1 and RX_3 can be considered the same in practice, since the radiation pattern of the TX antenna is symmetric and both antennas are separated 40 cm from the central receiver, RX_2. Therefore, RX_1 and RX_3 share identical attenuation factors and delays.

ACKNOWLEDGMENT

The authors would like to thank M. Bolívar-Lupiáñez and A. Gutiérrez-Martínez for their help in preparing the measurement set-up and in the acquisition and processing of some experimental results.

REFERENCES

[1] Ericsson. (2019). *Ericsson Mobility Report Nov. 2019*. [Online]. Available: https://www.ericsson.com/4acd7e/assets/local/ mobility-report/documents/2019/emr-november-2019.pdf

[2] W. D. de Mattos and P. R. L. Gondim, "M-health solutions using 5G networks and M2M communications," *IT Prof.*, vol. 18, no. 3, pp. 24–29, May 2016.

[3] S. Mattisson, "An overview of 5G requirements and future wireless networks: Accommodating scaling technology," *IEEE Solid StateCircuits Mag.*, vol. 10, no. 3, pp. 54–60, Aug. 2018.

[4] A. Ghosh, A. Maeder, M. Baker, and D. Chandramouli, "5G evolution: A view on 5G cellular technology beyond 3GPP release 15," *IEEE Access*, vol. 7, pp. 127639–127651, 2019.

[5] R. Lu, L. Zhang, J. Ni, and Y. Fang, "5G vehicle-to-everything services: Gearing up for security and privacy," *Proc. IEEE*, vol. 108, no. 2, pp. 373–389, Feb. 2020.

[6] M. A. Khan, N. Saeed, A. W. Ahmad, and C. Lee, "Location awareness in 5G networks using RSS measurements for public safety applications," *IEEE Access*, vol. 5, pp. 21753–21762, 2017.

[7] *Release 17 From 3GPP*. Accessed: Oct. 5, 2020. [Online]. Available: https://www.3gpp.org/release-17

[8] 5GCM. (Oct. 2016). *5G Channel Model for Bands Up to 100 GHz*. [Online]. Available: http://www.5gworkshops.com/5GCM.html

[9] K. Haneda, J. Zhang, L. Tan, G. Liu, Y. Zheng, H. Asplund, J. Li, Y. Wang, D. Steer, C. Li, and T. Balercia, "5G 3GPP-like channel models for outdoor urban microcellular and macrocellular environments," in *Proc. IEEE 83rd Veh. Technol. Conf. (VTC Spring)*, Nanjing, China, May 2016, pp. 1–7.

[10] N. Zhang, J. Dou, L. Tian, X. Yuan, X. Yang, S. Mei, and H. Wang, "Dynamic channel modeling for an indoor scenario at 23.5 GHz," *IEEE Access*, vol. 3, pp. 2950–2958, 2015.

[11] I. Rodriguez, H. C. Nguyen, I. Z. Kovacs, T. B. Sorensen, and P. Mogensen, "An empirical Outdoor-to-Indoor path loss model from below 6 GHz to cm-wave frequency bands," *IEEE Antennas Wireless Propag. Lett.*, vol. 16, pp. 1329–1332, 2017.

[12] J. Du, D. Chizhik, R. Feick, G. Castro, M. Rodriguez, and R. A. Valenzuela, "Suburban residential building penetration loss at 28 GHz for fixed wireless access," *IEEE Wireless Commun. Lett.*, vol. 7, no. 6, pp. 890–893, Dec. 2018.

[13] T. Zhou, H. Li, Y. Wang, L. Liu, and C. Tao, "Channel modeling for future high-speed railway communication systems: A survey," *IEEE Access*, vol. 7, pp. 52818–52826, 2019.

[14] C. Briso-Rodriguez, P. Fratilescu, and Y. Xu, "Path loss modeling for train-to-train communications in subway tunnels at 900/2400 MHz," *IEEE Antennas Wireless Propag. Lett.*, vol. 18, no. 6, pp. 1164–1168, Jun. 2019.

[15] C.-X. Wang, J. Bian, J. Sun, W. Zhang, and M. Zhang, "A survey of 5G channel measurements and models," *IEEE Commun. Surveys Tuts.*, vol. 20, no. 4, pp. 3142–3168, 4th Quart., 2018.

[16] I. A. Hemadeh, K. Satyanarayana, M. El-Hajjar, and L. Hanzo, "Millimeter-wave communications: Physical channel models, design considerations, antenna constructions, and link-budget," *IEEE Commun. Surveys Tuts.*, vol. 20, no. 2, pp. 870–913, 2nd Quart., 2018.

[17] W. Khawaja, I. Guvenc, D. W. Matolak, U.-C. Fiebig, and N. Schneckenburger, "A survey of air-to-ground propagation channel modeling for unmanned aerial vehicles," *IEEE Commun. Surveys Tuts.*, vol. 21, no. 3, pp. 2361–2391, 3rd Quart., 2019.

[18] G. Ferrara, M. Migliaccio, and A. Sorrentino, "Characterization of GSM non-line-of-sight propagation channels generated in a reverberating chamber by using bit error rates," *IEEE Trans. Electromagn. Compat.*, vol. 49, no. 3, pp. 467–473, Aug. 2007.
[19] S. Herbert, I. Wassell, T.-H. Loh, and J. Rigelsford, "Characterizing the spectral properties and time variation of the in-vehicle wireless communication channel," *IEEE Trans. Commun.*, vol. 62, no. 7, pp. 2390–2399, Jul. 2014.
[20] L. Gagliardi, D. Micheli, G. Gradoni, F. Moglie, and V. M. Primiani, "Coupling between multipath environments through a large aperture," *IEEE Antennas Wireless Propag. Lett.*, vol. 14, pp. 1463–1466, 2015.
[21] A. K. Fall, P. Besnier, C. Lemoine, M. Zhadobov, and R. Sauleau, "Design and experimental validation of a mode-stirred reverberation chamber at millimeter waves," *IEEE Trans. Electromagn. Compat.*, vol. 57, no. 1, pp. 12–21, Feb. 2015.
[22] M. Barazzetta, D. Micheli, L. Bastianelli, R. Diamanti, M. Totta, P. Obino, R. Lattanzi, F. Moglie, and V. M. Primiani, "A comparison between different reception diversity schemes of a 4G-LTE base station in reverberation chamber: A deployment in a live cellular network," *IEEE Trans. Electromagn. Compat.*, vol. 59, no. 6, pp. 2029–2037, Dec. 2017.
[23] X. Chen, J. Tang, T. Li, S. Zhu, Y. Ren, Z. Zhang, and A. Zhang, "Reverberation chambers for over-the-air tests: An overview of two decades of research," *IEEE Access*, vol. 6, pp. 49129–49143, 2018.
[24] E. Genender, C. L. Holloway, K. A. Remley, J. M. Ladbury, G. Koepke, and H. Garbe, "Simulating the multipath channel with a reverberation chamber: Application to bit error rate measurements," *IEEE Trans. Electromagn. Compat.*, vol. 52, no. 4, pp. 766–777, Nov. 2010.
[25] J. F. Valenzuela-Valdes, A. M. Martinez-Gonzalez, and D. A. Sanchez-Hernandez, "Emulation of MIMO nonisotropic fading environments with reverberation chambers," *IEEE Antennas Wireless Propag. Lett.*, vol. 7, pp. 325–328, 2008.
[26] J. F. Valenzuela-Valdes, A. M. Martinez-Gonzalez, and D. A. Sanchez-Hernandez, "Diversity gain and MIMO capacity for nonisotropic environments using a reverberation chamber," *IEEE Antennas Wireless Propag. Lett.*, vol. 8, pp. 112–115, 2009.
[27] M. S. Kildal, J. Carlsson, and A. Alayon Glazunov, "Measurements and simulations for validation of the random-LOS measurement accuracy for vehicular OTA applications," *IEEE Trans. Antennas Propag.*, vol. 66, no. 11, pp. 6291–6299, Nov. 2018.
[28] D. Solomitckii, Y. Koucheryavy, V. Semkin, A. Karttunen, V. Petrov, S. L. H. Nguyen, H. Nikopour, K. Haneda, S. Andreev, and S. Talwar, "Characterizing radio wave propagation in urban street canyon with vehicular blockage at 28 GHz," *IEEE Trans. Veh. Technol.*, vol. 69, no. 2, pp. 1227–1236, Feb. 2020.
[29] J. D. Sanchez-Heredia, J. F. Valenzuela-Valdes, A. M. Martinez-Gonzalez, and D. A. Sanchez-Hernandez, "Emulation of MIMO Rician-fading environments with mode-stirred reverberation chambers," *IEEE Trans. Antennas Propag.*, vol. 59, no. 2, pp. 654–660, Feb. 2011.
[30] J. D. Sanchez-Heredia, M. Gruden, J. F. Valenzuela-Valdes, and D. A. Sanchez-Hernandez, "Sample-selection method for arbitrary fading emulation using mode-stirred chambers," *IEEE Antennas Wireless Propag. Lett.*, vol. 9, pp. 409–412, 2010.
[31] O. Zetterstrom, E. Pucci, P. Padilla, L. Wang, and O. Quevedo-Teruel, "Low-dispersive leaky-wave antennas for mmWave point-to-point high-throughput communications," *IEEE Trans. Antennas Propag.*, vol. 68, no. 3, pp. 1322–1331, Mar. 2020.
[32] Q. Chen, O. Zetterstrom, E. Pucci, A. Palomares-Caballero, P. Padilla, and O. Quevedo-Teruel, "Glide-symmetric holey leaky-wave antenna with low dispersion for 60 GHz point-to-point communications," *IEEE Trans. Antennas Propag.*, vol. 68, no. 3, pp. 1925–1936, Mar. 2020.
[33] A. Palomares-Caballero, A. Alex-Amor, J. Valenzuela-Valdes, and P. Padilla, "Millimeter-wave 3D-printed antenna array based on gap-waveguide technology and split E-plane waveguide," *IEEE Trans. Antennas Propag.*, early access, Jul. 16, 2020, doi: 10.1109/TAP.2020.3008620.
[34] J. Koh, A. De, T. K. Sarkar, H. Moon, W. Zhao, and M. Salazar-Palma, "Free space radiation pattern reconstruction from non-anechoic measurements using an impulse response of the environment," *IEEE Trans. Antennas Propag.*, vol. 60, no. 2, pp. 821–831, Feb. 2012.
[35] A. Soltane, G. Andrieu, E. Perrin, C. Decroze, and A. Reineix, "Antenna radiation pattern measurement in a reverberating enclosure using the time-gating technique," *IEEE Antennas Wireless Propag. Lett.*, vol. 19, no. 1, pp. 183–187, Jan. 2020.
[36] T. L. Marzetta, E. G. Larsson, H. Yang, and H. Q. Ngo, *Fundamentals of Massive MIMO*. Cambridge, U.K.: Cambridge Univ. Press, 2018.
[37] S. Loyka and G. Levin, "On physically-based normalization of MIMO channel matrices," *IEEE Trans. Wireless Commun.*, vol. 8, no. 3, pp. 1107–1112, Mar. 2009.
[38] M. A. Jensen and J. W. Wallace, "A review of antennas and propagation for MIMO wireless communications," *IEEE Trans. Antennas Propag.*, vol. 52, no. 11, pp. 2810–2824, Nov. 2004.
[39] P.-S. Kildal and K. Rosengren, "Correlation and capacity of MIMO systems and mutual coupling, radiation efficiency, and diversity gain of their antennas: Simulations and measurements in a reverberation chamber," *IEEE Commun. Mag.*, vol. 42, no. 12, pp. 104–112, Dec. 2004.
[40] *LEHA Laboratory of the Technical University of Madrid*. Accessed: Oct. 5, 2020. [Online]. Available: https://www.gr.ssr.upm.es/index.php/en/leha/about-us
[41] Z. Chen and Z. Xiong, "Differences of time domain gating implementions in vector network analyzers," in *Proc. Joint Int. Symp. Electromagn. Compat., Sapporo Asia–Pacific Int. Symp. Electromagn. Compat. (EMC Sapporo/APEMC)*, Sapporo, Japan, Jun. 2019, pp. 597–600.

ALEJANDRO RAMÍREZ-ARROYO was born in Córdoba, Spain, in 1997. He received the B.Sc. degree in telecommunication engineering from the University of Granada, Spain, in 2019, where he is currently pursuing the M.Sc. degree in telecommunication engineering. His current research interests include heterogeneous networks, optimization techniques and propagation channels, and models for 5G networks.

ANTONIO ALEX-AMOR received the B.Sc. degree in telecommunication engineering from the Universidad de Granada, in 2016, and the M.Sc. degree in telecommunication engineering from the Universidad Politécnica de Madrid (UPM), in 2018, where he is currently pursuing the Ph.D. degree. Since 2016, he has been with the Radiation Group, Department of Signals Systems and Radiocommunications, UPM. From 2018 to 2019, he joined the Department of Language and Computer Science, Universidad de Málaga. In 2020, he joined the Department of Signal Theory, Telematics and Communications, University of Granada. His current research interests include the use of liquid crystal as tunable dielectric, metamaterials, structures with higher symmetries, and radiofrequency energy harvesting systems. He received the Best Electromagnetics Paper Award at the 14th European Conference on Antennas and Propagation (EuCAP 2020).

CARMELO GARCÍA-GARCÍA was born in Sanlúcar de Barrameda, Spain, in 1996. He received the B.Sc. degree in telecommunication engineering from the University of Seville (US), Seville, Spain, in 2019. He is currently pursuing the M.Sc. degree in telecommunication engineering with the University of Granada (UGR), Granada, Spain. His current research interests include electromagnetic compatibility (EMC) and optimization techniques for 5G networks.

ÁNGEL PALOMARES-CABALLERO was born Jaén, Spain, in 1994. He received the B.Sc. and M.Sc. degrees in telecommunication engineering from the University of Granada (UGR), Spain, in 2016 and 2018, respectively, where he is currently pursuing the Ph.D. degree with the Department of Signal Theory, Telematics and Communications, with a National Predoctoral Fellowship. Since 2017, he has been with the Department of Signal Theory, Telematics and Communications, UGR. His research interests include millimeter-wave antennas and phase shifters, gap-waveguide, structures with higher symmetries, and optimization algorithms.

PABLO PADILLA was born in Jaén, Spain, in 1982. He received the degree in telecommunication engineering and the Ph.D. degree from the Radiation Group, Department of Signals Systems and Radiocommunications, Technical University of Madrid (UPM), Spain, in 2005 and 2009, respectively. In 2007, he was with the Laboratory of Electromagnetics and Acoustics, École Polytechnique Fédérale de Lausanne, Switzerland, as an Invited Ph.D. Student. In 2009, he carried out a Postdoctoral stay with the Helsinki University of Technology (AALTO-TKK). In 2009, he became an Assistant Professor with the Department of Signal Theory, Telematics and Communications, University of Granada, where he has been an Associate Professor, since 2012. In 2017, he was an Invited Visiting Professor with the KTH Royal Institute of Technology, Stockholm. He has authored more than 65 high-impact journal contributions and more than 60 contributions to international symposia. His research interests include a variety of topics related mainly to electromagnetism and communication issues (radiofrequency devices, antennas, and propagation).

JUAN F. VALENZUELA-VALDÉS was born in Marbella, Spain. He received the degree in telecommunications engineering from the Universidad de Málaga, Spain, in 2003, and the Ph.D. degree from the Universidad Politécnica de Cartagena, Spain, in 2008. He joined the Department of Information Technologies and Communications, Universidad Politécnica de Cartagena, in 2004. In 2007, he joined EMITE Ing., as the Head of Research. In 2011, he joined the Universidad de Extremadura, and in 2015, he joined the Universidad de Granada, where he is currently an Associate Professor. He is also the Head of SWAT Research Group, University of Granada, and the Co-Head of the Singular Laboratory of Electromagnetic Characterization of Microwave and Millimeter Devices and Antennas. He also holds several national and international patents. His publication record comprised of more than 100 publications, including 50 JCR indexed articles and seven book chapters (updated March 2019). His current research interests include wireless communications, radiofrequency devices, antennas, and propagation. He received several prizes, including the National Prize for the Best Ph.D. in Mobile Communications by Vodafone.

• • •

2.2.3 Artificial Intelligence and Dimensionality Reduction: Tools for Approaching Future Communications

Artificial Intelligence has burst into multiple fields of science and technology in recent years, and telecommunications field has been no exception. In this work, unsupervised machine learning techniques, specifically, dimensionality reduction techniques, are proposed for the visual classification of multiple communication channels. By reducing the dimension of several channel parameters to a two-dimensional space, it is possible to separate communication channels into different clusters according to their nature. In particular, the use of t-SNE with an optimal selection of its hyperparameters proves to be the best choice compared to other state-of-the-art techniques such as PCA. The classification of these data based on supervised learning algorithms shows that dimensionality reduction preserves the data information since the accuracy obtained prior to t-SNE application is similar to that obtained *a posteriori*. Additionally, this work validates the recreation of scenarios by using the time-gating technique since the visual classification of the channels considers as similar the channels measured in real environments and the channels emulated from measurements in anechoic and reverberation chambers.

THIS IS THE PUBLISHED VERSION OF THE PAPER:

A. Ramírez-Arroyo, L. García, A. Alex-Amor and J. F. Valenzuela-Valdés, “Artificial Intelligence and Dimensionality Reduction: Tools for Approaching Future Communications,” *IEEE Open Journal of the Communications Society*, vol. 3, pp. 475-492, 2022.

- Journal Impact Factor (JIF) in JCR 2022: 7.9
- Category: ENGINEERING, ELECTRICAL & ELECTRONIC. JCI Rank: 43/349 (Q1).
- Category: TELECOMMUNICATIONS. JCI Rank: 18/116 (Q1).

Disclaimer:
This work has been published in IEEE Open Journal of the Communications Society. DOI: 10.1109/OJCOMS.2022.3156473

IEEE Open Journal of the
Communications Society

Received 20 December 2021; revised 9 February 2022; accepted 26 February 2022. Date of publication 7 March 2022; date of current version 22 March 2022.

Digital Object Identifier 10.1109/OJCOMS.2022.3156473

Artificial Intelligence and Dimensionality Reduction: Tools for Approaching Future Communications

ALEJANDRO RAMÍREZ-ARROYO[1], **LUZ GARCÍA**[1], **ANTONIO ALEX-AMOR**[2],
AND JUAN F. VALENZUELA-VALDÉS[1]

[1]Department of Signal Theory, Telematics and Communications, Universidad de Granada, 18071 Granada, Spain

[2]Information Technologies Department, Universidad CEU San Pablo, 28668 Madrid, Spain

CORRESPONDING AUTHOR: A. RAMÍREZ-ARROYO (e-mail: alera@ugr.es)

This work was supported in part by the Spanish Program of Research, Development, and Innovation under Project RTI2018-102002-A-I00; in part by the "Junta de Andalucía" under Project B-TIC-402-UGR18 and Project P18.RT.4830; and in part by the Ministerio de Universidades, Gobierno de España under Predoctoral Grant FPU19/01251.

ABSTRACT This article presents a novel application of the t-distributed Stochastic Neighbor Embedding (t-SNE) clustering algorithm to the telecommunication field. t-SNE is a dimensionality reduction algorithm that allows the visualization of large dataset into a 2D plot. We present the applicability of this algorithm in a communication channel dataset formed by several scenarios (anechoic, reverberation, indoor and outdoor), and by using six channel features. Applying this artificial intelligence (AI) technique, we are able to separate different environments into several clusters allowing a clear visualization of the scenarios. Throughout the article, it is proved that t-SNE has the ability to cluster into several subclasses, obtaining internal classifications within the scenarios themselves. t-SNE comparison with different dimensionality reduction techniques (PCA, Isomap) is also provided throughout the paper. Furthermore, post-processing techniques are used to modify communication scenarios, recreating a real communication scenario from measurements acquired in an anechoic chamber. The dimensionality reduction and classification by using t-SNE and Variational AutoEncoders show good performance distinguishing between the recreation and the real communication scenario. The combination of these two techniques opens up the possibility for new scenario recreations for future mobile communications. This work shows the potential of AI as a powerful tool for clustering, classification and generation of new 5G propagation scenarios.

INDEX TERMS Artificial intelligence, clustering, dimensionality reduction, propagation, t-SNE, unsupervised learning, wireless communications.

I. INTRODUCTION

THE GROWTH in wireless communication networks in recent years has been exponential. An increasingly interconnected world, together with technological advances, makes this field one of the main topics in the research community [1]–[3]. 5G emergence promises multiple improvements at the user level, including improved transmission rates, reduced end-to-end delay, reduced power consumption, improved energy efficiency and ultra-densified networks [4]–[6]. In order to provide all these benefits, a deep analysis must be performed over the communication channels considered for these wireless communications. As user demands are increasing, the diversity of communication scenarios do it as well. New environments are emerging, as for example, Vehicle-to-Vehicle (V2V) [7], UAV-to-UAV [8], Ship-to-Ship (S2S) [9], High Speed Train-to-High Speed Train [10], or any combination of the above [11]. The characterization of these environments will be fundamental to determine the communication channels key performance indicators (KPIs): data rate, reliability, latency or transmit power.

Since the number of these new scenarios is increasing, the complexity of their analysis is also escalating [12]. In order to solve this problem, Artificial Intelligence (AI) appears as a tool that can be applied in the telecommunication field. Several examples show the feasibility of its use in this field, such as deep learning for microwave imaging [13] and inverse scattering [14], support vector regression for antenna design [15] or deep neural networks for estimation of the Direction-of-Arrival (DoA) [16]. The AI field includes Machine Learning (ML), where classification, clustering and dimensionality reduction (DR) algorithms are found. Multiple classification algorithms have been developed over the last decade, like Deep Convolutional Neural Networks (DCNN) [17] or Variational AutoEncoders (VAEs) [18]. In the same way, several clustering methods have been developed, for instance, k-means [19] or Density-Based Spatial Clustering of Applications with Noise (DBSCAN) [20]. Finally, some examples of dimensionality reduction techniques include Principal Component Analysis (PCA) [21], Isometric feature mapping (Isomap) [22], t-distributed Stochastic Neighbor Embedding (t-SNE) [23] or Uniform Manifold Approximation and Projection (UMAP) [24].

Among the works that combine communication scenarios and AI techniques, the following are worth mentioning:

- Zhou *et al.* [25] propose a deep neural network (DNN) and a score fusion scheme for classification purposes. Four scenarios related to high-speed railway channels (Rural, Station, Suburban and Multi-link) are classified by using four channel features (K Factor, RMS delay spread, RMS Doppler power spectrum and RMS angular spread).
- Zhang *et al.* [26] apply several classifiers and clustering techniques [k-nearest neighbor (k-NN), support vector machine (SVM), k-means, and Gaussian mixture model (GMM)] to identify four simulated scenarios (Urban Macrocell (UMa) and Rural Macrocell (RMa) for Line-of-Sight and Non Line-of-Sight). In order to perform this analysis, four features are taken into account: Path loss, K Factor, RMS delay spread and RMS angular spread.
- Thrane *et al.* [27] propose deep learning techniques to predict the path loss in the propagation channel at 2.6 GHz. A DNN is able to learn from input as distances, positions and satellite images. The DNN output infers the radio quality parameters, which estimate the path loss of the communication channel.
- Yang *et al.* [28] classify four scenarios related to vehicular communications, i.e., urban, highways, NLoS channels and tunnels. They use a back-propagation neural network (BPNN) and a feature set formed by four features: power delay spectrum, shadow fading, RMS delay spread and K Factor.

This work combines communication scenarios with AI and ML techniques to propose a tool for clustering, classification and generation of new 5G communication channels. The main contributions of the work are as follows:

- We evaluate the potential application of t-SNE, an unsupervised algorithm for dimensionality reduction and clustering, in the communication field. Although t-SNE technique is well known as a clustering tool, it has not been widely applied in this field. To demonstrate its potential as a powerful and promising tool for the scientific community in this field, the authors cluster five different communication scenarios by using six channel communication features. The DR allows to perform a rapid visual classification of the scenarios. These scenarios, of diverse nature, include real wireless communication scenarios and measurements acquired in an anechoic and reverberation chamber.
- A fitness function that chooses the t-SNE hyperparameters is analyzed. This metric gives those hyperparameters which provide the best visualization of clusters in a two-dimensional plane. The clustering of scenarios is able to show the separation of environments in a very visual way. Moreover, it has been found that t-SNE is able to separate a certain scenario itself into several subclasses, showing its potential as clustering technique.
- The authors make use of post-processing techniques for scenario modification and generation, studying the effect of a modified scenario in the clustering. As previously stated, the recreation of new scenarios arises as one of the main challenges for future mobile communications. The application of a DR technique validates the scenario emulation. If an emulated scenario is embedded in the same cluster than a real scenario, it indicates that the DR technique considers both real and emulated scenario as similar. These post-processing techniques, together with classification and clustering algorithms open up the possibility of new scenario recreations.

The paper is organized as follows. Section II explains the measurement scenarios that are analyzed throughout the study and the domains in which the communication channels scenarios are presented. Section III presents the clustering technique, t-SNE, for the dimensionality reduction and the input propagation parameters for this algorithm. Section IV analyzes the results obtained from the clustering technique in several communication environments. Section V provides a comparison among several DR techniques for the analyzed environments. Section VI applies post-processing techniques in order to recreate propagation channel scenarios. Finally, Section VII summarizes the conclusions extracted in this work.

II. MEASUREMENT SCENARIOS

This section describes the measurements and environments that are studied and depicted throughout this work. A distinction must be made between two main types of measurements. On the one hand, controlled measurements are acquired in anechoic and reverberation environments, where the physical conditions of the propagation channel are managed. On the other hand, real measurements are collected in scenarios that could become part of real communications. Finally, this

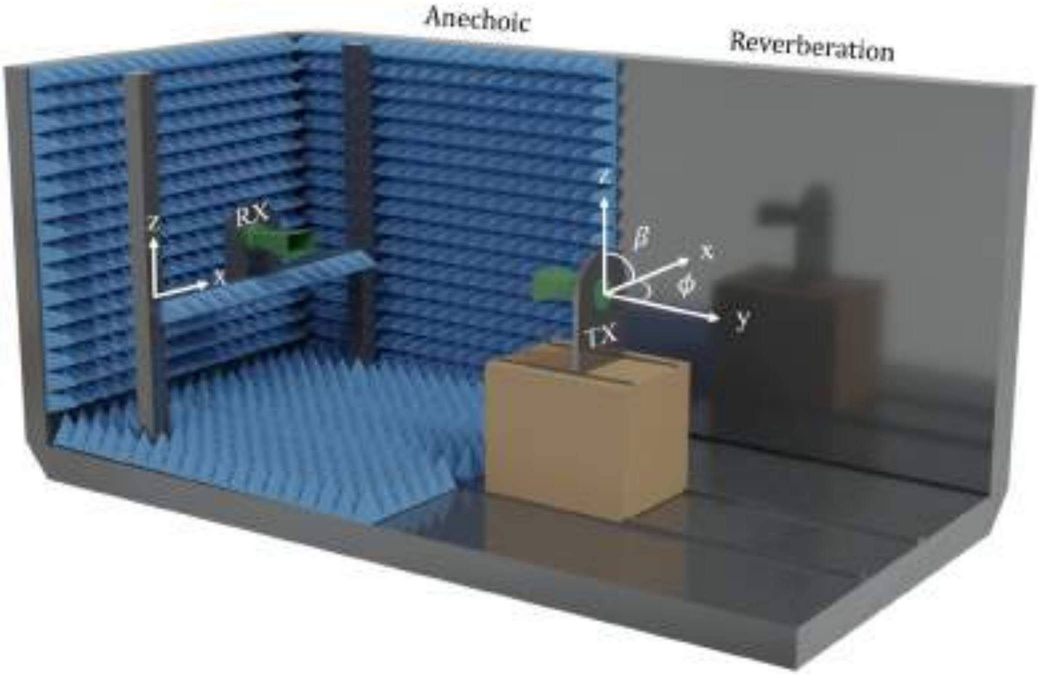

FIGURE 1. **Scheme of the semi-anechoic and semi-reverberation chamber. The scheme shows an anechoic setup, where the transmitter points at the receiver in LoS. In a reverberation setup, the transmitter is rotated 180° and it points at the metallic wall. The azimuth (ϕ) and roll (β) angles correspond to the rotation of the transmitter in the XY and XZ planes, respectively. The receiver is free to move in the XZ plane.**

section explains the two domains (time and frequency) in which the propagation channel is analyzed.

A. ANECHOIC AND REVERBERATION CHAMBER

The first group of channel measurements has been acquired in the facilities of the Smart Wireless Applications and Technologies (SWAT) research group, located at the University of Granada, Spain. The facilities consist of a half anechoic and half reverberation chamber with dimensions $5 \times 3.5 \times 3.5$ meters (61.25 m^3). Fig. 1 shows a three-dimensional view of the chamber. The semi-anechoic part is fully covered with absorbers which avoid any reflections. Thus, a receiver (RX) located inside the anechoic environment that is pointed by a transmitter (TX), receives exclusively the electromagnetic wave from the Line-of-Sight (LoS) path. The semi-reverberation part is composed of metallic walls. The presence of the metallic walls provokes that the incident wave is reflected and diffracted into several multipath components (MPCs) that reach the RX at different times. This chamber has been thoroughly described, used and validated in previous works for antenna and propagation measurements [29]–[34].

In this work, several communication channels are measured for both anechoic and reverberation environments to create a dataset that allows the study of the clustering of scenarios. For that purpose, the measurement system can move both the receiver and the transmitter. The first one can be shifted in the XZ plane, while the transmitter can be moved in y axis, azimuth (ϕ) and roll (β) angles (see Fig. 1). The receiver, initially aligned with the transmitter, is moved in 4 cm steps in the XZ plane, for a total of 11 positions in each axis, resulting in 121 positions that form a square of dimensions 40 x 40 cm. The transmitter adopts three azimuth positions ($-30°$, $0°$ and $30°$) in order to modify the pointing angle. In addition, three roll angles ($-30°$, $0°$ and $30°$) are measured to take into account the polarization effect. Zero degrees in the azimuth angle stand for the LoS path between the pair TX-RX, negative angles for counterclockwise rotation and positive angles for clockwise rotation. Zero degrees in the roll angle imply no depolarization losses between TX and RX. The combination of all possible configurations of the measurement system provides 1089 scenarios for both anechoic and reverberation cases. For the anechoic measurements, the distance between antennas has been set to 160 cm. For the reverberation measurements, the distance between antennas is 600 cm, corresponding to the LoS between the transmitter and the metallic wall plus the return path to the receiver. Note that TX-RX antenna range is different for the anechoic and reverberation cases. This fact increases the diversity of the measured communication channels due to the different ToA (Time of Arrival). Real communication scenarios consider several ToAs, which have high influence on the channel response. Therefore, this can be a critical parameter in scenario clustering. These measurements generate the first two environments that will be evaluated: (i) anechoic and (ii) reverberation.

The acquisition for environments (i) and (ii) is performed with a Vectorial Network Analyzer (VNA Rohde & Schwarz ZVA67), which measures the scattering parameters in the propagation channel and can operate up to 67 GHz. The


(a) (b) (c)

FIGURE 2. Photographs of the (a) indoor, (b) rooftop and (c) auditorium scenarios that form the dataset. Indoor photograph is taken from the RX perspective. Rooftop [36] and auditorium [37] scenarios have been acquired at the Fraunhofer-Heinrich-Hertz-Institut.

chosen antennas for the acquisition are standardized gain horns fed with a WR-34 waveguide-to-coaxial transition (Flann Kband antenna Model: #21240-20) for both transmitter and receiver. Radiating patterns of these elements can be found in [29]. Prior to the acquisition process, a TOSM (Through — Open — Short — Match) calibration is performed to eliminate the effect of the coaxial cable. Therefore the scattering parameters are measured from the aperture of the radiating elements. The transmit power is set to 10 dBm in the VNA. The frequency range for these scenarios goes from 24.25 GHz to 27.5 GHz, for a total of 651 frequency samples. This provides 5 MHz frequency separation. This band, also called 3GPP n258 [35], is considered fundamental for the deployment of 5G and millimeter wave communications in the European Union.

B. INDOOR AND OUTDOOR SCENARIOS

In addition to the anechoic and reverberation scenarios, three additional scenarios that could be part of real communication environments will be evaluated.

(iii) The third one is an indoor scenario located in the same facilities than those from Section II-A. In this case, the transmitter points at a furnished laboratory through the chamber door [see Fig. 2(a)]. The receiver, placed in a measurement system similar to the one in the previous section, has mobility in XZ plane. Therefore, we consider 121 positions in a square of dimension 40×40 cm. The transmitter moves in the azimuth ($-30°$, $-15°$ and $0°$) and roll angles ($-30°$, $0°$ and $30°$) for a total combination of 1089 configurations. When $\phi = -30°$, TX points through the window on the right side in Fig. 2(a). When $\phi = -15°$, TX points towards the chamber door frame. Finally, the case $\phi = 0°$ describes the angle where TX points directly at RX through the chamber door in LoS. The measurement configuration, i.e., radiating elements, calibration process, transmitted power, frequency range and frequency samples, is similar to the one shown in environments (i) and (ii).

(iv) The fourth environment consists of a dataset from a rooftop outdoor scenario located at the Fraunhofer-Heinrich-Hertz-Institut in Berlin, Germany [36] [see Fig. 2(b)]. Two antennas are aligned in LoS with a separation of 800 cm. Both TX and RX are steered in azimuth angle from $-45°$ to $45°$ with 64 possible positions for each antenna. Moreover, the dataset is increased by acquiring measurements placing the TX and RX misaligned between them and also switched. In order to keep a balance in the number of measurements of each type, 1089 of the total number of measurements are selected. The signal acquisition technique is based on real-time sampling, where the sampling rate is 3.52 GHz. The transmitted signal is centered in the millimeter wave band at 60.48 GHz.

(v) The fifth environment comes from a dataset measured in an auditorium at the Fraunhofer-Heinrich-Hertz-Institut [37]. Similar to the previous scenario, two antennas are aligned in LoS and the distance between them is chosen to be 700 cm and 800 cm. TX and RX can point in the vertical axis from $-45°$ to $45°$ degrees with 64 positions. 1089 measurements from this dataset are selected. The acquisition properties and operation frequencies are similar to those of the rooftop scenario.

The (iv) rooftop and (v) auditorium communication scenarios have been acquired at the Fraunhofer-Heinrich-Hertz-Institut in Berlin, Germany. The datasets have been made public through the NextG Channel Model Alliance. Further information about the dataset, i.e., the acquisition process, the channel sounder architecture and the scenario physical parameters for environments (iv) and (v), is thoroughly detailed in [36], [37].

C. PROPAGATION CHANNEL IN TEMPORAL AND FREQUENCY DOMAIN

In order to perform the clustering that will be shown in Section IV, we need to extract several properties from the communication channels that allow the differentiation of the five proposed scenarios. For that purpose, the propagation channels can be analyzed in two domains, the temporal domain through the Channel Impulse Response (CIR) and the frequency domain through the Channel Frequency Response (CFR).

Traditionally, CIR is modeled as follows [38]:

$$h(t_n) = \sum_{k=0}^{K-1} \alpha_k \delta(t_n - \tau_k) \tag{1}$$

where t_n refers to the n-th time sample, k is the index of considered sample, K is the number of samples in the time domain, $\delta(\cdot)$ stands for the Dirac delta function, τ_k shows the delay of the arrival in the propagation channel between the pair TX-RX and α_k denotes the complex amplitude which takes into account the attenuation and phase change due to the physical phenomena (reflection, scattering, refraction, diffraction) that occur during signal propagation.

The CIR has its equivalent in the frequency domain through the CFR:

$$H(f) = \sum_{k=0}^{K-1} b_k e^{-j2\pi f \tau_k} \tag{2}$$

where b_k stands for the complex amplitude of the CFR, and $e^{-j2\pi f \tau_k}$ denotes the complex exponential that depends on the frequency and the time of arrival.

Once a measurement in one of the two domains has been acquired, Discrete Fourier Transform (DFT) and Inverse Discrete Fourier Transform (IDFT) allow the calculation of the CFR from the CIR [eq. (3)] and vice versa [eq. (4)].

$$H(f) = \sum_{n=0}^{\frac{t_{\max}}{T}} h(t_n) e^{-j2\pi f t_l} \tag{3}$$

$$h(t) = \sum_{l=0}^{\frac{B}{\Delta f}} H(f_l) e^{j2\pi f_l t} \tag{4}$$

In eq. (3), $t_{\max}$ is the time of the last sample acquired and T is the sampling period. In eq. (4), B stands for the total bandwidth of the measurement band and Δf is the frequency step. Therefore, $t_{\max}/T$ and $B/\Delta f$ factors are the total number of points acquired in the time and frequency domain, respectively.

As previously explained, environments (i), (ii) and (iii) are analyzed through the scattering parameters acquired in the VNA. Therefore, these environments follow the notation of the eq. (2). On the other hand, environments (iv) and (v) are acquired through a channel sounder in the time domain. Consequently, the acquired data can be expressed as eq. (1). Since all environments need to be expressed in both domains to extract the propagation features that will be shown in Section III, we apply eq. (4) to the environments (i), (ii) and (iii), and eq. (3) to the environments (iv) and (v).

III. AI FOR PROPAGATION MEASUREMENTS

As stated in Section I, Artificial Intelligence is becoming one of the main topics in several research fields [39], [40]. In wireless communications, AI emerges as a potential tool for scenario recreation and generation in future mobile communications. This section shows the clustering algorithm that is implemented, the hyperparameters involved in its performance and the channel features that are considered as the input of this algorithm.

A. AN OVERVIEW OF T-SNE

The t-distributed Stochastic Neighbor Embedding [23], [41], [42] is an unsupervised learning algorithm that reduces the dimensionality of a high-dimensional dataset $\{\mathbf{x}_1, \mathbf{x}_2, \ldots, \mathbf{x}_N\}$ into a low-dimensional (2D) dataset $\{\mathbf{y}_1, \mathbf{y}_2, \ldots, \mathbf{y}_N\}$. The high-dimensional space is defined by the matrix $\mathbf{X} \in \mathbb{R}^{N\times F}$, where N is the number of communication channel measurements and F is the number of communication channel parameters contained in the high-dimensional space. Each row of $\mathbf{X}$ contains the channel parameters of the i-th observation; namely, $\mathbf{x}_i$ is a row vector that can be defined as

$$\mathbf{x}_i = \left[K_i, \tau_{RMS,i}, \tau_{\text{mean},i}, \tau_{\text{var},i}, \overline{PL}_i, \bar{\eta}_i\right] \tag{5}$$

These communication channel parameters will be identified later on Section III-B. Similarly, the low-dimensional space is defined by the matrix $\mathbf{Y} \in \mathbb{R}^{N\times 2}$. The dimension of this space is set to two due to the ease of visualization in a two-dimensional plane.

t-SNE arises as an improvement to the Stochastic Neighbor Embedding (SNE), where the distances between datapoints in the high-dimensional dataset are modeled as joint probability distributions p_{ij}, known as the similarity between the datapoints. Therefore, the similarity for every pair $\mathbf{x}_i$ and $\mathbf{x}_j$ is computed as the probability p_{ij}, calculated as follows:

$$p_{j|i} = \frac{\exp\left(-\left\|\mathbf{x}_i - \mathbf{x}_j\right\|^2/2\sigma_i^2\right)}{\sum_{k\neq i}\exp\left(-\|\mathbf{x}_i - \mathbf{x}_k\|^2/2\sigma_i^2\right)} \tag{6}$$

$$p_{ij} = \frac{p_{j|i} + p_{i|j}}{2N} \tag{7}$$

where σ_i^2 is the variance of a Gaussian probability density function (PDF) for the normal distribution centered in the datapoint $\mathbf{x}_i$, $p_{j|i}$ and $p_{i|j}$ are the conditional probabilities between the datapoints $\mathbf{x}_i$ and $\mathbf{x}_j$, and $\|\cdot\|$ stands for the Euclidean norm.

For the low-dimensional dataset, t-SNE uses a Student's t-distribution in order to define a joint probability denoted by q_{ij} and calculated as:

$$q_{ij} = \frac{\left(1 + \left\|\mathbf{y}_i - \mathbf{y}_j\right\|^2\right)^{-1}}{\sum_{k\neq l}\left(1 + \|\mathbf{y}_k - \mathbf{y}_l\|^2\right)^{-1}} \tag{8}$$

Once both joint probabilities p_{ij} and q_{ij} have been defined, t-SNE minimizes the Kullback-Leibler divergence

[KL(·)] between joint probability distributions in the high-dimensional (**P**) and low-dimensional (**Q**) spaces. Intuitively, large p_{ij} values [eq. (7)] indicate that $\mathbf{x}_i$ and $\mathbf{x}_j$ are closer in the high-dimensional space. In the same way, large q_{ij} values [eq. (8)] indicate that $\mathbf{y}_i$ and $\mathbf{y}_j$ are closer in the low-dimensional space. If the dimensionality reduction performs a proper mapping, the probability distributions **P** and **Q** should resemble each other. In order to quantify the quality of the dimensionality reduction, a cost function is defined as [23]:

$$C = \mathrm{KL}(\mathbf{P}\|\mathbf{Q}) = \sum_i \sum_j p_{ij} \log_2 \frac{p_{ij}}{q_{ij}} \tag{9}$$

The minimization of this function indicates an accurate mapping between the high-dimensional (probability distribution **P**) and low-dimensional (probability distribution **Q**) spaces. The minimization is made by using a gradient descend technique, where the gradient has the following form [23, Appendix A]:

$$\frac{\delta C}{\delta \mathbf{y}_i} = 4 \sum_j \left(p_{ij} - q_{ij}\right)\left(\mathbf{y}_i - \mathbf{y}_j\right)\left(1 + \left\|\mathbf{y}_i - \mathbf{y}_j\right\|^2\right)^{-1} \tag{10}$$

Through several iterations of the algorithm, the dimensionality reduction of the high-dimensional dataset $\{\mathbf{x}_1, \mathbf{x}_2, \ldots, \mathbf{x}_N\}$ into a low-dimensional dataset $\{\mathbf{y}_1, \mathbf{y}_2, \ldots, \mathbf{y}_N\}$ is improved. A detailed explanation of the whole technique can be found in [23].

One of the key features of this dimensionality reduction technique is its flexibility given a set of configuration hyperparameters. Previous works made by the authors [43] have shown the relevance of a correct choice of hyperparameters. Particularly, we detected three hyperparameters which are crucial in order to find a proper dimensionality reduction. These parameters are: the type of distance between datapoints, the perplexity, and the learning rate. A brief explanation, as well as its relation to the previous formulation, is given below.

1) *Distance:* Previous equations [eqs. (6), (8), (10)] consider the Euclidean distance between datapoints. When the variance between different features in the high-dimensional dataset $\{\mathbf{x}_1, \mathbf{x}_2, \ldots, \mathbf{x}_N\}$ is in a different range (see Section III-B), the Euclidean distance does not give the same importance to all the variables. In order to avoid this fact, the Mahalanobis distance takes into account the covariance matrix ξ. Therefore, this distance is used throughout the work. It is defined as:

$$d_m\left(\mathbf{x}_i, \mathbf{x}_j\right) = \sqrt{\left(\mathbf{x}_i - \mathbf{x}_j\right)\xi^{-1}\left(\mathbf{x}_i - \mathbf{x}_j\right)^T} \tag{11}$$

where ξ is the sample covariance of matrix **X** with dimensions $F \times F$.

2) *Perplexity:* In eq. (6), the conditional probability depends on the variance of a Gaussian PDF σ_i. This value is chosen such that the joint probability for all the datapoints is fixed to a certain perplexity, which is defined as:

$$\mathrm{Perp}_i = 2^{\psi_i} \tag{12}$$

$$\psi_i = -\sum_j p_{j|i} \log_2\left(p_{j|i}\right) \tag{13}$$

where ψ_i stands for the Shannon entropy. Since there is not a single perplexity value that provides the optimum performance, Section IV shows a search for a proper value of this parameter in terms of visualization for our datasets.

3) *Learning Rate:* This value is related to the convergence of the algorithm through several iterations. For each iteration, the learning rate ρ multiplies the gradient shown in eq. (10) [23]. On the one hand, if this value is too small, the gradient descent could be slow. On the other hand, if this value is too high the gradient descent might not converge correctly. In Section IV, a proper value of this parameter is discussed for the presented datasets.

B. COMMUNICATION CHANNEL PARAMETERS FOR T-SNE

In this paper, five datasets have been shown in Section II, containing 1089 communication channel measurements each one, for a total of 5445. This leads to a six-dimensional dataset composed by 5445 observations $\{\mathbf{x}_1, \mathbf{x}_2, \ldots, \mathbf{x}_{5445}\}$. Each measurement is characterized by six communication channel parameters:

1) *K Factor:* It represents the relation between the dominant multipath component, usually the LoS, and the rest of multipath components in the time domain. It is approximated as the ratio between the maximum power component $|h_i(t_{n_{\max}})|^2_{\max}$ and the sum power of the remaining taps in the power delay profile (PDP).

$$K_i = 10 \log_{10}\left(\frac{\left|h_i\left(t_{n_{\max}}\right)\right|^2_{\max}}{\sum_{n=0, n\neq n_{\max}} |h_i(t_n)|^2}\right) \tag{14}$$

2) τ_{mean}: The mean delay is defined as the first moment of the PDP [44]. It shows the average delay of the power measured in the communication channel.

$$\tau_{\mathrm{mean},i} = \frac{\sum_{n=0} t_n \cdot |h_i(t_n)|^2}{\sum_{n=0} |h_i(t_n)|^2} \tag{15}$$

3) τ_{var}: The variance delay is obtained as the second moment of the PDP and depicts how fast the PDP power varies in short time intervals.

$$\tau_{\mathrm{var},i} = \frac{\sum_{n=0} {t_n}^2 \cdot |h_i(t_n)|^2}{\sum_{n=0} |h_i(t_n)|^2} \tag{16}$$

4) τ_{RMS}: The root-mean-square delay spread is calculated as the second central moment root square of the PDP [44] and presents the power deviation of the communication channel. Large values indicate that the power is divided into several MPCs. On the other hand,

small values are representative of scenarios where the power is concentrated on the main MPC, typically the Line-of-Sight. In other words, this feature describes the power dispersion in the time domain of the communication channel.

$$\tau_{RMS,i} = \sqrt{\frac{\sum_{n=0}\left(t_n - \tau_{\text{mean},i}\right)^2 \cdot |h_i(t_n)|^2}{\sum_{n=0}|h_i(t_n)|^2}} \tag{17}$$

5) *Path Loss (PL):* This parameter shows the attenuation between the pair TX-RX due to propagation losses through the communication channel. For this study, this value includes the contribution of the antenna gain from the TX and RX antennas. This value is calculated as the absolute value of the channel frequency response averaged over the complete domain of the CFR, i.e., averaged over all frequencies ($\overline{PL_i}$).

$$PL_i(f) = 20\log_{10}(|H_i(f)|) \tag{18}$$

6) *Spectral Efficiency (η):* The spectral efficiency is defined as the information rate that can be sent through a communication system, i.e., a propagation channel. It is measured in bps/Hz and calculated as follows [45]:

$$\eta_i(f) = \log_2\left(1 + SNR \cdot |H_i(f)|^2\right) \tag{19}$$

where SNR stands for the Signal-to-Noise Ratio. Then, $\eta_i(f)$ is averaged over the whole frequency range of the measurement. The average spectral efficiency is noted as $\bar{\eta}_i$.

Notice that the former expressions [eqs. (14)-(19)] stand for the i-th observation. Once every communication channel feature has been calculated, they form the six-dimensional space $\mathbf{x}_i$ for the i-th observation.

IV. CLUSTERING RESULTS

Once the theoretical basis and t-SNE have been explained, this section presents and discusses the results obtained for several clustering of communication scenarios, where each subsection shows the results for a specific data subset. Good scenario separation using clustering techniques involves the unambiguous identification of communication environments. This fact can be crucial in the classification and generation of future communication scenarios, such as UAV-to-UAV, S2S or V2V systems.

As demonstrated in [43], the Mahalanobis distance is the distance metric that provides the best dimensionality reduction. However, clusters are also altered by the learning rate and perplexity. For these two hyperparameters, the choice of a proper value in terms of visualization is not trivial. In order to solve this fact, we define a fitness function F, which measures the ratio between the inter class distance and intra class distance. Intra class distance is described as the sum of distances in the low-dimensional space between datapoints belonging to the same class. On the other hand, inter class distance is defined as the sum of distances in the low-dimensional space between datapoints from different classes. If we use this fitness function, we are able to find those configuration parameters that provide the largest separation between classes. By maximizing this metric, the visualization of the figures is easier for the reader due to the formation of clear clusters. Mathematically, this fitness function can be defined as:

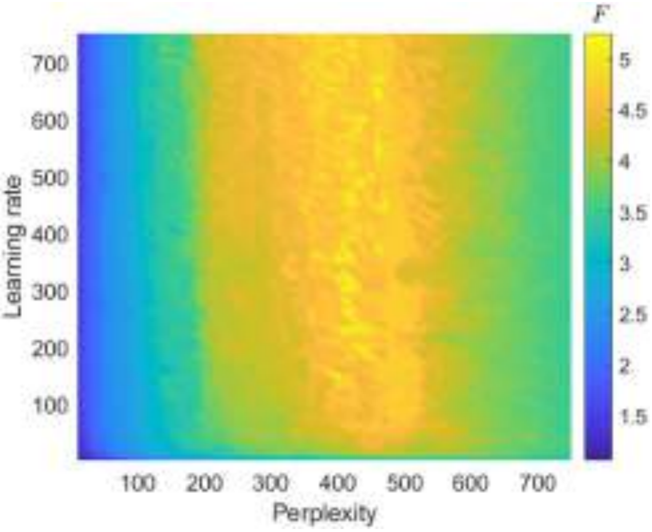

FIGURE 3. Fitness function for the subset composed by the anechoic, reverberation and indoor datasets (see Section IV-A).

$$F^{(\mathcal{X})} = \frac{\sum_{i\in\mathcal{X}}\sum_{\forall j\notin\mathcal{X}} d_e(i,j)}{\sum_{i\in\mathcal{X}}\sum_{k\in\mathcal{X}} d_e(i,k)} \tag{20}$$

$$F = \frac{1}{(N_c - 1)}\sum_{\mathcal{X}=1}^{N_c} F^{(\mathcal{X})} \tag{21}$$

where d_e stands for the Euclidean distance, $\mathcal{X}$ is the considered class, i, j, k are indexes represented by natural numbers, and $N_c > 1$ is the total number of classes.

For a better visualization of the results, it is intended that the inter class distance becomes as large as possible and the intra class distance becomes as small as possible. Therefore, the main idea is to find those parameters that maximize F. As an example of this fitness function, Fig. 3 shows results for the dataset composed by the anechoic, reverberation and indoor datasets for values of learning rate and perplexity in the range $[1, 750] \in \mathbb{N}$.

Two main conclusions can be drawn from Fig. 3. First, the algorithm tends to converge for learning rate above 15. Below this value, the gradient descent in eq. (10) is too slow and the algorithm is not able to find a good solution. Second, when the learning rate is in a good range, the critical configuration parameter is the perplexity. Too small or too large perplexity values do not find an optimal solution since small values do not properly group the clusters and large values tend to group inter classes, which minimizes the inter class distance. Therefore, the optimal solution lies somewhere in between. In this case, the maximum is found for

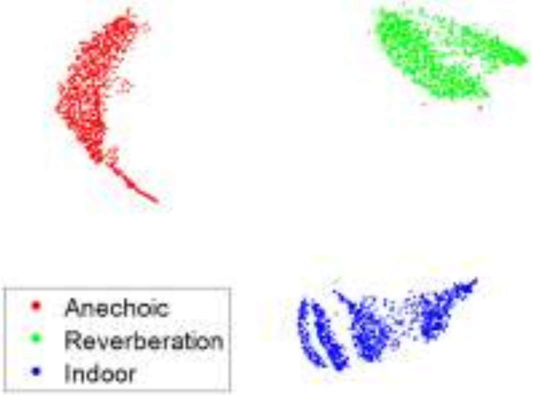

FIGURE 4. **Clustering of anechoic, reverberation and indoor scenarios. Learning rate and perplexity are fixed to 600 and 440.**

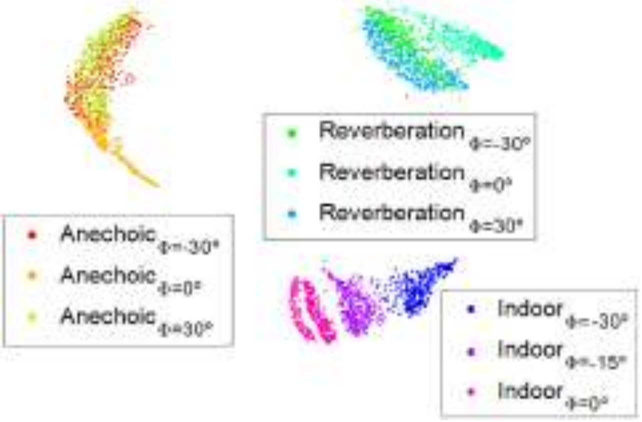

FIGURE 5. **Clustering of anechoic, reverberation and indoor scenarios for several values of the azimuth angle. Learning rate and perplexity are fixed to 600 and 440.**

perplexity values around 420. Specifically, the fitness function maximum is $F = 5.23$ for learning rate and perplexity values equal to 600 and 440. This value means that, in average, the distance between datapoints from different classes is 5.23 times higher than distances between datapoints from the same class. Due to this fact, the visualization of the clusters in the low-dimensional space is straightforward. These t-SNE hyperparameters (learning rate and perplexity) are detailed on the caption of subsequent figures throughout this Section.

In addition, a radar chart (see Fig. 10) with the numerical results of the mean and standard deviation of the communication channel properties for each possible scenario is shown at the end of this section. The channel features have a direct impact on the KPIs, i.e., they directly influence the behavior of the communication channel. As an example, the spectral efficiency is related to the network data rate performance. These results are discussed throughout this section to provide a rational explanation for the clustering results.

A. ANECHOIC, REVERBERATION AND INDOOR ENVIRONMENTS

As a proof of concept, the first clustering includes the anechoic, reverberation and indoor scenarios. These scenarios are characterized by different propagation conditions so that we expect a good separation between clusters. The anechoic environment is typically identified by an unique MPC since the reflections are attenuated by the absorbers. In the reverberation scenario, several MPCs following an exponential decay in the time domain are expected. These MPCs reach the RX at discrete times due to the presence of absorbers in the semi-anechoic part of the chamber. Finally, the indoor scenario presents several MPCs following a continuous exponential decay due to the presence of furniture in the room. The clustering presented in Fig. 4 shows an excellent separation in the low-dimensional space when t-SNE is applied for the communication channel parameters previously explained. Note that a cluster is defined as the two-dimensional area where the datapoint density is high, thus generating a grouping of observations expected to have some common behavior. Looking at the radar chart (see Fig. 10), this separation is obtained due to the following reasons. τ_{mean} is significantly lower in the anechoic case due to the proximity between antennas (160 cm), compared to the reverberation and indoor cases (600 cm), where multiple reflections enlarge this distance even further. The K Factor is substantially larger in the anechoic scenario due to LoS previously stated. However, in the reverberation and indoor scenarios, this number tends to be below 0 dB, meaning that the signal is more spread across multiple MPCs. τ_{RMS} and τ_{var} also play a key role since they are small for the anechoic and reverberation scenarios. This fact can be explained due to the presence of absorbers inside the chamber, obtaining a smoothed PDP that reduces these two values. In the anechoic case, there is one dominant MPC since the NLoS paths are attenuated by the absorbers. In the reverberation case, several MPCs impinge the RX. However, these MPCs have short delay offsets since large delay offsets MPCs are attenuated by the absorbers. Therefore, the absence of these absorbers in the indoor scenario induces higher τ_{RMS} and τ_{var}.

Inspecting Fig. 4, it can be observed that classes present a tendency towards internal separation. Actually, the azimuth angle can be considered as a discriminating parameter, dividing the main class into subclasses. This change leads to the results shown in Fig. 5. Indoor scenario can be separated into three subscenarios depending on the angle, and anechoic and reverberation scenarios tend to separate the central azimuth angle $\phi = 0°$ from the others two. Since clear differences are noticeable within the clusters themselves, Section IV-B goes one step beyond and analyzes these differences.

B. DEEP ANALYSIS OF ANECHOIC, REVERBERATION AND INDOOR SCENARIOS

Since Fig. 5 shows that intra class differences exist, t-SNE is computed for each scenario (1089 datapoints) in order to find intrapopulation separation evidences. The first case is displayed in Fig. 6, where the clustering of the anechoic scenario for three azimuth angles is performed. Two conclusions can be drawn. First, the measurements for $\phi = -30°$ and $\phi = 30°$ are mixed on the right side of the figure. This fact

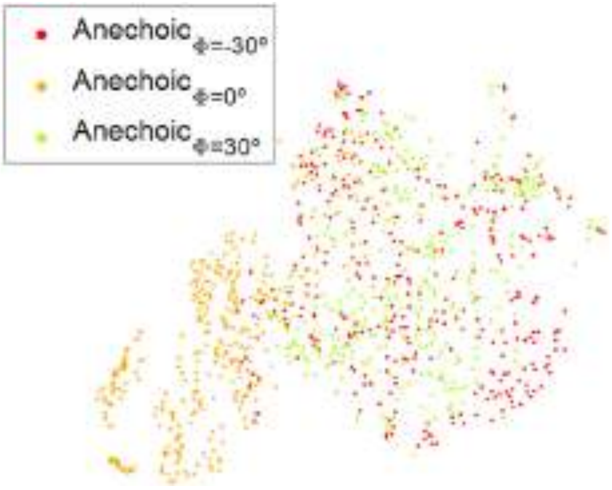

FIGURE 6. Clustering of the anechoic scenario for three azimuth angles (−30°, 0° and 30°). Learning rate and perplexity are fixed to 650 and 240.

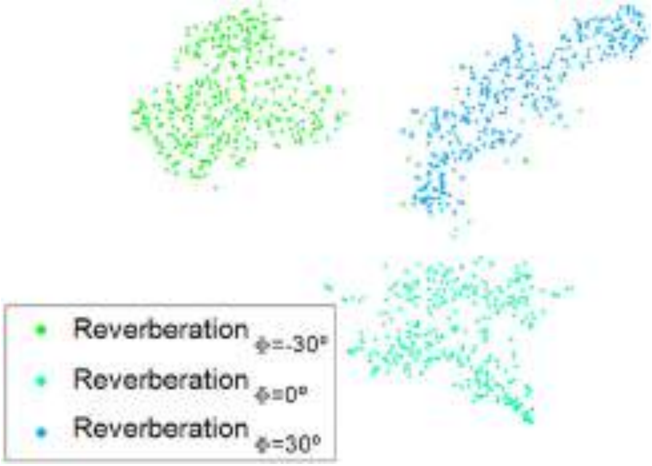

FIGURE 7. Clustering of the reverberation scenario for three azimuth angles (−30°, 0° and 30°). Learning rate and perplexity are fixed to 700 and 90.

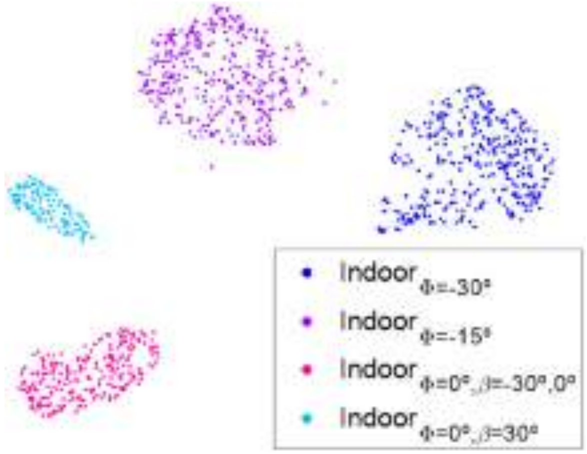

FIGURE 8. Clustering of the indoor scenario for three azimuth angles (0°, −15° and −30°) and three roll angles (−30°, 0° and 30°) for $\phi = 0°$. Learning rate and perplexity are fixed to 600 and 140.

can be explained from the symmetry of the semi-anechoic chamber in the YZ plane (see Fig. 1). Due to the presence of absorbers, the MPCs are attenuated, and the main MPC (LoS case) reaches the RX identically for a positive or negative azimuth angle. Since no information about the angle of arrival (AoA) is included in $\mathbf{x}_i$ [eq. (5)], it is reasonable that both angles are mixed. Secondly, the measurements for $\phi = 0°$ tend to be correctly separated from the two previous angles. For this angle, the perfect alignment for the TX-RX antennas causes lower values for the path loss, and therefore, higher spectral efficiency values. These differences between angles explain the large values of standard deviation for the spectral efficiency in Fig. 10(a).

The clustering for the reverberation scenario with three ϕ angles is shown in Fig. 7. Although the cases $\phi = -30°$ and $\phi = 30°$ were mixed in Fig. 5, it can be observed a good separation between both angles in Fig. 7. Considering the symmetry of the semi-reverberation chamber, these results may appear to be incorrect. However, the presence of the chamber door for $\phi = 30°$ has to be taken into account, as well as the measuring table [see Fig. 2(a)]. The door and the measuring table break the symmetry of the semi-reverberation scenario in the YZ plane, altering the MPCs. This leads us to conclude that the global dataset tends to discover global differences among classes (inter class), giving less importance to intra class differences. The input data must be adjusted to the specific classes when intra class differences are searched, as depicted in Fig. 7.

The third case is shown in Fig. 8, where three azimuth angles are clustered for the indoor environment. As shown by the trend in Fig. 5, the three subscenarios are separable into clusters. It is important to note that these three angles correspond to three completely different pointing angles: $\phi = -30°$ (TX points at the window of the reverberation chamber), $\phi = -15°$ (TX points at the chamber door frame), and $\phi = 0°$ (LoS through the chamber door). Another interesting detail is the separation of the angle $\phi = 0°$ into two subclusters. It has been found that the upper left cluster corresponds to $\beta = 30°$, while the lower left cluster groups the datapoints corresponding to angles $\beta = -30°$ and $\beta = 0°$. Therefore, it is proved that this clustering technique can also separate measurements as a function of the polarization of the incident wave. Note that the clustering of this roll angle implies that the datapoints have been previously separated according to scenario and azimuth angle. As a result, Fig. 8 is the consequence of a clustering in several layers since the roll angle is three-levels depth (scenario, ϕ and β). This fact proves t-SNE's potential to cluster communication scenarios at several depth levels.

C. ANECHOIC, REVERBERATION, INDOOR, ROOFTOP AND AUDITORIUM

The last example mixes the clustering of previously analyzed environments (anechoic, reverberation and indoor) with real communication scenarios (rooftop and auditorium). The clustering from these five environments is shown in Fig. 9. From

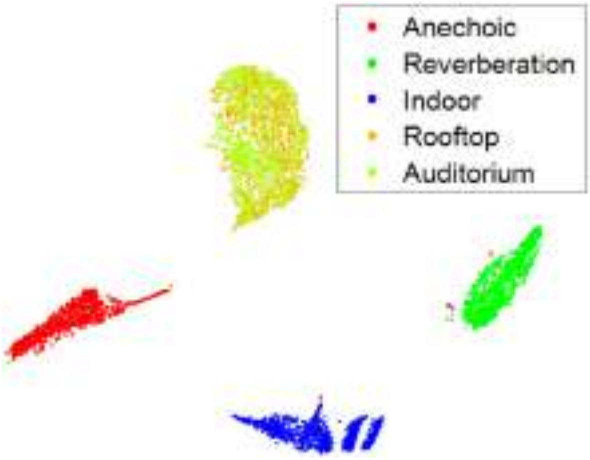

FIGURE 9. Clustering of the anechoic, reverberation, indoor, rooftop and auditorium scenarios. Learning rate and perplexity are fixed to 650 and 400.

an analytical viewpoint, it is observed an excellent separation between the three previous scenarios and new (rooftop and auditorium) scenarios. However, rooftop and auditorium seem to be totally mixed. The frequency, the distance and the antenna positions are identical in both scenarios, being the environment surrounding the radiating elements the only difference. In the rooftop scenario, it is expected to obtain a single peak in the PDP due to the outdoor nature. In the auditorium scenario, we would expect to get the main MPC due to the LoS and several reflections from the walls. However, due to the frequency and the distance to the walls of the antennas, the LoS is dominant over any reflection (that is attenuated) and a single peak is seen on the PDP. Therefore, the auditorium scenario behavior is identical to the rooftop scenario. Actually, Figs. 10(d) and 10(e) show how close the communication parameters are for both scenarios, affirming the previous explanation. Therefore, both scenarios are similar in terms of electromagnetic wave propagation. This fact explains that both scenarios are grouped in the same cluster.

As a last note, it should be remarked how part of the anechoic datapoints tends to approach the rooftop and auditorium data. This data subset represents the orange dots seen earlier in Figs. 5 and 6. These dots, belonging to the case $\phi = 0^\circ$, are characterized by a single peak in the time domain corresponding to the LoS path. Since the signal shape in the time domain is similar to the rooftop and auditorium cases, these dots tend to stay close. The difference between them is mainly due to the power amplitude and delay of the signal. This fact opens a way to the rooftop and auditorium recreation from a controlled scenario as the anechoic case.

V. COMPARING THE PERFORMANCE OF DIMENSIONALITY REDUCTION TECHNIQUES

Throughout the present work, clustering and dimensionality reduction of the communication channels have been performed using the t-SNE technique. Now, the efficiency of t-SNE is compared with other state-of-the-art techniques in order to demonstrate that this technique shows the best performance of the presented approaches.

Three datasets are considered in the comparison. The first one (Fig. 4) is composed by the anechoic, reverberation and indoor measurements. The second one (Fig. 5) includes these three scenarios plus the ϕ angle differentiation, for a total of 9 classes. The third one (Fig. 9) is formed by the three original scenarios plus the measurements obtained in the Fraunhofer HHI, for a total of 5 classes. With respect to the DR techniques, three state-of-the-art techniques are selected to perform this study: PCA [21], Kernel PCA [46] and Isomap [22]. Principal Component Analysis is one of the oldest techniques used for DR. In summary, this technique aims to reduce the dimensionality of a given dataset by preserving the variance statistical information. For that purpose, this technique calculates linear functions of the variables contained in the original dataset. These new variables, known as Principal Components (PCs), are uncorrelated to each other and contain the maximum possible variance from the original dataset. Typically, the PCs are derived by solving a singular value decomposition (see Appendix A). The analysis of the PCs in our dataset showed that the most influential communication channel parameters for the scenario discrimination are the path loss and the K-factor, followed by the spectral efficiency, and the time parameters (τ_{RMS}, τ_{mean}, τ_{var}). One step further, Kernel PCA is a PCA extension which allows a nonlinear dimensionality reduction. For that purpose, Kernel PCA applies a nonlinear transformation to the original dataset variables. This is done through the dataset projection with a kernel function, e.g., polynomial, Gaussian, Laplacian [47] (see Appendix A). If the dataset has a structure that can not be separated into a linear subspace, Kernel PCA tends to improve the dimensionality reduction performed by standard PCA. Finally, a technique based on isometric mapping (Isomap) is proposed. The Isomap aim is to preserve the geodesic distance of the dataset in the low-dimensional space. To this end, Isomap generates a neighborhood graph with K neighbors. Therefore, the geodesic distance is estimated as the shortest paths in the graph where each datapoint is connected to K neighbors. In the end, the dataset is embedded into a low-dimensional space through a eigenvalue decomposition of the matrix formed by geodesic distances (see Appendix B).

Fig. 11 shows the dimensionality reduction of the datasets previously detailed for PCA, Kernel PCA and Isomap DR techniques. Note that Kernel PCA utilizes a Laplacian kernel with $\gamma = 0.1$ and Isomap uses $K = 15$ neighbors. Visually, the three columns should be compared with the DRs in Figs. 4, 5 and 9, respectively. It can be seen that none of these new proposed techniques improves the performance of t-SNE in terms of visualization. There are several areas in the low-dimensional embedding space where multiple classes are mixed together. Although there is a tendency of separating classes, it is not as evident as we saw in t-SNE.

In order to quantify the quality of these embedding spaces, the fitness function proposed in Section IV

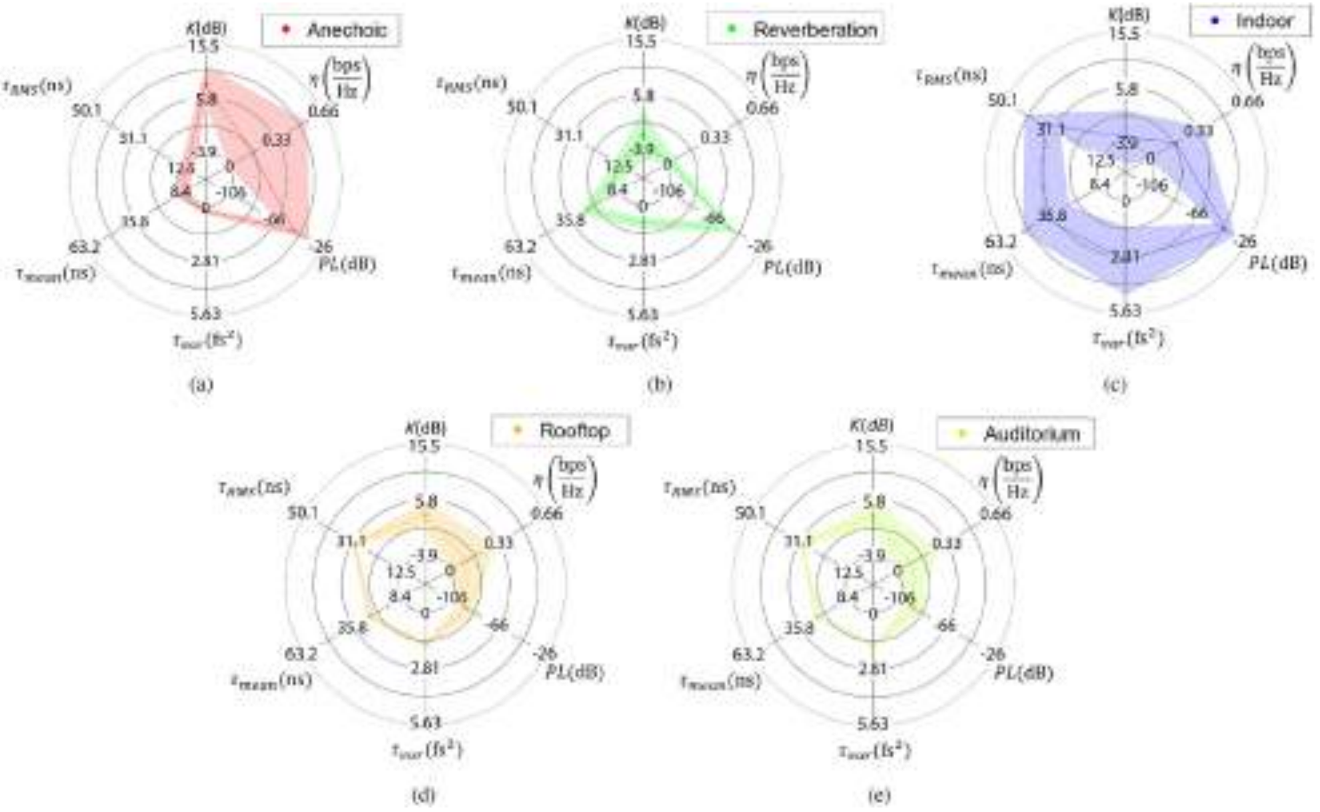

FIGURE 10. Radar chart of the anechoic (a), reverberation (b), indoor (c), auditorium (d) and rooftop (e) scenarios. The average value for each one of the five datasets is shown in a solid dot. The standard deviation is represented as the width of the lines.

[eqs. (20) and (21)] is applied to each low-dimensional space illustrated in Fig. 11. Table 1 presents the fitness function for several datasets and DR techniques. Note that a higher value of the fitness function is directly related to a better clustering visualization of the considered communication scenarios. Concerning the first and second dataset, t-SNE fitness function outperforms the results obtained by PCA, Kernel PCA and Isomap. For the third dataset, t-SNE also obtains a slightly better value. The results provided in Table 1 support the visual comparison made in Fig. 11. Both studies show that the performance of t-SNE for communication channel embedding is superior compared to other techniques.

As a final study, a classification of the classes in the low-dimensional space is carried out. If a trained classifier is able to correctly classify the observations in the low-dimensional space, it means that the DR technique properly infers and separates the discriminative aspects of each scenario. Therefore, those techniques where the classifier provides the highest accuracy are the ones whose low-dimensional space includes the most easily discriminable classes. Five well-established classifier families are considered: k-Nearest Neighbors (k-NN) [48], Support Vector Machine (SVM) [49], Naive Bayes [50], Bagging [51] and Linear Discriminant Analysis (LDA) [52]. k-NN classifies a given observation based on the class of its closest neighbors, where k is the number of considered neighbors. SVM finds a mapping such that the different classes of the dataset are divided into subspaces separable by a hyperplane with the largest possible margin. The support vectors (SVs) are those observations that bound the hyperplane (see Appendix C). Naive Bayes is a classifier based on Bayesian statistics where the observation features are considered independent. Under this assumption, Naive Bayes estimates that an observation belongs to a given class with the maximum *a posteriori* decision rule (see Appendix D). Bagging, also known as bootstrap aggregation, replicates the original dataset into several new learning datasets. These new datasets are trained independently by using independent classifiers (e.g., k-NN or decision trees). Finally, the classification of each independent classifier is aggregated into a single estimation by the majority of the classifier predictions. Linear Discriminant Analysis assumes that each scenario is modeled by a multivariate Gaussian distribution (see Appendix E). This model leads to a subspace formed by linear decision boundaries. Therefore, each region includes the observations for a given class.

In order to perform the classification with each of the five classifiers, a 10-fold cross validation is carried out. Each 10-fold cross validation is iterated 10 times for statistical validity purposes. Therefore, the accuracy is calculated as the average accuracy over the ten iterations of the 10-fold

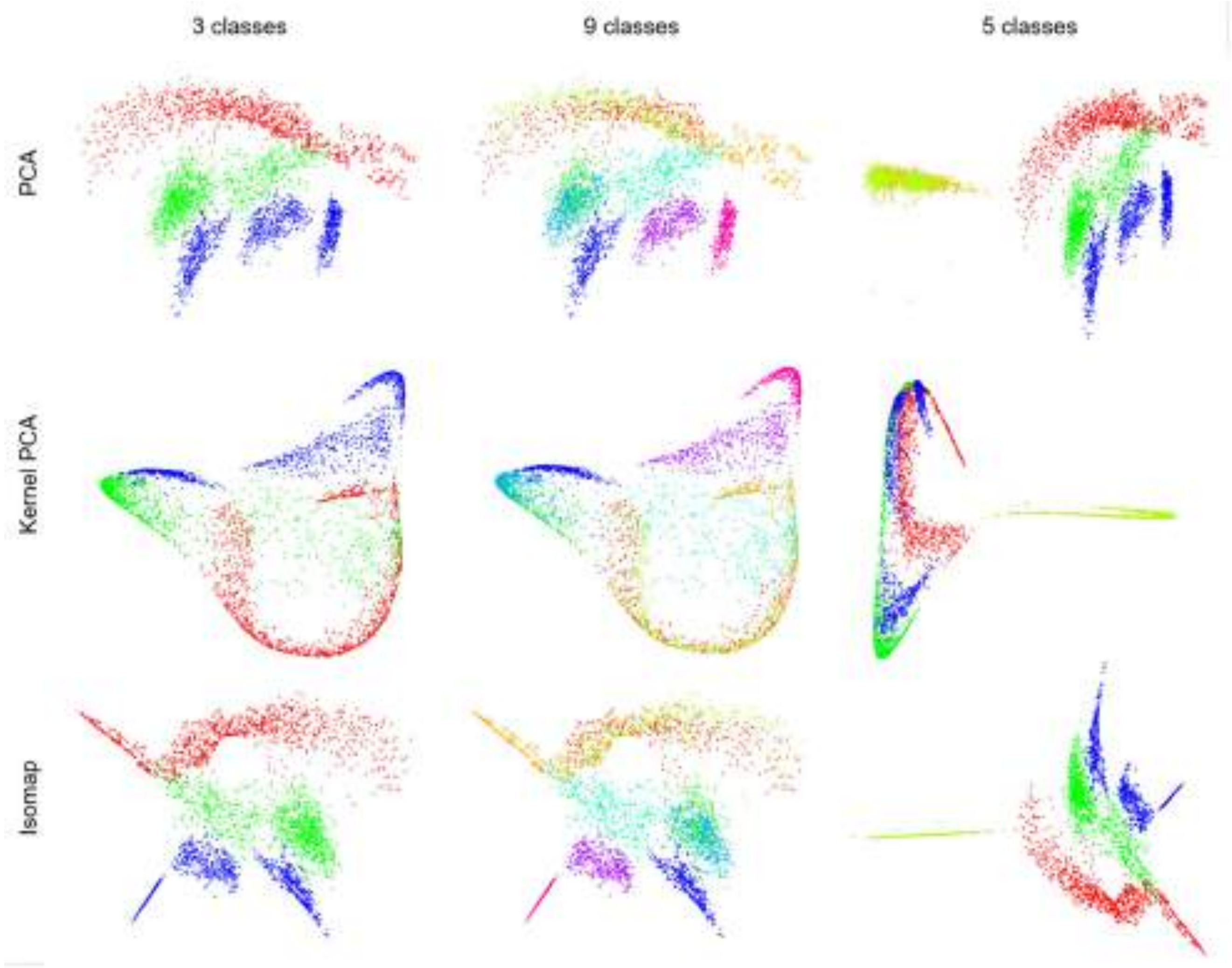

FIGURE 11. **2D dimensionality reduction comparison for multiple techniques and datasets. The rows show the following techniques: PCA, Kernel PCA and Isomap. The columns represent the three datasets used during the work. For comparison with t-SNE, the low-dimensionality spaces in the first, second and third column are equivalent to Figs. 4, 5 and 9, respectively.**

TABLE 1. **Fitness function for several datasets and dimensionality reduction techniques.**

	3 classes	9 classes	5 classes
PCA	1.476	2.653	4.184
Kernel PCA	1.620	3.124	2.778
Isomap	1.508	2.810	4.300
t-SNE	5.234	6.727	4.862

cross validation. This procedure avoids outliers due to a non representative sample choice of the training set in the classifiers. Each iteration of the 10-fold cross validation is randomised by shuffling the rows of the matrices **X** (6D space classification) and **Y** (2D space classification). Concerning the configuration parameters for the classifiers: k-NN classifier considers $k = 10$ neighbors. SVM classifier uses $({N_c}^2 - N_c)/2$ binary learners, i.e., a one-versus-one strategy. The kernel function is linear, which means that a linear boundary separates the classes. For the Naive Bayes classifier, the probabilities according to Bayes rule are distributed following a Gaussian distribution centered on a feature average value given a class. It uses a one-versus-one strategy, providing the same binary classifier number than in SVM. Finally, the bootstrap aggregation classifier is formed by 100 independent decision tree classifiers. Each decision tree includes on average 63% of the observations, which are randomly chosen from the original dataset.

Table 2 shows the classification accuracy for these five classifiers and three datasets. The accuracy is defined as the number of predicted scenarios that matches the true class over the total number of predicted scenarios for each class, and the considered accuracy is the average for all iterations. For a given classification technique and dataset (columns in Table 2), t-SNE generally obtains the best accuracy compared with PCA, Kernel PCA and Isomap. This fact implies that t-SNE exploits in a better way the discriminative aspects of each scenario. Although the accuracy for some datasets

TABLE 2. Classification accuracy (%) by using several classifiers for several datasets and dimensionality reduction techniques.

	k-NN			SVM			Naive Bayes			Bagging			LDA		
Classes / Technique	{3}	{9}	{5}	{3}	{9}	{5}	{3}	{9}	{5}	{3}	{9}	{5}	{3}	{9}	{5}
PCA	97.55	76.86	84.11	94.25	75.76	78.48	92.72	74.56	73.11	97.40	75.24	83.27	91.09	71.22	73.37
Kernel PCA	93.57	71.90	75.08	86.84	66.05	50.45	72.79	64.56	58.84	93.85	70.77	73.92	72.66	62.11	53.43
Isomap	97.70	76.22	83.38	96.63	75.85	76.71	95.35	74.99	72.25	97.43	74.96	82.74	95.50	73.64	72.76
t-SNE	99.85	81.24	84.00	99.85	79.13	82.04	99.85	75.18	82.06	99.94	80.07	83.23	99.85	75.66	81.03
Original 6D Space	99.94	88.06	87.16	99.88	86.84	82.31	97.36	83.28	80.73	99.94	90.17	88.28	99.88	84.57	81.68

is almost identical, note that the cluster visualization in the low-dimensional space throughout the work is more straightforward in t-SNE. This fact is supported by the proposed fitness function in eqs. (20) and (21), and Table 1.

As a final comparison, the classification accuracy of the original 6D space is shown in Table 2. Since no information is lost due to the application of a DR technique, the expected accuracy should be larger than cases where DR is applied. However, if DR works properly over the dataset, the classification accuracy with DR should be close to the classification accuracy without DR. Particularly, t-SNE for 3 classes dataset obtains similar accuracies than 6D space. This implies that t-SNE preserves the information from the 6D space into the two-dimensional space. For 9 and 5 classes datasets, t-SNE obtains a misclassification due to DR of 8.4% and 2.3% in average, respectively. In exchange for slightly decreasing classification accuracy, the space complexity decreases from 6D to 2D. An unique case is found for the Naive Bayes classifier, where t-SNE gets better classification accuracies than 6D space for 3 and 5 classes datasets. This is explained by the fact that Naive Bayes assumes independence between the communication channel parameters (see Appendix D). This is not meet in the 6D space and it induces classification errors. However, the large separation achieved by t-SNE in 2D (see Figs. 4 and 9) increases the classification accuracy. Finally, it should be remarked that the misclassification between the 6D space and PCA, Kernel PCA and Isomap is larger than in t-SNE, which implies increased information losses in the DR.

This section has demonstrated by three different experiments (visualization in Fig. 11, fitness function in Table 1 and accuracy in Table 2) that t-SNE provides the best performance compared to other state-of-the-art dimensionality reduction techniques.

VI. GENERATION OF SCENARIOS

In our previous works [29], [30], [53]–[55], we have applied post-processing techniques in order to modify several signals in anechoic and reverberation chambers. For example, a time-domain signal acquired in the semi-anechoic and semi-reverberation chamber can be modified to emulate several environments [29], [30]. These works illustrate that it is possible to recreate different types of communication scenarios from measurements acquired in the chambers. Now, the combination of post-processing techniques and clustering with DR techniques allows the generation and comparison of new communication environments.

In Section IV, it was explained that the anechoic scenario behaves similarly as the rooftop and auditorium scenarios due to similar PDP shapes. The main differences between both and what keeps them apart, are the distances between TX-RX antennas and the acquisition frequency. On the one hand, the time of arrival is affected by the TX-RX distance, which is 160 cm for the anechoic case and 800 cm the distance for the rooftop and auditorium. Therefore, for a propagation speed c, the time of arrival is 5.33 ns and 26.66 ns respectively (see Fig. 10). On the other hand, the attenuation is affected, again, by the TX-RX distance and the acquisition frequency (25.875 GHz in the anechoic dataset and 60.48 GHz in the rooftop and auditorium). Since the distance and the frequency are higher in real scenarios, it is logical to find higher path losses in the rooftop and auditorium in Fig. 10.

Once the theoretical basis is set, we are able to apply a certain delay and attenuation to the anechoic dataset to obtain a modified version as close as possible to the rooftop and auditorium scenarios. In order to do this, we apply in the frequency domain an attenuation factor to the anechoic dataset such that the average path loss is equal to the average path loss in the rooftop and auditorium, i.e., -93 dB. This attenuation factor is directly applied to the scattering parameters acquired in the CFR. In the time domain, 21.33 ns delay is applied in the anechoic dataset, corresponding to the time difference between the time of arrival of both datasets. This value is also the time that a signal needs to travel the distance difference between scenarios, i.e., 640 cm. Once these changes have been implemented, t-SNE is executed with the original datasets together with the anechoic modified version. The results, presented in Fig. 12, show the formation of a large cluster in the upper left corner. This cluster is formed by the anechoic, rooftop and auditorium datapoints, confirming that the modified anechoic datapoints have joined the real scenarios. The fact that t-SNE cannot separate those three scenarios proves that measurements taken in controlled scenarios can recreate measurements from real scenarios when post-processing techniques are applied.

To confirm this statement from another perspective, a Variational AutoEncoder (VAE) [18] is applied as classifier

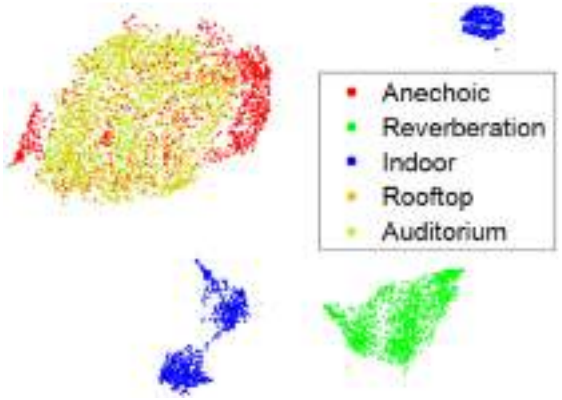

FIGURE 12. Clustering of the modified anechoic, reverberation, indoor, rooftop and auditorium scenarios. Learning rate and perplexity are fixed to 650 and 400.

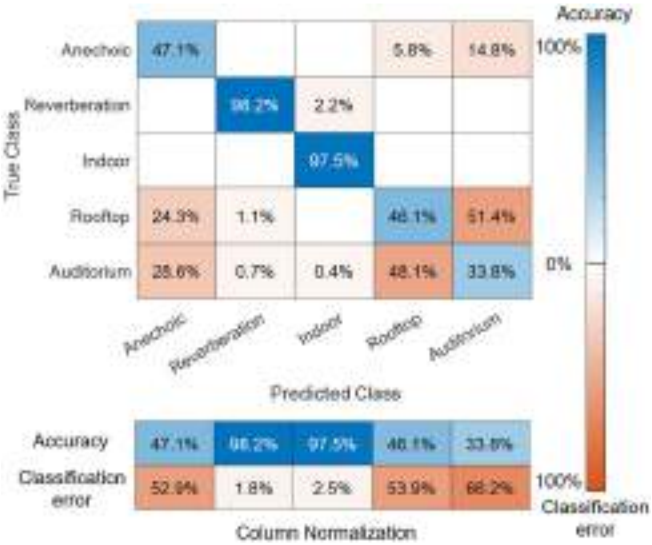

FIGURE 13. Classification of communication scenarios by using a Variational AutoEncoder.

to the parameters that constitute the communication channel. VAEs are composed by two neural networks, encoder and decoder, respectively. On the one hand, the encoder decreases the dimensionality of the inputs into a latent space. On the other hand, the decoder learns how to reconstruct the inputs from the latent space. Therefore, VAEs can be proposed for two different purposes: classification [56]–[58] and generation [59]–[61]. For classification purposes, the Variational AutoEncoder minimizes the reconstruction error for each class given the latent space. For generation purposes, the encoder provides a set of latent space parameters that characterizes the scenario, and the decoder generates an estimation $\hat{\mathbf{x}}_i$, which should be similar to the original input $\mathbf{x}_i$. In this section, the VAE is set as a classifier that assigns one of the five possible classes to each vector $\mathbf{x}_i$. Half of the data from each dataset is chosen to train the VAE, 25% for validation and 25% for test. Therefore, 545 datapoints from each class are the input for the training process and 272 datapoints are for validation and test purposes. Fig. 13 shows the classification accuracy of the communication scenarios for the test data once the VAE is trained. As discussed above, indoor and reverberation scenarios are well predicted with accuracy values above 97.5%. However, the classification of anechoic, rooftop and auditorium scenarios shows poor results with accuracies below 47.1%. The average combined accuracy of these three scenarios is 44.24%. Considering that the classification of the reverberation and indoor cases is good, a random classification between these three scenarios would imply a 33% accuracy, not far from the accuracy obtained with the VAE. Results in Fig. 13 also confirm that the VAE is not able to optimally separate the modified anechoic environment from the rooftop and auditorium environments. Therefore, the use of post-processing techniques to recreate real scenarios from anechoic measurements is satisfactory. As future research, we intend to emulate communication scenarios by using the VAEs generator function. Together with the time-gating technique, we expect it to be a powerful generation tool. This fact, together with the use of generative models and deep reinforcement learning, opens up new possibilities for the generation of future mobile communication scenarios as Vehicle-to-Vehicle, UAV-to-UAV, Ship-to-Ship or High Speed Train-to-High Speed Train.

VII. CONCLUSION

This work presents a deep analysis of the t-SNE technique to cluster several communication channel scenarios. t-SNE is a well-known technique in the AI and machine learning fields. However, this technique has not been widely exploited in the telecommunication field.

Six channel features have been extracted from 5089 measurements of five types of communication scenarios: (i) anechoic, (ii) reverberation, (iii) indoor, (iv) rooftop and (v) auditorium. A deep study on the configuration parameters (learning rate and perplexity) has been performed for the six-dimensional space formed by the communication channel features. For fitting configuration values, t-SNE exhibits outstanding performance in the ability to separate communication channel scenarios. Moreover, it has been seen how t-SNE is able to cluster at multiple sublevels, performing a deep clustering. The case shown in Section IV separates the scenario itself and the azimuth and roll angles into subclasses, reaching three-levels depth. In fact, Section V has proved the best performance of t-SNE as DR technique compared with other techniques of the state-of-the-art. Future research work includes the comparison of t-SNE performance with others non-linear techniques which preserve the data local structure, e.g., Uniform Manifold Approximation and Projection (UMAP).

Finally, we have modified, by applying suitable post-processing techniques, one of the controlled scenarios in order to recreate another of the real scenarios. The modification of the delay and attenuation of a dataset formed by an anechoic scenario has led to a scenario with similar propagation conditions. The application of the t-SNE technique as a clustering algorithm and a VAE as a classifier has proved that the modified version of the anechoic scenario is confused with the real scenarios. This fact demonstrates that the modification of communication scenarios with post-processing techniques is feasible to recreate new communication environments.

As stated in Section V, although VAEs are used for classification in this work, they have a much bigger potential as generative models once the probability distribution of known scenarios is well modeled. Therefore, future work will include the generation of new scenarios based on the knowledge acquired by the VAEs through the clustering and classification analysis. The generation of new communication scenarios seems fundamental from a technology perspective due to the exponential growth of the users and devices in the world. New mobile communication paradigms need a deep understanding of the propagation environments where the communications are held. The clustering technique for communication scenarios and the recreation of scenarios shown throughout this work arise as powerful tools to simplify the understanding of a telecommunication deployment in terms of the channels through which communications can take place for future mobile communications. These tools are able to provide a simple visualization of channel similarities which at first sight may appear to be different and thus increase the knowledge of the communication channels in a telecommunication deployment.

APPENDIX A
PRINCIPAL COMPONENT ANALYSIS

Let $\mathbf{X} \in \mathbb{R}^{N\times F}$ be the matrix that represents the high-dimensional space dataset, where $\mathbf{X}$ is centralized as $\mathbf{X} \rightarrow \mathbf{X} - \bar{\mathbf{X}}$. The single value decomposition (SVD) of $\mathbf{X}$ is:

$$\mathbf{X} = \mathbf{P}\Delta\mathbf{Q}^T \tag{22}$$

where $\mathbf{P} \in \mathbb{R}^{N\times L}$ contains the eigenvectors of the matrix $\mathbf{X}\mathbf{X}^T$ and $\mathbf{Q} \in \mathbb{R}^{F\times L}$ contains the eigenvectors of $\mathbf{X}^{\mathrm{T}}\mathbf{X}$. $\boldsymbol{\Delta}^2 = \boldsymbol{\Lambda}$, where $\boldsymbol{\Lambda}$ is the diagonal matrix that includes the eigenvalues of the matrix $\mathbf{X}\mathbf{X}^T$ (and $\mathbf{X}^T\mathbf{X}$). Note that L is the rank of $\mathbf{X}$. We can define $\mathbf{F} \in \mathbb{R}^{N\times L}$ as:

$$\mathbf{F} = \mathbf{P}\boldsymbol{\Delta} \tag{23}$$

where the rows of $\mathbf{F}$ include the principal components into the low-dimensional space, also called projections. By combining eqs. (22) and (23), it can be seen that

$$\mathbf{F} = \mathbf{X}\mathbf{Q} \tag{24}$$

Therefore, $\mathbf{Q}$ can be denoted as the projection matrix, since it provides the linear combination needed to obtain the low-dimensional space.

For the Kernel PCA technique, we have used a Laplacian transformation as kernel function:

$$\mathbf{K}(\mathbf{x}_i, \mathbf{x}_j) = \exp\left(-\gamma \left\|\mathbf{x}_i - \mathbf{x}_j\right\|\right) \tag{25}$$

$\mathbf{K} \in \mathbb{R}^{N\times N}$ is the kernel matrix and $\mathbf{x}_i$, $\mathbf{x}_j \in \mathbb{R}^{1\times F}$ are the rows i and j of $\mathbf{X}$. By using this kernel matrix $\mathbf{K}$ together with the kernel trick [46], it is possible to obtain the low-dimensional space of KPCA without an explicit mapping. This problem could by solved by applying the Laplacian transformation $\mathbf{X} \rightarrow \Phi(\mathbf{X})$, followed by standard PCA [eqs. (22), (23) and (24)]. However, this is not usually performed for computational reasons.

APPENDIX B
ISOMAP

Let $\mathbf{X} \in \mathbb{R}^{N\times F}$ be the high-dimensional space of our dataset and $\mathbf{x}_i$, $\mathbf{x}_j \in \mathbb{R}^{1\times F}$ be the rows of $\mathbf{X}$. In the first step, through k-NN, a graph G is created by connecting the node i with the node j if it is one of its closest K neighbors. In the second step, the Dijkstra's algorithm is applied to G in order to find the shortest path between observations i and j. These distances are saved in the matrix $\mathbf{D} \in \mathbb{R}^{N\times N}$. In the last step, the low-dimensional space is created by applying multidimensional scaling (MDS) [62] to the graph distances $\mathbf{D}$.

APPENDIX C
SUPPORT VECTOR MACHINE

SVM binary classifier is a supervised learning algorithm which looks for a hyperplane that optimally separates a dataset into two classes. The hyperplane is also intended to maximize the margin between both classes. Two types of classes can take place: separable classes, where the margin between the hyperplanes is not crossed by any observations, and inseparable classes, where the hyperplane can not separate both classes and a penalty is applied for the observations which cross the boundary. Under the inseparable classes assumption, the hyperplane function is given by:

$$f(\mathbf{x}_i) = \mathbf{x}_i\boldsymbol{\beta} + b = 0 \tag{26}$$

where $\boldsymbol{\beta} \in \mathbb{R}^{F\times 1}$ and $b \in \mathbb{R}^1$ are the coefficients that define a hyperplane orthogonal vector and a bias term, respectively.

The optimal hyperplane is found by minimizing:

$$\min \left(\frac{1}{2}\|\boldsymbol{\beta}\|^2 + \sum_i \kappa_i\right) \tag{27a}$$

$$\text{subject to: } y_i f(\mathbf{x}_i) \geq 1 - \kappa_i \tag{27b}$$

$$\kappa_i \geq 0 \tag{27c}$$

where κ_i is a penalty score applied to the i-th observation if it crosses the boundary decision defined by the hyperplane. $y_i = \{1, -1\}$ stands for the class of the observation.

This optimization problem is typically solved with the method of Lagrange multipliers. The solution defines the coefficients of $\boldsymbol{\beta}$ and the bias term b, which form the boundary decision.

APPENDIX D
NAIVE BAYES

Naive Bayes is a supervised learning algorithm that learns the data distribution through a training set. This algorithm takes advantage of the Bayes rule and uses density estimation in a certain test set. The key point for this classifier is to assume the features (communication channel parameters) to be independent given a class. Therefore, in a binary learner classifier, $2F$ independent predictors are created during the training process. Let $Zj|k \sim \mathcal{N}(\mu_{j|k}, {\sigma_{j|k}}^2)$ for $j = 1, \dots, F$ and $k = 1, -1$ be a normal distribution with $\mu_{j|k}$ mean and $\sigma_{j|k}$ standard deviation for feature j and class k. Mean and standard deviation are calculated as:

$$\mu_{j|k} = \frac{1}{N_k} \sum_{\{i:y_i=k\}} x_{ij} \tag{28}$$

$$\sigma_{j|k} = \sqrt{\frac{1}{N_k - 1} \sum_{\{i:y_i=k\}} \left(x_{ij} - \mu_{j|k}\right)^2} \tag{29}$$

where N_k indicates the number of observations of the class k in the training set, and $\sum_{\{i:y_i=k\}}$ is the summation only including the observations that belong to the class k.

Once the predictors are trained, the probability that an observation i belongs to the class k given F features is calculated as:

$$\widehat{P}(Y_i = k|Z_1, \dots, Z_F) = \frac{P_{prior}(Y_i = k) \prod_{j=1}^{F} P\left(Z_j|Y_i = k\right)}{\sum_{k=1} P_{prior}(Y_i = k) \prod_{j=1}^{F} P\left(Z_j|Y_i = k\right)} \tag{30}$$

$P_{prior}(Y_i = k)$ is the prior probability that an observation i belongs to the class k, calculated as the density of each class in the training set. Note that $\prod_{j=1}^{F} P(Z_j|Y_i = k)$ can be performed due to the feature independence assumption.

Finally, the i-th observation is assigned to the class that generates the maximum *a posteriori* probability.

APPENDIX E
LINEAR DISCRIMINANT ANALYSIS

Discriminant Analysis is a supervised learning algorithm that divides a feature space into regions. LDA implies that these regions are linearly separated, where each region includes an observation set which belongs to a certain class k. Mathematically, the observation $\mathbf{x}_i$ is assigned to the class k according to the classifier y_i, where $\widehat{y_i}$ estimation is calculated as:

$$\widehat{y_i} = \underset{y_i=1,\dots,K}{\arg\min} \sum_{k=1,k\neq y_i}^{K} \widehat{P}(k|\mathbf{x}_i) \tag{31}$$

$\widehat{P}(k|\mathbf{x}_i)$ is the estimated probability of belonging to class k, given the observation $\mathbf{x}_i$. It is calculated as:

$$\widehat{P}(k|\mathbf{x}_i) = \frac{P(k)}{P(\mathbf{x}_i)} P(\mathbf{x}_i|k) \tag{32}$$

where $P(\mathbf{x}_i|k)$ is a $F-$dimensional multivariate normal density function for the observation $\mathbf{x}_i$ given the class k:

$$P(\mathbf{x}_i|k) = \frac{1}{\sqrt{(2\pi)^F |\xi|}} e^{\left(-\frac{1}{2}(\mathbf{x}_i-\mu_k)\xi^{-1}(\mathbf{x}_i-\mu_k)^T\right)} \tag{33}$$

$\xi \in \mathbb{R}^{F\times F}$ is the covariance matrix of $\mathbf{X}$ and $\mu_k \in \mathbb{R}^{1\times F}$ is the mean for each feature given the class k. Both are computed through the training dataset. Finally, $P(k)$ is the class distribution on the training set and $P(\mathbf{x}_i)$ is a normalization factor calculated as $\sum_k P(\mathbf{x}_i|k) \cdot P(k)$.

The i-th observation is assigned to the class k that minimizes the expected cost in eq. (31).

ACKNOWLEDGMENT

The authors would like to thank the Fraunhofer-Heinrich-Hertz-Institut for acquiring and sharing the data associated to the rooftop and auditorium communication scenarios, the NextG Channel Model Alliance for creating a space to share public databases of propagation measurements, José Francisco Cortés-Gómez for the graphical support, Carmelo García-García for his help in the measurements acquisition, and Sohrab Vafa, Pablo Padilla and Francisco Luna-Valero for their valuable comments.

REFERENCES

[1] C.-X. Wang, J. Bian, J. Sun, W. Zhang, and M. Zhang, “A survey of 5G channel measurements and models,” *IEEE Commun. Surveys Tuts.*, vol. 20, no. 4, pp. 3142–3168, 4th Quart., 2018.

[2] M. Z. Chowdhury, M. Shahjalal, S. Ahmed, and Y. M. Jang, “6G wireless communication systems: Applications, requirements, technologies, challenges, and research directions,” *IEEE Open J. Commun. Soc.*, vol. 1, pp. 957–975, 2020.

[3] “Ericsson Mobility Report.” Ericsson. Nov. 2020. [Online]. Available: https://www.ericsson.com/en/mobility-report

[4] P. Popovski *et al.*, “Wireless access for ultra-reliable low-latency communication: Principles and building blocks,” *IEEE Netw.*, vol. 32, no. 2, pp. 16–23, Mar./Apr. 2018.

[5] H. Elayan, O. Amin, B. Shihada, R. M. Shubair, and M.-S. Alouini, “Terahertz band: The last piece of RF spectrum puzzle for communication systems,” *IEEE Open J. Commun. Soc.*, vol. 1, pp. 1–32, 2020.

[6] J. Liu, M. Sheng, L. Liu, and J. Li, “Network densification in 5G: From the short-range communications perspective,” *IEEE Commun. Mag.*, vol. 55, no. 12, pp. 96–102, Dec. 2017.

[7] C. R. Storck and F. Duarte-Figueiredo, “A survey of 5G technology evolution, standards, and infrastructure associated with vehicle-to-everything communications by Internet of Vehicles,” *IEEE Access*, vol. 8, pp. 117593–117614, 2020.

[8] M.-A. Lahmeri, M. A. Kishk, and M.-S. Alouini, “Artificial intelligence for UAV-enabled wireless networks: A survey,” *IEEE Open J. Commun. Soc.*, vol. 2, pp. 1015–1040, 2021.

[9] S. Aslam, M. P. Michaelides, and H. Herodotou, “Internet of Ships: A survey on architectures, emerging applications, and challenges,” *IEEE Internet Things J.*, vol. 7, no. 10, pp. 9714–9727, Oct. 2020.

[10] K. Guan *et al.*, “Towards realistic high-speed train channels at 5G millimeter-wave band—Part I: Paradigm, significance analysis, and scenario reconstruction,” *IEEE Trans. Veh. Technol.*, vol. 67, no. 10, pp. 9112–9128, Oct. 2018.

[11] J. Rodríguez-Piñeiro, T. Domínguez-Bolaño, X. Cai, Z. Huang, and X. Yin, “Air-to-ground channel characterization for low-height UAVs in realistic network deployments,” *IEEE Trans. Antennas Propag.*, vol. 69, no. 2, pp. 992–1006, Feb. 2021.

[12] A. Ramírez-Arroyo, P. H. Zapata-Cano, Á. Palomares-Caballero, J. Carmona-Murillo, F. Luna-Valero, and J. F. Valenzuela-Valdés, “Multilayer network optimization for 5G & 6G,” *IEEE Access*, vol. 8, pp. 204295–204308, 2020.

[13] W. Shao and Y. Du, “Microwave imaging by deep learning network: Feasibility and training method,” *IEEE Trans. Antennas Propag.*, vol. 68, no. 7, pp. 5626–5635, Jul. 2020.

[14] K. Xu, L. Wu, X. Ye, and X. Chen, “Deep learning-based inversion methods for solving inverse scattering problems with phaseless data,” *IEEE Trans. Antennas Propag.*, vol. 68, no. 11, pp. 7457–7470, Nov. 2020.

[15] D. R. Prado, J. A. López-Fernández, M. Arrebola, and G. Goussetis, "Support vector regression to accelerate design and crosspolar optimization of shaped-beam reflectarray antennas for space applications," *IEEE Trans. Antennas Propag.*, vol. 67, no. 3, pp. 1659–1668, Mar. 2019.

[16] Z.-M. Liu, C. Zhang, and P. S. Yu, "Direction-of-arrival estimation based on deep neural networks with robustness to array imperfections," *IEEE Trans. Antennas Propag.*, vol. 66, no. 12, pp. 7315–7327, Dec. 2018.

[17] A. Krizhevsky, I. Sutskever, and G. E. Hinton "ImageNet classification with deep convolutional neural networks," *Commun. ACM*, vol. 60, no. 6, pp. 84–90, 2017.

[18] D. Kingma and M. Welling, "Auto-encoding variational bayes," in *Proc. 2nd Int. Conf. Learn. Represent.*, Banff, AB, Canada, 2014, pp. 1–14.

[19] Y. Li and H. Wu, "A clustering method based on K-means algorithm," *Phys. Procedia*, vol. 25, pp. 1104–1109, Apr. 2012.

[20] W.-T. Wang, Y.-L. Wu, C.-Y. Tang, and M.-K. Hor, "Adaptive density-based spatial clustering of applications with noise (DBSCAN) according to data," in *Proc. Int. Conf. Mach. Learn. Cybern. (ICMLC)*, Guangzhou, China, 2015, pp. 445–451.

[21] I. T. Jolliffe and J. Cadima, "Principal component analysis: A review and recent developments," *Phylos. Trans. Roy. Soc. A, Math. Phys. Eng. Sci.*, vol. 374, Apr. 2016, Art. no. 20150202.

[22] J. B. Tenenbaum, V. de Silva, and J. C. Langford, "A global geometric framework for nonlinear dimensionality reduction," *Science*, vol. 290, pp. 2319–2323, Dec. 2000.

[23] L. van der Maaten and G. Hinton, "Visualizing data using t-SNE," *J. Mach. Learn. Res.*, vol. 9, no. 86, pp. 2579–2605, 2008.

[24] E. Becht *et al.*, "Dimensionality reduction for visualizing single-cell data using UMAP," *Nat. Biotechnol.*, vol. 37, pp. 38–44, Jan. 2019.

[25] T. Zhou, Y. Wang, C.-X. Wang, S. Salous, L. Liu, and C. Tao, "Multi-feature fusion based recognition and relevance analysis of propagation scenes for high-speed railway channels," *IEEE Trans. Veh. Technol.*, vol. 69, no. 8, pp. 8107–8118, Aug. 2020.

[26] J. Zhang, L. Liu, Y. Fan, L. Zhuang, T. Zhou, and Z. Piao, "Wireless channel propagation scenarios identification: A perspective of machine learning," *IEEE Access*, vol. 8, pp. 47797–47806, 2020.

[27] J. Thrane, D. Zibar, and H. L. Christiansen, "Model-aided deep learning method for path loss prediction in mobile communication systems at 2.6 GHz," *IEEE Access*, vol. 8, pp. 7925–7936, 2020.

[28] M. Yang *et al.*, "Machine-learning-based scenario identification using channel characteristics in intelligent vehicular communications," *IEEE Trans. Intell. Transp. Syst.*, vol. 22, no. 7, pp. 3961–3974, Jul. 2021.

[29] A. Ramírez-Arroyo, A. Alex-Amor, C. García-García, Á. Palomares-Caballero, P. Padilla, and J. F. Valenzuela-Valdés, "Time-gating technique for recreating complex scenarios in 5G systems," *IEEE Access*, vol. 8, pp. 183583–183595, 2020.

[30] A. Ramírez-Arroyo, A. Alex-Amor, C. García-García, Á. Palomares-Caballero, P. Padilla, and J. F. Valenzuela-Valdés, "Time-gating technique to emulate new scenarios," in *Proc. 15th Eur. Conf. Antennas Propag. (EuCAP)*, Dusseldorf, Germany, 2021, pp. 1–5.

[31] C. Segura-Gómez, A. Palomares-Caballero, A. Alex-Amor, J. Valenzuela-Valdés, and P. Padilla, "Modular design for a stacked SIW antenna array at Ka-band," *IEEE Access*, vol. 8, pp. 158568–158578, 2020.

[32] B. Hammu-Mohamed, Á. Palomares-Caballero, C. Segura-Gómez, F. G. Ruiz, and P. Padilla, "SIW cavity-backed antenna array based on double slots for mmWave communications," *Appl. Sci.*, vol. 11, no. 11, p. 4824, 2021.

[33] Q. Chen, O. Zetterstrom, E. Pucci, A. Palomares-Caballero, P. Padilla, and O. Quevedo-Teruel, "Glide-symmetric holey leaky-wave antenna with low dispersion for 60 GHz point-to-point communications," *IEEE Trans. Antennas Propag.*, vol. 68, no. 3, pp. 1925–1936, Mar. 2020.

[34] Á. Palomares-Caballero, A. Alex-Amor, J. Valenzuela-Valdés, and P. Padilla, "Millimeter-wave 3-D-printed antenna array based on gap-waveguide technology and split E-plane waveguide," *IEEE Trans. Antennas Propag.*, vol. 69, no. 1, pp. 164–172, Jan. 2021.

[35] *NR; User Equipment (UE) Radio Transmission and Reception; Part 2: Range 2 Standalone (Release 17)*, 3GPP Standard TS38.101-2 V17.1.0, 2021.

[36] *5G mmWave Channel Model Alliance Database Institute_Roof*, Fraunhofer Heinrich-Hertz-Institut, Berlin, Germany, 2021. [Online]. Available: https://5gmm.nist.gov

[37] 5G mmWave Channel Model Alliance Database, *Institute_Auditorium_20190813_Indoor_Using_TG_Channel_Sounder_60GHz*, Fraunhofer Heinrich-Hertz-Institut, Berlin, Germany, 2021. [Online]. Available: https://5gmm.nist.gov/

[38] H. Hashemi, "The indoor radio propagation channel," *Proc. IEEE*, vol. 81, no. 7, pp. 943–968, Jul. 1993.

[39] J. Cheng, H. Liu, F. Wang, H. Li, and C. Zhu, "Silhouette analysis for human action recognition based on supervised temporal t-SNE and incremental learning," *IEEE Trans. Image Process.*, vol. 24, pp. 3203–3217, 2015.

[40] J. Liu, Q. Li, H. Yang, Y. Han, S. Jiang, and W. Chen, "Sequence fault diagnosis for PEMFC water management subsystem using deep learning with t-SNE," *IEEE Access*, vol. 7, pp. 92009–92019, 2019.

[41] L. van der Maaten, "Accelerating t-SNE using tree-based algorithms," *J. Mach. Learn. Res.*, vol. 15, no. 1, pp. 3221–3245, 2014.

[42] N. Pezzotti, B. P. F. Lelieveldt, L. V. D. Maaten, T. Höllt, E. Eisemann, and A. Vilanova, "Approximated and user steerable tSNE for progressive visual analytics," *IEEE Trans. Vis. Comput. Graphics*, vol. 23, no. 7, pp. 1739–1752, Jul. 2017.

[43] A. Ramírez-Arroyo, L. García, A. Alex-Amor, and J. F. Valenzuela-Valdés, "An introduction to dimensionality reduction for propagation measurements," in *Proc. 16th Eur. Conf. Antennas Propag. (EuCAP)*, 2022, pp. 1–5.

[44] "Multipath propagation and parameterization of its characteristics," ITU, Geneva, Switzerland, ITU-Recommendation P.1407-7, 2019.

[45] T. L. Marzetta, E. G. Larsson, H. Yang, and H. Q. Ngo, *Fundamentals of Massive MIMO*. Cambridge, U.K.: Cambridge Univ. Press, 2018.

[46] B. Schölkopf, A. Smola, and K. R. Müller, "Kernel principal component analysis," in *Proc. Int. Conf. Artif. Neural Netw. (ICANN)*, Heidelberg, Germany, 1997, pp. 1–6.

[47] T. Hofmann, B. Schölkopf, and A. J. Smola, "Kernel methods in machine learning," *Ann. Stat.*, vol. 36, no. 3, pp. 1171–1220, 2008.

[48] P. Cunningham and S. J. Delany, "K-nearest neighbour classifiers—A tutorial," *ACM Comput. Surv.*, vol. 54, no. 6, pp. 1–25, 2021.

[49] S. Salcedo-Sanz, J. L. Rojo-ÁĄlvarez, M. Martínez-Ramón, and G. Camps-Valls, "Support vector machines in engineering: An overview," *WIREs Data Min. Knowl. Discov.*, vol. 4, no. 3, pp. 234–267, 2014.

[50] A. McCallum and K. Nigam, "A comparison of event models for naive bayes text classification," in *Proc. Workshop Learn. Text Categorization*, 1998, pp. 1–8.

[51] L. Breiman, "Bagging predictors," *Mach. Learn.*, vol. 24, pp. 123–140, Aug. 1996.

[52] T. Hastie, R. Tibshirani, and J. H. Friedman, *The Elements of Statistical Learning: Data Mining, Inference, and Prediction*. New York, NY, USA: Springer, 2009.

[53] J. F. Valenzuela-Valdes, A. M. Martinez-Gonzalez, and D. A. Sanchez-Hernandez, "Emulation of MIMO nonisotropic fading environments with reverberation chambers," *IEEE Antennas Wireless Propag. Lett.*, vol. 7, pp. 325–328, 2008.

[54] J. D. Sanchez-Heredia, M. Gruden, J. F. Valenzuela-Valdes, and D. A. Sanchez-Hernandez, "Sample-selection method for arbitrary fading emulation using mode-stirred chambers," *IEEE Antennas Wireless Propag. Lett.*, vol. 9, pp. 409–412, 2010.

[55] J. D. Sanchez-Heredia, J. F. Valenzuela-Valdes, A. M. Martinez-Gonzalez, and D. A. Sanchez-Hernandez, "Emulation of MIMO Rician-fading environments with mode-stirred reverberation chambers," *IEEE Trans. Antennas Propag.*, vol. 59, no. 2, pp. 654–660, Feb. 2011.

[56] A. M. Abdelhameed and M. Bayoumi, "Semi-supervised EEG signals classification system for epileptic seizure detection," *IEEE Signal Process. Lett.*, vol. 26, no. 12, pp. 1922–1926, Dec. 2019.

[57] X. Chen, Y. Sun, M. Zhang, and D. Peng, "Evolving deep convolutional variational autoencoders for image classification," *IEEE Trans. Evol. Comput.*, vol. 25, no. 5, pp. 815–829, Oct. 2021.

[58] J. Klys, J. Snell, and R. Zemel, "Learning latent subspaces in variational autoencoders," in *Advances in Neural Information Processing Systems 31 (NeurIPS)*. Red Hook, NY, USA: Curran, 2018, pp. 1–15.

[59] P. Cristovao, H. Nakada, Y. Tanimura, and H. Asoh, "Generating in-between images through learned latent space representation using variational autoencoders," *IEEE Access*, vol. 8, pp. 149456–149467, 2020.

[60] J. Bao, D. Chen, F. Wen, H. Li, and G. Hua, "CVAE-GAN: Fine-grained image generation through asymmetric training," in *Proc. IEEE Int. Conf. Comput. Vis. (ICCV)*, Venice, Italy, 2017, pp. 2764–2773.

[61] A. Hawkins-Hooker, F. Depardieu, S. Baur, G. Couairon, A. Chen, and D. Bikard, "Generating functional protein variants with variational autoencoders," *PLoS Comput. Biol.*, vol. 7, no. 2, 2021, Art. no. e1008736.

[62] S. L. France and J. D. Carroll, "Two-way multidimensional scaling: A review," *IEEE Trans. Syst., Man, Cybern. C, Appl. Rev.*, vol. 41, no. 5, pp. 644–661, Sep. 2011.

ALEJANDRO RAMÍREZ-ARROYO was born in Córdoba, Spain, in 1997. He received the B.Sc. and M.Sc. degrees (Hons.) in telecommunication engineering from the University of Granada, Spain, in 2019 and 2021, respectively, where he is currently pursuing the Ph.D. degree with the Smart Wireless Applications and Technologies Research Group, Department of Signal Theory, Telematics, and Communications. His current research interests include optimization techniques, propagation channels, and machine learning models for 5G networks.

LUZ GARCÍA received the M.Sc. degree in telecommunication engineering from the Polytechnic University of Madrid, Madrid, Spain, in 2000, and the Ph.D. degree from the University of Granada, Granada, Spain, in 2008. After being a Support Engineer for Communication Networks with Ericsson, Madrid, for five years, she joined the European Research Project with the University of Granada. She has been with the Department of Signal Theory, Telematics and Communications, University of Granada since 2005, where she was an Assistant Professor and is currently an Associate Professor. Her research interests include signal processing, pattern recognition, and machine learning in the fields of speech and geophysics.

ANTONIO ALEX-AMOR received the B.Sc. degree in telecommunication engineering from the Universidad de Granada, Granada, Spain, in 2016, and the M.Sc. and Ph.D. degrees in telecommunication engineering from the Universidad Politécnica de Madrid (UPM) in 2018 and 2021, respectively. From 2016 to 2021, he was with the Radiation Group, Signal, Systems and Radiocommunications Department, UPM. From 2018 to 2019, he was with the Department of Language and Computer Science, Universidad de Málaga. From 2020 to 2021, he was with the Departamento de Teoría de la Señal, Telemática y Telecomunicaciones, Universidad de Granada. He is currently an Assistant Professor with Universidad CEU San Pablo, Madrid, Spain. He was a visiting student with the KTH Royal Institute of Technology in 2019 for four months and conducted a Short Postdoctoral Mission with the Universidade de Lisboa, Lisbon, Portugal, in 2021. His current research interests include the analysis and design of metamaterial structures and antennas, and wireless communication systems. In 2020, he received the Best Electromagnetics Paper Award at the 14th European Conference on Antennas and Propagation 2020. He is also an Active Science Communicator in blogs and social media.

JUAN F. VALENZUELA-VALDÉS was born in Marbella, Spain. He received the Telecommunication Engineering degree from the Universidad de Málaga, Málaga, Spain, in 2003, and the Ph.D. degree from the Universidad Politécnica de Cartagena, Cartagena, Spain, in 2008. He joined the Department of Information Technologies and Communications, Universidad Politécnica de Cartagena in 2004. In 2007, he joined EMITE Ing., Murcia, Spain, as the Head of Research. In 2011, he joined the Universidad de Extremadura, Mérida, Spain, and in 2015, he joined the Universidad de Granada, Granada, Spain, where he is currently an Associate Professor. He is also the Head of the SWAT Research Group, University of Granada and the Co-Head of the Singular Laboratory of Electromagnetic Characterization of Microwave and Millimeter Devices and Antennas. His publication record composed of more than 100 publications, including 50 Journal Citation Reports indexed articles and seven book chapters. He holds several national and international patents. His current research interests include wireless communications, radio-frequency devices, antennas, and propagation. He received several prizes, including a National Prize to the Best Ph.D. in mobile communications by Vodafone.

2.3 Characterization of Ultra-Wide Band Propagation Channels

2.3.1 Joint Direction-of-Arrival and Time-of-Arrival Estimation with Ultra-wideband Elliptical Arrays

The characterization of the Direction-of-Arrival and Time-of-Arrival in communication channels is fundamental to understanding and making optimal use of the channel. This paper proposes the joint estimation of the DoA and ToA through phase-mode expansions and the use of nearly frequency-invariant filters for elliptical arrays at mmWave frequencies. The proposed method generalizes the state-of-the-art approximation performed with circular arrays providing new degrees of freedom: (i) semi-major axis aperture, (ii) eccentricity, and (iii) angle of rotation, which allow the approximation of pseudo-random array patterns by a superposition of elliptical arrays. The method is validated on the basis of simulations and measurements in anechoic chambers.

THIS IS A POSTPRINT VERSION OF THE PAPER:

A. Ramírez-Arroyo, A. Alex-Amor, P. Padilla and J. F. Valenzuela-Valdés, “Joint Direction-of-Arrival and Time-of-Arrival Estimation with Ultra-wideband Elliptical Arrays,” *IEEE Transactions on Wireless Communications*, 2023.

- Journal Impact Factor (JIF) in JCR 2022: 10.4
- Category: ENGINEERING, ELECTRICAL & ELECTRONIC. JIF Rank: 16/275 (D1).
- Category: TELECOMMUNICATIONS. JIF Rank: 6/88 (D1).

Disclaimer:
This work has been published in IEEE Transactions on Wireless Communications. DOI: 10.1109/TWC.2023.3268949

Joint Direction-of-Arrival and Time-of-Arrival Estimation with Ultra-wideband Elliptical Arrays

Alejandro Ramírez-Arroyo, Antonio Alex-Amor, Pablo Padilla, and Juan F. Valenzuela-Valdés

***Abstract*—This paper presents a general technique for the joint Direction-of-Arrival (DoA) and Time-of-Arrival (ToA) estimation in multipath environments. The proposed ultra-wideband technique is based on phase-mode expansions and the use of nearly frequency-invariant elliptical arrays. New possibilities open with the present approach, as not only elliptical, but also circular and linear (highly flattened) arrays can be considered with the same implementation. Systematic selection/rejection of signals-of-interest/signals-not-of-interest in smart wireless environments is possible, unlike with previous approaches based on circular arrays. Concentric elliptical arrays of many sizes and eccentricities can be jointly considered, with the subsequent improvement that entails in DoA and ToA detection. This leads to the realization of pseudo-random array patterns; namely, quasi-arbitrary geometries created from the superposition of multiple elliptical arrays. Some simulation and experimental tests (measurements in an anechoic chamber) are carried out for several frequency bands to check the correct performance of the method. The method is proven to give accurate estimations in all tested scenarios, and to be robust against noise and position uncertainty in sensor placement.**

***Index Terms*—Direction-of-arrival (DoA), time-of-arrival (ToA), elliptical arrays, propagation, wireless channels, broadband communications.**

I. INTRODUCTION

DIRECTION-of-arrival (DoA) estimation has been one of the main lines of research in the field of wireless communications in the last decades [1]–[6]. Knowing the position (and time) at which a wave arrives is essential in mobile networks [7], [8], vehicular networks [9], [10], MIMO systems [11], tracking and navigation systems such as GPS [12]–[14], radar [15], [16], sonar [17], and many other wireless systems. Even more exotic applications such as failure detection in electronic components are starting to use DoA techniques as a novel alternative [18], [19]. In fact, new communication environments are materializing these days; namely, vehicle-to-everything (V2X), ship-to-ship (S2S), high speed train-to-train or UAV-to-UAV [20]–[24]. Thus, a great deal of effort is being put into characterizing their most important parameters and *key performance indicators*, direction of arrival (DoA) and time of arrival (ToA) among them, with the aim of improving bandwidth, latency, data rate, power consumption and reliability in present and future communication systems [25]–[31].

Conventional DoA and ToA estimation methods, i.e., delay-and-sum beamforming [32] or the more classical implementations of MUSIC [1], ESPRIT [33] and maximum-likehood [34] algorithms, were originally developed to work under a narrowband assumption. Naturally, their use is not adequate for today's broadband communication channels such as the high-frequency millimeter-wave links (26, 38, and 60 GHz) dedicated to 5G wireless networks. Thus, many broadband DoA methods have emerged in recent years to overcome the limitations of narrowband approaches [35]. Among the well-established broadband methods, we can find narrowband decomposition (a wideband channel is decomposed into small bins that are treated independently with narrowband techniques) [36] or the use of tapped-delay filters with adaptive coefficients [37]. Although they are simple solutions, both demand high computational resources since the number of required filters increases as the considered bandwidth does.

Alternatively, *frequency-independent* beamformers (FIB) [38], [39] were formulated to reduce the number of required filters in a fixed bandwidth, and thus the computational demands. Originally, FIB focused on the use of linear arrays. Then, FIB-based algorithms were smartly combined with the omnidirectional characteristics that uniform circular arrays offer to develop efficient methods for DoA and ToA estimation [40]. The outcomes of this original work were promising, as the spatial response of the filter was equalized with a remarkably reduced number of weight coefficients. Nonetheless, some important aspects of the method were later clarified in [41]. Subsequently, [40] was rapidly extended in different ways. For instance, in [42], it was demonstrated that the bandwidth of FIB circular arrays can be broadened and the precision on the DoA estimation improved by employing multiple concentric arrays instead of a single one. In [43], [44], multipath components and spherical 3-D propagation were also considered. Moreover, the approach was directly applied to the millimeter-wave frequency range.

In this document, we propose a generalization of the method successfully developed in [40]–[44] for the joint estimation of the direction-of-arrival and time-of-arrival in multipath environments. Those previous works were based on the use of wideband circular arrays. Here, we demonstrate that *wideband elliptical arrays* can extent the capabilities of the joint estimation in many forms:

This work was supported in part by the Spanish Government under Project PID2020-112545RB-C54, and Project TED2021-129938B-I00; in part by "Junta de Andalucía" under Project A-TIC-608-UGR20, Project P18.RT.4830, and Project PYC20-RE-012-UGR; and in part by the Predoctoral Grant FPU19/01251. (*Corresponding author: Alejandro Ramírez-Arroyo.*)

Alejandro Ramírez-Arroyo, Pablo Padilla and Juan F. Valenzuela-Valdés are with the Department of Signal Theory, Telematics and Communications, Universidad de Granada (UGR), 18071 Granada, Spain (e-mail: alera@ugr.es; pablopadilla@ugr.es; juanvalenzuela@ugr.es).

Antonio Alex-Amor is with the Department of Information Technologies, Universidad San Pablo-CEU, CEU Universities, Campus Montepríncipe, 28668 Boadilla del Monte (Madrid), Spain (e-mail: antonio.alexamor@ceu.es).

(i) Circular geometries are subcases contained by more general elliptical shapes. Thus, we present one of the few methods reported in the literature that is able to deal with circular and elliptical arrays in a single stroke. Moreover, linear arrays can be approximated and analyzed as highly-flattened elliptical arrays.

(ii) Elliptical arrays present new degrees of freedom compared to circular arrays. Particularly, the ellipse radius is not fixed, which provides many configurations for several arrangements based on different eccentricities and rotation angles.

(iii) Highly flattened elliptical arrays (and so, linear arrays) show an excellent directivity along the direction of its semi-major axis, as well as remarkable estimation performance for many elevation angles in this direction. Thus, the present methodology allows for the efficient and systematic selection of signals-of-interest (SOI) and rejection of signals-not-of-interest (SNOI) in smart radio environments, unlike conventional FIB-DoA methods implemented with circular arrays.

(iv) Concentric elliptical arrays (CEAs) can be analyzed with the present formulation. As reported by previous works, the use of concentric arrays is expected to significantly improve the accuracy in the joint estimation as well as the bandwidth [42]. Furthermore, the use of concentric elliptical arrays can lead to the implementation of *pseudo-random* grids, a fact that will be exploited in Section III.D for DoA and ToA estimation. These pseudorandom grids have the advantage of not being limited to a certain number of sensor arrangements.

(v) The method is proven to be robust to noise and position uncertainty in DoA and ToA detection. In addition, its computational demands are comparable to state-of-art approaches.

The document is organized as follows. Section II presents the theoretical framework for the joint DoA and ToA estimation with ultra-wideband elliptical arrays. Furthermore, we discuss on the advantages and limitations of the method. Section III presents some numerical simulation results in order to validate the present approach. Section IV presents some experimental results extracted from the measurement facilities at the University of Granada. Finally, conclusions are drawn in Section V.

II. THEORETICAL FRAMEWORK

Let us consider the situation illustrated in Fig. 1. An incident spherical wave l, described by the *unknown* azimuth and elevation angles ϕ_l and θ_l, respectively, impinges on the P sensors ($p = 0, 1, ..., P-1$) that conform the elliptical array. The elliptical array is defined by its eccentricity $\xi = \sqrt{1 - b^2/a^2}$, which relates the semi-major (a) and semi-minor (b) axes, respectively. The frequency response at the center of the elliptical array is given by

$$H_l(f) = \kappa_l \, \mathrm{e}^{\mathrm{j}2\pi f \tau_l} \,, \tag{1}$$

where κ_l is the attenuation for path/wave l for any given path loss exponent, and τ_l stands for the propagation delay for path/wave l. Both parameters are to be determined.

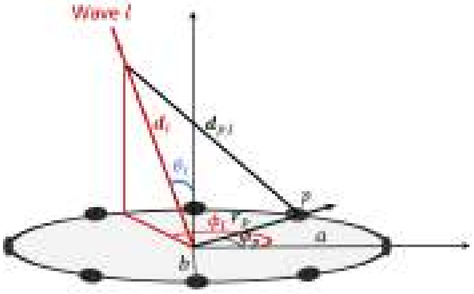

Fig. 1. Scheme illustrating the different parameters involved in the joint estimation of DoA and ToA with a single elliptical array.

The frequency response at the p-th sensor, $H_{p,l}(f)$, will include a phase shift with respect to the frequency response estimated at the center of the array, $H_l(f)$. By applying trigonometric relations, we arrive to

$$H_{p,l}(f) = \left(\sqrt{\frac{d_\ell}{d_{p,\ell}}}\right)^{\gamma} H_\ell(f) \, \mathrm{e}^{\mathrm{j}2\pi f \Delta d_{p,\ell}/c} \,, \tag{2}$$

where c is the speed of light, the term $\left(\sqrt{d_\ell/d_{p,\ell}}\right)^{\gamma}$ accounts for amplitude attenuation given a path loss exponent γ between the center of the array and the p-th sensor, and

$$\Delta d_{p,l} = d_l - d_{p,l} \,, \tag{3}$$

with

$$d_{p,l} = ||\mathbf{d}_l - \mathbf{r}_p|| = \sqrt{d_l^2 + r_p^2 - 2 d_l r_p \sin(\theta_l) \cos(\phi_l - \phi_p)} \,. \tag{4}$$

In the former expression, d_l is the distance from the center of the elliptical array to the source point, r_p is the distance from the center of the array to sensor p, ϕ_p is the azimuth angle associated to sensor p (see Fig. 1), both given by

$$r_p = \sqrt{x_p^2 + y_p^2} \,, \tag{5}$$

$$\phi_p = \arctan\left(\frac{y_p}{x_p}\right) . \tag{6}$$

Additionally, the Taylor series for $\Delta d_{p,l}$ allows to expand this term as [44]

$$\Delta d_{p,l} \approx r_p \sin(\theta_l) \cos(\phi_l - \phi_p) \,. \tag{7}$$

Thus, (2) can be expressed as

$$H_{p,l}(f) = \left(\sqrt{\frac{d_\ell}{d_{p,\ell}}}\right)^{\gamma} H_l(f) \, \mathrm{e}^{\mathrm{j}2\pi f r_p \sin(\theta_l) \cos(\phi_l - \phi_p)/c} \,. \tag{8}$$

Considering that the source l is located far from the elliptical array, the term $d_l/d_{p,l} \approx 1$, so (8) can be simplified to

$$H_{p,l}(f) = H_l(f) \, \mathrm{e}^{\mathrm{j}2\pi f r_p \sin(\theta_l) \cos(\phi_l - \phi_p)/c} \,. \tag{9}$$

Now, we particularize the study to the case $\theta_l = 90^\circ$; namely, where the incident plane coincides with the plane where the elliptical array is located. Thus, (9) reduces to

$$H_{p,l}(f) = H_l(f) \, \mathrm{e}^{\mathrm{j}2\pi f r_p \cos(\phi_l - \phi_p)/c} \,. \tag{10}$$

This approximation is fundamental in order to develop further steps of the method. Although it may seem prohibitive, this approach was demonstrated to work over a wide range of elevation angles different from $\theta_l = 90^{\text{o}}$ [44].

The Jacobi-Anger identity [45] allows us to expand the former expression and *decouple* the frequency-dependent and phase-dependent components in two different terms as

$$H_{p,l}(f) = H_l(f) \sum_{n=-\infty}^{\infty} \mathrm{j}^n J_{n,p}\left(\frac{2\pi f r_p}{c}\right) \mathrm{e}^{\mathrm{j}n(\phi_l - \phi_p)}, \quad (11)$$

where $J_{n,p}(\cdot)$ is the Bessel function of the first kind of order n associated to sensor p. At a first glance, some differences can be observed with respect to the cases shown in [41], [42], [44] for circular arrays. When considering elliptical arrays, the frequency-dependent component $[J_{n,p}(\cdot)]$ varies for each sensor p. This is due to the fact that the distance between the center of the array and the position of sensor p is not constant $[r_p = r_p(\phi_p) \neq r]$, unlike in circular arrays where this distance is the same for all sensors ($r_p = r$).

The azimuth angle ϕ_l can be estimated by applying a phase-mode expansion, $H_{m,l}(f)$, [41], [42], [44] to the former expression that includes basis functions of the form $\mathrm{e}^{\mathrm{j}m\phi_p}$ (m being the integer order of the phase-mode) and a frequency-dependent filter $W_{m,p}(f)$, leading to

$$\begin{aligned} H_{m,l}(f) &= \frac{1}{P} \sum_{p=0}^{P-1} H_{p,\ell}(f)\, \mathrm{e}^{\mathrm{j}m\phi_p}\, W_{m,p}(f) \\ &= \frac{1}{P} H_\ell(f) \sum_{p=0}^{P-1} \sum_{n=-\infty}^{+\infty} \mathrm{j}^n J_{n,p}\left(2\pi f \frac{r_p}{c}\right) W_{m,p}(f) \\ &\qquad \times\, e^{\mathrm{j}n\phi_\ell}\, e^{\mathrm{j}(m-n)\phi_p}\,. \end{aligned} \quad (12)$$

The infinite sum in n can be split in two different addends: the term $n = m$ and a series for all $n \neq m$. This allows to rewrite (12) as

$$\begin{aligned} H_{m,l}(f) &= \frac{1}{P} H_\ell(f) \sum_{p=0}^{P-1} W_{m,p}(f) \\ &\times \Bigg[\mathrm{j}^m J_{m,p}\left(2\pi f \frac{r_p}{c}\right) \mathrm{e}^{\mathrm{j}m\phi_\ell} \\ &\quad + \sum_{\substack{n=-\infty \\ n\neq m}}^{+\infty} \mathrm{j}^n J_{n,p}\left(2\pi f \frac{r_p}{c}\right) \mathrm{e}^{\mathrm{j}n\phi_\ell}\, \mathrm{e}^{\mathrm{j}(m-n)\phi_p}\Bigg]. \end{aligned} \quad (13)$$

Previous works [41], [42], [44] focused on circular arrays took advantage of the independence of the Bessel functions with respect to p $[J_{n,p}(\cdot) = J_n(\cdot)]$ and the orthogonality relations of the sum $\sum_{p=0}^{P-1} \mathrm{e}^{\mathrm{j}(m-n)\phi_p}/P$ to cancel out the infinite series ($\forall n \neq m$) in eq. (13). However, this is not exactly the situation for elliptical arrays. Thus, some approximations have to be considered in order to proceed. Under the assumption of low eccentricity ξ levels (ellipses that are not too flattened, $\xi \ll 1$), the former discussion still applies since $r_p \approx r$ (constant radius in average) and the sensors in the elliptical array are quasi-uniformly distributed ($\phi_p \approx 2\pi p/P$). As a consequence, $J_{n,p}(2\pi f r_p/c) \approx J_n(2\pi f r/c)$ can be cleared out from the sum in p and the orthogonality relation $\sum_{p=0}^{P-1} \mathrm{e}^{\mathrm{j}(m-n)\phi_p}/P = 0$,$\forall n \neq m$, remains valid. Thus, the last double sum in eq. (13) is approximately zero under low-eccentricity assumption; namely,

$$\begin{aligned} &\frac{1}{P} \sum_{p=0}^{P-1} W_{m,p}(f) \sum_{\substack{n=-\infty \\ n\neq m}}^{+\infty} \mathrm{j}^n J_{n,p}\left(2\pi f \frac{r_p}{c}\right) \mathrm{e}^{\mathrm{j}n\phi_\ell}\, \mathrm{e}^{\mathrm{j}(m-n)\phi_p} \\ &\overset{\xi\ll1}{\approx} W_m(f) \sum_{\substack{n=-\infty \\ n\neq m}}^{+\infty} \mathrm{j}^n J_n\left(2\pi f \frac{r}{c}\right) \mathrm{e}^{\mathrm{j}n\phi_\ell} \sum_{p=0}^{P-1} \frac{\mathrm{e}^{\mathrm{j}(m-n)\phi_p}}{P} = 0\,. \end{aligned} \quad (14)$$

Thus, eq. (13) is simplified to

$$H_{m,l}(f) \approx \frac{\mathrm{j}^m}{P} H_\ell(f)\, \mathrm{e}^{\mathrm{j}m\phi_\ell} \sum_{p=0}^{P-1} J_{m,p}\left(2\pi f \frac{r_p}{c}\right) W_{m,p}(f). \quad (15)$$

The approximation taken above, although originally derived for low eccentricities, will be demonstrated in Sections III and IV to be applicable to a wide range of elliptical arrays, even those that reach eccentricity values of $\xi = 0.99$, as long as the number of considered sensors is large. The reason is that, even for high eccentricities, the main contribution of the transformation is given by the phase mode $n = m$, while the rest of the contributions (sum $\forall n \neq m$) is normally negligible [see eq.(13)]. Nonetheless, an increment of the artifact levels is expected as the eccentricity increases, thus degrading the joint DoA and ToA estimation in some angular regions. In practice, P should be selected so the sensor separation is less than $\lambda/2$, where λ stands for the wavelength.

Then, we can reduce (13) to

$$H_{m,l}(f) \approx H_\ell(f)\, \mathrm{e}^{\mathrm{j}m\phi_\ell}\,, \quad (16)$$

if we consider the filter $W_{m,p}(f)$ to be

$$W_{m,p}(f) = \frac{1}{\mathrm{j}^m\, J_{m,p}\left(2\pi f \frac{r_p}{c}\right)}\,. \quad (17)$$

Alternatively, we can choose $W_{m,p}(f)$ as

$$W_{m,p}(f) = \frac{2}{\mathrm{j}^m\left[J_{m,p}(2\pi f r_p/c) - \mathrm{j}\, J'_{m,p}(2\pi f r_p/c)\right]}\,, \quad (18)$$

since it was proven in [44] to give more accurate results in realistic scenarios where elevation angles different from $\theta_l = 90^{\text{o}}$ were involved. Additionally, eq. (17) involves deep nulls for some frequencies f, a fact that limits the channel bandwidth. The situation is different for the filter depicted in eq. (18), whose performance is similar to that in eq. (17) but operates over a noticeably larger bandwidth. A detailed discussion on the filter choice can be found in [43]. In eq. (18), $J'_{m,p}(\cdot)$ is the first derivative of the Bessel function of order n related to sensor p.

The array response for the m-th phase mode is calculated by taking into account the contribution of the L incident waves as

$$H_m(f) = \sum_{l=1}^{L} H_{m,\ell}(f) \approx \sum_{l=1}^{L} H_\ell(f)\, \mathrm{e}^{\mathrm{j}m\phi_\ell}\,, \quad (19)$$

which admits a matrix-form representation $\mathbf{H}(m,f)$. Finally, the joint DoA and ToA estimation is extracted by computing the 2-D fast Fourier transform (FFT) of $\mathbf{H}(m,f)$,

$$\widetilde{\mathbf{H}}(\phi,\tau)=\mathrm{FFT}\{\mathbf{H}(m,f)\}, \tag{20}$$

which includes a general representation of the wireless channel properties for all considered angular and time steps. Note that DoA and ToA resolution of $\widetilde{\mathbf{H}}(\phi,\tau)$ is given by the number of phase modes and frequency samples in $\mathbf{H}(m,f)$. Concretely, DoA resolution is calculated as $360°/M$, where M is the number of considered phase modes. Thus, higher DoA resolution requires of a larger number of phase modes. ToA resolution is calculated as $1/B$, where B is the bandwidth of the channel. The maximum observable time in the estimation is $(K-1)/B$, which is determined by B and the number of frequency samples K. Therefore, channel bandwidths belonging to the range of ultra-wideband technologies are required to achieve good spatial resolution in the estimation since there exists a trade-off between the spatial resolution and B.

The maximum number of considered phase modes M [eq. (15)] is restricted by the denominator in $W_{m,p}(f)$ [eq. (18)]. This denominator may introduce numerical errors as it approaches zero. In order to avoid numerical instabilities, M must be chosen such that

$$\mathrm{j}^m\left[J_{m,p}(2\pi f r_p/c)-\mathrm{j}\,J'_{m,p}(2\pi f r_p/c)\right]\not\approx 0 \quad \forall m. \tag{21}$$

To fulfill the previous condition, we know that there is a number of phase modes, namely $|M_{lim}|$, above which the Bessel function $J_{m,p}(\cdot)$ and its derivative tend to zero [41]. Therefore, stability can be guaranteed if M is chosen below $|M_{lim}|$ [43]. This limit value is dependent on the argument of $J_{m,p}(\cdot)$ and $J'_{m,p}(\cdot)$. The larger the argument $(2\pi f r_p/c)$, the larger $|M_{lim}|$. Consequently, i) high frequencies provide higher resolution in DoA estimation, and ii) $|M_{lim}|$ is defined by the sensor p whose distance r_p is the smallest for a given frequency f. This distance turns out to be the semi-minor axis in elliptical arrays. Throughout Sections III and IV, it is shown that eccentricity values up to 0.99 allow the method to work properly even when $|M_{lim}|$ is reduced.

A. Improving the Efficiency of the Method

It can be noted from eqs. (17), (18) that each sensor p that conforms the elliptical array has a different filter $W_{m,p}(f)$. Considering M phase modes in the computation, elliptical arrays will require of $M\times P$ filters for the DoA and ToA estimation. This situation is different in circular arrays, where all the sensors share the same filter for the m-th phase mode. Thus, only $M\times 1$ filters are needed in the case of considering circular arrays. This causes that the joint estimation with ultra-wideband elliptical arrays is less computationally efficient than with ultra-wideband circular arrays, despite the multiple benefits that elliptical arrays offer (generality, selectivity, pseudo-random grids, etc.) compared to circular ones. Nonetheless, we can exploit the symmetries of elliptical geometries and Bessel functions to improve the efficiency of the proposed method.

Let us name as α_p an azimuth angle that is contained in the first quadrant of the elliptical array. Angles of the form $180^{\mathrm{o}}-\alpha_p$ (second quadrant) , $180^{\mathrm{o}}+\alpha_p$ (third quadrant), and $360^{\mathrm{o}}-\alpha_p$ (fourth quadrant) have associated the same value of r_p. Therefore, the number of required filters in the joint estimation can be reduced to $M\times[P/4+1]$ by exploiting the symmetries of the ellipse. Thus, when P is large, the required number of filters is approximately reduced by a factor of 4 compared to the raw processing.

We can further reduce the complexity of the problem by considering the symmetry of Bessel functions. Concretely, we can take advantage of the following expression

$$J_{-m,p}(\chi_p)=(-1)^m J_{m,p}(\chi_p)\,, \tag{22}$$

that relates negative and positive integer orders m. Thus, the number of filters would reduce to $[M/2+1]\times[P/4+1]$. For large values of M and P, the number of required filters is asymptotically reduced from $M\times P$ to $M/2\times P/4$, that is, by a factor of 8.

Additionally, the use of a *single average filter* $\overline{W}_m(f)$ can provide good DoA and ToA estimations when low- and medium-eccentricity elliptical arrays are involved. The average filter is given by replacing all r_p values in eqs. (17)-(18) by r, computed as the average between the semi-major and semi-minor axes of the ellipse. Note that in the case of considering a single average filter, the number of required filters is reduced to $M\times 1$, as in the case of circular arrays. Therefore, a good approximation for elliptical arrays with low and medium eccentricities can be obtained, notably reducing the computational complexity of the problem. The single-average-filter approach is expected to give accurate results as long as the elliptical array is not highly flattened. In practice, this approach has been found to be valid up to $\xi\lesssim 0.7$. Finally, note that the time required in the total propagation channel characterization process is limited by the measurement acquisition. The previous fact is true for setups based on virtual arrays. Due to the high number of sensors required to fulfill the spatial Nyquist theorem, phase-mode expansion for DoA and ToA characterization makes use of these virtual arrays [41], [43], [44]. Therefore, the measurement process takes orders of magnitude longer than the time required to apply the estimation method. Thus, the global time for taking measurements and applying the method ends up being similar in both circular and elliptical arrays.

B. Rotated Elliptical Arrays

A simple modification can be applied to the present formulation for the convenient use of rotated elliptical arrays in DoA and ToA estimation. Actually, this will serve as the basis for the analysis of advanced scenarios (concentric arrays, pseudo-random grids) in next sections. Considering that the elliptical array is azimuthally rotated counterclockwise by an angle α [see Fig. 2(a)], the values of x_p and y_p in eq. (5) should be simply replaced by

$$\begin{aligned} x_p &\rightarrow x_p\cos\alpha+y_p\sin\alpha \\ y_p &\rightarrow x_p\sin\alpha-y_p\cos\alpha \end{aligned}\;. \tag{23}$$

Alternatively, it could be convenient to work with the elliptic coordinate system, formed by the radial coordinate $\rho\in[0,\infty)$

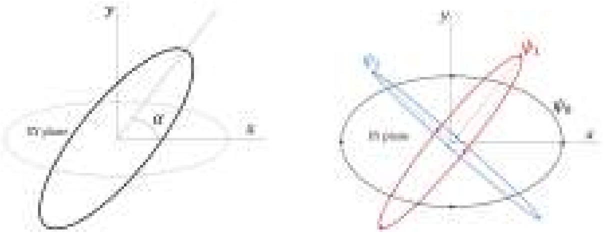

(a) (b)

Fig. 2. Representation of a (a) single rotated elliptical array and (b) three concentric elliptical arrays. All the arrays are lying in the XY plane.

and the angular coordinate $\eta \in [0, 2\pi)$, when positioning the sensors that conform the rotated elliptical array. In that case, the p-th sensor will be located at

$$\begin{aligned} x_p &= a\cos\eta_p\cos\alpha - b\sin\eta_p\sin\alpha \\ y_p &= a\cos\eta_p\sin\alpha + b\sin\eta_p\cos\alpha \end{aligned} \quad , \tag{24}$$

where a and b are the semi-major and semi-minor axes of the elliptical array, respectively. Both parameters are related through the eccentricity value ξ. Note that a uniform angular placement for the sensors in elliptical coordinates, η, does not necessarily imply a uniform angular placement in polar coordinates, ϕ_p.

C. Concentric Elliptical Arrays

As an additional step, the joint estimation of the direction-of-arrival and time of arrival can be generalized to the case where multiple concentric elliptical arrays are considered [see Fig. 2(b)]. As pointed out in previous works [42], the fact of including several concentric arrays is expected to increase the accuracy in the estimation, as well as the frequency response of the entire array if the geometry of the concentric elliptical array is appropriately selected. This is because the response of the entire array is a combination of the individual arrays that compose it [42]. Additionally, the use of ultra-wideband concentric elliptical arrays will lead to advanced functionalities in DoA and ToA detection. These advanced functionalities will be deeply explored in Sections III and IV of the present manuscript.

Let us consider Ψ concentric elliptical arrays ($\psi = 0, 1, ..., \Psi - 1$) lying in the same plane (XY plane), each of them constituted by P sensors. The phase-mode expansion for the ψ-th elliptical array will be now

$$\begin{aligned} H_{m,l,\psi}(f) &= \frac{1}{P}\sum_{p=0}^{P-1} H_{p,l,\psi}(f)\, \mathrm{e}^{\mathrm{j}m\phi_{p,\psi}}\, W_{m,p,\psi}(f) \\ &= \frac{1}{P} H_\ell(f) \sum_{p=0}^{P-1} \sum_{n=-\infty}^{+\infty} \mathrm{j}^n J_{m,p,\psi}\left(2\pi f \frac{r_{p,\psi}}{c}\right) \\ &\qquad \times\; W_{m,p,\psi}(f)\, e^{\mathrm{j}n\phi_\ell}\, e^{\mathrm{j}(m-n)\phi_{p,\psi}} \,. \end{aligned} \tag{25}$$

Thus, the phase-mode expansion of the whole system, $H_{m,l}(f)$, will be of the form

$$H_{m,l}(f) = \frac{1}{\Psi}\sum_{\psi=0}^{\Psi-1} H_{m,l,\psi}(f) \approx H_\ell(f)\, e^{\mathrm{j}m\phi_\ell} \,, \tag{26}$$

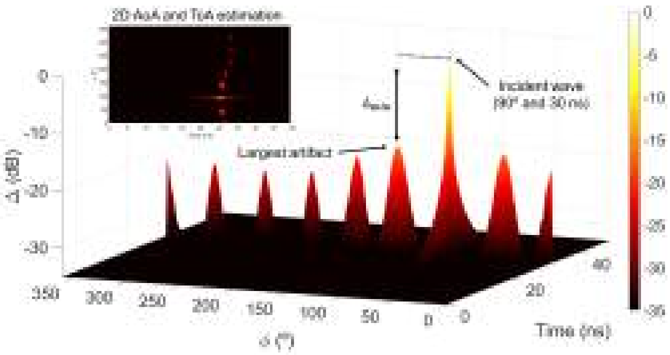

Fig. 3. DoA and ToA estimation example for a single incident wave at $\phi_l = 90°$ and $\tau_l = 30$ ns. A 2D representation of the angular-temporal domain is shown in the upper left corner.

which is simply the average of the individual phase-mode contributions of each elliptical array. In fact, notice that the resulting expression for $H_{m,l}(f)$ in eq. (26) is identical to eq. (16), despite the computation of the filters $W_{m,p,\psi}(f)$ is different in this case for each elliptical array.

Naturally, the computational complexity increases when considering concentric arrays. Now, the system is formed by $P \times \Psi$ sensors, so the number of required filters for DoA and ToA estimation increases to $M \times P \times \Psi$. Nonetheless, by following the recommendations given in Sec. II.A, the number of filters can be similarly reduced by a factor of 8.

III. SIMULATIONS

This Section shows and discusses some results obtained through the formulation derived in Sec. II for DoA and ToA estimation in ultra-wideband elliptical arrays. Regarding the organization, Sec. III.A analyzes the accuracy of the method for single elliptical arrays and the influence of eccentricity ξ and rotation angle α in the estimation. Sec. III.B introduces concentric elliptical arrays and their benefits compared to single elliptical arrays. Sec. III.C presents the performance of the joint estimation for elevation angles different than 90°. Finally, Sec. III.D explores the use of pseudorandom grids based on concentric elliptical arrays.

In order to validate the estimation for elliptical arrays, it must be ensured that DoA and ToA estimation matches ϕ_l and τ_l for the incident wave, as well as the artifacts (non-desired values expected to be several orders of magnitude below the real path of the incident wave) do not disguise the correct angles and delays. As an example, Fig. 3 shows the joint angular and delay domain of a particular $\widetilde{\mathbf{H}}(\phi, \tau)$, with a single incident wave at $\phi_l = 90°$ and $\tau_l = 30$ ns. Both parameters are correctly estimated. However, some artifacts can be observed. If they were large compared to the real incident wave, they could misled the real path. Thus, we define Δ as the ratio between the correct estimation and the largest artifact in the azimuth and delay domain. The larger the Δ, the better the estimation. Throughout this document, this ratio will be considered as a metric.

A. Single Elliptical Arrays

The main benefits of elliptical arrays compared to circular arrays are the new degrees of freedom related to the sensor position. While in circular arrays we only have the control of the radius r, three different independent parameters can be modified in elliptical arrays: i) semi-major axis a, ii) eccentricity ξ, and iii) rotation angle α. This fact allows for a wide variety of sensor arrangements.

The first simulation aims to determine the influence of the eccentricity on the joint DoA and ToA estimation. For this purpose, four ellipses with $\xi = 0$, 0.7, 0.95 and 0.99 are simulated for an incident azimuth range $\phi_l = [-90°, 90°]$ and $\tau_l = 30$ ns. The frequency band is chosen to be from 28 GHz to 30 GHz ($B = 2$ GHz) for $K = 100$ frequency samples. These frequencies are part of the band n257 defined by the 3rd Generation Partnership Project (3GPP) and are expected to be fundamental in the deployment of 5G New Radio (5G NR) [46]. In order to ensure a proper DoA and ToA estimation, spatial Nyquist theorem must be fulfilled. This implies that the separation between adjacent sensors must be less than half wavelength. In the present work, we have typically assumed a distribution of $P = 720$ sensors per array (angular spacing of 0.5°), ensuring that spatial Nyquist theorem is fulfilled for all sensors. Naturally, the number of sensors could be further reduced from 720, normally at the expense of degrading the performance in the estimation. The considered semi-major axis $a = 0.5$ m and the ellipse is placed with its semi-major axis oriented along the horizontal direction ($\alpha = 0°$). Given the highest frequency $f = 30$ GHz, we can ensure that the largest separation between sensors is 0.437λ for any value of eccentricity. Finally, the elevation incident angle is $\theta_l = 90°$, i.e., matching the plane of the elliptical array sensors.

Fig. 4(a) shows the metric Δ for several azimuth angles ϕ_l and eccentricity values ξ. Δ is constant for the circular array ($\xi = 0$) through the whole azimuth range due to the constant directivity at any given azimuth angle. When the eccentricity increases, the ellipse tends to flatten on the semi-minor axis. Therefore, the directivity of the estimation increases in the direction of the semi-major axis. For $\xi = 0.7$, the estimation is correct in the whole range. For $\xi = 0.95$, $\Delta > 0$ for azimuth values up to ±50°, where the largest artifact begins to mislead the correct incident angle. The same behavior can be found for $\xi = 0.99$, where the estimation is valid up to ±15°. The reasoning behind these results is that for very high eccentricities, the angular response of an elliptical array closely resembles that of a linear array in the direction of the semi-major axis. Therefore, when the incident wave is perpendicular to the semi-major axis of the elliptical array, ambiguity affects the estimation and, consequently, an artifact appears at $\phi_l + 180°$, since the near-zero curvature of the array only exploits half of the angular domain, i.e., 180°. This evolution can be seen as the eccentricity increases and the array flattens out in Fig. 4(a). As previously explained in Fig. 3, Δ value is calculated by taking into account the highest artifact found in the DoA and ToA estimation since ϕ_l can take any value on the entire range, i.e., $\phi_l \in [0°, 360°)$. However, if there were information on a bounded ϕ_l range, it would be possible to discard artifacts outside that range, thus improving the estimation of Δ value if the highest artifact is not part of the considered interval. Note that the formulation derived in Sec. II is valid for circular, elliptical and linear arrays. Although it is not explicitly shown, due to the array symmetry, the estimation is similar in the range $\phi_l = [90°, 270°]$. Also notice that the larger the eccentricity, the lower the number of considered phase modes M, as detailed in Sec. II. The computation time, as shown in the complexity analysis (see Section II.A), is expected to be higher for elliptical arrays. In the circular array case, the DoA and ToA computation time is 7.39 s. For the elliptical arrays with eccentricities 0.7, 0.95 and 0.99, computation times are 98.11 s, 54.06 s and 13.62 s, respectively. These times are obtained as the average for 10 iterations of the method in a laptop with an i7-10750H processor and 16 GB RAM. Table I summarizes the main features of the different geometries. t_B stands for the required time to numerically compute the Bessel functions for the filters $W_{m,p}(f)$ and t_f is the required time to apply $W_{m,p}(f)$ to

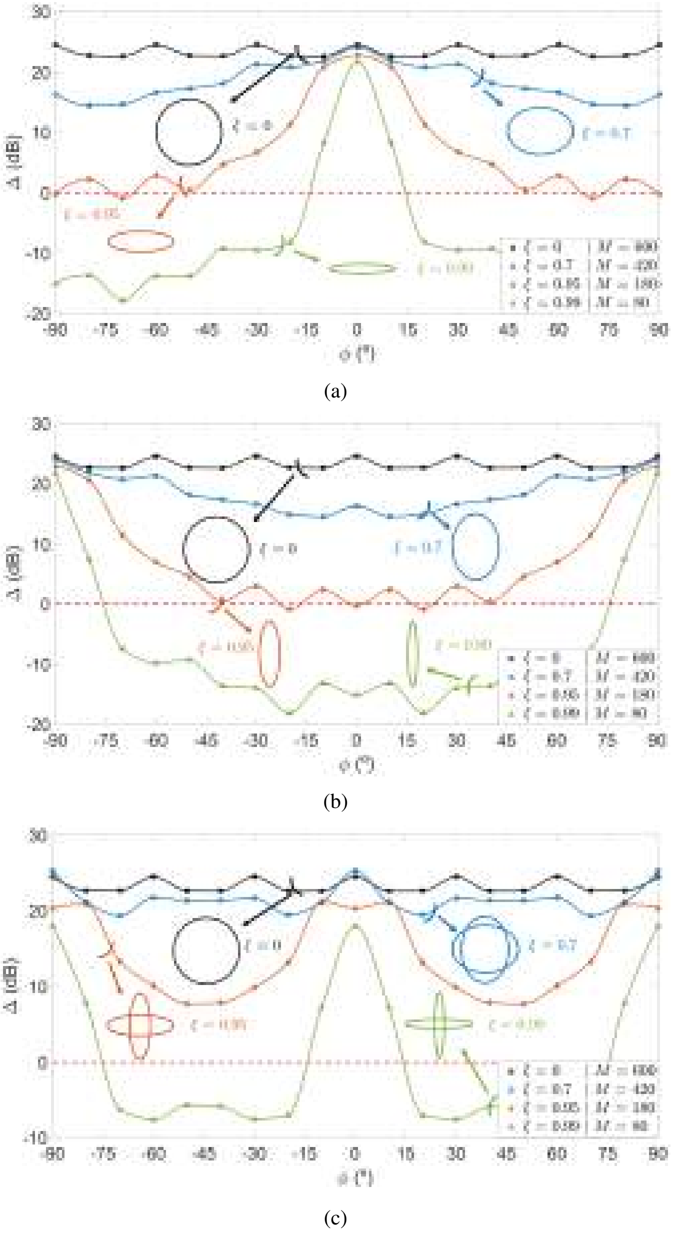

(a)

(b)

(c)

Fig. 4. Metric Δ (dB) for several incident azimuth angles ϕ_l and several eccentricities ξ. a) Single ellipse with $\alpha = 0°$, b) single ellipse with $\alpha = 90°$, and c) two concentric ellipses with $\alpha = 0°$ and $\alpha = 90°$. These geometries show angular selectivity for $\phi_l = 0°$ and $\phi_l = 90°$.

TABLE I
COMPUTATIONAL COMPLEXITY, COMPUTATION TIME, DEGREES OF FREEDOM AND Δ FOR SEVERAL GEOMETRIES

Geometry	Computational complexity	Parameters	t_B(s)	t_f(s)	t_t(s)	Δ(dB)	Degrees of freedom	Pseudorandom patterns	Angular selectivity
Circular	$\mathcal{O}(M\,\Psi)$	$r = 0.5$ m	1.96	5.43	7.39	24.53	1	✗	✗
Elliptical	$\mathcal{O}(PM\,\Psi)$	$a = 0.5$ m, $\alpha = 0°$, $\xi = 0.7$	93.68	4.43	98.11	24.07	3	✓	✓
		$a = 0.5$ m, $\alpha = 0°$, $\xi = 0.95$	52.58	1.48	54.06	22.81			
		$a = 0.5$ m, $\alpha = 0°$, $\xi = 0.99$	13.04	0.58	13.62	21.70			

$H_{p,l}(f)$ and compute the 2-D FFT. t_t is the sum of the two previous times. Despite the longer required time, elliptical arrays provide three degrees of freedom that generalize the circular case and allow the creation of pseudorandom patterns discussed in depth in Section III.D.

At the beginning of this Section, three degrees of freedom related to ellipses were discussed: semi-major axis, eccentricity and rotation angle. As Fig. 4(a) has shown, highly flattened ellipses are angularly selective along direction of the semi-major axis. In order to tune the angular response, Fig. 4(b) analyses the effect of a rotation angle α in the ellipse geometry. Particularly, it includes a rotation angle $\alpha = 90°$ compared to the geometry of Fig. 4(a). The direct consequence is the 90° shift on the azimuth angle estimation. Now, the semi-major axis is located in the vertical axis, providing excellent estimation for very flattened ellipses when the incident angle is nearby ±90°. However, incident angles in the horizontal axis (0° and 180°) get poor estimations if eccentricities are large, contrary to what is observed in Fig. 4(a). Additionally, as it is previously stated, the number of sensors can be reduced at the expense of degrading the estimation performance. In order to show the effect of this reduction, Fig. 5 shows the joint DoA and ToA estimation for an incident wave at $\tau_l = 15$ ns ($d_l = 450$ cm) and $\phi_l = 180°$ in an elliptical array with $a = 0.5$ m, $\alpha = 135°$ and $\xi = 0.7$. Three different numbers of sensors $P = 720, 300$ and 100 are considered. While for $P = 720$, the maximum spacing between sensors remains below $\lambda/2$, for $P = 300$ and 100, these distances becomes 1.048λ and 3.143λ. This causes the artifacts to move from 19.34 dB below the estimation to 13.73 dB and 5.99 dB respectively. Thus, although it is possible to perform the estimation even for adjacent sensor distances larger than $\lambda/2$, it is advisable to comply with the spatial Nyquist theorem to minimize the appearance of artifacts.

In summary, the proposed formulation performs proper estimation of DoA and ToA for the whole azimuth range for eccentricity values up to 0.7. Above this value, the estimation shows a directional behavior in the direction where the semi-major axis is located. By rotating the ellipses, the angular response can be tuned. This can be easily achieved in virtual arrays. Logically, mechanical or electrical reconfiguration in a real-world implementation always adds an extra level of technical complexity that is beyond the features of the method and the scope of the present work. Thus, the angular selectivity of the elliptical geometries could be of potential application for the selection (suppression) of signals-of-interest (signals-not-of-interest) in smart wireless environments.

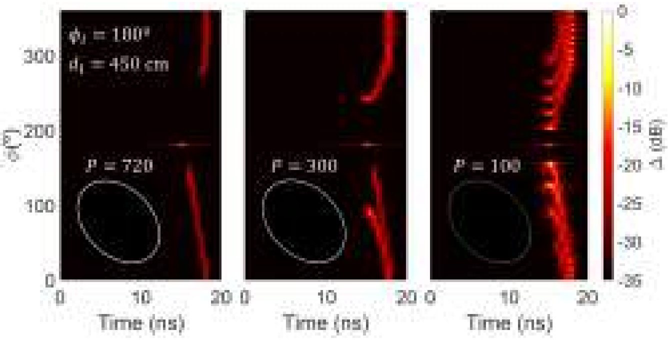

Fig. 5. DoA and ToA estimation for an incident wave at $\phi_l = 180°$ and $\tau_l = 15$ ns ($d_l = 450$ cm) when varying the number of sensors P. Non-compliance with the spatial Nyquist theorem (cases $P = 300, 100$) leads to the appearance of new artifacts and an undesired increase in their contribution to the joint DoA and ToA estimation.

B. Concentric Elliptical Arrays

Sec. II.C introduced the analysis of concentric elliptical arrays. Since previous subsection has shown the eccentricity effect on the estimation, we can take advantage of the concentric arrays in order to improve the estimation. By combining $H_{m,l}(f)$ from the ellipses shown in Figs. 4(a) and 4(b) [see eq. (26)], a new ellipse arrangement can be formed. Fig. 4(c) presents the metric Δ for the joint DoA and ToA estimation when two concentric elliptical arrays are considered. For high eccentricities, an interesting behavior can be found. Δ is maximized for all those DoA coinciding with the semi-major axes of the concentric ellipses (i.e., $\phi_l = 0°$ and $\phi_l = 90°$). A clear example can be seen for $\xi = 0.95$. In Figs. 4(a) and 4(b), Δ indicates good estimations for approximately an 80° azimuth range. However, in Fig. 4(c), $\Delta > 8$ dB in the whole range. Therefore, concentric ellipses with different rotation angles can provide different Δ patterns. This fact opens up the possibility of implementing pseudorandom grids contained within elliptical geometries, which will be discussed in later sections.

C. Technique performance for $\theta_l \neq 90^{\circ}$

Up to this point, simulations have been carried out for a fixed elevation angle of $\theta_l = 90^{\circ}$. In [43], it was demonstrated that the filter from eq. (18) provides accurate estimations for $\theta_l \neq 90^{\circ}$. With the purpose of validating the estimation for different elevation angles, Fig. 6 shows the metric Δ for

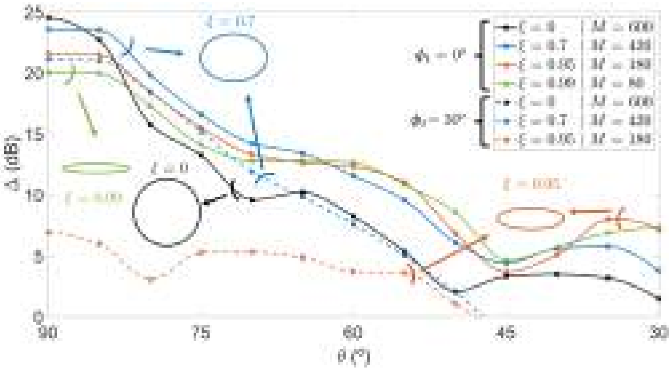

Fig. 6. Metric Δ (dB) for several elevation angles θ_l when $\phi_l = 0°$ (solid line) and $\phi_l = 30°$ (dashed line).

different values of θ_l for two different incident azimuth angles, $\phi_l = 0°$ and $\phi_l = 30°$. The configuration parameters are the same as those shown in Sec. III.A. For the case $\phi_l = 0°$, although the analytical framework discussed in Sec. II was originally derived under the assumption of $\theta_l = 90°$, it can be observed in Fig. 6 that the accuracy in DoA estimation is still satisfactory in a wide range of elevation angles. This is a remarkable feature, as elevation/tilt angles typically vary between 90 and 75 degrees in real deployments [47], [48]. In this range, $\Delta > 13$ dB for all the considered eccentricities. Concerning ToA, it is estimated as 30 ns for $\theta_l = 90°$, matching τ_l. When θ_l moves toward 30°, ToA estimation suffers a slight variation of $+0.5$ ns. This effect was also noticed for circular arrays in [44]. Finally, it is worth noting that elliptical arrays outperform DoA and ToA estimation compared to circular arrays for several elevation angles when $\phi_l = 0°$. This is due to the fact that when the angle of incidence ϕ_l coincides with the semi-major axis, the elliptical shape of the array preserves the directivity of the array better for $\theta_l \neq 90°$ compared to the circular shape. For the case $\phi_l = 30°$, Δ with $\theta_l = 90°$ for high eccentricities is lower as previously depicted in Fig. 4(a) due to the directivity attribute. Similar to the case $\phi_l = 0°$, Δ decreases as the wave incident plane separates from the plane where the elliptical array lies.

D. Pseudorandom Grids

Previous subsections have shown that elliptical arrays present directive behaviour for DoA estimation. Fig. 7 shows some examples of generic geometries formed through the superposition of concentric ellipses. In contrast to concentric circular arrays where only concentric ring shapes can be obtained [42], concentric ellipses provide a wide range of possible sensor arrangements. Hence, some of these geometries may be approximated as pseudorandom grids and the joint DoA and ToA estimation could be performed with sensors located in pseudorandom positions. In real deployments, the use of circular arrays may not be feasible due to space limitations. Conversely, elliptical arrays take up a smaller area and can adapt better to the geometry of any structure. Additionally, we can take advantage of the directivity property in the direction of the semi-major axis to steer the elliptical arrays in a specific range of angles.

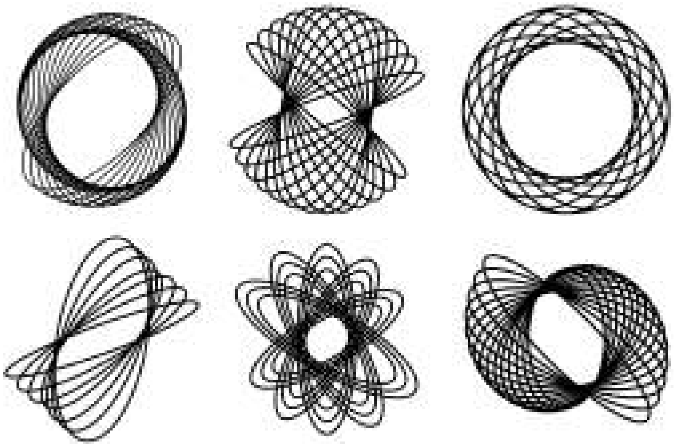

Fig. 7. Generic geometries generated from the superposition of concentric ellipses. Each ellipse is characterized by semi-major axis a, eccentricity ξ and angle of rotation α. The combination of several ellipses results in pseudorandom grids.

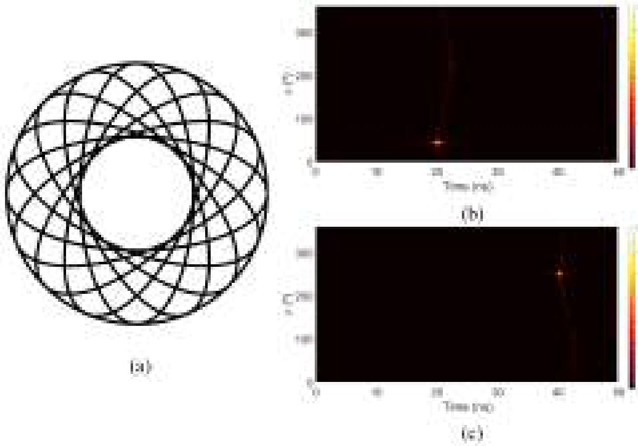

Fig. 8. (a) Superposition of nine concentric elliptical arrays. DoA and ToA estimation when the incident wave is located at (b) $\phi_l = 45°$ and $\tau_l = 20$ ns, and (c) $\phi_l = 250°$ and $\tau_l = 40$ ns.

As a study case, Fig. 8(a) shows a superposition of concentric ellipses to form a pseudorandom grid. Throughout this subsection, it will be studied in depth to analyze its performance compared to single and concentric circular arrays. This geometry consists of 8 ellipses with semi-major axis $a = 34.5$ cm, eccentricity $\xi = 0.9$ and rotation angle $\alpha = 22.5°$ for consecutive ellipses, plus an outer circle of $a = 34.5$ cm and $\xi = 0$. In this case, the frequency band goes from 39.5 GHz to 43.5 GHz (n259 band and B = 4 GHz) [46]. 720 sensors are considered per ellipse, which gives a maximum separation between consecutive sensors of 3 mm (0.437λ at $f = 43.5$ GHz). The number of considered frequency samples is $K = 200$ and the number of phase modes is fixed to $M = 250$.

By applying the formulation for concentric elliptical arrays, Figs. 8(b) and 8(c) present two cases of joint estimation for this geometry. Particularly, Fig. 8(b) shows the estimation of the angular-delay domain for an incident wave at $\phi_l = 45°$ and $\tau_l = 20$ ns. Fig. 8(c) illustrates the same domain for $\phi_l = 250°$ and $\tau_l = 40$ ns. In both cases, the estimation is clearly maximized around ToA and DoA. In addition to

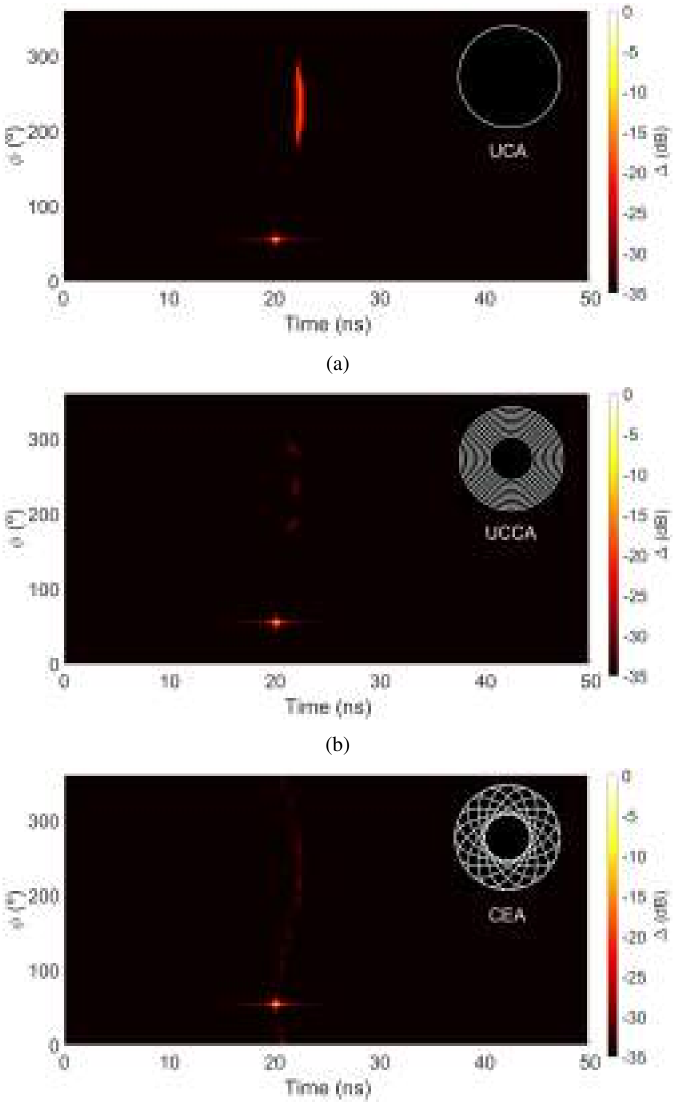

(a)

(b)

(c)

Fig. 9. DoA and ToA estimation for an incident wave at $\phi_l = 55°$ and $\tau_l = 20$ ns for different geometries: (a) Uniform Circular Array, (b) Uniform Concentric Circular Array, and (c) Concentric Elliptical Array.

these cases, the geometry has been tested for incident waves in the entire range of ϕ_l and τ_l, showing excellent results with artifacts below 20 dB in the worst case.

In order to compare the performance of concentric elliptical arrays with other array arrangements, Fig. 9 shows the angular-delay estimation for three different arrangements. Fig. 9(a) is obtained from a uniform circular array (UCA) with radius $r = 34.5$ cm and $P = 720$. Fig. 9(b) represents the estimation for a nine ring uniform concentric circular array (UCCA) whose outer circle is equal to the one shown in Fig. 9(a). The inner circle has radius $r = 15$ cm and all nine rings are equidistant. Finally, Fig. 9(c) uses the geometry presented in Fig. 8(a), i.e., a concentric elliptical array (CEA). Some conclusions can be extracted by looking at Fig. 9. First, the figure illustrates that the proposed method works as a generalization of former approaches, being able to deal with circular and elliptical geometries at the same time. This leads to the realization of elliptical-based pseudorandom mesh grids that can be used to improve the joint DoA and ToA estimation. In that sense, the level of artifacts (sidelobes) has been reduced more than 10 dB when considering concentric arrays instead of a single circular array, the UCCA and CEA outperforming the UCA array due to a better mapping of the spatial region. Naturally, the improvement in the estimation comes at a price. Computational complexity increases when a greater number of arrays is considered. Thus, there exists a trade-off between performance and computational complexity. Scenarios where the impact of the artifacts in the joint estimation should be minimized benefit for the inclusion of a greater number of concentric (elliptical) arrays. Conversely, scenarios where the processing time should be minimized benefit from placing a fewer number of arrays.

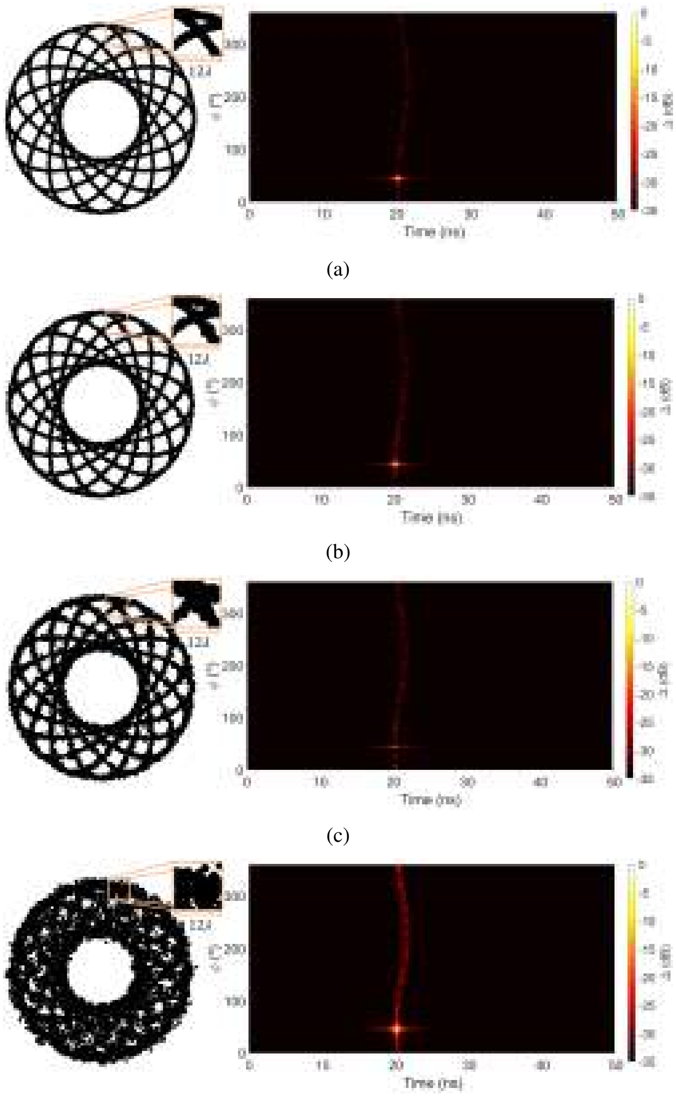

(a)

(b)

(c)

(d)

Fig. 10. DoA and ToA estimation when the incident wave reaches the CEA at $\phi_l = 45°$ and $\tau_l = 20$ ns. Uncertainty in sensor placement is considered, with respect to the center position $\{x_p, y_p\}$, by means of the standard deviation σ. Cases: (a) $\sigma = 0.5\lambda$ (3.45 mm), (b) $\sigma = \lambda$ (6.89 mm), (c) $\sigma = 2\lambda$ (13.78 mm) and (d) $\sigma = 5\lambda$ (34.46 mm).

Previously, the degrees of freedom of the position of the sensors in an ellipse have been discussed. Actually, it is possible to go one step further. The theoretical framework developed in Sec. II has demonstrated that non constant r_p values are feasible for the joint estimation. In order to achieve a real pseudorandom grid, an independent and uncorrelated bivariate normal distribution $\mathcal{N}_2(0,\,\sigma^2)$, with $\sigma_x = \sigma_y = \sigma/\sqrt{2}$, is included in the sensor positions x_p and y_p [eq. (24)]. This distribution adds noise in the sensor position, which randomizes the grid. Figs. 10(a)-(d) shows the angular-delay domain estimation for arrangements with different σ values. Simulation parameters are equal to those ones shown for Fig. 8 with incident wave at $\phi_l = 45°$ and $\tau_l = 20$ ns. Standard deviation σ is chosen in terms of wavelength and it ranges from 0.5λ to 5λ. The maximum artifacts from Fig. 10(a) to Fig. 10(d) are found to be 23.9 dB, 23.5 dB, 21.4 dB and 18.2 dB below the correct estimation, respectively. Although artifacts increase as the position noise does, they are still low enough to correctly detect the DoA and ToA. A remarkable result is that shown in Fig. 10(d), where the elevated value σ directly hides the elliptical shape of the CEA. Even in this case, the joint estimation is remarkably good. For a dense enough sensor arrangement, most of the sensors satisfy the spatial Nyquist theorem. If, on average, the spatial Nyquist theorem is fulfilled, a good estimation is expected. Therefore, it can be concluded that, if a dense pseudorandom mesh is approximated by a set of concentric ellipses, the joint estimation of DoA and ToA can be properly performed.

As a last proof of concept, the estimation of DoA and ToA from a completely random sensor distribution approximated by a set of concentric ellipses is proposed. For the sensor distribution, 10000 sensors are placed in a square based on a bivariate uniform distribution $\mathcal{U}_2\,(-0.345, 0.345)$. As an example, this distribution expects to be approximated by three concentric ellipses with $P = 720$, $a = 34.5$ cm, $\xi = 0.9$ and $\alpha = [30°,\,50°,\,90°]$. Frequency band goes from 39.5 GHz to 43.5 GHz, $K = 200$ and $M = 250$. For this approximation, those sensors of the random distribution whose distance to the theoretical sensor in the three ellipses is minimum are chosen. Fig. 11 shows the random sensor distribution (gray dots) and the sensors chosen to form the concentric elliptical array (black dots). This figure also presents the DoA and ToA estimation for an incident wave at $\phi_l = 230°$ and $\tau_l = 30$ ns, with the largest artifact appearing 13.45 dB below the real path. Thus, the method is valid for elliptical arrays generated from random distributions. Note that the random grid can be used in order to generate any other geometry with several ellipses and several semi-major axis, eccentricity and rotation angle values. Finally, note that the pseudorandom and random grids shown in Figs. 10 and 11 cannot be rigorously analyzed with previous approaches [40]–[44], as sensors with different radius r_p must be considered.

IV. MEASUREMENTS

In order to validate the simulations and theoretical framework, multiple measurements have been carried out at the facilities of the University of Granada. These facilities consist of a semi-anechoic and semi-reverberation chamber whose dimensions are $5 \times 3.5 \times 3.5$ meters (61.25 m^3). The measurements are performed in the semi-anechoic part, where multiple absorbers are found in the walls in order to avoid any reflection. Therefore, the Line-of-Sight (LoS) can be analyzed in the propagation channel between a transmitter (TX) and a receiver (RX). To recreate the simulation setup, TX is placed at a distance d_l and azimuth angle ϕ_l with respect to the center of a certain ellipse, which is formed by a virtual array at RX. Fig. 12 shows the measurement setup in the semi-anechoic chamber. The transmitter antenna is fixed, while the receiver antenna, located in the measurement system, can move in the XY plane positioned at the same height ($z = 179$ cm) as the transmitter antenna. The measuring system allows a maximum displacement of 1 m in both x and y axes. The communication channel is acquired through a Vector Network Analyzer (VNA Rohde & Schwarz ZVA67), which measures the scattering parameters up to 67 GHz. In order to prevent the effect of the coaxial cables in the communication channel, a Through — Open — Short — Match (TOSM) calibration is performed. Thus, $H_{p,l}$ includes the contribution of the propagation channel and the radiation pattern of the antennas in TX and RX. Particularly, TX is a standardized gain horn fed with a WR-15 waveguide-to-coaxial transition (Flann Kband antenna Model: #25240-20). RX is a monopole antenna based on a 1.85 mm coaxial transition to free space, centered at 60 GHz, with a matching bandwidth higher than 8 GHz below -10 dB, and omnidirectional radiation pattern for $\theta_l = 90°$ in the XY plane. The frequency range is chosen to be from 58 GHz to 62 GHz, for measurements and simulations, i.e., $B = 4$ GHz in the mmWave range. $K = 200$ frequency samples are acquired, providing 20 MHz frequency step. Given the bandwith B, the temporal and distance resolution are 0.25 ns and 7.5 cm respectively. Consequently, the maximum observable time and distance are 49.75 ns and 14.925 m.

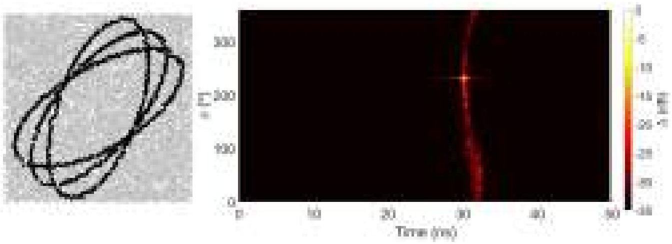

Fig. 11. DoA and ToA estimation for an incident wave at $\phi_l = 230°$ and $\tau_l = 30$ ns for a sensor distribution based on a bivariate uniform random distribution (gray dots). Three concentric elliptical arrays are approximated from the randomly arranged sensors (black dots).

In the first experiment, TX is placed at distance $d_l = 120$ cm and angle $\phi_l = 330°$. RX forms an ellipse with $a = 24.2$ cm, $\xi = 0.7$ and $\alpha = 0°$. $P = 720$ sensors are considered, for a maximum separation of 2.1 mm between sensors (0.437λ for $f = 62$ GHz). Finally, the number of phase modes M is set to 250. Figs. 13(a) and 13(b) show the DoA and ToA estimation for the simulated and measured cases, respectively. As expected, the estimation is maximized for $\tau_l = 4$ ns ($d_l = 120$ cm) and $\phi_l = 330°$, with an artifact located at $\phi_l \pm 180°$. In Fig. 13(b), the estimation of DoA and ToA is slightly more spread due to measurement imperfections with respect to simulation. However, the maximum is still found at $\tau_l = 4.25$ ns ($d_l = 127.5$ cm) and $\phi_l = 330°$. The variation

Fig. 12. Photograph of the measurement setup. TX is fixed and RX forms the elliptical array due to the movement of the measurement system located at the bottom.

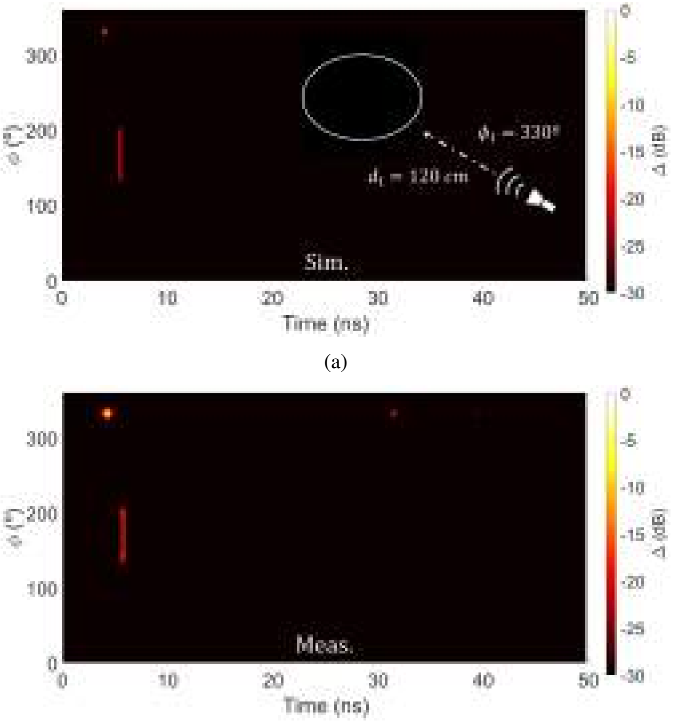

(a)

(b)

Fig. 13. DoA and ToA estimation for an incident wave at $\phi_l = 330°$ and $\tau_l = 4$ ns ($d_l = 120$ cm). (a) Simulation and (b) measurement in the semi-anechoic chamber.

of 7.5 cm is mainly due to the calibration process; namely, horn length (7.6 cm) and monopole transition (2 cm) are not initially considered. The distance resolution is 7.5 cm, thus the estimated value of d_l is within the expected error band in measurement. Finally, note that two reflections due to back propagation in the semi-reverberation chamber can be found at 31.5 ns and 39.25 ns in Fig. 13(b).

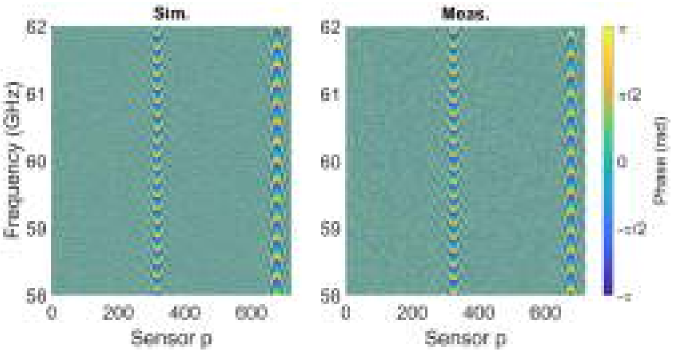

Fig. 14. Simulated and measured $H_{p,l}(f)$ phase distribution when a single wave impinges at $\phi_l = 330°$ and $\tau_l = 4$ ns. Ellipse parameters are $a = 24.2$ cm, $\xi = 0.7$, $\alpha = 0°$ and $P = 720$.

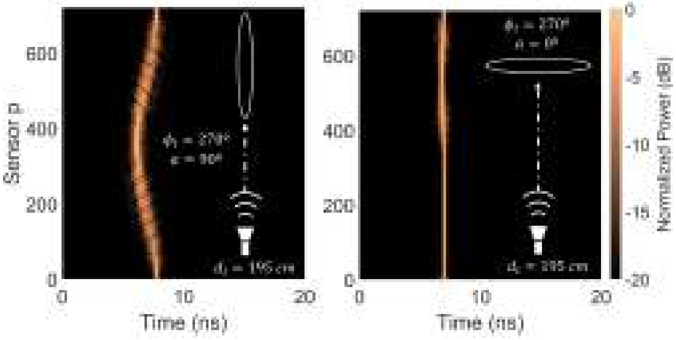

Fig. 15. Normalized measured PDP for an incident wave at $\phi_l = 270°$ and $\tau_l = 6.5$ ns in two different setups: (left panel) rotated ellipse and (right panel) non-rotated ellipse.

Fig. 13 has shown a good agreement between the theoretical framework and the simulations proposed for this estimation method. As explained in Sec. II, this technique is based on a correct modeling of the incident signal on the P sensors, i.e., $H_{p,l}$. Thus, phase-mode expansion $H_{m,l}$ and 2-D FFT lead to the joint DoA and ToA estimation. A proper modeling of the phase is fundamental in $H_{p,l}$. As an example, Fig. 14 illustrates the $H_{p,l}$ phase distribution for every sensor and frequency in the setup previously shown in Fig. 13. High similarity of the phase distribution in simulations and measurements can be observed. This fact demonstrates the proper modeling of the incident wave for elliptical cases in real measurements, thus yielding good joint DoA and ToA estimations.

One of the features observed in the simulation is the high angular selectivity offered by highly flattened elliptical arrays. One way to explain this behavior is based on understanding how the wave reaches the array. For this purpose, two different setups have been measured. The first one has the TX positioned at a distance of $d_l = 195$ cm and an angle $\phi_l = 270°$. The RX is a virtual array with parameters: $a = 24.2$ cm, $\xi = 0.99$, $\alpha = 90°$ and $P = 720$. The second setup is similar, except for the rotation angle $\alpha = 0°$. Fig. 15 shows the normalized Power Delay Profile (PDP) for every sensor p in RX. This PDP is calculated as the square of the IFFT of the channel frequency response $H_{p,l}$ for each sensor. On the left panel, it can be seen that the wave impinges in the direction of the semi-major axis. Therefore, this wave travels sensor by sensor through the entire array. This fact generates the curvature observed in the PDP for the different sensor positions. On the right panel, the wave impinges in the direction of the semi-minor axis. In this case, for high eccentricities, the wave simultaneously reaches all the sensors of the array. This results in no curvature in the PDP, i.e, the

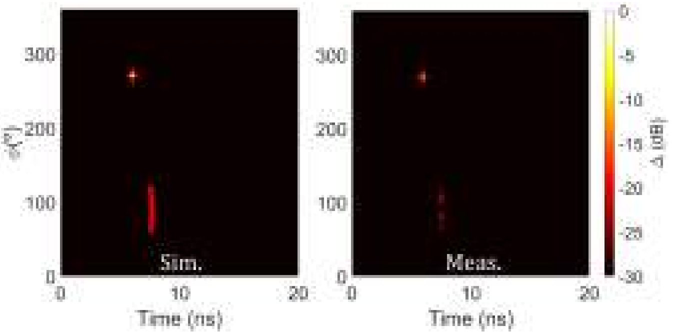

Fig. 16. Simulated and measured DoA and ToA estimation for an incident wave at $\phi_l = 270°$ and $\tau_l = 5.66$ ns when the elevation angle is $\theta_l = 70°$.

measured channel for the different sensors is similar. In the first case, the curvature is unambiguous, since only this DoA generates such curvature. In the second case, the practical absence of curvature causes ambiguity in the estimation, since $\phi_l = 90°$ would generate exactly the same PDP. Hence, it can be concluded by the measurement study that this technique takes advantage of the curvature of the elliptical array, thus justifying the curves simulated in Fig. 4. As it was noted in Sec. III.A, the selectivity is an attribute of the sensor arrangement.

Sec. III.C presented the technique performance for elevation angles $\theta_l \neq 90°$. In order to validate previous simulations, a setup with $\theta_l = 70°$ is measured. TX antenna is placed at height $z = 120$ cm with $\phi_l = 270°$, and the elliptical array is kept at $z = 179$ cm. The distance in the XY plane between TX and the center of the elliptical array is 160 cm. Therefore, by applying basic trigonometry, $d_l = 170$ cm ($\tau_l = 5.66$ ns) and θ_l turns out to be 70°. RX parameters are $a = 24.2$ cm, $\xi = 0.7$, $\alpha = 90°$, $P = 720$ and $M = 250$. Fig. 16 shows the simulated and measured joint estimation of the DoA and ToA for the previous scenario. The measured scenario matches the simulation with 270° DoA and 6 ns ToA estimation. The artifacts appear 16 dB below the estimation, showing a good agreement with the simulation prediction (see $\xi = 0.7$ in Fig. 6).

For the sake of completeness of the experimental study, it will be shown that the use of this technique is valid for i) multipath environments, and ii) concentric elliptical arrays. For that purpose, i) two measured rays are combined in the semi-anechoic chamber as the sum of the frequency response of each of the rays incident at the p-th sensor [see eq. (19)]. The first wave reaches the center of the array from 330° and 4 ns (120 cm) delay, while the second wave impinges the ellipse from 300° azimuth angle and 8 ns (240 cm) delay. ii) Two ellipses are combined to form a concentric elliptical array. The phase-mode response from the sum of the two previous waves is summed to create the new arrangement [see eq. (26)]. The parameters for the first elliptical array are $a = 24.2$ cm, $\xi = 0.7$, $\alpha = 0°$, $P = 720$ and $M = 250$, while the second array is characterized by the same parameters except for $\alpha = 90°$. Fig. 17 shows the joint estimation for the multipath scenario and the superposition of ellipses. Both waves can be clearly depicted in the simulations and measurements for the correct values of DoA and ToA. A good estimation is seen, which validates the proposed approach and the experimental setup for usage in multipath environments in wireless communication links.

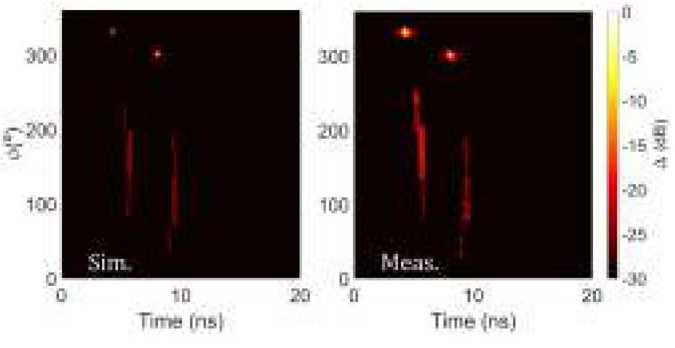

Fig. 17. Simulated and measured DoA and ToA estimation for a multipath component scenario and concentric elliptical arrays. The first ray reaches RX for 330° DoA and 4 ns ToA, and the second ray for 300° DoA and 8 ns. Two ellipses with $\xi = 0.7$ and different rotation angle are considered.

In general, it should be stated that the level of the main artifacts varies as multiple concentric arrays of different geometries are considered. Flattened elliptical arrays present angular selectivity, normally in angular regions near the semi-major axis (see Fig. 4). This fact provokes that the level of artifacts either decreases or increases depending on the location of the DoA. In the case that the semi-major axis of the elliptical array is aligned with the DoAs, the level of the artifacts decreases (the metric Δ increases). On the other hand, if the DoAs are not aligned with the semi-major axis, the level of the artifacts is expected to increase (the metric Δ decreases). More than a limitation of the proposed method, the modification of Δ as a consequence of the orientation of the array should be considered an inherent property of flattened elliptical and linear arrays.

V. CONCLUSIONS

This work proposes a technique for joint DoA and ToA estimation based on ultra-wideband elliptical arrays. The theoretical framework introduces a generalization of frequency-independent beamformers based on uniform circular arrays. This new approach is a generalization not only valid for elliptical arrays, but also feasible for circular and linear arrays. The geometry of the elliptical array provides new degrees of freedom compared to the circle, where only the radius can be modified. The ellipses, besides tuning the semi-major axis, also allow to adjust their eccentricity or rotation angle. These degrees of freedom, together with the superposition of concentric ellipses, result in pseudo-random sensor geometries. This novel concept avoids the problem of being limited to a specific set of geometries, being able to adapt the array to several arrangements in a real deployment.

The analysis of the technique through simulations has shown good joint DoA and ToA estimations, with artifacts appearing orders of magnitude below the main component. The study has been performed for the whole range of azimuth angles ϕ_l, as well as for multiple time-of-arrival τ_l, and three frequency bands within the mmWave range: 28-30 GHz, 39.5-43.5 GHz and 58-62 GHz. Additionally, the effect of modifying the rotation angle α, eccentricity ξ and elevation angles θ_l on the joint estimation has been analyzed. Through these degrees of freedom, arrangements of nine geometries with pseudo-random array distribution have been simulated. One step further, an independent and uncorrelated bivariate normal distribution is included in the sensor position in order to recreate a random grid. The results show that even including this random distribution, the estimation can be properly performed.

Finally, the simulations have been validated through multiple measurements in a semi-anechoic chamber at 58-62 GHz frequency band. DoA and ToA estimation has been initially carried out for single ellipses and single-path environments. Then, this has been extended to multipath scenarios and concentric elliptical arrays, simultaneously. Both the measured frequency response, phase distributions and the joint estimation of the DoA and ToA agree with those predicted by the simulations. These experimental results validate the theoretical framework, thus providing a method which gives accurate estimations for a large number of sensor arrangements and arbitrary geometries.

REFERENCES

[1] R. Schmidt, “Multiple emitter location and signal parameter estimation,” *IEEE Trans. Antennas Propag.*, vol. 34, no. 3, pp. 276-280, March 1986.

[2] A. H. El Zooghby, C. G. Christodoulou and M. Georgiopoulos, “Performance of radial-basis function networks for direction of arrival estimation with antenna arrays,” *IEEE Trans. Antennas Propag.*, vol. 45, no. 11, pp. 1611-1617, Nov. 1997.

[3] Li Cong and Weihua Zhuang, ”Hybrid TDOA/AOA mobile user location for wideband CDMA cellular systems,” *IEEE Trans. Wirel. Commun.*, vol. 1, no. 3, pp. 439-447, July 2002.

[4] C. Yang and H. Shao, “WiFi-based indoor positioning,” *IEEE Commun. Mag.*, vol. 53, no. 3, pp. 150-157, March 2015.

[5] K. Shamaei and Z. M. Kassas, “A Joint TOA and DOA Acquisition and Tracking Approach for Positioning With LTE Signals,” *IEEE Trans. Signal Process.*, vol. 69, pp. 2689-2705, 2021.

[6] Z. Gong et al., “Joint TOA and DOA Estimation With CFO Compensation Using Large-Scale Array,” *IEEE Transactions on Signal Processing*, vol. 69, pp. 4204-4218, 2021.

[7] R. Bai and M. Singhal, ”DOA: DSR over AODV Routing for Mobile Ad Hoc Networks,” *IEEE Trans. Mob. Comput.*, vol. 5, no. 10, pp. 1403-1416, Oct. 2006.

[8] M. Koivisto et al., “Joint Device Positioning and Clock Synchronization in 5G Ultra-Dense Networks,” *IEEE Trans. Wirel. Commun.*, vol. 16, no. 5, pp. 2866-2881, May 2017.

[9] H. Wang, L. Wan, M. Dong, K. Ota and X. Wang, “Assistant Vehicle Localization Based on Three Collaborative Base Stations via SBL-Based Robust DOA Estimation,” *IEEE Internet Things J.*, vol. 6, no. 3, pp. 5766-5777, June 2019.

[10] L. Wan, Y. Sun, L. Sun, Z. Ning and J. J. P. C. Rodrigues, “Deep Learning Based Autonomous Vehicle Super Resolution DOA Estimation for Safety Driving,” *IEEE Trans. Intell. Transp. Syst.*, vol. 22, no. 7, pp. 4301-4315, July 2021.

[11] D. Zhu, J. Choi and R. W. Heath, “Auxiliary Beam Pair Enabled AoD and AoA Estimation in Closed-Loop Large-Scale Millimeter-Wave MIMO Systems,” *IEEE Transactions on Wireless Communications*, vol. 16, no. 7, pp. 4770-4785, July 2017.

[12] M. Meurer, A. Konovaltsev, M. Appel, and M. Cuntz, “Direction-of-Arrival Assisted Sequential Spoofing Detection and Mitigation,” *Proceedings of the 2016 International Technical Meeting of The Institute of Navigation*, pp. 181-192, 2016.

[13] Z. Tang and A. Manikas, ”Multi Direction-of-Arrival Tracking Using Rigid and Flexible Antenna Arrays,” *IEEE Trans. Wirel. Commun.*, vol. 20, no. 11, pp. 7568-7580, Nov. 2021.

[14] Y. Chen, L. Yan, C. Han and M. Tao, ”Millidegree-Level Direction-of-Arrival Estimation and Tracking for Terahertz Ultra-Massive MIMO Systems,” *IEEE Trans. Wirel. Commun.*, vol. 21, no. 2, pp. 869-883, Feb. 2022.

[15] Y. Yu, A. P. Petropulu and H. V. Poor, “MIMO Radar Using Compressive Sampling,” *IEEE J. Sel. Top. Signal Process.*, vol. 4, no. 1, pp. 146-163, Feb. 2010.

[16] X. Zhang, L. Xu, L. Xu and D. Xu, “Direction of Departure (DOD) and Direction of Arrival (DOA) Estimation in MIMO Radar with Reduced-Dimension MUSIC,” *IEEE Commun. Lett.*, vol. 14, no. 12, pp. 1161-1163, December 2010.

[17] A. -A. Saucan, T. Chonavel, C. Sintes and J. -M. Le Caillec, “CPHD-DOA Tracking of Multiple Extended Sonar Targets in Impulsive Environments,” *IEEE Trans. Signal Process.*, vol. 64, no. 5, pp. 1147-1160, March1, 2016.

[18] Z. Chen, “Review of direction of arrival estimation algorithms for partial discharge localisation in transformers”, *IET Sci. Meas. Technol.*, vol. 13, pp. 529-535, 2019.

[19] N. Xue et al., “The Location of Partial Discharge Sources Inside Power Transformers Based on TDOA Database With UHF Sensors,” *IEEE Access*, vol. 7, pp. 146732-146744, 2019.

[20] C. R. Storck and F. Duarte-Figueiredo, “A survey of 5G technology evolution, standards, and infrastructure associated with vehicle-to-everything communications by Internet of Vehicles,” *IEEE Access*, vol. 8, pp. 117593–117614, 2020.

[21] S. Aslam, M. P. Michaelides, and H. Herodotou, “Internet of Ships: A survey on architectures, emerging applications, and challenges,” *IEEE Internet Things J.*, vol. 7, no. 10, pp. 9714–9727, Oct. 2020.

[22] J. Rodríguez-Piñeiro, T. Domínguez-Bolaño, X. Cai, Z. Huang, and X. Yin, “Air-to-ground channel characterization for low-height UAVs in realistic network deployments,” *IEEE Trans. Antennas Propag.*, vol. 69, no. 2, pp. 992–1006, Feb. 2021.

[23] K. Guan et al., “Towards realistic high-speed train channels at 5G millimeter-wave band—Part I: Paradigm, significance analysis, and scenario reconstruction,” *IEEE Trans. Veh. Technol.*, vol. 67, no. 10, pp. 9112–9128, Oct. 2018.

[24] H. Jiang et al., “A Novel 3D UAV Channel Model for A2G Communication Environments Using AoD and AoA Estimation Algorithms,” *IEEE Transactions on Communications, vol. 68, no. 11, pp. 7232-7246, Nov. 2020.*

[25] A. Ramírez-Arroyo, L. García, A. Alex-Amor and J. F. Valenzuela-Valdés, “Artificial Intelligence and Dimensionality Reduction: Tools for Approaching Future Communications,” *IEEE Open J. Commun. Soc*, vol. 3, pp. 475-492, 2022.

[26] A. Ramírez-Arroyo, P. H. Zapata-Cano, Á. Palomares-Caballero, J. Carmona-Murillo, F. Luna-Valero and J. F. Valenzuela-Valdés, ”Multilayer Network Optimization for 5G & 6G,” *IEEE Access*, vol. 8, pp. 204295-204308, 2020.

[27] A. Mourad, R. Yang, P. H. Lehne, A. De La Oliva, “Baseline Roadmap for Advanced Wireless Research Beyond 5G,” *Electronics*. vol. 9, pp. 351, 2020.

[28] A. Ramírez-Arroyo, A. Alex-Amor, C. García-García, Á. Palomares-Caballero, P. Padilla and J. F. Valenzuela-Valdés, “Time-Gating Technique for Recreating Complex Scenarios in 5G Systems,” *IEEE Access*, vol. 8, pp. 183583-183595, 2020.

[29] W. Fan, I. Carton, J.Ø. Nielsen, K. Olesen and G.F. Pedersen, “Measured wideband characteristics of indoor channels at centimetric and millimetric bands,” *Journal on Wireless Communications and Networking*, pp. 58, 2016.

[30] M. Koivisto, J. Talvitie, E. Rastorgueva-Foi, Y. Lu and M. Valkama, “Channel Parameter Estimation and TX Positioning With Multi-Beam Fusion in 5G mmWave Networks,” *IEEE Trans. Wirel. Commun.*, vol. 21, no. 5, pp. 3192-3207, May 2022.

[31] X. Cai, G. Zhang, C. Zhang, W. Fan, J. Li and G. F. Pedersen, ”Dynamic Channel Modeling for Indoor Millimeter-Wave Propagation Channels Based on Measurements,” *IEEE Trans. Commun.*, vol. 68, no. 9, pp. 5878-5891, 2020.

[32] V. Perrot, M. Polichetti, F. Varray, D. Garcia, “So you think you can DAS? A viewpoint on delay-and-sum beamforming,” *Ultrasonics*, vol. 111, 2021.

[33] R. Roy and T. Kailath, “ESPRIT-estimation of signal parameters via rotational invariance techniques,” *IEEE Trans. Audio Speech Lang. Process.*, vol. 37, no. 7, pp. 984-995, July 1989.

[34] P. Stoica and K. C. Sharman, “Maximum likelihood methods for direction-of-arrival estimation,” *IEEE Trans. Audio Speech Lang. Process.*, vol. 38, no. 7, pp. 1132-1143, July 1990.

[35] Tuan-Do-Hong and P. Russer, ”Signal processing for wideband smart antenna array applications,” *IEEE Microw. Mag.*, vol. 5, no. 1, pp. 57-67, March 2004.

[36] B. D. Van Veen and K. M. Buckley, ”Beamforming: a versatile approach to spatial filtering,” *IEEE ASSP Mag.*, vol. 5, no. 2, pp. 4-24, April 1988.

[37] O. L. Frost, “An algorithm for linearly constrained adaptive array processing”*Proc. IEEE*, vol. 60, No. 8. August 1972.

[38] K. Nishikawa, T. Yamamoto, K. Oto and T. Kanamori, ”Wideband beamforming using fan filter,” *1992 IEEE International Symposium on Circuits and Systems (ISCAS)*, 1992, pp. 533-536 vol. 2.

[39] T. Chou, “Frequency-independent beamformer with low response error,” *1995 International Conference on Acoustics, Speech, and Signal Processing*, 1995, pp. 2995-2998 vol. 5.

[40] S. C. Chan and C. K. S. Pun, “On the design of digital broadband beamformer for uniform circular array with frequency invariant characteristics,” *2002 IEEE International Symposium on Circuits and Systems*. Proceedings (Cat. No.02CH37353), 2002.

[41] C. Gentile, A. J. Braga and A. Kik, ”A Comprehensive Evaluation of Joint Range and Angle Estimation in Ultra-Wideband Location Systems for Indoors,” in *IEEE International Conference on Communications*, pp. 4219-4225, 2008.

[42] S. C. Chan and H. H. Chen, ”Uniform Concentric Circular Arrays With Frequency-Invariant Characteristics—Theory, Design, Adaptive Beamforming and DOA Estimation,” *IEEE Trans. Signal Process.*, vol. 55, no. 1, pp. 165-177, 2007.

[43] F. Zhang, W. Fan, and G. F. Pedersen, “Frequency-invariant uniform circular array for wideband mm-Wave channel characterization,” *IEEE Antennas Wirel. Propag. Lett.*, vol. 16, pp. 641–644, 2017.

[44] X. Cai and W. Fan, ”A Complexity-Efficient High Resolution Propagation Parameter Estimation Algorithm for Ultra-Wideband Large-Scale Uniform Circular Array,” *IEEE Trans. Commun.*, vol. 67, no. 8, pp. 5862-5874, 2019.

[45] M. Abramowitz and I. A. Stegun, *Handbook of Mathematical Functions*. New York: Dover, 1965.

[46] 3GPP TS38.101-2 V17.6.0., “NR; User Equipment (UE) radio transmission and reception; Part 2: Range 2 Standalone (Release 17)”, 2022.

[47] A. Imran, M. A. Imran, A. Abu-Dayya and R. Tafazolli, ”Self Organization of Tilts in Relay Enhanced Networks: A Distributed Solution,” *IEEE Trans. Wirel. Commun.*, vol. 13, no. 2, pp. 764-779, 2014.

[48] R. Hernandez-Aquino, S. A. R. Zaidi, D. McLernon, M. Ghogho and A. Imran, ”Tilt Angle Optimization in Two-Tier Cellular Networks—A Stochastic Geometry Approach,” *IEEE Trans. Commun.*, vol. 63, no. 12, pp. 5162-5177, 2015.

Alejandro Ramírez-Arroyo was born in Córdoba, Spain, in 1997. He received the B.Sc. degree with honors and M.Sc degree with honors in telecommunication engineering from the University of Granada (UGR), Spain, in 2019 and 2021. Since 2020, he is pursuing the Ph.D. degree with the Smart Wireless Applications and Technologies (SWAT) Research Group in the Department of Signal Theory, Telematics, and Communications, University of Granada. In 2022, he was with the Wireless Communication Networks section, Aalborg University (AAU), Denmark, as an invited Ph.D. Student. His current research interests include optimization techniques, radio propagation and channel characterization for mmWaves and 5G communications.

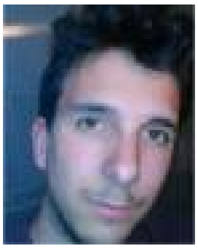

Antonio Alex-Amor received the B.Sc. degree in Telecommunication Engineering from Universidad de Granada, in 2016, and the M.Sc. and Ph.D. degrees in Telecommunication Engineering from Universidad Politécnica de Madrid (UPM), in 2018 and 2021, respectively. From 2016 to 2021, he has been with the Radiation Group, Signal, Systems and Radiocommunications Department, UPM. From 2018 to 2019, he joined the Department of Language and Computer Science, Universidad de Málaga. From 2020 to 2021, he joined the Departamento de Teoría de la Señal, Telemática y Telecomunicaciones, Universidad de Granada (Granada, Spain). Currently, he is an Assistant Professor at Universidad CEU San Pablo (Madrid, Spain). He was a Visiting Student at KTH Royal Institute of Technology during four months in 2019 and conducted a Short Postdoc Mission at Universidade de Lisboa (Lisbon, Portugal) in 2021. In 2020, he received the Best Electromagnetics Paper Award at the 14th European Conference on Antennas and Propagation (EuCAP 2020). His current research interests include the analysis and design of metamaterial structures and antennas, and wireless communication systems. He is also an active science communicator in blogs and social media.

Pablo Padilla was born in Jaén, Spain, in 1982. He received the Telecommunication Engineering degree and the Ph.D. degree from the Radiation Group (Signal, Systems and Radiocommunications Department) of the Technical University of Madrid (UPM), Spain, in 2005 and 2009, respectively. In 2007, he was with the Laboratory of Electromagnetics and Acoustics, Ecole Polytechnique Fédérale de Lausanne, Switzerland, as an invited Ph.D. Student. In 2009, he carried out a Postdoctoral stay at the Helsinki University of Technology (AALTO-TKK). In 2009, he became Assistant Professor at the Signal Theory, Telematics and Communications Department of the University of Granada, where he is currently Associate Professor, since 2012. In 2017, he was an invited Visiting Professor at the Royal Institute of Technology of Stockholm. He has authored more than 65 high-impact journal contributions and more than 60 contributions to international symposia. His research interests include a variety of topics related mainly to electromagnetism and communication issues (radiofrequency devices, antennas and propagation).

Juan F. Valenzuela-Valdés was born in Marbella, Spain. He received the Telecommunication Engineering degree from the Universidad de Málaga, Málaga, Spain, in 2003, and the Ph.D. degree from the Universidad Politécnica de Cartagena, Cartagena, Spain, in 2008. He joined the Department of Information Technologies and Communications, Universidad Politécnica de Cartagena, in 2004. In 2007, he joined EMITE Ing., Murcia, Spain, as the Head of research. In 2011, he joined the Universidad de Extremadura, Mérida, Spain, and in 2015, he joined the Universidad de Granada, where he is currently a Full Professor. He is also the Head of the SWAT Research Group, University of Granada, Granada, Spain, and the Co-Head of the Singular Laboratory of electromagnetic characterization of microwave and millimeter devices and antennas. His publication record comprised of more than 100 publications, including 50 JCR (Journal Citation Reports) indexed articles and seven book chapters. He holds several national and international patents. His current research interests include wireless communications, radio frequency devices, antennas, and propagation. Dr. Valenzuela-Valdés received several prizes, including a National Prize to the Best Ph.D. in mobile communications by Vodafone.

2.3.2 Joint Ultra-wideband Characterization of Azimuth, Elevation and Time of Arrival with Toric Arrays

Based on the principles of the previous work, this paper presents a generalization of the joint DoA and ToA characterization derived from the use of circular arrays. In two-dimensional arrays, the angle of arrival can only be correctly estimated in the plane where the array is located when applying phase-mode expansions. This means that in circular arrays, only the azimuth angle can be estimated, while the elevation of an incident wave is unknown. As a solution to this issue, the use of toric arrays is proposed to achieve nearly frequency-invariant beamformers in circular arrays deployed in several planes around the torus. This is possible due to the definition of the torus as a Cartesian product of two circular arrays. This allows the joint characterization of azimuth and elevation Direction of Arrival and Time of Arrival, i.e., a fully 3D characterization of the propagation channel. The simulations show the correct performance of the method to jointly estimate the channel parameters at mmWave frequencies (30 GHz and 60 GHz) with UWB communication channels.

THIS IS A PREPRINT VERSION OF THE PAPER:

A. Ramírez-Arroyo, A. Alex-Amor, R. Medina, P. Padilla and J. F. Valenzuela-Valdés, “Joint Ultra-wideband Characterization of Azimuth, Elevation and Time of Arrival with Toric Arrays,” submitted to *IEEE Transactions on Wireless Communications*, 2023.

Joint Ultra-wideband Characterization of Azimuth, Elevation and Time of Arrival with Toric Arrays

Alejandro Ramírez-Arroyo, Antonio Alex-Amor, Rubén Medina, Pablo Padilla, and Juan F. Valenzuela-Valdés

Abstract—**In this paper, we present an analytical framework for the joint characterization of the 3D direction of arrival (DoA), i.e., azimuth and elevation components, and time of arrival (ToA) in multipath environments. The analytical framework is based on the use of nearly frequency-invariant beamformers (FIB) formed by toric arrays. The frequency response of the toric array is expanded as a series of phase modes, which leads to azimuth–time and elevation–time diagrams from which the 3D DoA and the ToA of the incoming waves can be extracted over a wide bandwidth. Firstly, we discuss some practical considerations, advantages and limitations of using the analytical method. Subsequently, we perform a parametric study to analyze the influence of the method parameters on the quality of the estimation. The method is tested in single-path and multipath mm-wave environments over a large bandwidth. The results show that the proposed method improves the quality of the estimation, i.e., decreases the level of the artifacts, compared to other state-of-art FIB approaches based on the use of single/concentric circular and elliptical arrays.**

Index Terms—**Direction-of-arrival (DoA), time-of-arrival (ToA), 3D characterization, toric arrays, propagation, wireless channels.**

I. INTRODUCTION

KEY performance indicators (KPI) are parameters that quantify the overall yield of a wireless communication channel [1], [2]. Examples of KPIs are throughput, bandwidth, latency, jitter, mobility and energy consumption. Improving KPIs, and therefore the performance of wireless links, requires a proper characterization and knowledge of all channel parameters: direction of arrival (DoA), time of arrival (ToA), delay spread, path loss, and K factor, among others. With knowledge of the channel parameters, different scenarios can be effectively distinguished [3], even recreated and emulated through the use of post-processing techniques based on the creation/removal of reflections in the communication channel [4], [5]. This is fundamental in today's interconnected society, considering the huge variety of propagation environments associated with different communication scenarios: 5G/6G mobile [6]–[8], RIS-aided [9]–[11], industrial [12]–[14], and vehicle-to-everything [15]–[18] networks.

Among all the channel parameters, DoA and ToA are among the most noteworthy. A joint estimation of DoA and ToA is essential because current communication scenarios suffer from temporal variations of the physical properties of the channel. Accurate DoA and ToA information can account for the changes occurring in the channel. In the sub-6 GHz regime, DoA and ToA estimation techniques have been widely explored in the literature [19]. Most of the applied techniques are of narrowband nature [20]–[25], which generally limits their use for modern broadband applications in the mm-wave frequency range. As a consequence, new efficient wideband alternatives are being sought that feature DoA and ToA simultaneously.

The implementation of *nearly frequency-invariant* beamformers (FIB) has proven to be a suitable alternative for (ultra)-wideband DoA estimation [26]–[28]. The objective of FIB is to parameterize the array coefficients so that the spectral and spatial dependences can be treated independently [29]. Previous implementations of FIB have ranged from the use of one-dimensional (1D) arrays [30] to two-dimensional (2D) configurations based on the use of circular arrays [31]–[34]. Recently, the use of FIB was extended by the authors to include elliptical geometries [35], [36]. This is a generalization of previous approaches based on circular geometries, as circular and linear arrays are subcases included in the more general elliptical arrays. However, many of the DoA and ToA estimation methods are only capable to accurately estimate the time of arrival and one of the two spatial DoA components, i.e., either azimuth or elevation, but not both at the same time [31]–[33], [35], [36]. In this regard, it is not so common to find analytical approaches that accurately estimate azimuth, elevation and time of arrival in one go.

In this paper, we present a novel estimation method for joint 3D DoA (azimuth, elevation) and ToA characterization. The technique is based on the use of nearly frequency-invariant toric arrays. Following a similar rationale than in [31]–[38], the multipath frequency response, acquired in the different spatial points that are part of the toric array, can be expanded as a series of phase modes and a preselected frequency-dependent filter. This leads to diagrams in the azimuth–time (AoA–ToA) and elevation–time (EoA–ToA) domains, from which the direction and time of arrival of the incoming waves can be accurately estimated in a wideband range of frequencies

This work has been supported by grant TED2021-129938B-I00 funded by MCIN/AEI/10.13039/501100011033 and by the European Union NextGenerationEU/PRTR. It has also been supported by grants PDC2022-133900-I00, PID2020-112545RB-C54 and TED2021-131699B-I00; and by Universidad de Granada through grant PPJIB2022-05; and in part by the Predoctoral Grant FPU19/01251 and FPU19/04085. (*Corresponding author: Alejandro Ramírez-Arroyo.*)

Alejandro Ramírez-Arroyo, Pablo Padilla and Juan F. Valenzuela-Valdés are with the Department of Signal Theory, Telematics and Communications, Research Centre for Information and Communication Technologies (CITIC-UGR), Universidad de Granada, 18071 Granada, Spain (e-mail: alera@ugr.es; pablopadilla@ugr.es; juanvalenzuela@ugr.es).

Antonio Alex-Amor is with the Department of Information Technologies, Universidad San Pablo-CEU, CEU Universities, Campus Montepríncipe, 28668 Boadilla del Monte (Madrid), Spain (e-mail: antonio.alexamor@ceu.es).

Rubén Medina is with the Department of Mathematical Analysis, Universidad de Granada (UGR), 18071 Granada, Spain (e-mail: rubenmedina@ugr.es).

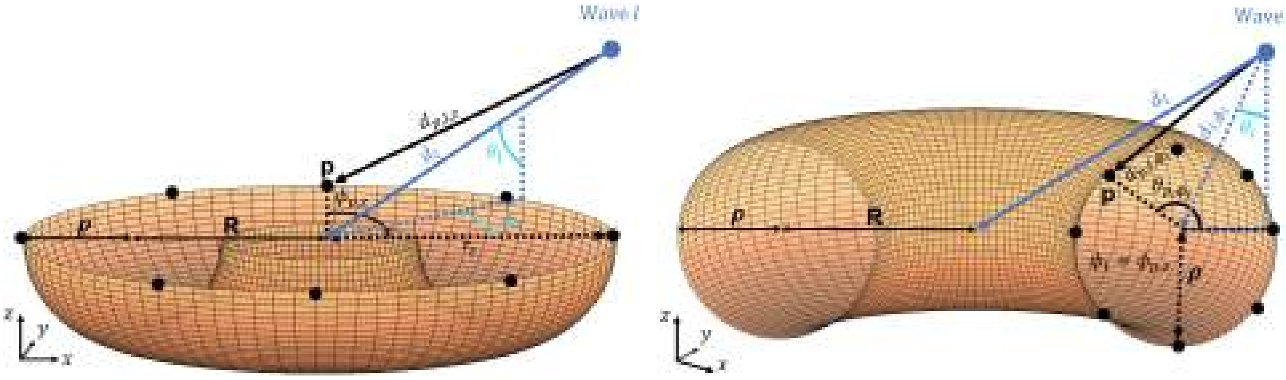

(a) (b)

Fig. 1. Torus geometry: Representation of the circles arranged in (a) the XY plane, and (b) Φ_lZ plane.

in either single-path or multipath environments. This is a remarkable feature of the proposed method, as a joint 3D-DoA and ToA characterization is rarely found in the literature. Moreover, the accuracy in the joint DoA and ToA estimation is improved with respect to previous state-of-art frequency-invariant beamformers. This is essentially due to the geometry of the torus. The geometrical disposal of spatial samples in a toric array efficiently exploits the geometrical disposal of the spatial samples for an optimal estimation. Within a torus, multiple concentric circular arrays can be defined in horizontal planes, thus improving the estimation of the azimuth angle. Then, the optimal vertical plane, which includes a single circular array, is selected for a precise estimation of the elevation angle and time of arrival. Finally, it is worth mentioning that the proposed technique works efficiently in under-sampling conditions, which can be used to reduce processing time and the number of samples employed.

The document is organized as follows. Section II presents the mathematical framework for the joint characterization of the azimuth, elevation and time of arrival. It also discusses some practical considerations, advantages and limitations of the method. Section III illustrates some numerical examples, including single-path and multipath scenarios, in order to validate the proposed theoretical framework. A parametric study on how the main involved parameters affect the performance of the method is also carried out. Finally, general conclusions are drawn in Section IV.

II. THEORETICAL FRAMEWORK

A torus is defined as a closed surface formed by the Cartesian product of two circles. Parametrically, it can be defined as:

$$\begin{aligned} x(\phi,\theta) &= (R+\rho\sin\theta)\cos\phi \\ y(\phi,\theta) &= (R+\rho\sin\theta)\sin\phi, \\ z(\phi,\theta) &= -\rho\cos\theta \end{aligned} \tag{1}$$

where R is the distance from the torus center to the tube center, and ρ is the tube radius. ϕ is the azimuth angle, which represents the rotation around the axis of revolution. θ is the elevation angle, i.e., the rotation angle around the tube. $R > \rho$ is considered in order to ensure a ring torus shape.

Due to the nature of this geometry, circles can be generated in the XY plane given a specific z height. Since $z(\phi,\theta)$ only depends on θ for any value of ϕ, θ can be directly substituted in $x(\phi,\theta)$ and $y(\phi,\theta)$ as $\sin(\theta) = \sin(\arccos(-z/\rho)) = \sqrt{1-(-z/\rho)^2}$. This expression can be further simplified, leading (1) to:

$$\begin{aligned} x(z,\phi) &= (R \pm \sqrt{\rho^2 - z^2})\cos\phi \\ y(z,\phi) &= (R \pm \sqrt{\rho^2 - z^2})\sin\phi. \end{aligned} \tag{2}$$

An example of circumference in this XY plane is illustrated in Fig. 1(a) when $z = 0$. Similarly to the previous case, two circumferences are found in the plane formed by the Z-axis and a given angle ϕ. Fig 1(b) shows this plane when $\phi = \phi_l$, which represents a smart selection of the plane given the ϕ-axis, as will be detailed in later sections. These properties of the torus to define circumferences in several planes will be used to accurately estimate the 3D DoA (azimuth ϕ and elevation θ), as well as the ToA τ in multipath environments.

Now, let us assume an incident spherical wave l characterized by the azimuth angle ϕ_l, elevation θ_l and time of arrival τ_l. This signal impinges on a torus formed by P samples on each circumference arranged in the XY plane, and P samples on each circumference of the Φ_lZ plane, for a total of P^2 spatial samples. The estimation of the three previous parameters is performed in two steps: (i) The first one takes advantage of the circumferences located in the XY plane to make an accurate estimation of ϕ_l. (ii) The second step makes use of the previous value of ϕ_l to accurately estimate θ_l and τ_l.

A. Azimuth of Arrival (AoA)

In the first step, the frequency response at the center of the circumferences lying in the XY plane is expressed as

$$H_{l,z}(f) = \kappa_l \mathrm{e}^{\mathrm{j}2\pi f \tau_{l,z}} = \kappa_l \mathrm{e}^{\mathrm{j}2\pi f(\tau_l+\tau_z)}, \tag{3}$$

where κ_l stands for the complex amplitude for the l-th wave and $\tau_{l,z}$ for the delay of the l-th wave for a given height z. The term $\tau_{l,z}$ can be expressed as $\tau_{l,z} = \tau_l + \tau_z$, where τ_l is the delay characterized at the center of the torus ($z = 0$) and τ_z is an additional delay introduced by the height z. According to the torus geometry, the largest difference between τ_z values is

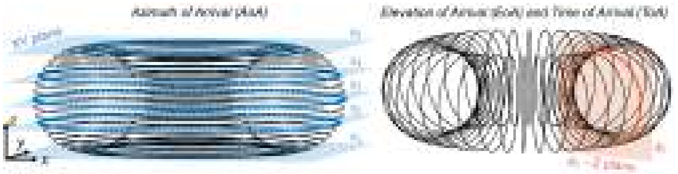

Fig. 2. Planes where the circular arrays are placed on the torus. P circular arrays can be found in the XY plane given several heights z (left panel). For visualization purposes, only five circles are marked in blue in the XY plane. A single circular array is located in the Φ_lZ plane (right panel). The P circular arrays in the XY plane and the single array in the Φ_lZ plane allow us to estimate the AoA and the pair {EoA, ToA}, respectively.

given by $2\rho/c$, which is the diameter of the torus tube divided by the wave propagation speed, i.e., the speed of light c. This is the case for $\theta_l = 0°$ and $\theta_l = 180°$. For $\theta_l = 90°$, the incident wave impinges on the different circles at the same time, so the difference between values of τ_z becomes zero. Generally, it is satisfied that $\tau_l \gg 2\rho/c$, so we can assume that $\tau_{l,z} \approx \tau_l$. This effect generates a slight temporal spread in the time domain estimation, which will be analyzed in the following sections. Regardless of this fact, note that there is no negative effect on the estimation since the ToA is not yet estimated in this step.

For each circle at a height z, $H_{p,l,z}(f)$ reads as the channel frequency response acquired at the p-th sample. Since the spatial samples are uniformly distributed around the position of $H_{l,z}(f)$, $H_{p,l,z}(f)$ is given by

$$H_{p,l,z}(f) = \left(\frac{d_{l,z}}{d_{p,l,z}}\right)^{\gamma/2} H_{l,z}(f)\, \mathrm{e}^{\mathrm{j}2\pi f \Delta d_{p,l,z}/c}\,, \tag{4}$$

where $d_{l,z} = c\,\tau_{l,z}$, and $d_{p,l,z}$ is the distance traveled by the wave to reach the p-th spatial sample. Therefore, the term $\left(d_{l,z}/d_{p,l,z}\right)^{\gamma/2}$ is the attenuation factor given the distance between the torus center at a height z, and the p-th sample for a path loss exponent γ. The complex exponential term stands for the phase shift introduced by the additional distance to the center of the torus, where

$$\Delta d_{p,l,z} = d_{l,z} - d_{p,l,z}. \tag{5}$$

According to the torus geometry, the previous term can be expanded as

$$\Delta d_{p,l,z} = d_{l,z} - \sqrt{d_{l,z}^2 + {r_z}^2 - 2 d_{l,z} r_z \sin(\theta_l)\cos\left(\phi_l - \phi_{p,z}\right)} \tag{6}$$

where $\phi_{p,z}$ is the azimuth angle for the p-th sample located at a height z, which is evenly spaced in the angular domain $\phi \in [0, 2\pi)$. The term r_z stands for the radius of the circles deployed at different heights. From (2), it is defined as

$$r_z = R \pm \sqrt{\rho^2 - z^2}. \tag{7}$$

Through the expansion in Taylor series, (6) can be approximated as

$$\Delta d_{p,l,z} \approx r_z \sin(\theta_l)\cos(\phi_l - \phi_{p,z}). \tag{8}$$

which allows us to simplify (4) to

$$H_{p,l,z}(f) = \left(\frac{d_{l,z}}{d_{p,l,z}}\right)^{\gamma/2} H_{l,z}(f)\, \mathrm{e}^{\mathrm{j}2\pi f r_z \sin(\theta_l)\cos(\phi_l - \phi_{p,z})/c}\,, \tag{9}$$

As a starting point, this first step considers a fixed elevation incidence angle $\theta_l = 90°$. Although this approximation might seem restrictive, it is possible to perform an accurate estimation of the azimuth angle ϕ_l for several angles θ_l [37], while the estimation of the elevation angle θ_l is performed in a subsequent step. Additionally, $d_{l,z}/d_{p,l,z} \approx 1$ for $d_{l,z} \gg \Delta d_{p,l,z}$, i.e. the wave source is far away from the toric array (plane wave approximation). After these two considerations, (9) can be simplified to

$$H_{p,l,z}(f) = H_{l,z}(f)\, \mathrm{e}^{\mathrm{j}2\pi f r_z \cos(\phi_l - \phi_{p,z})/c}\,. \tag{10}$$

As observed in (10), phase and frequency components are linked in the complex exponential term. The Jacobi-Anger identity, given by [39]

$$\mathrm{e}^{\mathrm{j}\upsilon \cos\alpha} = \sum_{n=-\infty}^{\infty} \mathrm{j}^n J_n(\upsilon)\mathrm{e}^{\mathrm{j}n\alpha}\,, \tag{11}$$

allows us to decouple phase (ϕ_l) and frequency (f) terms, extending (10) to

$$H_{p,l,z}(f) = H_{l,z}(f) \sum_{n=-\infty}^{\infty} \mathrm{j}^n J_{n,z}\left(\frac{2\pi f r_z}{c}\right) \mathrm{e}^{\mathrm{j}n(\phi_l - \phi_{p,z})}. \tag{12}$$

The former step opens up the possibility of a solution based on nearly frequency-independent beamformers (FIBs). Note that $J_{n,z}(\cdot)$ is the Bessel function of the first kind of order n for the circular array with radius r_z.

The former expression can be projected onto basis functions of the form $\mathrm{e}^{\mathrm{j}m\phi_{p,z}}$ that excite the frequency response $H_{p,l,z}(f)$ when $\phi_{p,z} = \phi_l$. This method is known as phase-mode expansion [31], [38], which provides the phase-mode domain $\widehat{H}_{m,l,z}(f)$:

$$\begin{aligned}
&\widehat{H}_{m,l,z}(f) \\
&= \frac{1}{P} \sum_{p=0}^{P-1} H_{p,l,z}(f)\, \mathrm{e}^{\mathrm{j}m\phi_{p,z}} \\
&= H_{l,z}(f) \sum_{n=-\infty}^{+\infty} \mathrm{j}^n J_{n,z}\left(\frac{2\pi f r_z}{c}\right) \mathrm{e}^{\mathrm{j}n\phi_l} \sum_{p=0}^{P-1} \frac{\mathrm{e}^{\mathrm{j}(m-n)\phi_{p,z}}}{P}.
\end{aligned} \tag{13}$$

Note that the rightmost term $(1/P)\sum_{p=0}^{P-1} \mathrm{e}^{j(m-n)\phi_{p,z}}$ becomes zero when $n \neq m$. Otherwise, when $n = m$ this term is one, leading to:

$$\widehat{H}_{m,l,z}(f) = H_{l,z}(f)\, \mathrm{j}^m J_{m,z}\left(\frac{2\pi f r_z}{c}\right) \mathrm{e}^{\mathrm{j}m\phi_l}. \tag{14}$$

This excited frequency response $\widehat{H}_{m,l,z}(f)$ contains the frequency-dependent component, which can be eliminated by the optimal choice of an inverse filter $W_{m,z}(f)$. Mathematically, the phase-mode response $H_{m,l,z}(f)$ can be calculated as

$$\begin{aligned} H_{m,l,z}(f) &= \widehat{H}_{m,l,z}(f)\, W_{m,z}(f) \\ &= H_{l,z}(f)\, \mathrm{j}^m J_{m,z}\left(\frac{2\pi f r_z}{c}\right) W_{m,z}(f)\, \mathrm{e}^{\mathrm{j}m\phi_l} \\ &= H_{l,z}(f)\, \mathrm{e}^{\mathrm{j}m\phi_l} = \kappa_l\, \mathrm{e}^{\mathrm{j}2\pi f \tau_{l,z}}\, \mathrm{e}^{\mathrm{j}m\phi_l}, \end{aligned} \tag{15}$$

with

$$W_{m,z}(f) = \frac{2}{\mathrm{j}^m \left[J_{m,z}\left(\frac{2\pi f r_z}{c}\right) - \mathrm{j}\, J'_{m,z}\left(\frac{2\pi f r_z}{c}\right)\right]}, \tag{16}$$

where $J'_{m,z}(\cdot)$ is the first derivative of $J_{m,z}(\cdot)$. This filter has demonstrated to be an optimal choice since $J'_{m,z}(\cdot)$ avoid deep nulls in $W_{m,z}(f)$, providing larger bandwidth for the estimation [37].

In order to improve the estimation, the phase-mode average domain between all the circles at different heights z is calculated, being the phase-mode expansion

$$H_{m,l}(f) = \frac{1}{P} \sum_{z=z_0}^{z_{P-1}} H_{m,l,z}(f) \approx H_l(f) e^{\mathrm{j}m\phi_l}. \tag{17}$$

The distribution of the P circles in the XY plane is shown in Fig. 2. These circles are distributed in the range of heights $z_i \in [-\rho, \rho]$. Previous work has shown that the use of multiple arrays significantly improves the estimation of DoA and ToA [32], [35], [36]. Note that $H_l(f)$ represents the frequency response at the origin.

In multipath environments ($l > 1$), the phase-mode response for every wave impinging the toric array is the sum of the individual contribution from each wave, which leads to

$$H_m(f) = \sum_{\forall l} H_{m,l}(f) = \sum_{\forall l} H_l(f)\, \mathrm{e}^{\mathrm{j}m\phi_l}. \tag{18}$$

The 2-D Discrete Fourier Transform (DFT) of the former expression provides the joint azimuth DoA and ToA estimation as:

$$\widetilde{\mathbf{H}}(\phi, \tau) = \sum_{\forall m} \sum_{\forall k} H_m(f)\, \mathrm{e}^{-\mathrm{j}\left(\frac{m\phi}{M} + \frac{2\pi(f_{\min} + k f_s)\tau}{K}\right)}, \tag{19}$$

where K stands for the number of frequency samples and frequency spacing $f_s = B/K$ with B being the signal bandwidth and M is the total number of considered phase modes. The term f_{min} is the lowest frequency considered in the bandwidth and m and k are the indexes that characterize M phase modes and K frequency samples, respectively. The ToA τ_l is extracted through the frequency f obtained in $\mathrm{e}^{\mathrm{j}2\pi f \tau_l}$, while ϕ_l is related to the phase-mode domain in the complex exponential $e^{\mathrm{j}m\phi_l}$ [see (15)]. Consequently, the time domain resolution and the maximum observable time are given by $1/B$ and $(K-1)/B$. Similarly, the angular resolution is given by $2\pi/M$ in the phase domain. The previous expression can be efficiently calculated through the Fast Fourier Transform (FFT) algorithm.

B. Elevation of Arrival (EoA) and Time of Arrival (ToA)

The second step takes advantage of the previous estimation of the azimuth ϕ_l to accurately estimate the elevation angle θ_l and the time of arrival τ_l. Basically, the same P^2 spatial samples previously defined to generate P circles with P samples in the XY plane can be used to form circles in the planes defined by the $\phi - Z$ axes. These P circles, also with P samples per circle, are those contained in perpendicular cuts to the tube [see Fig. 1(b)].

Similarly to (3), the frequency response at the center of the tube, given an angle ϕ_l, is

$$H_{l,\phi_l}(f) = \eta_l\, \mathrm{e}^{\mathrm{j}2\pi f \tau_{l,\phi_l}}, \tag{20}$$

where η_l is the complex attenuation, and τ_{l,ϕ_l} is the delay of the wave l from the source to the tube center at ϕ_l. Therefore, the frequency response at the p-th sample reads

$$H_{p,l,\phi_l}(f) = \left(\frac{d_{l,\phi_l}}{d_{p,l,\phi_l}}\right)^{\gamma/2} H_{l,\phi_l}(f)\, \mathrm{e}^{\mathrm{j}2\pi f \Delta d_{p,l,\phi_l}/c}, \tag{21}$$

with

$$\Delta d_{p,l,\phi_l} = d_{l,\phi_l} - \sqrt{d_{l,\phi_l}^2 + \rho^2 - 2 d_{l,\phi_l} \rho \cos(\theta_l - \theta_{p,\phi_l})}. \tag{22}$$

After Taylor's series expansion (8), we arrive to

$$H_{p,l,\phi_l}(f) = \left(\frac{d_{l,\phi_l}}{d_{p,l,\phi_l}}\right)^{\gamma/2} H_{l,\phi_l}(f)\, \mathrm{e}^{\mathrm{j}2\pi f \rho \cos\left(\theta_l - \theta_{p,\phi_l}\right)/c}, \tag{23}$$

Note that, by choosing the ring coincident with the ϕ_l estimation, we ensure to align the wave incidence plane with the distribution of the P tube samples. Thus, the sine dependent variable term that appeared in eqs. (6), (8) and (9), becomes constant and is removed from eq. (23). Visually, the chosen circular array laying in the Φ_lZ plane is illustrated in Fig. 2. This fact ensures the correct estimation of θ_l and τ_{l,ϕ_l} as the optimal estimation is provided when the plane of incidence coincides with the plane where the spatial sampling lies [35].

Therefore, considering a negligible attenuation between the edge and the center of the tube, $H_{p,l,\phi_l}(f)$ is given by

$$H_{p,l,\phi_l}(f) = H_{l,\phi_l}(f)\, \mathrm{e}^{\mathrm{j}2\pi f \rho \cos\left(\theta_l - \theta_{p,\phi_l}\right)/c}, \tag{24}$$

The former expression is similar to the one proposed in (10), with the difference of: (i) considering a radius ρ; (ii) the cosine term depends on the elevation θ_l; and (iii) the considered center is that of the tube and not that of the torus. Hence, a development in the form of basis functions $\mathrm{e}^{\mathrm{j}m\theta_{p,\phi_l}}$, and the choice of an optimal $W_{m,\phi_l}(f)$ filter, similar to that in (11)-(16), results in

$$H_{m,l,\phi_l}(f) = \eta_l\, \mathrm{e}^{\mathrm{j}2\pi f \tau_{l,\phi_l}}\, \mathrm{e}^{\mathrm{j}m\theta_l}. \tag{25}$$

The summation of the multiple incident waves (18) leads to $H_{m,\phi_l}(f)$. Finally, the application of the 2-D FFT to $H_{m,\phi_l}(f)$ provides the joint angular-time domain for the DoA elevation angle θ and the ToA at the center of the tube τ_{ϕ_l}, i.e., $\widetilde{\mathbf{H}}(\theta, \tau_{\phi_l})$. According to the torus geometry, the delay at the center of the tube, τ_{l,ϕ_l}, is related to the delay at the center of the torus, τ_l, as follows:

$$\tau_l - \tau_{l,\phi_l} = \frac{R\,|\sin(\theta_l)|}{c}. \tag{26}$$

This last step completely characterizes the DoA and ToA of the l-th wave by extracting the angles ϕ_l, θ_l, and the time τ_l.

C. *Considerations of the method*

Subsections II.A and II.B have presented the theoretical framework for the 3D characterization of the communication channel. Although the method has been shown to work correctly in 2D scenarios with several geometries, due to some simplifications that are carried out, it is necessary to perform a correct assignment of the considered parameters. These approximations involve the appearance of artifacts, i.e. spectral contributions in $\widetilde{\mathbf{H}}(\phi, \tau)$ and $\widetilde{\mathbf{H}}(\theta, \tau_{\phi_l})$ that may mislead with the real incident wave. As long as these artifacts are controlled, the characterization can be properly performed. For this purpose, we define a metric Δ, which indicates the difference between the power of the incident signal and the largest artifacts. If the value of Δ is greater than 0 dB, the incident signal is distinguishable from the artifacts [35, Fig. 3].

Concerning the number of spatial samples P, it must be chosen in such a way that we ensure compliance with the Nyquist spatial sampling theorem, i.e., a separation between samples less than half wavelength. Otherwise, spatial aliasing appears, which translates into an increase in the level of the artifacts. Fundamentally, this depends on the radii considered for the circles in the different planes of the torus. In Section II.A, the boundary is given by the outer circle when $z = 0$, where $r_z = R + \rho$, while in Section II.B, the considered radius is directly ρ.

Given the maximum value of r_z, we can ensure that the sampling theorem is satisfied on the torus with P equispaced samples per circle if

$$2(R + \rho)\sin(\pi/P) < \lambda/2. \tag{27}$$

Regarding the number of phase modes M, it can be demonstrated that $J_n(\cdot) \approx 0$ for a sufficiently large order n [33], [39]. Thus, M must be chosen so that it is lower than the above threshold. Otherwise, the denominator in (16) would tend to zero, generating numerical instabilities in the method.

Logically, the greater the number of filters, the greater the required computational time. The number of raw $W_{m,z}(f)$ filters needed is $M \times P$ in the first step. However, by taking advantage of the reflection (mirror) symmetry of the torus on the z-axis, the number of filters can be decreased to $M \times (P/2 + 1)$. Also, by taking advantage of the symmetry of the Bessel functions for positive and negative indexes m [$J_{-m}(x) = (-1)^m J_m(x)$], the total number of filters is reduced to $(M/2 + 1) \times (P/2 + 1)$. In the second step, only a single circle is considered, thus, $M/2 + 1$ filters are needed in this case. In total, $(M/2 + 1) \times (P/2 + 2)$ filters are required for a joint characterization of the AoA, EoA and ToA.

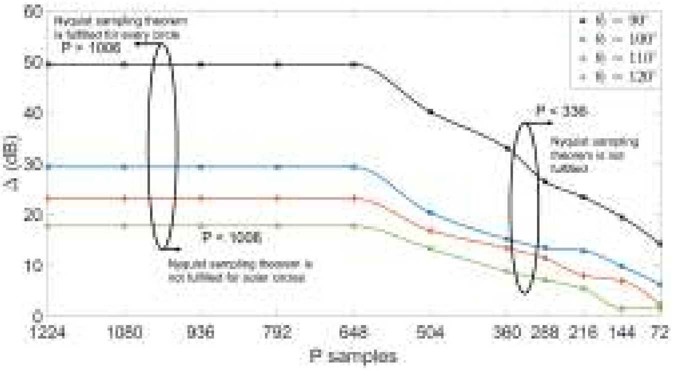

Fig. 3. Relation between the power of the estimated wave and artifacts (Δ) as a function of the number of spatial samples P for several incident elevation angles θ_l. Parameters of the considered scenario: $R = 0.5$ m, $\rho = 0.25$ m, $\phi_l = 180°$ and $\tau_l = 15$ ns. Non-compliance with the spatial sampling theorem increases the artifacts, thus decreasing the value of Δ in the estimation.

III. VALIDATION OF THE METHOD

This Section discusses and validates several aspects of the method presented in Section II. Specifically, a parametric study shows the main implications of the different parameters involved in the joint characterization of the AoA, EoA and ToA. According to the torus geometry, several aspect ratios, i.e., R/ρ, and sizes are considered to show the good performance of the method for diverse cases. Later, the joint estimation is validated through simulations at several frequency ranges for different scenarios based on both single-path and multipath scenarios.

A. *Parametric analysis*

Regarding the physical geometry of the torus, R, ρ and P are the main parameters to be considered. As previously stated, these are directly related to the Nyquist spatial sampling theorem [see (27)]. In order to analyze the effect of fulfilling this theorem, it is considered a case with a single-path scenario impinging the toric array with $\tau_l = 15$ ns ($d_l = 4.5$ m), and $\phi_l = 180°$ for several values of θ_l. The torus size is given by $R = 0.5$ m and $\rho = 0.25$ m, with a frequency range that goes from 28 GHz to 32 GHz ($B = 4$ GHz) and $K = 200$ frequency samples. $M = 300$ phase modes are considered. Given R, ρ, and $f_{max} = 32$ GHz ($\lambda_{min} = 9.37$ mm), the Nyquist theorem is satisfied even for outer circles ($r_z = 0.75$ m) if $P > 1006$. For $336 < P < 1006$, it is exclusively satisfied for some inner circles. If $P < 336$, it is not fulfilled even for the inner circles ($r_z = 0.25$ m).

For the given parameters, Fig. 3 illustrates the value of the metric Δ when the number of samples P is varied. Note that a higher value of Δ implies a better DoA and ToA estimation, as the level of the artifacts is reduced. For the case $\theta_l = 90°$, the quality of the estimation is optimal due to the approximation performed in (10). However, even non-coincident waves in the elevation plane ($\theta_l \neq 90°$) provide good results for Δ.

Concerning the number of spatial samples P, a flat behavior is observed in Fig. 3 when the Nyquist theorem is fulfilled ($P > 1006$). This implies that the estimation will not improve

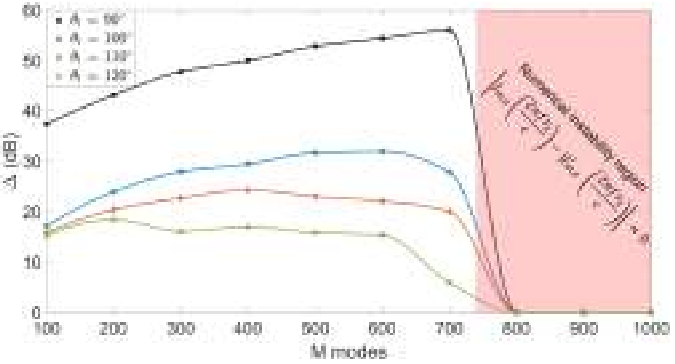

Fig. 4. Relation between the power of the estimated wave and artifacts (Δ) as a function of the number phase modes M for several elevation angles θ_l. Parameters of the considered scenario: $R = 0.75$ m, $\rho = 0.25$ m, $\phi_l = 180°$ and $\tau_l = 15$ ns.

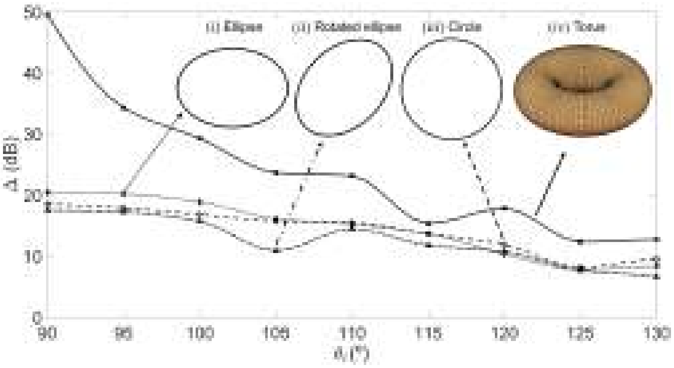

Fig. 5. Degradation of the estimation as θ_l increases for the joint AoA ($\phi_l = 180°$) and ToA ($\tau_l = 15$ ns) values. Four different geometries are considered: (i) elliptical array, (ii) rotated elliptical array, (iii) circular array, and (iv) toric array.

even if the number of samples is increased. In an intermediate region ($336 < P \leq 1006$), even though sampling is not performed correctly for the outer circles, a flat behavior is still observed until the sampling theorem is no longer satisfied for about half of the circles, i.e., $r_z = R$. This fact contrasts with estimation on single arrays, where not complying with the sampling theorem dramatically increases the artifacts [35]. The geometry of the torus, which supports estimation from concentric circles [see (17)], allows the number of P sensors to be reduced below the sampling theorem, compensating for this decrease with the larger number of arrays deployed. When P is further reduced ($P < 336$), the value of Δ begins to significantly decay. In any case, note that despite the presence of artifacts, $\Delta > 0$ dB, which makes the incident wave distinguishable from the artifacts even for a reduced number of samples.

In a second study, the influence of the number of phase modes M in the DoA and ToA estimation is analyzed. All the parameters remain the same as in the previous experiment, except from the torus geometry. The parameters of the torus are: $R = 0.75$ m, $\rho = 0.25$ m and $P = 1440$. Fig. 4 shows the value of Δ when varying the number of considered phase modes M. Above a certain threshold, approximately $M > 700$ in this case, $J_n(\cdot) \approx 0$. This causes numerical instabilities in the computation of the filter $W_{m,z}(f)$ [eq. (16)] as the denominator approaches zero. As a result, the quality of the estimation significantly degrades. In the range $300 < M < 600$, an almost flat region is found, showing that, regardless of the number M chosen, the estimation performs correctly. Finally, if M is even more decreased, the estimation tends to degrade, besides decreasing the angular resolution (see Sec. II.A). Ideally, one should operate in the nearly flat region where Δ approaches the maximum. This region depends exclusively on the $2\pi f r_z/c$ argument of the Bessel function, so a prior analysis of the optimal working regions is essential.

Finally, to demonstrate the potential of the toric geometry, the metric Δ is compared with previous two-dimensional geometrical approaches that make use of frequency-independent beamformers and phase-mode transformations. For this purpose, we consider the same incident wave (ϕ_l and τ_l) as in the previous experiments, and the same frequency range, B and K. Fig. 5 shows the value of Δ, given the azimuth (AoA) – time (ToA) domain, for different elevation angles θ_l given four different geometries: (i) elliptical array, (ii) rotated elliptical array, (iii) circular array and (iv) toric array. The number of phase modes is fixed to $M = 300$. Both elliptical arrays have a semi-major axis of 0.5 m, an eccentricity of 0.7, and $P = 720$. Additionally, the rotated ellipse includes an angle rotation of 45°. For further details regarding the estimation with elliptical arrays, the reader is referred to [35], [36]. The single circular array has a radius of 0.5 m, and $P = 720$. The toric array parameters are $R = 0.5$ m, $\rho = 0.25$ m and $P = 720$. It can be appreciated that the toric array estimation outperforms all other geometries. This is due to the joint estimation based on the use of the concentric circular arrays that are discerned in the toroid geometry itself. Note that this sample distribution will later allow us to perform the accurate estimation of the elevation angle θ_l, while in the other geometries, it is not possible due to the two-dimensional distribution of the samples.

B. Single-path Characterization

Once some of the key parameters for the method have been analyzed, this Section illustrates some examples of the 3D joint characterization of the AoA (ϕ_l), EoA (θ_l), and ToA (τ_l). Let us assume a frequency range $f \in [58, 62]$ GHz with $B = 4$ GHz and $K = 200$ frequency samples. According to Section II.A, for $R = 0.25$ m and $\rho = 0.125$ m, $P = 720$ spatial samples and $M = 300$ phase modes are enough to reduce the level of the artifacts and ensure a proper estimation. Let us assume a wave impinging the toric array with $\tau_l = 20$ ns, $\phi_l = 45°$, and $\theta_l = 90°$. Fig. 6(a) shows the azimuth–time domain extracted from the phase-mode transformation. As observed, the value of the metric Δ is maximum around the correct values of the AoA ($\phi_l = 45°$) and ToA ($\tau_l = 20$ ns). The level of the artifacts is below -30 dB, so they do not appear in the figure. This effect is obtained due to the joint estimation of the multiple concentric circles contained in the torus.

Given the azimuth estimation, the circumference lying on this angle ϕ_l is chosen. Fig. 6(b) illustrates the elevation–time

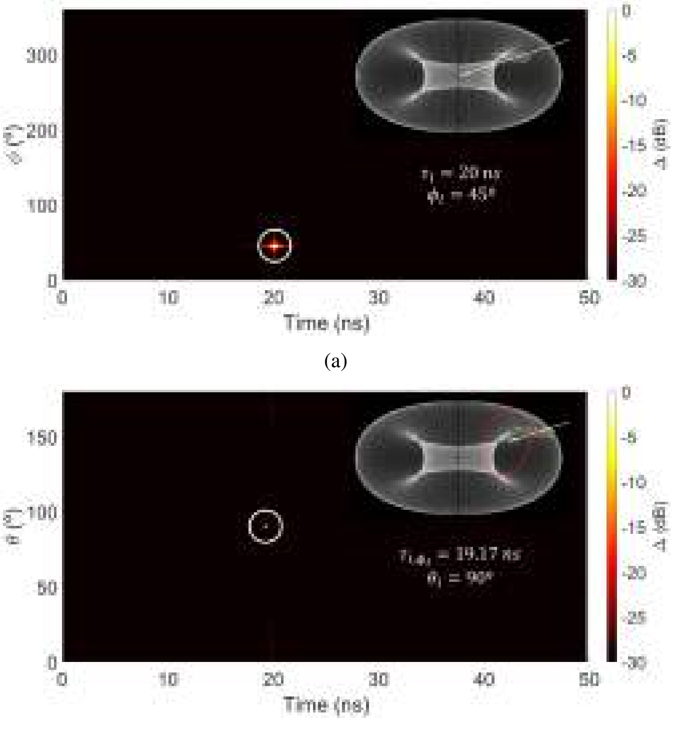

(a)

(b)

Fig. 6. Joint azimuth ($\phi_l = 45°$), elevation ($\theta_l = 90°$), and time ($\tau_l = 20$ ns) of arrival estimation for a toric array. (a) Azimuth–time domain. (b) Elevation–time domain. Parameters of the scenario: $R = 0.25$ m, $\rho = 0.125$ m, $P = 720$, $M = 300$ and $f \in [58, 62]$ GHz.

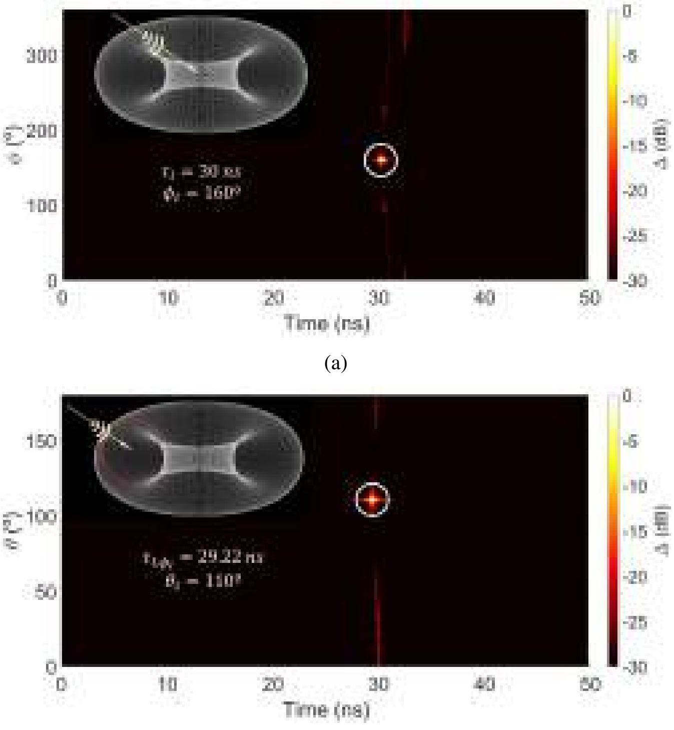

(a)

(b)

Fig. 7. Joint azimuth ($\phi_l = 160°$), elevation ($\theta_l = 110°$), and time ($\tau_l = 20$ ns) of arrival estimation with a toric array. (a) Azimuth–time domain. (b) Elevation–time domain. Parameters of the scenario: $R = 0.25$ m, $\rho = 0.125$ m, $P = 720$, $M = 300$ and $f \in [58, 62]$ GHz.

domain. Note that the value of Δ is maximum at the EoA ($\theta_l = 90°$) and ToA ($\tau_{l,\phi_l} = 19.25$ ns). According to eq. (26), the exact time of arrival should be 19.17 ns, appearing this difference due to the temporal resolution $1/B$. Nonetheless, this value is within the resolution range of the method, being a correct τ_{l,ϕ_l} estimation. In Fig. 6(b), the level of the artifacts is below -23 dB.

In a second experiment for the single-path scenario, we consider a wave with $\phi_l = 160°$, $\theta_l = 110°$, and $\tau_l = 30$ ns. The additional parameters remain identical to the previous experiment. Figs. 7(a) and 7(b) illustrate the azimuth–time and elevation–time domains, respectively, for the joint estimation of this incident wave. As observed, the maximum value of Δ coincides with the AoA, EoA and ToA positions in both figures. Artifacts amplitude appears 20.3 dB and 18.4 dB below the correct estimation in Figs. 7(a) and 7(b), respectively. Note that the temporal dispersion explained in Section II.A due to an elevation $\theta_l \neq 90°$ is not appreciable because of the high working frequencies ($f_c = 60$ GHz), since the physical size of the array decreases notably, being $\tau_{l,z} \approx \tau_l$. The two previous experiments have shown the ability to correctly identify waves in the three-dimensional space and in the mm-wave frequency range.

C. Multipath Characterization

The previous section has validated the performance of the FIB for the 3D channel characterization in a single-path scenario. According to (18), for a multipath scenario ($l > 1$), the spectral response of the beamformer is directly the sum of the responses of each incident wave. However, in practice, the amplitude of the spectral response is actually dependent on the elevation θ_l due to the assumption made in (10). This fact was corroborated in Fig. 5 with differences of up to 30 dB when going from $\theta_l = 90°$ to $\theta_l = 130°$. This implies that, under the assumption of a set of L incident waves with similar θ_l, the DoA-ToA domain provides a correct characterization of the scenario. However, if this set of waves has θ_l different from each other, the waves with θ_l close to 90° may fade the rest of the incident waves. Therefore, estimation in multipath environments with several θ_l values, i.e., the most general case, can be performed based on a subtraction strategy of the previously estimated waves. Given the estimation of the l-th path, the influence of the previous $l-1$ paths can be removed as $\sum_{n=l}^{L} H_{p,l,z}(f) = \sum_{n=1}^{L} H_{p,l,z}(f) - \sum_{n=1}^{l-1} H_{p,l,z}(f)$. If the estimation is performed correctly, the effect of the substracted $l-1$ waves is removed from $\widetilde{\mathbf{H}}(\phi, \tau)$ and $\widetilde{\mathbf{H}}(\theta, \tau_{\phi_l})$. In case that the subtraction is not effective due to the temporal ($1/B$ seconds) and angular ($2\pi/M$ radians) resolution values, one can proceed to reconstruct $H_{p,z}(f)$ as a discretized set of waves based on a low-complexity search with expectation-maximization algorithms such as Space Alternating Generalized Expectation-maximization (SAGE) [34], [40].

To summarize the rationale previously described, Algorithm 1 presents a pseudocode that illustrates the main steps to be followed in a general multipath environment. The method, originally based on DoA and ToA estimation for circular arrays, has been generalized to toric arrays where the geometry of the torus has been exploited to define circles in multiple planes. Through an appropriate choice of the parameters involved in the method, good performance of the characterization will be obtained.

In order to validate the multipath characterization, a scenario with $L = 3$ waves is simulated. The first, second and third wave parameters are: first ($\phi_1 = 270°$, $\theta_1 = 90°$, $\tau_1 = 30$ ns), second ($\phi_2 = 225°$, $\theta_2 = 60°$, $\tau_2 = 20$ ns), and third ($\phi_3 = 315°$, $\theta_3 = 120°$, $\tau_3 = 40$ ns), respectively. For a frequency range $f \in [58, 62]$ GHz with $K = 200$ frequency samples, a toric array with $R = 0.25$ m, $\rho = 0.125$ m, $P = 720$, $M = 300$ is chosen. Fig. 8 shows the whole process for the multipath estimation of the three waves. Each column illustrates the estimation of the l-th wave. For the first path (left column), $\widetilde{\mathbf{H}}(\phi, \tau)$ domain is maximum around the pair $\{\phi_1, \tau_1\}$. Note that the other two waves are not visible in a dynamic range of 30 dB due to the amplitude difference introduced by the different values of θ_l (see Fig. 5). According to ϕ_1 estimation, $\widetilde{\mathbf{H}}(\theta, \tau_{\phi_1})$ is calculated by taking into account the samples distributed through the ring with $\phi = 270°$. This domain is maximum for the pair $\{\theta_1, \tau_{1,\phi_1}\}$. The appearance of two vertical lines denotes the presence of two additional waves. In this first step, the estimation does not converge correctly for the two additional waves ($l = 2, 3$) because the plane of incidence is not close to the ring at $\phi = 270°$.

Given the first path estimation, we can proceed to estimate the second path after subtracting the first path from the signal $H_{p,z}(f)$. After the application of the phase mode transforma-

Algorithm 1 Joint Characterization of Azimuth, Elevation and Time of Arrival based on Toric Arrays. Multipath case.

```
Input: Channel Frequency Response samples
       at the toric array, i.e., $H_{p,z}(f)$.
Output: Azimuth, Elevation and Time of Arrival
        $\{\phi_l, \theta_l, \tau_l\}$.
for $l = 1 : L$
    Azimuth of Arrival (AoA)
    if $l > 1$
        $H_{p,z}(f) = \sum_{n=l}^{L} H_{p,l,z}(f)$
    end
    $\widehat{H}_{m,z}(f) = 1/P \sum_{p=0}^{P-1} H_{p,z}(f)\, e^{jm\phi_{p,z}}$
    $H_{m,z}(f) = \widehat{H}_{m,z}(f)\, W_{m,z}(f)$
    $H_m(f) = \sum_z H_{m,z}(f)$
    $\widetilde{\mathbf{H}}(\phi, \tau) = \text{2-D FFT}\{H_m(f)\}$
    $\phi_l = \arg\max_{\phi,\tau} \left(\widetilde{\mathbf{H}}(\phi, \tau)\right)$
    Elevation of Arrival (EoA) and Time of Arrival (ToA)
    Choose $H_{p,\phi_l}(f)$ based on the estimated $\phi_l$
    $\widehat{H}_{m,\phi_l}(f) = 1/P \sum_{p=0}^{P-1} H_{p,\phi_l}(f)\, e^{jm\theta_{p,\phi_l}}$
    $H_{m,\phi_l}(f) = \widehat{H}_{m,\phi_l}(f)\, W_{m,\phi_l}(f)$
    $\widetilde{\mathbf{H}}(\theta, \tau_{\phi_l}) = \text{2-D FFT}\{H_{m,\phi_l}(f)\}$
    $\{\theta_l, \tau_{l,\phi_l}\} = \arg\max_{\theta,\tau_{\phi_l}} \left(\widetilde{\mathbf{H}}(\theta, \tau_{\phi_l})\right)$
    $\tau_l = R\,|\sin(\theta_l)|/c + \tau_{l,\phi_l}$
end
```

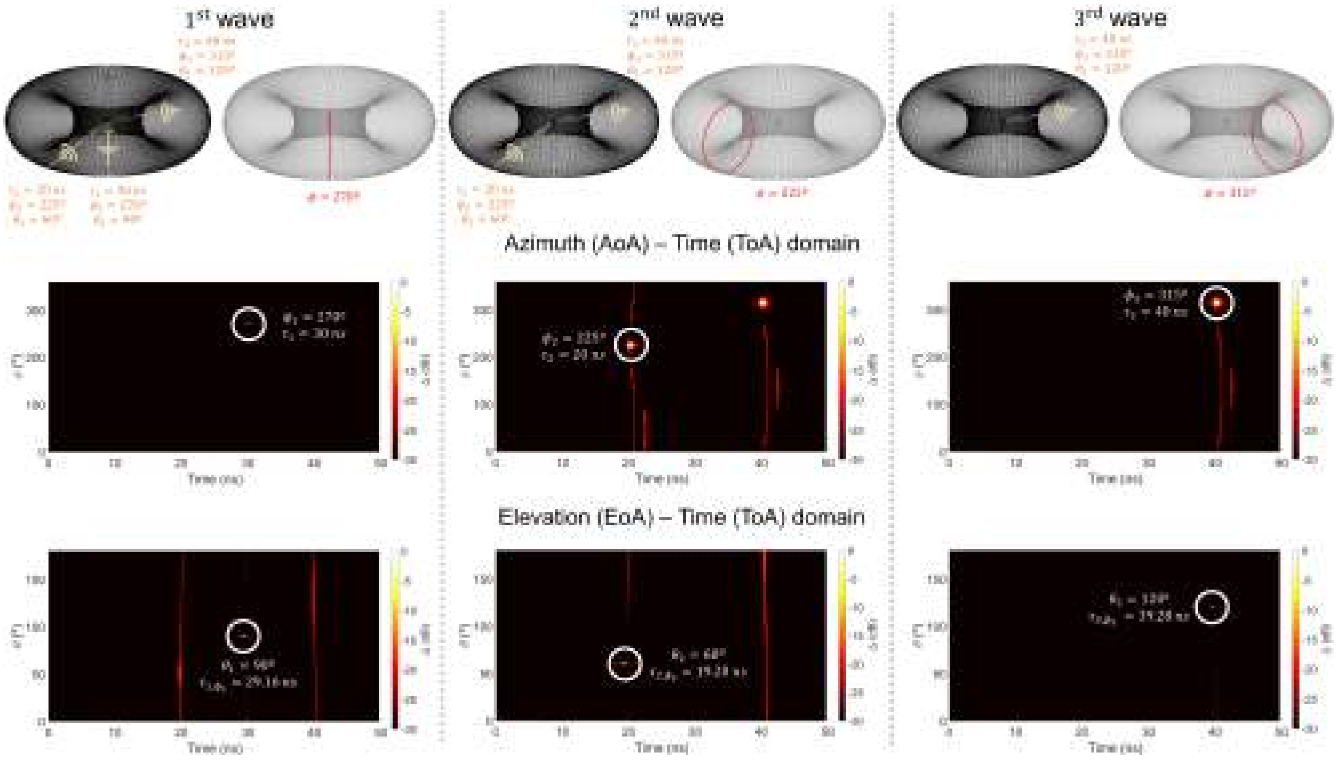

Fig. 8. Joint azimuth, elevation, and time of arrival estimation for a toric array with $R = 0.25$ m, $\rho = 0.125$ m, $P = 720$, $M = 300$, $K = 200$ and $f \in [58, 62]$ GHz. A multipath environment with $L = 3$ waves is considered. AoA: $\{\phi_1 = 270°, \phi_2 = 225°, \phi_3 = 315°\}$. EoA: $\{\theta_1 = 90°, \theta_2 = 60°, \theta_3 = 120°\}$. ToA: $\{\tau_1 = 30$ ns, $\tau_2 = 20$ ns, $\tau_3 = 40$ ns$\}$. Left, central and right panels show the estimation for the 1st, 2nd and 3rd wave, respectively.

tion, the inverse filter and the 2D-FFT, we arrive at $\widetilde{\mathbf{H}}(\phi, \tau)$. In this case, the two previously hidden waves are now visible (central column). Note that a slight time dispersion, previously stated in Sect. II.A, is observed since $\theta_l \neq 90°$. This dispersion is not particularly high due to the size of the array, where it is satisfied that $\tau_l \gg 2\rho/c$. Generally, the physical size of the array, and therefore ρ, decreases for higher frequencies, which implies a lower dispersion. Nonetheless, the estimation of τ_2 is performed from τ_{2,ϕ_2}, thus avoiding the uncertainty of the dispersion. Given $\phi_2 = 225°$, $\widetilde{\mathbf{H}}(\theta, \tau_{\phi_2})$ points out the values of θ_2 and τ_{2,ϕ_2}. No spectral amplitude is found around $\tau = 30$ ns since the first wave ($l = 1$) has been previously subtracted, while the third wave ($l = 3$) appears around $\tau = 40$ ns, although with high artifact amplitude in the elevation domain. This is because the azimuth estimation plane in the central panel ($\phi_2 = 225°$) is far from the plane where the third wave is located ($\phi_3 = 315°$). Finally, the third path (right column) is estimated in the same way as in the two previous cases, thus obtaining the trio of values formed by $(\tau_3, \phi_3, \theta_3)$.

IV. CONCLUSIONS

This work proposes a method for the joint 3D DoA (azimuth ϕ, elevation θ) and time of arrival (τ) characterization of communication channels. The method is based on the use of frequency-invariant (wideband) beamformer, originally developed for circular arrays and now extended to toric arrays. Through a phase-mode expansion of the channel frequency response in a toric array, this response can be approximated by a function that only depends on the ToA and the DoA coincident with the plane where the circle is located. By taking advantage of the torus definition, a closed surface formed by the Cartesian product of two circles, several arrays can be defined in multiple planes. Therefore, under an optimal distribution of spatial sampling in the torus, it is possible to use the same sampling to define circular arrays in several planes. Thus, an optimal choice of the samples generates multiple beamformers which are able to estimate the triplet $\{\phi, \theta, \tau\}$.

A parametric analysis of the variables involved has been performed, showing the optimal working range of these variables. Multiple simulations have been carried out for frequencies in the mm-wave range (30 GHz and 60 GHz) providing good results regarding the 3D propagation channel characterization in both, single-path and multipath scenarios. The proposed method is shown to improve the quality of the estimation by decreasing the level of the artifacts compared to other geometries such as single circles or ellipses, even enabling the estimation with under-sampling conditions due to the use of several arrays, i.e., several FIBs, simultaneously. Given the trend in the industry to move into the mm-wave frequency range and the growing number of propagation scenarios for cellular communications, the present method arises as a powerful tool to fully characterize these 3D environments. In addition, future research includes the selection of samples from the toric array based on oblique planes passing through the center of the torus. These planes generate circles, known as Villarceau circles, which define new circular arrays in relation to those already shown in this work, and which could improve the response of the frequency-invariant beamformers.

REFERENCES

[1] W. Jiang, B. Han, M. A. Habibi and H. D. Schotten, “The Road Towards 6G: A Comprehensive Survey,” *IEEE Open J. Commun. Soc.*, vol. 2, pp. 334-366, 2021.

[2] M. Xiao *et al.*, “Millimeter Wave Communications for Future Mobile Networks,” *IEEE J. Sel. Areas Commun.*, vol. 35, no. 9, pp. 1909-1935, 2017.

[3] A. Ramírez-Arroyo, L. García, A. Alex-Amor and J. F. Valenzuela-Valdés, “Artificial Intelligence and Dimensionality Reduction: Tools for Approaching Future Communications,” *IEEE Open J. Commun. Soc*, vol. 3, pp. 475-492, 2022.

[4] A. Ramírez-Arroyo, A. Alex-Amor, C. García-García, Á. Palomares-Caballero, P. Padilla and J. F. Valenzuela-Valdés, “Time-Gating Technique for Recreating Complex Scenarios in 5G Systems,” *IEEE Access*, vol. 8, pp. 183583-183595, 2020.

[5] A. Ramírez-Arroyo, A. Alex-Amor, C. García-García, Á. Palomares-Caballero, P. Padilla and J. F. Valenzuela-Valdés, “Time-Gating Technique to Emulate New Scenarios,” in *2021 15th European Conference on Antennas and Propagation (EuCAP)*, Dusseldorf, Germany, pp. 1-5, 2021.

[6] M. Koivisto *et al.*, “Joint Device Positioning and Clock Synchronization in 5G Ultra-Dense Networks,” *IEEE Trans. Wirel. Commun.*, vol. 16, no. 5, pp. 2866-2881, 2017.

[7] W. Saad, M. Bennis and M. Chen, ”A Vision of 6G Wireless Systems: Applications, Trends, Technologies, and Open Research Problems,” *IEEE Network*, vol. 34, no. 3, pp. 134-142, 2020.

[8] A. Dogra, R. K. Jha and S. Jain, “A Survey on Beyond 5G Network With the Advent of 6G: Architecture and Emerging Technologies,” *IEEE Access*, vol. 9, pp. 67512-67547, 2021.

[9] W. Tang *et al.*, “Wireless Communications With Reconfigurable Intelligent Surface: Path Loss Modeling and Experimental Measurement,” *IEEE Trans. Wirel. Commun.*, vol. 20, no. 1, pp. 421-439, 2021.

[10] X. Pei *et al.*, “RIS-Aided Wireless Communications: Prototyping, Adaptive Beamforming, and Indoor/Outdoor Field Trials,” *IEEE Trans. Commun.*, vol. 69, no. 12, pp. 8627-8640, 2021.

[11] Á. Palomares-Caballero *et al.*, “Enabling Intelligent Omni-Surfaces in the Polarization Domain: Principles, Implementation and Applications,” *IEEE Commun. Mag.*, in press, 2023.

[12] I. Rodriguez *et al.*, “5G Swarm Production: Advanced Industrial Manufacturing Concepts Enabled by Wireless Automation,” *IEEE Commun. Mag.*, vol. 59, no. 1, pp. 48-54, 2021.

[13] S. Vitturi, C. Zunino and T. Sauter, “Industrial Communication Systems and Their Future Challenges: Next-Generation Ethernet, IIoT, and 5G,” *Proc. IEEE*, vol. 107, no. 6, pp. 944-961, 2019.

[14] T. Jiang *et al.*, “3GPP Standardized 5G Channel Model for IIoT Scenarios: A Survey,” *IEEE Internet Things J.*, vol. 8, no. 11, pp. 8799-8815, 2021.

[15] C. R. Storck and F. Duarte-Figueiredo, “A survey of 5G technology evolution, standards, and infrastructure associated with vehicle-to-everything communications by Internet of Vehicles,” *IEEE Access*, vol. 8, pp. 117593–117614, 2020.

[16] K. Guan *et al.*, “Towards realistic high-speed train channels at 5G millimeter-wave band—Part I: Paradigm, significance analysis, and scenario reconstruction,” *IEEE Trans. Veh. Technol.*, vol. 67, no. 10, pp. 9112–9128, 2018.

[17] J. Rodríguez-Piñeiro, T. Domínguez-Bolaño, X. Cai, Z. Huang, and X. Yin, “Air-to-ground channel characterization for low-height UAVs in realistic network deployments,” *IEEE Trans. Antennas Propag.*, vol. 69, no. 2, pp. 992–1006, 2021.

[18] S. Aslam, M. P. Michaelides, and H. Herodotou, “Internet of Ships: A survey on architectures, emerging applications, and challenges,” *IEEE Internet Things J.*, vol. 7, no. 10, pp. 9714–9727, 2020.

[19] H. Krim and M. Viberg, ”Two decades of array signal processing research: the parametric approach,”*IEEE Signal Process. Mag.*, vol. 13, no. 4, pp. 67-94, 1996.

[20] P. Stoica and A. Nehorai, ”MUSIC, maximum likelihood, and Cramer-Rao bound: further results and comparisons,” *IEEE Trans Acoust Speech Signal Process*, vol. 38, no. 12, pp. 2140-2150, 1990.

[21] R. Schmidt, “Multiple emitter location and signal parameter estimation,” *IEEE Trans. Antennas Propag.*, vol. 34, no. 3, pp. 276-280, 1986.

[22] R. Roy and T. Kailath, "ESPRIT-estimation of signal parameters via rotational invariance techniques," *IEEE Trans. Audio Speech Lang. Process.*, vol. 37, no. 7, pp. 984-995, 1989.

[23] P. Stoica and K. C. Sharman, "Maximum likelihood methods for direction-of-arrival estimation," *IEEE Trans. Audio Speech Lang. Process.*, vol. 38, no. 7, pp. 1132-1143, 1990.

[24] J.-P. Delmas, Y. Meurisse, "Robustness of narrowband DOA algorithms with respect to signal bandwidth," *Signal Processing*, vol. 83, no. 3, pp. 493-510, 2003.

[25] A. J. Weiss, "Direct position determination of narrowband radio frequency transmitters," *IEEE Signal Process. Lett.*, vol. 11, no. 5, pp. 513-516, 2004.

[26] K. Nishikawa, T. Yamamoto, K. Oto and T. Kanamori, "Wideband beamforming using fan filter," in *1992 IEEE International Symposium on Circuits and Systems (ISCAS)*, vol. 2, pp. 533-536, 1992.

[27] T. Chou, "Frequency-independent beamformer with low response error," in *1995 International Conference on Acoustics, Speech, and Signal Processing*, vol. 5, pp. 2995-2998, 1995.

[28] W. Liu and S. Weiss, "Design of Frequency Invariant Beamformers for Broadband Arrays," *IEEE Trans. Signal Process.*, vol. 56, no. 2, pp. 855-860, 2008.

[29] L. C. Parra, "Steerable frequency-invariant beamforming for arbitrary arrays," *J. Acoust. Soc. Am.*, vol. 119, pp. 3839–3847, 2006.

[30] D. B. Ward, R. A. Kennedy, and R. C. Williamson, "Theory and design of broadband sensor arrays with frequency invariant far-field beam patterns," *J. Acoust. Soc. Am.*, vol. 97, no. 2, pp. 1023-1034, 1995.

[31] S. C. Chan and C. K. S. Pun, "On the design of digital broadband beamformer for uniform circular array with frequency invariant characteristics," in *2002 IEEE International Symposium on Circuits and Systems*. Proceedings, 2002.

[32] S. C. Chan and H. H. Chen, "Uniform Concentric Circular Arrays With Frequency-Invariant Characteristics—Theory, Design, Adaptive Beamforming and DOA Estimation," *IEEE Trans. Signal Process.*, vol. 55, no. 1, pp. 165-177, 2007.

[33] C. Gentile, A. J. Braga and A. Kik, "A Comprehensive Evaluation of Joint Range and Angle Estimation in Ultra-Wideband Location Systems for Indoors," in *IEEE International Conference on Communications*, pp. 4219-4225, 2008.

[34] X. Cai and W. Fan, "A Complexity-Efficient High Resolution Propagation Parameter Estimation Algorithm for Ultra-Wideband Large-Scale Uniform Circular Array," *IEEE Trans. Commun.*, vol. 67, no. 8, pp. 5862-5874, 2019.

[35] A. Ramírez-Arroyo, A. Alex-Amor, P. Padilla and J. F. Valenzuela-Valdés, "Joint Direction-of-Arrival and Time-of-Arrival Estimation with Ultra-wideband Elliptical Arrays," *IEEE Trans. Wirel. Commun.*, 2023.

[36] A. Ramírez-Arroyo, A. Alex-Amor, P. Padilla and J. F. Valenzuela-Valdés, "Wideband Elliptical Arrays for DoA and ToA Estimation in Multipath Environments," in *2023 17th European Conference on Antennas and Propagation (EuCAP)*, Florence, Italy, pp. 1-5, 2023.

[37] F. Zhang, W. Fan, and G. F. Pedersen, "Frequency-invariant uniform circular array for wideband mm-Wave channel characterization," *IEEE Antennas Wirel. Propag. Lett.*, vol. 16, pp. 641–644, 2017.

[38] D.E.N. Davies, "A transformation between the phasing techniques required for linear and circular aerial arrays", *Proceedings of the Institution of Electrical Engineers*, vol. 112, no. 11, pp. 2041-2045, 1965.

[39] M. Abramowitz and I. A. Stegun, *Handbook of Mathematical Functions*. New York: Dover, 1965.

[40] B. H. Fleury, M. Tschudin, R. Heddergott, D. Dahlhaus and K. Ingeman Pedersen, "Channel parameter estimation in mobile radio environments using the SAGE algorithm," *IEEE J. Sel. Areas Commun.*, vol. 17, no. 3, pp. 434-450, 1999.

Alejandro Ramírez-Arroyo was born in Córdoba, Spain, in 1997. He received the B.Sc. degree with honors and M.Sc degree with honors in telecommunication engineering from the University of Granada (UGR), Spain, in 2019 and 2021. Since 2020, he is pursuing the Ph.D. degree with the Smart Wireless Applications and Technologies (SWAT) Research Group in the Department of Signal Theory, Telematics, and Communications, University of Granada. In 2022, he was with the Wireless Communication Networks section, Aalborg University (AAU), Denmark, as an invited Ph.D. Student. His current research interests include optimization techniques, radio propagation and channel characterization for mmWaves and 5G communications.

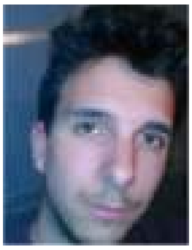

Antonio Alex-Amor received the B.Sc. degree in Telecommunication Engineering from Universidad de Granada, in 2016, and the M.Sc. and Ph.D. degrees in Telecommunication Engineering from Universidad Politécnica de Madrid (UPM), in 2018 and 2021, respectively. From 2016 to 2021, he has been with the Radiation Group, Signal, Systems and Radiocommunications Department, UPM. From 2018 to 2019, he joined the Department of Language and Computer Science, Universidad de Málaga. From 2020 to 2021, he joined the Departamento de Teoría de la Señal, Telemática y Telecomunicaciones, Universidad de Granada (Granada, Spain). Currently, he is an Assistant Professor at Universidad CEU San Pablo (Madrid, Spain). He was a Visiting Student at KTH Royal Institute of Technology during four months in 2019 and conducted a Short Postdoc Mission at Universidade de Lisboa (Lisbon, Portugal) in 2021. In 2020, he received the Best Electromagnetics Paper Award at the 14th European Conference on Antennas and Propagation (EuCAP 2020). His current research interests include the analysis and design of metamaterial structures and antennas, and wireless communication systems. He is also an active science communicator in blogs and social media.

Rubén Medina was born in Pamplona, Spain in 1997. He received the B.Sc. degree in Mathematics and M.Sc degree in Physics and Mathematics from the University of Granada (UGR), Spain, in 2019 and 2020 respectively. Since 2020, he is a Ph.D. student in an international joint Ph.D. program between the department of Mathematical Analysis (Research group in geometry of Banach spaces) of the University of Granada and the department of Mathematics of the Czech Technical University in Prague. His current research interests include linear and nonlinear geometry of Banach spaces as well as metric geometry, with applications to computer science.

Pablo Padilla was born in Jaén, Spain, in 1982. He received the Telecommunication Engineering degree and the Ph.D. degree from the Radiation Group (Signal, Systems and Radiocommunications Department) of the Technical University of Madrid (UPM), Spain, in 2005 and 2009, respectively. In 2007, he was with the Laboratory of Electromagnetics and Acoustics, Ecole Polytechnique Fédérale de Lausanne, Switzerland, as an invited Ph.D. Student. In 2009, he carried out a Postdoctoral stay at the Helsinki University of Technology (AALTO-TKK). In 2009, he became Assistant Professor at the Signal Theory, Telematics and Communications Department of the University of Granada, where he is currently Associate Professor, since 2012. In 2017, he was an invited Visiting Professor at the Royal Institute of Technology of Stockholm. He has authored more than 65 high-impact journal contributions and more than 60 contributions to international symposia. His research interests include a variety of topics related mainly to electromagnetism and communication issues (radiofrequency devices, antennas and propagation).

Juan F. Valenzuela-Valdés was born in Marbella, Spain. He received the Telecommunication Engineering degree from the Universidad de Málaga, Málaga, Spain, in 2003, and the Ph.D. degree from the Universidad Politécnica de Cartagena, Cartagena, Spain, in 2008. He joined the Department of Information Technologies and Communications, Universidad Politécnica de Cartagena, in 2004. In 2007, he joined EMITE Ing., Murcia, Spain, as the Head of research. In 2011, he joined the Universidad de Extremadura, Mérida, Spain, and in 2015, he joined the Universidad de Granada, where he is currently a Full Professor. He is also the Head of the SWAT Research Group, University of Granada, Granada, Spain, and the Co-Head of the Singular Laboratory of electromagnetic characterization of microwave and millimeter devices and antennas. His publication record comprised of more than 100 publications, including 50 JCR (Journal Citation Reports) indexed articles and seven book chapters. He holds several national and international patents. His current research interests include wireless communications, radio frequency devices, antennas, and propagation. Dr. Valenzuela-Valdés received several prizes, including a National Prize to the Best Ph.D. in mobile communications by Vodafone.

2.4 Measurement Campaigns at mmWave frequencies

2.4.1 FR2 5G Networks for Industrial Scenarios: An Experimental Characterization and Beam Management Procedures in Operational Conditions

Measurement campaigns are fundamental in the wireless communications field. These measurements allow the validation of the theoretically proposed channel models and propagation models. Over the last decade, one of the focuses has been set on industrial communication scenarios. This is due to the motivation to ensure reliable communications under Machine-to-Machine (M2M) based scenarios, which provide automating production and monitoring industrial processes. In this work, we propose the experimental characterization of a factory environment in operational conditions with a FR2 5G network deployment. Two measurement campaigns carried out under two operator configurations have been compared, analyzing fundamental aspects such as the power received at different locations on the factory, or the maximum cell radius to be considered. Based on these measurements, path gain models previously proposed in the state-of-the-art have also been validated. Finally, the analysis of beam management procedures has been carried out, studying mobility aspects of the agents involved in communications.

THIS IS A PREPRINT VERSION OF THE PAPER:

A. Ramírez-Arroyo, M. López, I. Rodríguez, T. B. Sørensen, S. Caporal del Barrio, P. Padilla, J. F. Valenzuela-Valdés and P. Mogensen, “FR2 5G Networks for Industrial Scenarios: An Experimental Characterization and Beam Management Procedures in Operational Conditions,” submitted to *IEEE Transactions on Vehicular Technology*, 2023.

Disclaimer:
This work has been submitted to IEEE Transactions on Vehicular Technology.

FR2 5G Networks for Industrial Scenarios: An Experimental Characterization and Beam Management Procedures in Operational Conditions

Alejandro Ramírez-Arroyo, Melisa López, Ignacio Rodríguez, Troels B. Sørensen,
Samantha Caporal del Barrio, Pablo Padilla, Juan F. Valenzuela-Valdés, Preben Mogensen

***Abstract*—Industrial environments constitute a challenge in terms of radio propagation due to the presence of machinery and the mobility of the different agents, especially at mmWave bands. This paper presents an experimental evaluation of a FR2 5G network deployed in an operational factory scenario at 26 GHz. The experimental characterization, performed with autonomous mobile robots that self-navigate the industrial lab, leads to the analysis of the received power along the factory and the evaluation of reference path gain models. The proposed assessment deeply analyzes the physical layer of the communication network under operational conditions. Thus, two different network configurations are assessed by measuring the power received in the entire factory, providing a comparison between deployments. Additionally, beam management procedures, such as beam recovery, beam sweeping or beam switching, are analyzed since they are crucial in environments where mobile agents are involved. They aim for a zero interruption approach based on reliable communications. The results analysis shows that beam recovery procedures can perform a beam switching to an alternative serving beam with power losses of less than 1.6 dB on average. Beam sweeping analysis demonstrates the prevalence of the direct component in Line-of-Sight conditions despite the strong scattering component and large-scale fading in the environment.**

***Index Terms*—5G Network, beam management, industrial scenario, radio propagation.**

I. INTRODUCTION

COMMUNICATIONS in factory environments are becoming of great interest in the scientific community during recent years [1]–[3]. Industry 4.0 and Industrial Internet-of-Things (IIoT) aim at ensuring reliable communications under Machine-to-Machine (M2M) based scenarios [4]–[7]. In parallel, 5G technology considers use cases based on ultra-reliable and low-latency communications (URLLC), which target end-to-end latencies below 1 ms [8], [9]. The combination of the above concepts is impacting the wireless deployments in factories, automating production and monitoring processes, while facilitating a simplification of current industrial network layouts [10], [11].

To provide efficient and reliable communications in factory environments, it is fundamental to deeply analyze radio propagation phenomena in these environments. Millimeter waves (mmWaves)/Frequency Range 2 (FR2) arise as a suitable solution due to the higher bandwidth available, which implies higher channel capacity, less interference between frequencies, and higher localization accuracy due to the shorter wavelength compared to sub-6 GHz/Frequency Range 1 (FR1) [12]. However, industrial scenarios prove to be challenging environments since radio propagation at mmWaves may exhibit disruptive characteristics for communications due to:

(i) High attenuation and blockage probability: mmWaves undergo high attenuation. This effect is enhanced by the presence of metallic structures, machinery and equipment that generate a propagation channel rich in multipath components [13].
(ii) Variations in the environment and mobility from the agents involved: the scenario is time-dependent due to the variable conditions because the mobile agents involved are constantly changing position [14].
(iii) Network deployment design and configuration: antenna gain, directivity and radiation pattern are critical parameters. Optimal design and configuration can significantly improve the coverage for mmWave communications [15].

The previous issues can be solved by performing analog beamforming and smart allocation of radio resources [16], [17]. Highly directive beams can compensate for high attenuation losses. Combined with analog beamforming, mobile agents can be tracked to maximize coverage. In 5G NR, all these procedures are included in the beam management architecture, such as, recovery, sweeping, measurement, or switching [18]. In order to successfully apply the described technical solutions in industrial scenarios, detailed knowledge about the varying radio propagation behavior of the different

---

This work has been supported by grant TED2021-129938B-I00 funded by MCIN/AEI/10.13039/501100011033 and by the European Union NextGenerationEU/PRTR. in part by the Spanish Ministry of Science and Innovation under Ramon y Cajal Fellowship number RYC-2020-030676-I funded by MCIN/AEI/10.13039/501100011033 and by the European Social Fund "Investing in your future". It has also been supported in part by grants PDC2022-133900-I00, PID2020-112545RB-C54 and TED2021-131699B-I00; and in part by the Ministerio de Universidades, Gobierno de España under Predoctoral Grant FPU19/01251.

Alejandro Ramírez-Arroyo, Pablo Padilla and Juan F. Valenzuela-Valdés are with the Research Centre for Information and Communication Technologies, Department of Signal Theory, Telematics and Communications, Universidad de Granada (UGR), 18071 Granada, Spain (e-mail: alera@ugr.es, pablopadilla@ugr.es, juanvalenzuela@ugr.es).

Melisa López, Troels B. Sørensen and Preben Mogensen are with the Department of Electronic Systems, Aalborg University (AAU), 9220 Aalborg, Denmark (e-mail: mll@es.aau.dk, tbs@es.aau.dk, pm@es.aau.dk).

Ignacio Rodríguez is with the Department of Electrical Engineering, University of Oviedo (UNIOVI), 33203 Gijon, Spain (e-mail: irl@uniovi.es).

Samantha Caporal del Barrio and Preben Mogensen are with Nokia, 9220 Aalborg, Denmark (e-mail: samantha.caporal_del_barrio@nokia.com, preben.mogensen@nokia.com).

(a) (b) (c)

Fig. 1. Photographs of (a) the measurement equipment at both sides, TX (wall-mounted FR2 micro BS) and RX (AMR-mounted radio scanner), (b) the view of the industrial automation and robotics clutter in the sparse hall, and (c) the view of the heavy machinery in the dense hall.

beams is needed, especially to guarantee service continuity when addressing demanding services in terms of high throughput and reliability under operational mobility conditions.

In this work, an experimental evaluation of a 5G operational network at FR2 frequencies in a factory environment is performed. This study illustrates the previously described issues and analyzes FR2 coverage in a small operational factory, considering two different network deployment configurations. The study surveys different coverage-related aspects leading to the optimal BS configuration and cell design, and benchmarks the experienced radio propagation levels with those from reference path loss models typically applied to industrial scenarios, evaluating their suitability in this type of environments. Further, the study considers beam-specific analysis to assess the quality of service given a specific serving beam, and study beam management procedures relevant for mobile elements such as (i) beam sweeping and switching, which is fundamental for analyzing the spatial distribution of the beams in the factory; (ii) and beam recovery, that allows signal recovery in the event that a specific beam is affected by high attenuation.

In particular, the novelties of the study are:

- Comparison of two measurement campaigns carried out at the same factory for two different base station configurations under operational conditions.
- Development of design rules from signal strength coverage maps based on the two operating conditions: These coverage maps allow estimating a cell size for deployments in industrial environments, as well as evaluating the path gain based on state-of-the-art reference models.
- Analysis of beam management procedures: In particular, a study of beam recovery, beam sweeping and beam switching procedures is carried out based on the measurements performed with autonomous mobile robots that self-navigate the factory.
- Beam switch-off optimization study: Based on the coverage maps generated from the self-navigation agents, it is proposed to turn off a subset of beams looking for a trade-off between the coverage areas and the number of beams turned on simultaneously. Therefore, this study may lead to the beam switch-off as an energy-saving solution.

The results are expected to be useful for academic researchers and engineers for radio planning of similar industrial hall scenarios based on FR2 wall-mounted directional antennas, taking into account not only propagation aspects but also mobility and beam management.

The work is organized as follows. Section II presents the industrial lab test environment, the measurement equipment and the measurement campaigns performed. Section III analyzes the radio propagation aspects in the industrial scenario. Section IV studies the beam management procedures involved in industrial communications. Section V shows the coverage maps according to the beam management procedures and a beam switch-off study. Finally, Section VI summarizes the main contributions of this document.

II. INDUSTRIAL SCENARIO AND ACQUISITION PROCESS FOR 5G NR

A. *Measurement scenario*

The present study is conducted at the experimental setup formed by the 5G Smart Production Lab in Aalborg University (AAU), Denmark [19]. This industrial research lab resembles a small factory with an extension of approximately 1350 m^2, equipped with real manufacturing and production equipment. The factory environment is formed by two different halls, hereinafter referred to as sparse and dense halls. The sparse hall, with dimensions $15\ m^2 \times 40\ m^2\ (600\ m^2)$ and shown in Figs. 1(a) and 1(b), contains wide corridors and metal machinery with heights ranging from 1.5 m to 2.5 m. The dense hall, with dimensions $25\ m^2 \times 30\ m^2\ (750\ m^2)$ and shown in Fig. 1(c), consists of a larger number of heavy machinery with heights between 2.5 m and 3.5 m. The higher density of machinery results in narrower aisles. In both cases, the radio propagation conditions are determined by a strong multipath effect due to reflections and scattering in the heavy machinery [20].

B. *5G NR Physical channel and measurement equipment*

In 5G NR, physical time-frequency resources are organized in orthogonal frequency-division multiplexing (OFDM) symbols and subcarriers for the time and frequency domains, respectively. In the frequency domain, a physical resource block (PRB) is formed by 12 subcarriers, while 14 consecutive

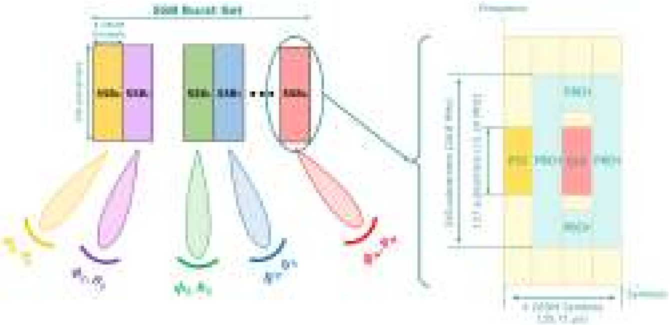

Fig. 2. Synchronization Signal Block structure and beamforming through the burst set.

OFDM symbols form a slot in the time domain [21]. In order to provide a wide range of configurations, 5G NR allows OFDM subcarrier spacing (SCS) of 15×2^n kHz where n is an integer value. This flexible numerology determines the slot duration, given by $1/2^n$ ms, and consequently the OFDM symbol duration. In particular, 3GPP defines up to five use cases from A to E according to the subcarrier spacing and the frequency range [21], [22]. In this work, the analysis is performed for case D, which is expected to be employed in 5G NR taking into account a subcarrier spacing of 120 kHz $(n = 3)$ and operating frequencies in the FR2-1 range (24.25 GHz - 52.6 GHz). Thus, OFDM symbol duration with cyclix prefix is fixed to $8.91\,\mu$s.

In the physical layer, the synchronization signal (SS) and physical broadcast channel (PBCH) are enclosed in the same block, known as synchronization signal block (SSB). This block, depicted in Fig. 2, is formed by 4 OFDM symbols and 240 subcarriers. Specifically, primary (PSS) and secondary (SSS) synchronization signals expand over 127 subcarriers. For high frequencies, where narrow beams can be considered, SSBs are beamformed in order to provide good spatial coverage, as it is shown in Fig. 2. Therefore, these blocks are beamformed and transmitted periodically and repeatedly through SSBs burst sets. The periodicity and the burst set duration are defined in the 3GPP standard [23]. In this work, these values are configured to 20 ms and 5 ms, respectively. The periodicity of the SSBs can be used for beam management tasks, as will be shown in later sections.

In order to statistically characterize the factory propagation environment, a R&S TSME6 radio scanner [24] is employed to capture radio parameters. In particular, the radio scanner measures the Reference Signal Received Power (RSRP) as the average power over the SSS bandwidth (15.24 MHz for SCS = 120 kHz) given a specific SSB. This scanner, shown in Fig. 1(a), is mounted on the top of an Autonomous Mobile Robot (AMR), which can be configured to follow routes throughout the factory. Additionally, the AMRs are configured to self-navigate the industrial lab, following predefined routes and missions. This fact, initially designed to maximize the performance in industrial processes involving mobile robots [25], simplifies the radio propagation analysis by automating the measurement process, ensuring route repeatability with cm-level accuracy. Thus, the RSRP can be acquired given the different locations of the AMR in the factory. In order to capture the SSB from the network, the TSME6 is configured with a biconical receiver (RX) antenna [26] mounted on the top of the robotic arm, illustrated in Fig. 1(a), with ultra wide-band bandwidth ranging from 3 GHz to 40 GHz. The RX height is 1.5 m above the floor. Note that the maximum AMR speed is 2 m/s, which implies a maximum frequency shift of 173 Hz considering the operating frequencies. This shift is negligible according to the frequency carrier in the FR2 band and the subcarrier spacing [27].

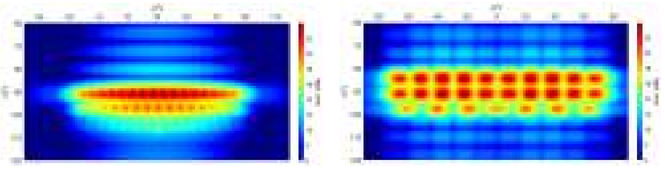

(a) (b)

Fig. 3. SSB beamforming for the TX module in (a) configuration A, and (b) configuration B.

TABLE I
TX MODULE PARAMETERS IN TERMS OF CONFIGURATION

Parameter	Configuration A	Configuration B
Number of beams	32	27
Beams per elevation angle	16,15 and 1	10, 10 and 7
ϕ and θ aperture	120° and 15°	150° and 15°
Coverage scanning	$\phi \in [-30°, 90°]$ $\theta \in [90°, 105°]$	$\phi \in [-75°, 75°]$ $\theta \in [83°, 98°]$

The 5G NR network under test consists of a transmitter (TX) based on a Nokia 5G Airscale mmWave Radio module [28]. This module operates in the FR2 n258 band (24.25 GHz - 27.5 GHz) according to case D previously described in this subsection. By using an extender module, that can be used in combination with the main 5G radio module, a total of 32 beams with different azimuth and elevation angles can be generated. The horizontal beamwidth ranges from 8° to 12°, while the vertical beamwidth goes from 6° to 10°, thus providing high directivity beams covering several spatial regions in the factory.

In this work, two TX module configurations are analyzed in depth:

- Configuration A (illustrated in Fig. 3(a)): The main module with 32 beams covering a horizontal angle of 120° is considered. These are distributed in three elevation angles with 0°, 7° and 15° downtilt, respectively.
- Configuration B (shown in Fig. 3(b)): The main module operates together with the extension module, providing a total of 27 effective beams with 150° horizontal scanning. In this case, beams are distributed in three elevation angles. Specifically, $-7°, 0°$ and 8° downtilt values are considered.

Table I summarizes the main parameters for each configuration. Note that ϕ and θ stand for the horizontal and vertical angles, respectively. Configuration A has a higher density of

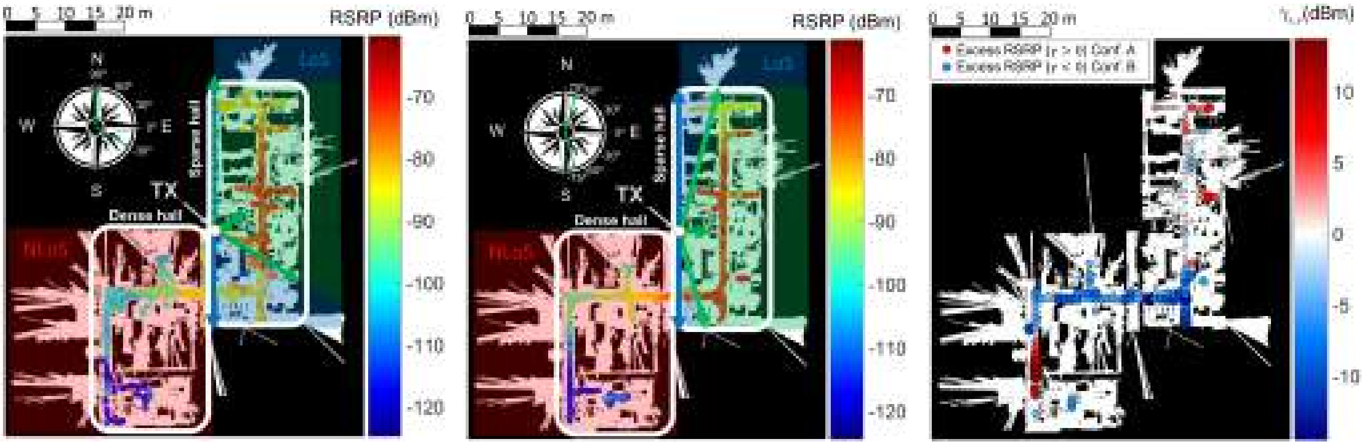

(a) (b) (c)

Fig. 4. Maximum SS-RSRP received at each position in the factory for (a) configuration A and (b) configuration B. (c) Difference of the average SS-RSRP in favor of each of the configurations. There is LoS condition in the sparse hall (blue area) and NLoS condition in the dense hall (red area). Areas under antenna boresight influence are marked in green.

beams in the horizontal scan. This causes the angular distance between adjacent beams to be minimal. Configuration B, on the other hand, has a greater separation of beams, allowing it to cover almost the entire sparse hall. The effect of both configurations will be discussed in later sections. For the sake of clarity, throughout the work, beams are numbered according to their corresponding SSB$_{\zeta,r,c}$, where ζ stands for the module configuration, and r and c are the beam row (from top to bottom) and column (from left to right), respectively.

III. RADIO PROPAGATION ANALYSIS

This Section presents several aspects related to the FR2 5G Network deployed in the 5G Smart Production Lab under operational conditions. A comparison is made between the two configurations of the TX module presented in Section II.B. The SS-RSRP analysis along the industrial environment allows to estimate the coverage and define a maximum cell radius according to a threshold target. Both measurement campaigns are used to fit path gain models in Line-of-Sight (LoS) and Non Line-of-Sight (NLoS) condition, which are validated with state-of-the-art channel models for indoor industrial scenarios. The correct modeling of the previous aspects is fundamental for the radio planning of wireless communications systems.

A. RSRP analysis

To analyze the nature of the propagation environment, the AMR is configured to cover several routes across the factory with 1.5 m/s average speed. Every 20 ms, the radio scanner detects the SS-RSRP coming from each SSB in the burst set. Figs. 4(a) and 4(b) show the strongest SS-RSRP for each burst set on each TX configuration. Note that the TX module is located on the west side of the sparse hall at a height of 3 m. Given this location, the factory is divided into two areas depending on the visual line of sight between TX and RX: Line-of-Sight and Non Line-of-Sight. In Fig. 4(a), the area under the boresight influence experiences SS-RSRP values between -62 and -80 dBm. In the southern part of the sparse hall, the decrease of the SS-RSRP is remarkable when leaving the influence of the beams. Finally, in the east-west-oriented corridor the SS-RSRP ranges between -85 dBm and -100 dBm, while in the southern part of the dense hall, completely obstructed by the heavy machinery, the SS-RSRP is below -100 dBm.

For the configuration B, depicted in Fig. 4(b), the boresight of the beams almost completely covers the sparse hall. This causes the southern part of the sparse hall to be covered with SS-RSRP values up to -75 dBm. Additionally, due to reflections and scattering from metallic structures such as pipelines and ventilation ducts, shown in Fig. 1(b), the east-west-oriented corridor SS-RSRPs are in the range of -75 dBm to -95 dBm.

In order to compare both configurations, the factory is divided into a squared grid of size 1×1 m^2. The SS-RSRP of all points belonging to each square is averaged. In terms of wavelengths, the averaging is performed on squares of dimensions $86.7\lambda \times 86.7\lambda$, which makes it possible to obtain the local average SS-RSRP while removing the fast fading effect [29]. The comparison between both values of each campaign indicates whether the radio propagation is more favorable in one case or the other. Fig. 4(c) shows the difference between averaged SS-RSRP values on each square in the grid. Therefore, $\gamma_{x,y}$ is defined as:

$$\gamma_{x,y} = \overline{RSRP}_{A,x,y} - \overline{RSRP}_{B,x,y}, \qquad (1)$$

where $\overline{RSRP}_{A,x,y}$ and $\overline{RSRP}_{B,x,y}$ stand for the averaged SS-RSRP in the coordinates (x, y) for configuration A and B, respectively. Thus, $\gamma_{x,y}$ indicates the difference in terms of SS-RSRP for both configurations at each location. Red colors mark areas where the SS-RSRP is stronger in configuration A compared to configuration B. The blue colors indicate areas where coverage is better in configuration B than in configuration A.

It can be concluded that, even when the beams in configuration B do not impinge directly on the corridor connecting

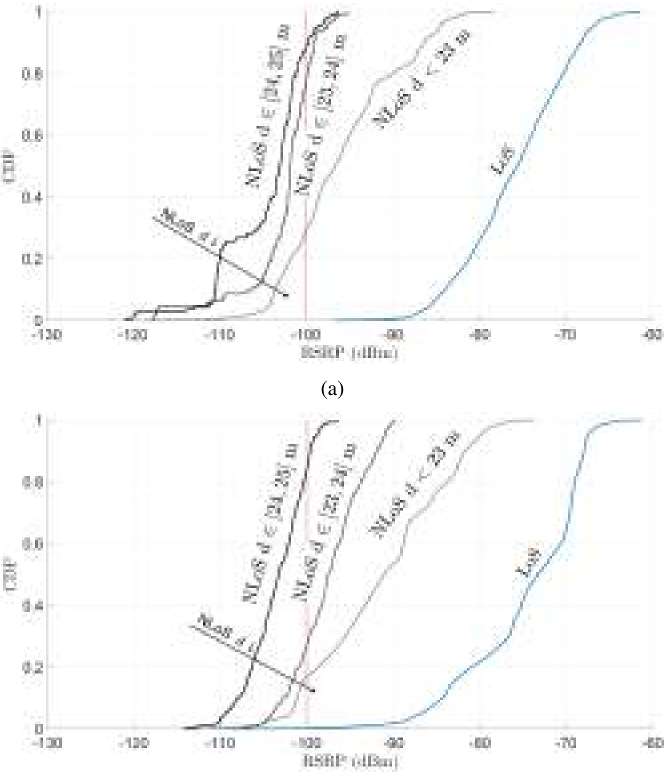

(a)

(b)

Fig. 5. RSRP CDF for LoS and NLoS regions in (a) configuration A and (b) configuration B. NLoS regions are divided into several distance ranges.

both halls, there is a noticeable improvement of the SS-RSRP due to the better coverage of the southern part of the sparse hall. This is a direct consequence of the higher separation of the beams in the azimuthal direction. This separation does not negatively affect the range $\phi \in [-30°, 75°]$ originally covered by configuration A, since the values of $\gamma_{x,y}$ in this range are close to zero. Thus, considering the average spatial coverage given by the SS-RSRP from the strongest beam, configuration B is considered a better solution for network deployment.

B. Cell coverage

Regarding network deployment, the cell size is fundamental in order to determine the number of access points required to provide service on the downlink. The cell coverage in the network can be estimated as the service availability given a certain cell radius r. For a fixed cell radius r, if the RSRP is above a certain threshold, good quality of service can be guaranteed. Assuming a RSRP threshold of -100 dBm [34], an estimation of the maximum size of the cell can be made through the probability $P(\text{RSRP} < -100 \text{ dBm} \mid r)$. For that purpose, Fig. 5 shows the RSRP CDF for several distances and both configurations. In Figs. 5(a) and (b), the RSRP is higher than -100 dBm in 99.8% of the measurements for any distance in the LoS region. Given that the maximum distance measured in the LoS case is 26 meters, a similar cell radius could be considered with the assurance of providing good coverage. In the NLoS region, 29.8% and 17.3% of measurements are below the threshold when distances lower than 23 meters are considered. These values increase drastically when considering measurements in the ranges $d \in [23, 24]$ m and $d \in [24, 25]$ m, with percentages of 77.9%, and 88.1% (configuration A) and 27.9%, and 84.9% (configuration B). Therefore, cell radii of less than 23 meters should be used in the design of 5G NR networks at mmWave frequencies in industrial environments with NLoS assuming a target of RSRP > -100 dBm. Note that the RSRP improvement illustrated in Fig. 4 for configuration B results in a shift of the CDFs to the right, which implies lower probabilities for $P(\text{RSRP} < -100 \text{ dBm} \mid r)$. From the capacity perspective, it has been demonstrated that data rates higher than 130 Mbps can be obtained in industrial environments in the FR2 range for 90% coverage taking into account ranges up to 64 m [15].

C. Path Gain analysis

To estimate the Path Gain (PG) in the factory environment, it is calculated from the SS-RSRP as:

$$PG[\text{dB}] = RSRP[\text{dBm}] - P_{TX}[\text{dBm}] - G_{TX}[\text{dB}] - G_{RX}[\text{dB}], \tag{2}$$

where G_{TX} and G_{RX} are the nominal gain for the TX and RX antennas given ϕ and θ angles for a specific TX-RX link. P_{TX} is the transmitted power over a resource element since RSRP is referred to the power contribution of a single resource element. Given a total transmission power over 100 MHz carrier bandwidth of $P_c = 21.2$ dBm, the transmitted power over a resource element can be calculated as P_c/N_{RE} where N_{RE} is the number of resource elements (subcarriers) in the carrier bandwidth. According to [30], for 120 kHz subcarrier spacing and 100 MHz carrier bandwidth, $N_{RE} = 66 \cdot N_{RB} = 792$. Additionally, as a consequence of scattering effects and obstruction in the factory, the effective gain of high directivity antennas is degraded, especially in NLoS conditions. Thus, the nominal gain of TX is compensated by 1 dB in LoS and 4.9 dB in NLoS to account for the typical median effective gain degradation in factories at mmWave frequencies [15].

To model the scenario, a generic slope intercept model is proposed as:

$$PG(d) = PG_{1m} - 10n\log_{10}(d) + \mathcal{N}\left(0, \sigma^2\right), \tag{3}$$

where PG_{1m} is the path gain at 1 m distance, n is the path loss exponent which determines the slope given d and σ is the standard deviation for the model, stating the goodness of fit for the model.

Figs. 6(a) and 6(b) show the path gain in terms of the distance in the LoS and NLoS regions. Measurements correspond to both measurement campaigns after RSRP compensation according to eq. (2). Note that after RSRP compensation, the path gain is an inherent property of the scenario and does not depend on the chosen configuration. For this reason, data from both measurement campaigns are merged for the analysis.

For the LoS case, the measurement fit indicates a path loss exponent $n = 2.29$ and a standard deviation $\sigma = 4.6$ dB. This fit is compared with Friis free space model [31], close-in

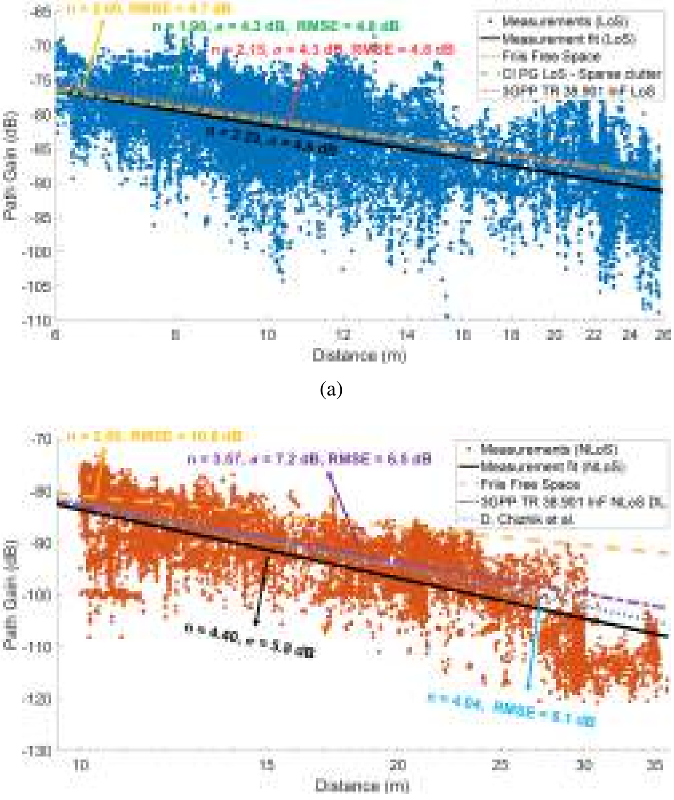

(a)

(b)

Fig. 6. Path Gain in terms of the distance for the measurements performed in both campaigns in: (a) LoS and (b) NLoS condition. Several slope intercept models are included for comparison purposes.

free space (CI) path-gain model for LoS in sparse clutter at 28 GHz [32], and 3GPP TR 38.901 InF for LoS [33]. The path loss exponent close to two indicates a channel propagation dominated by the LoS path, resembling a free space channel on average. However, a noticeable high variability of $\sigma = 4.6$ dB is found in the channel due to scattering in the sparse clutter, resulting in a multipath channel with constructive and destructive interference. Note that σ indicates the goodness of fit on the data for which the model is designed, while RMSE indicates the goodness of fit between the model and the data in this work. An excellent agreement is found between the data and the models.

In the NLoS case, the measurement fit ($n = 4.40$, $\sigma = 5.8$ dB) shows a scenario with high attenuation and distance dependant and high variability in the PG level. This is a direct consequence of the channel blockage, the received signal being the sum of the multipath channel contributions in the dense clutter machinery of the hall. This fit is compared with the Friis free space model, 3GPP TR 38.901 InF DL for NLoS [33], and the model proposed in [15]. Friis model fails to fit the data due to the assumption of free space propagation. The latter two models agree well with the measurement fit, although they estimate a slightly lower path loss exponent.

The fitness results are summarized in Table I, where it is shown that the RMSE values are around 4.7 dB for the LoS cases and 6.6 dB for the NLoS cases. In both situations, the measured path gain exhibits a good agreement with the reference propagation models, which indicates that these models are a good choice for radio propagation prediction or coverage estimation in such industrial scenarios considering FR2 wall-mounted deployments with directional antennas.

TABLE II
SLOPE INTERCEPT PATH GAIN MODELS FOR FACTORIES IN LOS AND NLOS

Line-of-Sight			
PG model	PG_{1m}	n	σ \ RMSE
Measurement Fit (LoS)	−58.8	2.29	4.6 \ −
Friis Free Space	−60.9	2.00	− \ 4.7
CI PG LoS - SC	−60.9	1.98	4.3 \ 4.8
3GPP TR 38.901 InF LoS	−58.9	2.15	4.3 \ 4.8

Non Line-of-Sight			
PG model	PG_{1m}	n	σ \ RMSE
Measurement Fit (NLoS)	−39.6	4.40	5.8 \ −
Friis Free Space	−60.9	2.00	− \ 10.8
3GPP TR 38.901 InF NLoS DL	−47.1	3.57	7.2 \ 6.5
D. Chizhik *et al.*	−41.9	4.04	− \ 6.1

IV. BEAM MANAGEMENT PROCEDURES

The beam management concept is essential in 5G NR due to the use of several beams at both TX/RX sides. High gains from narrow beams ensure better communication performance in the TX-RX link. However, these narrow beams imply less spatial coverage, so they must be combined with management mechanisms that optimize the allocation of resources in the network in real-time, especially when considering mobile elements. In factory scenarios, the synchronization of AMRs in industrial processes is essential. That is why mechanisms such as beam sweeping, switching, and recovery are necessary. This Section analyzes some of the previous procedures given the two proposed TX configurations. A comprehensive understanding of these procedures in operational conditions is fundamental from the radio planning perspective. This is especially critical in factories, where the mobility of the agents involved, e.g. AMRs, is a factor to be taken into account. Therefore, the network must be able to quickly adjust the transmission beams to maintain a continuous and stable connection, aiming at a zero-interruption and optimizing the network resource allocation.

A. Beam Recovery

As previously stated, lower spatial coverage by the narrow beams implies a higher probability of beam failure in highly dynamic environments. The beam failure concept appears when the coverage provided by a beam cannot be maintained due to degradation of the TX/RX link for any reason, such as blocking or fading. To solve this issue, 5G NR performs

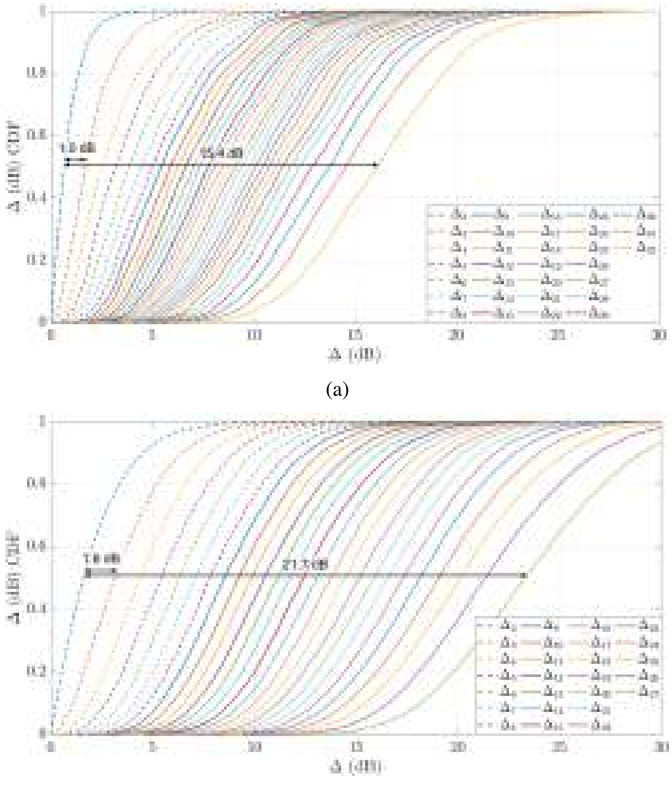

(a)

(b)

Fig. 7. Δ_i CDF for (a) configuration A and (b) configuration B.

TABLE III
Δ VALUES FOR SEVERAL PROBABILITIES IN BOTH CONFIGURATIONS

	Configuration A			Configuration B		
$P(\Delta_i < x)$	Δ_2	Δ_3	Δ_4	Δ_2	Δ_3	Δ_4
25%	0.3 dB	1.0 dB	1.6 dB	0.7 dB	1.9 dB	3.0 dB
50%	0.7 dB	1.7 dB	2.5 dB	1.6 dB	3.2 dB	4.4 dB
75%	1.2 dB	2.6 dB	3.9 dB	3.0 dB	4.8 dB	6.2 dB

a beam switching procedure to another beam which can guarantee good quality on the link [16], [18].

In order to ensure the success of the beam failure recovery procedure, the new beam to which the user connects should provide the same or similar quality as prior to beam failure. Assuming that the user is served by the beam with the strongest RSRP, the quality of the beam recovery procedure can be quantified as $\Delta_i = \text{RSRP}_{1^{st}} - \text{RSRP}_{i^{th}}$ where $\text{RSRP}_{i^{th}}$ is the i-th strongest beam given a specific location in the scenario. Therefore, Δ_i specifies the RSRP difference between the strongest and the i-th strongest beam in case a beam failure recovery procedure is required. Values tending to zero would indicate that the channel would barely be degraded due to this procedure. Figs. 7(a) and 7(b) show the CDF for Δ_i values in both measurement campaigns. Two main differences are found: (i) Configuration A shows CDF curves closer to zero compared to the second module configuration. Specifically, Δ_2 median value is only 0.7 dB, which means a degradation of the TX-RX link below 1 dB if a switching procedure is performed from the strongest to the second strongest beam. However, Δ_2 median for configuration B is 1.6 dB. (ii) Distance between adjacent Δ_i curves is smaller in configuration A. For example, $\Delta_3 - \Delta_2$ is 1.0 dB for configuration A, while this value goes to 1.6 dB for configuration B when $P(\Delta_i < 50\%)$. This leads to a mitigation of power loss during the beam switching process in configuration A when the serving beam is unavailable due to, for instance, a Line-of-Sight blockage. Specifically, the average median distance between two consecutive curves is 0.5 dB and 0.9 dB, for configurations A and B, respectively.

The two previous differences are mainly due to the configuration of beams previously described in Fig. 3. In configuration A, a higher number of available beams as well as a higher density of beams in the spatial domain lead to better Δ values in the case of requiring a beam recovery procedure. Configuration B distributes the beams in the spatial domain achieving a better global coverage for the strongest beam, as shown in Fig. 4, but this higher spatial separation implies higher Δ when beam switching is required. Table III summarizes the three strongest backup beams, i.e., Δ_2, Δ_3 and Δ_4 for both configurations and multiple percentiles $P(\Delta_i < x)$. In summary, in communications where the decrease of RSRP in case of beam failure is not critical, configuration B is suitable as long as the strongest beam is available, as shown in the overall coverage in Fig. 4. However, if it is necessary to maintain a constant RSRP, configuration A is more appropriate as the beams are grouped in a smaller spatial region. This fact is reflected in Δ_i values, which are minimized for configuration A, as illustrated in Fig. 7 and Table III.

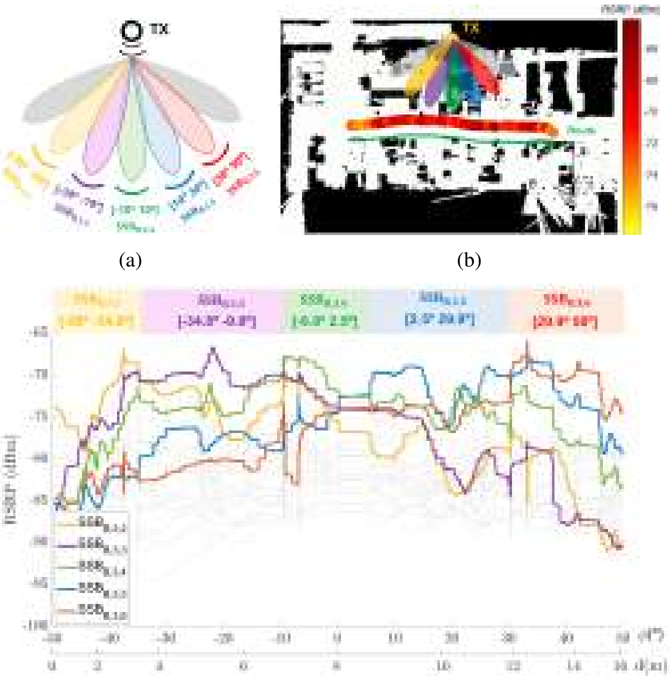

(a)

(b)

(c)

Fig. 8. (a) Azimuth bean sweeping diagram for the bottom row of beams in the configuration B, (b) route followed by the AMR in the LoS hall and (c) angular distribution of the RSRP for every SSB.

B. Beam sweeping and switching

In addition to the beam recovery procedure, beam switching scheduling is essential for the optimal management of signaling resources on the TX side [16], [18]. If a serving beam pattern is found based on the location in the industrial environment, an a priori scheduling for the beam assignment can be made. While in free space, this scheduling would be obvious based on the antenna radiation pattern, in an industrial environment such as the one studied, this scheduling could differ due to scattering in the environment. In order to analyze the effect of the propagation channel on the radiation pattern, a 16-meter route is configured with the AMR along the main corridor of the hall with LoS. This corridor is chosen since it is considered the operating area according to the RSRP level and cell radii analyzed in previous sections. This route, which covers azimuth angles from $-50°$ to $50°$, coincides with the boresight of the following beams in the configuration B: $\text{SSB}_{B,3,2}$, $\text{SSB}_{B,3,3}$, $\text{SSB}_{B,3,4}$, $\text{SSB}_{B,3,5}$ and $\text{SSB}_{B,3,6}$. Fig. 8(a) depicts these five SSBs in the lowest row of the beam pattern, illustrated in Fig. 3(b). The angular ranges denote the spatial region in which the beam gain is higher than the others. Fig. 8(b) shows the specific route followed by the AMR and the maximum RSRP received at each location. Fig. 8(c) presents the RSRP for every SSB in each azimuth angle in

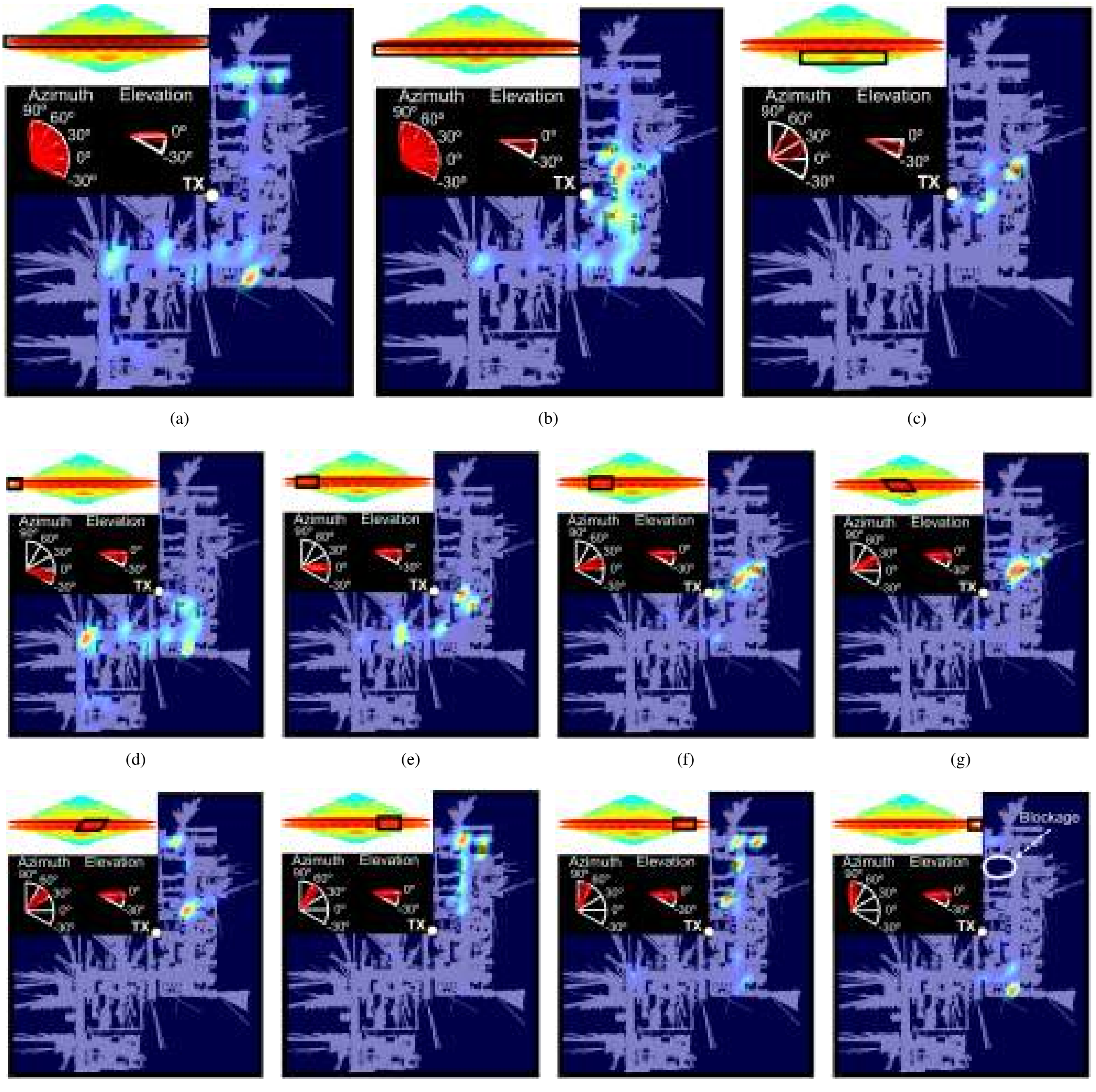

(a) (b) (c)

(d) (e) (f) (g)

(h) (i) (j) (k)

Fig. 9. Coverage maps of the factory in terms of SSB clusters: (a)-(c) separate the SSBs in three elevation angles and (d)-(k) consider eight azimuth regions.

the route after removing the small-scale fading effect. This has been performed by averaging the acquired measurements in the route over 40 wavelengths [29], [35]. A second axis is included with the distance traveled by the AMR. Note that the relationship is not linear with ϕ since the distance between the AMR and the TX is not constant along the route. The RSRP from beams shown in Fig. 8(a) are highlighted. The angular ranges in which these beams predominate are denoted at the top. It is shown a good agreement between the beams predicted in Fig. 8(a) by the radiation pattern, and the strongest beams along the angular domain of the route. This fact demonstrates that in the LoS zone, the direct ray prevails even with the strong scattering and the large-scale fading expected in an industrial environment. Therefore, in order to decrease the signaling in the network, scheduling of the beam assignment based on the AMR position can be considered if the route is known.

V. BEAM-SPECIFIC COVERAGE AND SWITCH-OFF OPTIMIZATION STUDY

As mentioned in previous Sections, 5G NR support for beamforming is intended to improve the spatial coverage by taking advantage of the highly directive beams provided in the mmWave/FR2 band. To check the effectiveness of optimal spatial coverage at the factory, this section analyzes some coverage maps provided by the beams involved in the beam sweeping procedure for the first measurement campaign. These maps are calculated by dividing the factory into a grid with inner areas whose dimensions are 2.7×2.4 m^2. In each area, it is determined how many times a subgroup of SSBs is found to be the strongest among all available SSBs. Those areas with the highest presence of the strongest SSB subset will be the ones under the influence of those beams. Figs. 9(a)-(k) show density maps that illustrate the SSB influence area for different SSBs subsets. Red color denotes zones where a specific SSB subset is found to be the one with strongest SS-RSRP, while blue tones indicate areas where the SS-RSRP is not maximum among all SSBs. Figs. 9(a)-(c) groups the SSBs according to elevation/downtilt angle. Fig. 9(a) considers those SSBs with $\theta = 0°$. These SSBs cover the farthest areas of the factory, even in the NLoS area that does not correspond angularly with the azimuth angle of the beams. This fact is explained by the reflections and scattering that occurs in the ventilation ducts that are at the same height as the transmitter module, shown in Fig. 1(b). This environment favors reflection and scattering phenomena covering the NLoS areas of the dense hall. As the downtilt is increased in Figs. 9(b), $\theta = 7°$, and 9(c), $\theta = 15°$, the coverage areas are concentrated around the location of the transmitter module. In fact, in the latter case, it is depicted that the beam with the higher downtilt only provides coverage to a small area just below the transmitter. Figs. 9(d)-(k) group the SSBs according to several azimuth angles considering the two uppermost ($\theta = 0°$ and $\theta = 7°$) elevation/downtilt cases. Specifically, the four most south-facing SSBs, shown in Fig. 9(d), are the ones that cover the dense hall due to reflections and scattering in the ventilation ducts, following the same reasoning as in Fig. 9(a). As the beams are beamformed to cover northward areas, it is found that the areas under the influence of the beam also move towards the north part of the factory. The only exception is found in Fig. 9(k), where the beam points out directly at the only metal structure whose height is higher than the transmitter in the sparse hall. This causes the beam to be obstructed, reflecting off that structure, thus appearing the coverage area in the southern part of the sparse hall. In summary, beam-specific coverage areas show that the beam determination in LoS condition can be approximated by an a priori assignment due to the high correlation between the beam Direction-of-Departure and the regions with the maximum SS-RSRP. This is due to the maximum contribution of LoS versus other multipath components, as previously predicted in Fig. 8. On the NLoS side, the density maps show that reflection and scattering phenomena at metallic interfaces allow radio propagation to areas outside the angular range of the beams. This fact can be exploited in network design and deployment to cover NLoS blocked by walls or large machinery.

As a last experiment, the beam switch-off problem is considered [36]. It is desired to know how the coverage in

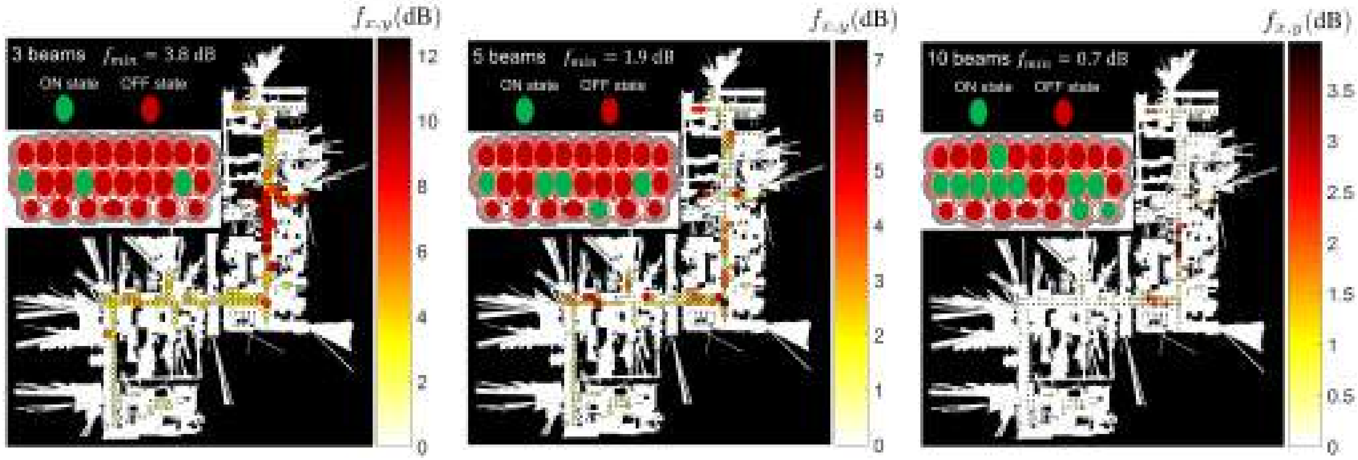

(a) (b) (c)

Fig. 10. Solution of the genetic algorithm for the beam switch-off problem with (a) $\xi = 3$, (b) $\xi = 5$ and (c) $\xi = 10$.

the factory degrades if some of the 27 SSBs available in the transmitter are turned off (configuration B). If the degradation in terms of RSRP is not high, the selective shutdown of some beams can be considered as an energy-saving solution, thus increasing the energy efficiency in the network. For this purpose, the following optimization problem is proposed:

$$\min\left(f(set)=\frac{1}{N}\sum_{x}\sum_{y}\overline{\mathrm{RSRP}}_{\max,x,y}-\overline{\mathrm{RSRP}}_{set,x,y}\right) \tag{4}$$

$$\text{subject to:} \quad \#SSB_{set}\leq\xi \tag{5}$$

where x and y denotes the indices of the squared grid previously defined for Fig. 4(c), N is the number of grids, $\overline{\mathrm{RSRP}}_{\max,x,y}$ stands for the average RSRP over all the measurements in the grid (x, y) when every beam is turned on. $\overline{\mathrm{RSRP}}_{set,x,y}$ is the average RSRP over all the measurements in the grid (x, y) when a subgroup of SSBs specified in set is turned on. $\#SSB_{set}$ is the number of SSBs turned on simultaneously, under the constraint that it must be less than the threshold ξ.

This problem has been solved by using the MI-LXPM genetic algorithm [37], which is able to deal with binary optimization problems. The space of feasible solutions is a binary vector with 27 elements, each corresponding to the on/off state of each SSB. The algorithm is run 10 times independently for three possible ξ threshold values: 3, 5 and 10. In all 10 iterations, the same solution was found for each threshold. Figs. 10(a)-(c) show the SSB configuration found by the genetic algorithm for each case. In Fig. 10(a), when only three SSBs are turned on, the algorithm chooses all of them from the middle row. Two of them point to the south side of the factory, thus covering the dense hall, while one of them points to the north side. With this configuration, the central part of the sparse hall is uncovered, as it is illustrated by the high values of $f_{x,y}$ found in this area. On average, with 3 beams on, the average RSRP degrades by 3.8 dB. In Fig. 10(b), ξ is raised to five, with the algorithm finding the same three beams as in the previous case, but adding two more in the central part. This solves the problem previously described where the sparse hall was uncovered by the beams, thus decreasing the average RSRP degradation to 1.9 dB. Finally, Fig. 10(c) shows the case where 10 SSBs are turned on. Observing the factory map it can be concluded that the signal degradation is minimal, being the average degradation of 0.7 dB. In summary, the previous results indicate that an energy-saving solution based on beam switch-off is feasible due to the fact that the degradation of the average received power is minimal. It has been demonstrated that with 10 out of 27 beams on, the RSRP decreases on average by only 0.7 dB with respect to the case where all SSBs are on. Although it has to be taken into consideration that, in the case of applying this technique, the reliability of the network may decrease in terms of beam failure due to the lower availability of beams, as shown in Section III.B.

VI. CONCLUSION

This work presents two measurement campaigns performed in the 5G Smart Production Lab, which resembles a small factory. The analysis of both campaigns has been carried out in a 5G NR network at 26 GHz in the FR2 frequency range under operational conditions. These measurement campaigns have been carried out with AMRs which are configured to self-navigate the industrial lab, following predefined routes. The analysis of the RSRP received by an AMR in terms of the configuration of a transmitter module has been carried out, allowing the generation of coverage maps throughout the factory.

The experimental characterization based on the comparison of both campaigns proves: (i) A higher separation of the beams in the TX (configuration B) provides better overall coverage in the factory. In exchange, the higher separation decreases the average power of the best backup beam, worsening the quality of the beam recovery procedure. Otherwise, a set of angularly closer beams (configuration A), obtains a backup channel with higher RSRP. (ii) Path gain fitting of the factory measurements for both campaigns agrees with models developed at these frequencies for industrial environments in both LoS and NLoS condition, which validates previous models for radio planning in factory-based scenarios. (iii) For an RSRP target above -100 dBm, cell radii up to 26 meters can be considered with 99.8% coverage. In NLoS condition, the coverage decreases to 70.2% (configuration A) and 82.7% (configuration B) for 23-meter cell radii.

Concerning the beam management procedure analysis, the following conclusions are drawn: (i) For beam sweeping and switching analysis, the beam angular coverage distribution in the LoS region can be approximated by that expected in free space, which allows an a priori allocation of resources based on the AMR position. (ii) The beam recovery analysis shows that an alternative serving beam is available with power losses between 0.7 dB and 1.6 dB on average when all beams are available. TX beam distributions with high spatial density decrease the power gap between the serving and the backup beam. (iii) The development of coverage maps based on subsets of beams demonstrates that reflection and scattering propagation mechanisms in the factory ventilation ducts allow the signal to propagate to NLoS areas of the factory. (iv) A beam switch-off problem optimization indicates the feasibility of beam switch-off as an energy-saving solution with average RSRP losses of 0.7 dB when 17 of the 27 available beams are switched off (63%).

The results detailed in this study, which consider propagation, mobility and beam management aspects, offer valuable insights for the radio planning of similar industrial hall scenarios using FR2 wall-mounted directional antennas.

ACKNOWLEDGMENTS

The authors would like to thank D. Chizhik, J. Du and R. A. Valenzuela, from Nokia Bell Labs, for their constructive comments.

References

[1] J. Wan *et al.*, "Toward Dynamic Resources Management for IoT-Based Manufacturing," *IEEE Communications Magazine*, vol. 56, no. 2, pp. 52-59, 2018.

[2] G. Hampel, C. Li and J. Li, "5G Ultra-Reliable Low-Latency Communications in Factory Automation Leveraging Licensed and Unlicensed Bands," *IEEE Communications Magazine*, vol. 57, no. 5, pp. 117-123, 2019.

[3] F. Spinelli and V. Mancuso, "Toward Enabled Industrial Verticals in 5G: A Survey on MEC-Based Approaches to Provisioning and Flexibility," *IEEE Communications Surveys & Tutorials*, vol. 23, no. 1, pp. 596-630, 2021.

[4] Y. Liao, E. de Freitas Rocha Loures and F. Deschamps, "Industrial Internet of Things: A Systematic Literature Review and Insights," *IEEE Internet of Things Journal*, vol. 5, no. 6, pp. 4515-4525, 2018.

[5] C. D. Ho, T. -V. Nguyen, T. Huynh-The, T. -T. Nguyen, D. B. da Costa and B. An, "Short-Packet Communications in Wireless-Powered Cognitive IoT Networks: Performance Analysis and Deep Learning Evaluation," *IEEE Transactions on Vehicular Technology*, vol. 70, no. 3, pp. 2894-2899, 2021.

[6] S. Vitturi, C. Zunino and T. Sauter, "Industrial Communication Systems and Their Future Challenges: Next-Generation Ethernet, IIoT, and 5G," *Proceedings of the IEEE*, vol. 107, no. 6, pp. 944-961, 2019.

[7] I. Rodriguez *et al.*, "An Experimental Framework for 5G Wireless System Integration into Industry 4.0 Applications," *Energies*, vol. 14, no. 15, p. 4444, Jul. 2021

[8] A. Karimi, K. I. Pedersen, N. H. Mahmood, G. Berardinelli and P. Mogensen, "On the Multiplexing of Data and Metadata for Ultra-Reliable Low-Latency Communications in 5G," *IEEE Transactions on Vehicular Technology*, vol. 69, no. 10, pp. 12136-12147,2020.

[9] R. Hashemi, S. Ali, N. H. Mahmood and M. Latva-aho, "Average Rate and Error Probability Analysis in Short Packet Communications Over RIS-Aided URLLC Systems," *IEEE Transactions on Vehicular Technology*, vol. 70, no. 10, pp. 10320-10334, 2021.

[10] M. Khoshnevisan, V. Joseph, P. Gupta, F. Meshkati, R. Prakash and P. Tinnakornsrisuphap, "5G Industrial Networks With CoMP for URLLC and Time Sensitive Network Architecture," *IEEE Journal on Selected Areas in Communications*, vol. 37, no. 4, pp. 947-959, 2019.

[11] H. Ren, C. Pan, Y. Deng, M. Elkashlan and A. Nallanathan, "Joint Power and Blocklength Optimization for URLLC in a Factory Automation Scenario," *IEEE Transactions on Wireless Communications*, vol. 19, no. 3, pp. 1786-1801, 2020.

[12] I. A. Hemadeh, K. Satyanarayana, M. El-Hajjar and L. Hanzo, "Millimeter-Wave Communications: Physical Channel Models, Design Considerations, Antenna Constructions, and Link-Budget," *IEEE Communications Surveys & Tutorials*, vol. 20, no. 2, pp. 870-913, 2018.

[13] G. Ghatak, S. R. Khosravirad and A. D. Domenico, "Stochastic Geometry Framework for Ultrareliable Cooperative Communications With Random Blockages," in IEEE Internet of Things Journal, vol. 9, no. 7, pp. 5150-5161, 2022.

[14] G. Fortino, F. Messina, D. Rosaci, G. M. L. Sarné and C. Savaglio, "A Trust-Based Team Formation Framework for Mobile Intelligence in Smart Factories," *IEEE Transactions on Industrial Informatics*, vol. 16, no. 9, pp. 6133-6142, 2020.

[15] D. Chizhik *et al.*, "Directional Measurements and Propagation Models at 28 GHz for Reliable Factory Coverage," *IEEE Transactions on Antennas and Propagation*, vol. 70, no. 10, pp. 9596-9606, 2022.

[16] M. Giordani, M. Polese, A. Roy, D. Castor and M. Zorzi, "A Tutorial on Beam Management for 3GPP NR at mmWave Frequencies," *IEEE Communications Surveys & Tutorials, vol. 21, no. 1, pp. 173-196, 2019*

[17] C. S. Morejón García *et al.*, "Robust Decentralized Cooperative Resource Allocation for High-Dense Robotic Swarms by Reducing Control Signaling Impact," *IEEE Access*, vol. 10, pp. 111477-111492, 2022.

[18] A. Zaidi, F. Athley, J. Medbo, U. Gustavsson, G. Durisi and X. Chen, *5G Physical Layer: Principles, Models and Technology Components*. London: Academic Press, 2018.

[19] I. Rodriguez *et al.*, "5G Swarm Production: Advanced Industrial Manufacturing Concepts Enabled by Wireless Automation," *IEEE Communications Magazine*, vol. 59, no. 1, pp. 48-54, 2021.

[20] A. Ramírez-Arroyo *et al.*, "A Study of FR2 Radio Propagation with Focus on Mobility Management in an Industrial Scenario," in *2023 17th European Conference on Antennas and Propagation (EuCAP)*, Florence, Italy, pp. 1-5, 2023.

[21] *NR; Physical channels and modulation (Release 17)*, 3GPP Standard TS38.211 V17.4.0, 2023.

[22] *NR; Physical layer procedures for control (Release 17)*, 3GPP Standard TS38.213 V17.4.0, 2023.

[23] *NR; User Equipment (UE) radio transmission and reception; Part 4: Performance requirements (Release 17)*, 3GPP Standard TS38.101-4 V17.7.0, 2023.

[24] Rohde & Schwarz. (2023). *R&S TSME Drive Test Scanner*. [Online]. Available: https://www.rohde-schwarz.com/us/manual/r-s-tsme6-user-manual-manuals_78701-556097.html

[25] A. Schjørring, A. L. Cretu-Sircu, I. Rodriguez, P. Cederholm, G. Berardinelli, and P. Mogensen, "Performance Evaluation of a UWB Positioning System Applied to Static and Mobile Use Cases in Industrial Scenarios," *Electronics*, vol. 11, no. 20, p. 3294, 2022.

[26] SZ-3004000/P Bi-Conical Antenna 3-40 GHz. [Online]. Available: https://www.ainfoinc.com/amfilerating/file/download/file_id/4510/

[27] P. H. Moose, "A technique for orthogonal frequency division multiplexing frequency offset correction," *IEEE Transactions on Communications*, vol. 42, no. 10, pp. 2908-2914, 1994.

[28] Nokia. (2022). *AirScale mmWave Radio*. [Online]. Available: https://www.nokia.com/networks/mobile-networks/airscale-radio-access/mmwave-radio/

[29] W. C. Y. Lee, "Estimate of local average power of a mobile radio signal," *IEEE Transactions on Vehicular Technology*, vol. 34, no. 1, pp. 22-27, 1985.

[30] *NR; Base Station (BS) radio transmission and reception (Release 18)*, 3GPP Standard TS38.104 V18.0.0, 2023.

[31] H. T. Friis, "A Note on a Simple Transmission Formula," *Proceedings of the IRE*, vol. 34, no. 5, pp. 254-256, 1946.

[32] T. Jiang *et al.*, "3GPP Standardized 5G Channel Model for IIoT Scenarios: A Survey," *IEEE Internet of Things Journal*, vol. 8, no. 11, pp. 8799-8815, 2021.

[33] *Study on channel model for frequencies from 0.5 to 100 GHz (Release 17)*, 3GPP Standard TR38.901 V17.0.0, 2022.

[34] M. López, T. B. Sørensen, I. Z. Kovács, J. Wigard and P. Mogensen, "Measurement-Based Outage Probability Estimation for Mission-Critical Services," *IEEE Access*, vol. 9, pp. 169395-169408, 2021.

[35] T. B. Sorensen, R. L. Bruun, R. D. Marcker and P. E. Mogensen, "Comparison of cm- and mm-Wave Channel Characteristics between Autonomous Mobile Robots in a Small I4.0 Manufacturing Facility," in *2022 25th International Symposium on Wireless Personal Multimedia Communications (WPMC)*, Herning, Denmark, pp. 345-350, 2022.

[36] F. Luna, P.H. Zapata-Cano, J.C. González-Macías and J.F. Valenzuela-Valdés, "Approaching the cell switch-off problem in 5G ultra-dense networks with dynamic multi-objective optimization," *Future Gener. Comput. Syst.*, vol. 110, pp. 876–891, 2020.

[37] K. Deep, K. Pratap, M. L. Kansal, and C. Mohan, "A real coded genetic algorithm for solving integer and mixed integer optimization problems," *Appl. Math. Comput.*, vol. 212, pp. 505–518, 2009.

Alejandro Ramírez-Arroyo was born in Córdoba, Spain, in 1997. He received the B.Sc. degree with honors and M.Sc degree with honors in telecommunication engineering from the University of Granada (UGR), Spain, in 2019 and 2021. Since 2020, he is pursuing the Ph.D. degree with the Smart Wireless Applications and Technologies (SWAT) Research Group in the Department of Signal Theory, Telematics, and Communications, University of Granada. In 2022, he was with the Wireless Communication Networks section, Aalborg University (AAU), Denmark, as an invited Ph.D. Student. His current research interests include optimization techniques, radio propagation and channel characterization for mmWaves and 5G communications.

Melisa López received the B.Sc. and M.Sc. degrees in Telecommunication Engineering from Universidad Politécnica de Catalunya (UPC) in Barcelona, Spain, in 2016 and 2018, respectively. In 2022 she received her Ph.D. degree in Wireless Communications from Aalborg University, Denmark, where she is currently a postdoctoral researcher. Her research interests include radio propagation and the integration of terrestrial and non-terrestrial networks to provide global seamless connectivity.

Ignacio Rodríguez received the Telecommunication Engineering degree from University of Oviedo, Spain, in 2016; and M.Sc. degree in Mobile Communications and Ph.D. degree in Wireless Communications from Aalborg University, Denmark, in 2011 and 2016, respectively. He is currently a Ramón y Cajal Research Fellow at University of Oviedo, Spain. Previously, he was an Assistant Professor at Aalborg University, Denmark, where he was leading the 5G for Industries Research Group, and an External Research Engineer with Nokia Bell Labs. His research interests are mostly related to radio propagation, ultra-reliable and low-latency communications, and industrial IoT. He was a co-recipient of the IEEE VTS 2017 Neal Shepherd Memorial Best Propagation Paper Award, and in 2019, he was co-awarded with the 5G-prize by the Danish Energy Agency and the Danish Society of Telecommunication Engineers.

Troels B. Sørensen received the Ph.D. degree in wireless communications from Aalborg University in 2002. Upon completing his M.Sc. E.E. degree in 1990, he worked with type approval test methods as part of ETSI standardization activities. Since 1997 he has been at Aalborg University, where he is now Associate Professor in the section for Wireless Communication Networks. His research and teaching activities include cellular network performance and evolution, radio resource management, propagation characterisation and related experimental activities. He has successfully supervised more than 15 PhD students, and published more than 120 journal and conference papers.

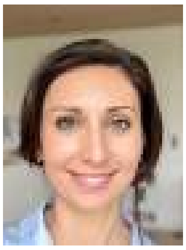

Samantha Caporal del Barrio was born in 1987. She received the Engineering degree in mobile communications from ECE Grande Ecole, Paris, France, in 2008, the M.Sc. degree (with a specialization in antennas and propagation) from both Paris ECE Grande Ecole, Paris, France, and from Aalborg University, Aalborg, Denmark, in 2010, and the Ph.D. degree from Aalborg University, Aalborg, Denmark, in 2013. Her research interests include small terminal performances, user's influence on multiple input multiple output (MIMO) handsets, and frequency-reconfigurable antennas and implementation. She was hired as an industrial post-doc with WiSpry to investigate the integration of MEMS tunable capacitor into 4G antenna designs for handsets. She was also involved in the COST Action IC 1004 on "Cooperative Radio Communications for Green Smart Environments" and the COST Action IC 1102 on "Versatile, Integrated and Signal-aware Technologies for Antennas." She joined Nokia in 2019 to contribute in the 3GPP Standardization group for 5G and 6G in the Physical Layers.

Pablo Padilla was born in Jaén, Spain, in 1982. He received the Telecommunication Engineering degree and the Ph.D. degree from the Radiation Group (Signal, Systems and Radiocommunications Department) of the Technical University of Madrid (UPM), Spain, in 2005 and 2009, respectively. In 2007, he was with the Laboratory of Electromagnetics and Acoustics, Ecole Polytechnique Fédérale de Lausanne, Switzerland, as an invited Ph.D. Student. In 2009, he carried out a Postdoctoral stay at the Helsinki University of Technology (AALTO-TKK). In 2009, he became Assistant Professor at the Signal Theory, Telematics and Communications Department of the University of Granada, where he is currently Associate Professor, since 2012. In 2017, he was an invited Visiting Professor at the Royal Institute of Technology of Stockholm. He has authored more than 65 high-impact journal contributions and more than 60 contributions to international symposia. His research interests include a variety of topics related mainly to electromagnetism and communication issues (radiofrequency devices, antennas and propagation).

Juan F. Valenzuela-Valdés was born in Marbella, Spain. He received the Telecommunication Engineering degree from the Universidad de Málaga, Málaga, Spain, in 2003, and the Ph.D. degree from the Universidad Politécnica de Cartagena, Cartagena, Spain, in 2008. He joined the Department of Information Technologies and Communications, Universidad Politécnica de Cartagena, in 2004. In 2007, he joined EMITE Ing., Murcia, Spain, as the Head of research. In 2011, he joined the Universidad de Extremadura, Mérida, Spain, and in 2015, he joined the Universidad de Granada, where he is currently a Full Professor. He is also the Head of the SWAT Research Group, University of Granada, Granada, Spain, and the Co-Head of the Singular Laboratory of electromagnetic characterization of microwave and millimeter devices and antennas. His publication record comprised of more than 100 publications, including 50 JCR (Journal Citation Reports) indexed articles and seven book chapters. He holds several national and international patents. His current research interests include wireless communications, radio frequency devices, antennas, and propagation. Dr. Valenzuela-Valdés received several prizes, including a National Prize to the Best Ph.D. in mobile communications by Vodafone.

Preben Mogensen received the M.Sc. and Ph.D. degrees from Aalborg University, in 1988 and 1996, respectively. Since 1995, he has been a part-time associated with Nokia in various research positions and has made contributions from 2G to 5G cellular technologies. He has been at Aalborg University, since graduation, in 1988. In 2000, he became a Full Professor with Aalborg University, where he is currently leading the Wireless Communication Networks Section, Department of Electronic Systems. He is also a Principal Scientist with the Standardization Research Laboratory, Nokia Bell Labs. He has coauthored over 450 papers in various domains of wireless communication and his Google Scholar H-index is 70. His current research interests include industrial use cases for 5G, 5G evolution, and 6G. He is a Bell Labs Fellow.

Chapter 3

Conclusions and Future Work

This thesis has mainly focused on the characterization and measurement of the communication channel for the mmWave band. Throughout this document, several proposals, methods and techniques have been presented for the study of the propagation channel in this frequency band, which are outlined in *simulation*, *optimization*, *emulation*, *classification*, *characterization* and *measurement* of communication channels. This chapter summarizes the main conclusions drawn from each of the studies presented in this thesis and presents the research future lines based on the results obtained.

3.1 Conclusions

The conclusions of each contribution to the thesis are presented below:

- On the subject of [J1], the simulation and optimization of a heterogeneous network deployment are presented. The results show that optimizing the transmit power of the deployed base stations enhances the network performance from a multilayer point of view. These simultaneously maximize the throughput of the network users while reducing the energy consumption and signaling costs associated with cell handovers. Two families of optimization algorithms have been tested for the optimization, genetic algorithms and particle swarm optimization, the latter achieving the best results based on the proposed merit factors.
- With regard to [J2], the performance of distributed MIMO systems is analyzed in several environments and frequency bands. For this purpose, a study of the spectral efficiency of the channel is carried out through simulations and laboratory measurements. The results show the importance of channel spatial diversity reflected in the channel

correlation in D-MIMO systems, significantly increasing the spectral efficiency for low correlated channels, i.e. high spatial diversity. In addition, evenly distributed received power in the user equipment among the various available channels ensures optimal spectral efficiency of the communications system. Therefore, the design of communications systems should seek to meet both conditions for the optimal deployment of these D-MIMO-based mobile networks.

- Concerning [J3], the time-gating technique is proposed for channel emulation in propagation channels. By using time-domain window functions, ultra-wide band signals undergo modifications through time-shifting and attenuation or amplification of several multipath components. The analysis of channel parameters such as spectral efficiency or correlation between signals demonstrates the good agreement between the emulated channels and the target channels. These experimental results, conducted in both anechoic and reverberation environments, validate the channel emulation technique as a method to recreate and characterize propagation channels based on laboratory measurements, thereby simplifying the complexity of conducting real scenario on-site measurements.

- Regarding [J4], dimensionality reduction techniques are presented as a method for visual classification of various propagation scenarios. Several parameters of the propagation channel are considered as the high-dimensional space formed by a dataset encompassing up to five different environments. The application of a nonlinear dimensionality reduction algorithm is able to classify the scenarios in the low-dimensional space while also distinguishing them based on the Direction-of-Departure. The outcomes of this algorithm outperform techniques such as PCA or Isomap. The classification of low-dimensional spaces by supervised learning algorithms shows that, despite the dimensionality reduction, the information is preserved compared to the high-dimensional original space with similar classification accuracies in both high-dimensional and low-dimensional spaces. Finally, it is shown that the application of time-gating is able to modify a given scenario so that it resembles a target scenario in the visual classification.

- In relation to [J5], the work proposes the use of frequency invariant beamformers for joint estimation of Direction-of-Arrival and Time-of-Arrival based on elliptical array geometries. This technique involves the generalization of estimation with circular arrays, since elliptical shapes include the circle, as well as pseudolinear arrays. This is due to the degrees of freedom added by the eccentricity and rotation angle of the elliptical geometry. Furthermore, it is shown that a sufficiently dense random configuration of sensors can be approximated by concentric elliptical arrays, which implies the possibility to perform joint estimation from pseudorandom arrays with the proposed technique. Finally, the theoretical framework is validated by experimental measurements in an anechoic chamber where multipath environments are emulated. The results show an excellent agreement between simulations and experimental measurements.

- Addressing [J6], based on the frequency invariant beamformer framework presented in the previous work, the use of toric arrays is proposed to extend the joint Direction-of-Arrival and Time-of-Arrival characterization to 3D scenarios. The geometry of the torus involves the definition of circles in multiple planes, which allows for multiple 2D estimations. The smart combination of these estimations allows for 3D characterization of the propagation channel, i.e. azimuth and elevation angles, and Time-of-Arrival. This technique has been validated through simulations showing results with good accuracy in multipath environments in the mmWave band.

- In connection with [J7], two measurement campaigns are carried out in an industrial environment given an FR2 5G network under operational conditions. Using an autonomous mobile robot capable of self-navigating the factory, measurements of the received power are acquired throughout the entire scenario, and coverage maps are generated. The subsequent analysis of these measurements allows the development of path loss analysis as a function of distance and the study of cell size. Finally, the comparison between both campaigns performed with different configurations of the transmitter module allows the study of beam management procedures involved in the network, such as beam recovery, beam sweeping and beam switching. Thus, these results are expected to be useful for radio planning tasks in directional antenna deployments in industrial environments.

3.2 Future Work

Based on the research conducted in this thesis, the following lines for future research are presented:

- **Extension of communication channel characterization to the sub-THz band.** This thesis has focused on the study of the propagation channel in the mmWave wave band, particularly in the spectrum defined by FR2 (24.25 GHz - 71 GHz). While this frequency range is the most evident prospect for the deployment of new mobile communication systems, the sub-THz frequency band (90 GHz - 300 GHz) is beginning to be considered for the deployment of the sixth generation (6G) for mobile communications [187]. Therefore, in the near future, it will be essential to characterize these bands in depth.

- **Integration of channel emulation using hardware approaches.** In this thesis, channel emulation has been carried out using post-processing techniques such as the time-gating method. The next step in channel emulation is the hardware integration of these solutions by implementing amplifiers or attenuators, as well as delay lines, which modify the properties of certain multipath components of the channel in real-time. This integration would allow real-time emulation of target channels given a channel model distribution.

- **Expansion of the environments included in the visual classification of dimensionality reduction.** The inclusion of a wide range of propagation channels would allow a general mapping of scenarios expected to be relevant for future mobile generations, identifying the similarities and differences between each current scenario.

- **Generalization of the joint estimation of DoA and ToA to new geometries.** After the arrays with elliptical and toric geometries proposed in this thesis, it is possible to extend the use of frequency invariant beamformers to new geometries such as ellipsoids or spheres. The former is the 3D extension of the elliptical arrays, including the advantages of the analyzed ellipses. The latter involves a compact three-dimensional geometry with respect to that studied in the torus.

- **Conducting new measurement campaigns in operational deployments.** Validation of the propagation channel through measurement campaigns in real deployments is essential to ensure good quality of service. The study of deployments under operational conditions in the mmWave band in conventional communication environments, such as outdoor-to-outdoor or outdoor-to-indoor, is crucial to assess whether beam management procedures are capable of ensuring a good link budget in the communication channel.

Bibliography

[1] A. F. Molisch, *Wireless Communications*, 2nd ed. Wiley Publishing, 2011.

[2] M. Agiwal, A. Roy, and N. Saxena, "Next Generation 5G Wireless Networks: A Comprehensive Survey," *IEEE Communications Surveys & Tutorials*, vol. 18, no. 3, pp. 1617–1655, 2016.

[3] M. Xiao, S. Mumtaz, Y. Huang, L. Dai, Y. Li, M. Matthaiou, G. K. Karagiannidis, E. Björnson, K. Yang, C.-L. I, and A. Ghosh, "Millimeter Wave Communications for Future Mobile Networks," *IEEE Journal on Selected Areas in Communications*, vol. 35, no. 9, pp. 1909–1935, 2017.

[4] A. P. K. Reddy, M. S. Kumari, V. Dhanwani, A. K. Bachkaniwala, N. Kumar, K. Vasudevan, S. Selvaganapathy, S. K. Devar, P. Rathod, and V. B. James, "5G New Radio Key Performance Indicators Evaluation for IMT-2020 Radio Interface Technology," *IEEE Access*, vol. 9, pp. 112 290–112 311, 2021.

[5] S. He, Y. Zhang, J. Wang, J. Zhang, J. Ren, Y. Zhang, W. Zhuang, and X. Shen, "A Survey of Millimeter-Wave Communication: Physical-Layer Technology Specifications and Enabling Transmission Technologies," *Proceedings of the IEEE*, vol. 109, no. 10, pp. 1666–1705, 2021.

[6] X. Wang, L. Kong, F. Kong, F. Qiu, M. Xia, S. Arnon, and G. Chen, "Millimeter Wave Communication: A Comprehensive Survey," *IEEE Communications Surveys & Tutorials*, vol. 20, no. 3, pp. 1616–1653, 2018.

[7] W. Hong, Z. H. Jiang, C. Yu, J. Zhou, P. Chen, Z. Yu, H. Zhang, B. Yang, X. Pang, M. Jiang, Y. Cheng, M. K. T. Al-Nuaimi, Y. Zhang, J. Chen, and S. He, "Multibeam Antenna Technologies for 5G Wireless Communications," *IEEE Transactions on Antennas and Propagation*, vol. 65, no. 12, pp. 6231–6249, 2017.

[8] I. A. Hemadeh, K. Satyanarayana, M. El-Hajjar, and L. Hanzo, "Millimeter-Wave Communications: Physical Channel Models, Design Considerations, Antenna Constructions, and Link-Budget," *IEEE Communications Surveys & Tutorials*, vol. 20, no. 2, pp. 870–913, 2018.

[9] E. G. Larsson, O. Edfors, F. Tufvesson, and T. L. Marzetta, "Massive MIMO for next generation wireless systems," *IEEE Communications Magazine*, vol. 52, no. 2, pp. 186–195, 2014.

[10] M. Giordani, M. Polese, A. Roy, D. Castor, and M. Zorzi, "Standalone and Non-Standalone Beam Management for 3GPP NR at mmWaves," *IEEE Communications Magazine*, vol. 57, no. 4, pp. 123–129, 2019.

[11] O. E. Ayach, S. Rajagopal, S. Abu-Surra, Z. Pi, and R. W. Heath, "Spatially Sparse Precoding in Millimeter Wave MIMO Systems," *IEEE Transactions on Wireless Communications*, vol. 13, no. 3, pp. 1499–1513, 2014.

[12] T. Rappaport, *Wireless Communications: Principles and Practice*, 2nd ed. USA: Prentice Hall PTR, 2001.

[13] T. S. Rappaport, G. R. MacCartney, M. K. Samimi, and S. Sun, "Wideband Millimeter-Wave Propagation Measurements and Channel Models for Future Wireless Communication System Design," *IEEE Transactions on Communications*, vol. 63, no. 9, pp. 3029–3056, 2015.

[14] J. G. Andrews, T. Bai, M. N. Kulkarni, A. Alkhateeb, A. K. Gupta, and R. W. Heath, "Modeling and Analyzing Millimeter Wave Cellular Systems," *IEEE Transactions on Communications*, vol. 65, no. 1, pp. 403–430, 2017.

[15] T. S. Rappaport, Y. Xing, G. R. MacCartney, A. F. Molisch, E. Mellios, and J. Zhang, "Overview of Millimeter Wave Communications for Fifth-Generation (5G) Wireless Networks—With a Focus on Propagation Models," *IEEE Transactions on Antennas and Propagation*, vol. 65, no. 12, pp. 6213–6230, 2017.

[16] C. Gentile, P. B. Papazian, N. Golmie, K. A. Remley, P. Vouras, J. Senic, J. Wang, D. Caudill, C. Lai, R. Sun, and J. Chuang, "Millimeter-Wave Channel Measurement and Modeling: A NIST Perspective," *IEEE Communications Magazine*, vol. 56, no. 12, pp. 30–37, 2018.

[17] Z. Lin, X. Du, H.-H. Chen, B. Ai, Z. Chen, and D. Wu, "Millimeter-Wave Propagation Modeling and Measurements for 5G Mobile Networks," *IEEE Wireless Communications*, vol. 26, no. 1, pp. 72–77, 2019.

[18] T. Manabe, K. Sato, H. Masuzawa, K. Taira, T. Ihara, Y. Kasashima, and K. Yamaki, "Polarization dependence of multipath propagation and high-speed transmission characteristics of indoor millimeter-wave channel at 60 GHz," *IEEE Transactions on Vehicular Technology*, vol. 44, no. 2, pp. 268–274, 1995.

[19] T. Manabe, Y. Miura, and T. Ihara, "Effects of antenna directivity and polarization on indoor multipath propagation characteristics at 60 GHz," *IEEE Journal on Selected Areas in Communications*, vol. 14, no. 3, pp. 441–448, 1996.

[20] K. Sato, T. Manabe, T. Ihara, H. Saito, S. Ito, T. Tanaka, K. Sugai, N. Ohmi, Y. Murakami, M. Shibayama, Y. Konishi, and T. Kimura, "Measurements of reflection and transmission characteristics of interior structures of office building in the 60-GHz band," *IEEE Transactions on Antennas and Propagation*, vol. 45, no. 12, pp. 1783–1792, 1997.

[21] T. S. Rappaport, S. Sun, R. Mayzus, H. Zhao, Y. Azar, K. Wang, G. N. Wong, J. K. Schulz, M. Samimi, and F. Gutierrez, "Millimeter Wave Mobile Communications for 5G Cellular: It Will Work!" *IEEE Access*, vol. 1, pp. 335–349, 2013.

[22] S. Rangan, T. S. Rappaport, and E. Erkip, "Millimeter-Wave Cellular Wireless Networks: Potentials and Challenges," *Proceedings of the IEEE*, vol. 102, no. 3, pp. 366–385, 2014.

[23] S. Sun, T. S. Rappaport, M. Shafi, P. Tang, J. Zhang, and P. J. Smith, "Propagation Models and Performance Evaluation for 5G Millimeter-Wave Bands," *IEEE Transactions on Vehicular Technology*, vol. 67, no. 9, pp. 8422–8439, 2018.

[24] Y. Xing, T. S. Rappaport, and A. Ghosh, "Millimeter Wave and Sub-THz Indoor Radio Propagation Channel Measurements, Models, and Comparisons in an Office Environment," *IEEE Communications Letters*, vol. 25, no. 10, pp. 3151–3155, 2021.

[25] 3GPP, "Release 15 Description; Summary of Rel-15 Work Items," 3rd Generation Partnership Project (3GPP), Technical Report (TR) 21.915, 2019, version 15.0.0. [Online]. Available: https://portal.3gpp.org/desktopmodules/Specifications/SpecificationDetails.aspx?specificationId=3389

[26] 3GPP, "Study on channel model for frequencies from 0.5 to 100 GHz," 3rd Generation Partnership Project (3GPP), Technical Report (TR) 38.901, 2022, version 17.0.0. [Online].

Available: https://portal.3gpp.org/desktopmodules/Specifications/SpecificationDetails.aspx?specificationId=3173

[27] S. Mohebi, F. Michelinakis, A. Elmokashfi, O. Grøndalen, K. Mahmood, and A. Zanella, "Sectors, Beams and Environmental Impact on the Performance of Commercial 5G mmWave Cells: An Empirical Study," *IEEE Access*, vol. 10, pp. 133 309–133 323, 2022.

[28] A. Narayanan, M. I. Rochman, A. Hassan, B. S. Firmansyah, V. Sathya, M. Ghosh, F. Qian, and Z.-L. Zhang, "A Comparative Measurement Study of Commercial 5G mmWave Deployments," in *IEEE INFOCOM 2022 - IEEE Conference on Computer Communications*, 2022, pp. 800–809.

[29] Y. Xu, G. Gui, H. Gacanin, and F. Adachi, "A Survey on Resource Allocation for 5G Heterogeneous Networks: Current Research, Future Trends, and Challenges," *IEEE Communications Surveys & Tutorials*, vol. 23, no. 2, pp. 668–695, 2021.

[30] M. Hata, "Empirical formula for propagation loss in land mobile radio services," *IEEE Transactions on Vehicular Technology*, vol. 29, no. 3, pp. 317–325, 1980.

[31] F. Jameel, S. Wyne, S. J. Nawaz, and Z. Chang, "Propagation Channels for mmWave Vehicular Communications: State-of-the-art and Future Research Directions," *IEEE Wireless Communications*, vol. 26, no. 1, pp. 144–150, 2019.

[32] K. Mao, Q. Zhu, M. Song, H. Li, B. Ning, G. F. Pedersen, and W. Fan, "Machine-Learning-Based 3-D Channel Modeling for U2V mmWave Communications," *IEEE Internet of Things Journal*, vol. 9, no. 18, pp. 17 592–17 607, 2022.

[33] R. Amorim, H. Nguyen, P. Mogensen, I. Z. Kovács, J. Wigard, and T. B. Sørensen, "Radio Channel Modeling for UAV Communication Over Cellular Networks," *IEEE Wireless Communications Letters*, vol. 6, no. 4, pp. 514–517, 2017.

[34] D. He, B. Ai, K. Guan, J. M. García-Loygorri, L. Tian, Z. Zhong, and A. Hrovat, "Influence of Typical Railway Objects in a mmWave Propagation Channel," *IEEE Transactions on Vehicular Technology*, vol. 67, no. 4, pp. 2880–2892, 2018.

[35] D. He, B. Ai, C. Briso-Rodriguez, and Z. Zhong, "Train-to-Infrastructure Channel Modeling and Simulation in MmWave Band," *IEEE Communications Magazine*, vol. 57, no. 9, pp. 44–49, 2019.

[36] K. Guan, B. Peng, D. He, J. M. Eckhardt, H. Yi, S. Rey, B. Ai, Z. Zhong, and T. Kürner, “Channel Sounding and Ray Tracing for Intrawagon Scenario at mmWave and Sub-mmWave Bands,” *IEEE Transactions on Antennas and Propagation*, vol. 69, no. 2, pp. 1007–1019, 2021.

[37] G. R. Maccartney, T. S. Rappaport, S. Sun, and S. Deng, “Indoor Office Wideband Millimeter-Wave Propagation Measurements and Channel Models at 28 and 73 GHz for Ultra-Dense 5G Wireless Networks,” *IEEE Access*, vol. 3, pp. 2388–2424, 2015.

[38] S. Ju, Y. Xing, O. Kanhere, and T. S. Rappaport, “Millimeter Wave and Sub-Terahertz Spatial Statistical Channel Model for an Indoor Office Building,” *IEEE Journal on Selected Areas in Communications*, vol. 39, no. 6, pp. 1561–1575, 2021.

[39] H. Zhang, Y. Zhang, J. Cosmas, N. Jawad, W. Li, R. Muller, and T. Jiang, “mmWave Indoor Channel Measurement Campaign for 5G New Radio Indoor Broadcasting,” *IEEE Transactions on Broadcasting*, vol. 68, no. 2, pp. 331–344, 2022.

[40] K. Haneda, J. Järveläinen, A. Karttunen, M. Kyrö, and J. Putkonen, “A Statistical Spatio-Temporal Radio Channel Model for Large Indoor Environments at 60 and 70 GHz,” *IEEE Transactions on Antennas and Propagation*, vol. 63, no. 6, pp. 2694–2704, 2015.

[41] V. Raghavan, A. Partyka, L. Akhoondzadeh-Asl, M. A. Tassoudji, O. H. Koymen, and J. Sanelli, “Millimeter Wave Channel Measurements and Implications for PHY Layer Design,” *IEEE Transactions on Antennas and Propagation*, vol. 65, no. 12, pp. 6521–6533, 2017.

[42] C. Cano, G. H. Sim, A. Asadi, and X. Vilajosana, “A Channel Measurement Campaign for mmWave Communication in Industrial Settings,” *IEEE Transactions on Wireless Communications*, vol. 20, no. 1, pp. 299–315, 2021.

[43] S. Zeb, A. Mahmood, S. A. Hassan, M. Gidlund, and M. Guizani, “Analysis of Beyond 5G Integrated Communication and Ranging Services Under Indoor 3-D mmWave Stochastic Channels,” *IEEE Transactions on Industrial Informatics*, vol. 18, no. 10, pp. 7128–7138, 2022.

[44] M. E. Diago-Mosquera, A. Aragón-Zavala, A. Rodrigues-López, and M. Rodriguez, “mmWave Channel Measurements for 3-D Path Loss Analysis and Model Design in Stadiums,” *IEEE Wireless Communications Letters*, vol. 11, no. 9, pp. 2005–2009, 2022.

[45] M. K. Samimi, T. S. Rappaport, and G. R. MacCartney, “Probabilistic Omnidirectional Path Loss Models for Millimeter-Wave Outdoor Communications,” *IEEE Wireless Communications Letters*, vol. 4, no. 4, pp. 357–360, 2015.

[46] A. I. Sulyman, A. Alwarafy, G. R. MacCartney, T. S. Rappaport, and A. Alsanie, “Directional Radio Propagation Path Loss Models for Millimeter-Wave Wireless Networks in the 28-, 60-, and 73-GHz Bands,” *IEEE Transactions on Wireless Communications*, vol. 15, no. 10, pp. 6939–6947, 2016.

[47] G. Castro, R. Feick, M. Rodríguez, R. Valenzuela, and D. Chizhik, “Outdoor-to-Indoor Empirical Path Loss Models: Analysis for Pico and Femto Cells in Street Canyons,” *IEEE Wireless Communications Letters*, vol. 6, no. 4, pp. 542–545, 2017.

[48] G. R. MacCartney and T. S. Rappaport, “Rural Macrocell Path Loss Models for Millimeter Wave Wireless Communications,” *IEEE Journal on Selected Areas in Communications*, vol. 35, no. 7, pp. 1663–1677, 2017.

[49] H. Friis, “A Note on a Simple Transmission Formula,” *Proceedings of the IRE*, vol. 34, no. 5, pp. 254–256, 1946.

[50] I. Shayea, T. Abd. Rahman, M. Hadri Azmi, and M. R. Islam, “Real Measurement Study for Rain Rate and Rain Attenuation Conducted Over 26 GHz Microwave 5G Link System in Malaysia,” *IEEE Access*, vol. 6, pp. 19 044–19 064, 2018.

[51] F. Norouzian, E. Marchetti, M. Gashinova, E. Hoare, C. Constantinou, P. Gardner, and M. Cherniakov, “Rain Attenuation at Millimeter Wave and Low-THz Frequencies,” *IEEE Transactions on Antennas and Propagation*, vol. 68, no. 1, pp. 421–431, 2020.

[52] G. A. Siles, J. M. Riera, and P. Garcia-del Pino, “Atmospheric Attenuation in Wireless Communication Systems at Millimeter and THz Frequencies [Wireless Corner],” *IEEE Antennas and Propagation Magazine*, vol. 57, no. 1, pp. 48–61, 2015.

[53] Y. Zhang, C. R. Anderson, N. Michelusi, D. J. Love, K. R. Baker, and J. V. Krogmeier, “Propagation Modeling Through Foliage in a Coniferous Forest at 28 GHz,” *IEEE Wireless Communications Letters*, vol. 8, no. 3, pp. 901–904, 2019.

[54] J. Ko, S. Hur, Y.-S. Noh, K. Whang, J. Park, D.-J. Park, and D.-H. Cho, “Measurements and Analysis of Radio Propagation at 28 GHz in

Vegetated Areas of Typical Residential Environments," *IEEE Transactions on Antennas and Propagation*, vol. 68, no. 5, pp. 4149–4154, 2020.

[55] R. Feick, G. Castro, M. Rodríguez, J. Du, D. Chizhik, and R. Valenzuela, "Measurements of Beamswitching Gains and Fade Dynamics for 28 GHz Indoor Static Links in the Presence of Pedestrian Traffic," *IEEE Antennas and Wireless Propagation Letters*, vol. 18, no. 3, pp. 442–446, 2019.

[56] Y. Kumar S and T. Ohtsuki, "Influence and Mitigation of Pedestrian Blockage at mmWave Cellular Networks," *IEEE Transactions on Vehicular Technology*, vol. 69, no. 12, pp. 15 442–15 457, 2020.

[57] F. Fernandes, C. Rom, J. Harrebek, S. Svendsen, and C. N. Manchón, "Hand Blockage Impact on 5G mmWave Beam Management Performance," *IEEE Access*, vol. 10, pp. 106 033–106 049, 2022.

[58] J. Du, D. Chizhik, R. Feick, G. Castro, M. Rodríguez, and R. A. Valenzuela, "Suburban Residential Building Penetration Loss at 28 GHz for Fixed Wireless Access," *IEEE Wireless Communications Letters*, vol. 7, no. 6, pp. 890–893, 2018.

[59] M.-T. Martínez-Inglés, J.-V. Rodríguez, J. Pascual-García, J.-M. Molina-Garcia-Pardo, and L. Juan-Llácer, "On the Influence of Diffuse Scattering on Multiple-Plateau Diffraction Analysis at mm-Wave Frequencies," *IEEE Transactions on Antennas and Propagation*, vol. 67, no. 4, pp. 2130–2135, 2019.

[60] R. Charbonnier, C. Lai, T. Tenoux, D. Caudill, G. Gougeon, J. Senic, C. Gentile, Y. Corre, J. Chuang, and N. Golmie, "Calibration of Ray-Tracing With Diffuse Scattering Against 28-GHz Directional Urban Channel Measurements," *IEEE Transactions on Vehicular Technology*, vol. 69, no. 12, pp. 14 264–14 276, 2020.

[61] S. Deng, G. R. MacCartney, and T. S. Rappaport, "Indoor and Outdoor 5G Diffraction Measurements and Models at 10, 20, and 26 GHz," in *2016 IEEE Global Communications Conference (GLOBECOM)*, 2016, pp. 1–7.

[62] M. R. Akdeniz, Y. Liu, M. K. Samimi, S. Sun, S. Rangan, T. S. Rappaport, and E. Erkip, "Millimeter Wave Channel Modeling and Cellular Capacity Evaluation," *IEEE Journal on Selected Areas in Communications*, vol. 32, no. 6, pp. 1164–1179, 2014.

[63] S. Salous, V. Degli Esposti, F. Fuschini, R. S. Thomae, R. Mueller, D. Dupleich, K. Haneda, J.-M. Molina Garcia-Pardo, J. Pascual Gar-

cia, D. P. Gaillot, S. Hur, and M. Nekovee, “Millimeter-Wave Propagation: Characterization and modeling toward fifth-generation systems. [Wireless Corner],” *IEEE Antennas and Propagation Magazine*, vol. 58, no. 6, pp. 115–127, 2016.

[64] S. Geng, J. Kivinen, X. Zhao, and P. Vainikainen, “Millimeter-Wave Propagation Channel Characterization for Short-Range Wireless Communications,” *IEEE Transactions on Vehicular Technology*, vol. 58, no. 1, pp. 3–13, 2009.

[65] H. Xu, V. Kukshya, and T. Rappaport, “Spatial and temporal characteristics of 60-GHz indoor channels,” *IEEE Journal on Selected Areas in Communications*, vol. 20, no. 3, pp. 620–630, 2002.

[66] D. Chizhik, J. Du, R. Feick, M. Rodriguez, G. Castro, and R. A. Valenzuela, “Path Loss and Directional Gain Measurements at 28 GHz for Non-Line-of-Sight Coverage of Indoors With Corridors,” *IEEE Transactions on Antennas and Propagation*, vol. 68, no. 6, pp. 4820–4830, 2020.

[67] J. Du, D. Chizhik, R. A. Valenzuela, R. Feick, G. Castro, M. Rodriguez, T. Chen, M. Kohli, and G. Zussman, “Directional Measurements in Urban Street Canyons From Macro Rooftop Sites at 28 GHz for 90Coverage,” *IEEE Transactions on Antennas and Propagation*, vol. 69, no. 6, pp. 3459–3469, 2021.

[68] P. Pajusco, N. Malhouroux-Gaffet, and G. El Zein, “Comprehensive Characterization of the Double Directional UWB Residential Indoor Channel,” *IEEE Transactions on Antennas and Propagation*, vol. 63, no. 3, pp. 1129–1139, 2015.

[69] V. Semkin, D. Solomitckii, R. Naderpour, S. Andreev, Y. Koucheryavy, and A. V. Räisänen, “Characterization of Radio Links at 60 GHz Using Simple Geometrical and Highly Accurate 3-D Models,” *IEEE Transactions on Vehicular Technology*, vol. 66, no. 6, pp. 4647–4656, 2017.

[70] M. Steinbauer, A. Molisch, and E. Bonek, “The double-directional radio channel,” *IEEE Antennas and Propagation Magazine*, vol. 43, no. 4, pp. 51–63, 2001.

[71] P. Almers, E. Bonek, A. Burr, N. Czink, M. Debbah, V. Degli-Esposti, H. Hofstetter, P. Kyosti, D. Laurenson, G. Matz, A. F. Molisch, C. Oestges, and H. Ozcelik, “Survey of channel and radio propagation models for wireless MIMO systems,” *EURASIP Journal on Wireless Communications and Networking*, vol. 2007, p. 19070, 2007.

[72] J. McKown and R. Hamilton, “Ray tracing as a design tool for radio networks,” *IEEE Network*, vol. 5, no. 6, pp. 27–30, 1991.

[73] V. Degli-Esposti, F. Fuschini, E. M. Vitucci, and G. Falciasecca, “Measurement and Modelling of Scattering From Buildings,” *IEEE Transactions on Antennas and Propagation*, vol. 55, no. 1, pp. 143–153, 2007.

[74] Z. Yun and M. F. Iskander, “Ray Tracing for Radio Propagation Modeling: Principles and Applications,” *IEEE Access*, vol. 3, pp. 1089–1100, 2015.

[75] S. Hur, S. Baek, B. Kim, Y. Chang, A. F. Molisch, T. S. Rappaport, K. Haneda, and J. Park, “Proposal on Millimeter-Wave Channel Modeling for 5G Cellular System,” *IEEE Journal of Selected Topics in Signal Processing*, vol. 10, no. 3, pp. 454–469, 2016.

[76] A. Saleh and R. Valenzuela, “A Statistical Model for Indoor Multipath Propagation,” *IEEE Journal on Selected Areas in Communications*, vol. 5, no. 2, pp. 128–137, 1987.

[77] T. Zwick, C. Fischer, and W. Wiesbeck, “A stochastic multipath channel model including path directions for indoor environments,” *IEEE Journal on Selected Areas in Communications*, vol. 20, no. 6, pp. 1178–1192, 2002.

[78] 3GPP, “Study on channel model for frequency spectrum above 6 GHz,” 3rd Generation Partnership Project (3GPP), Technical Report (TR) 38.900, 2018, version 15.0.0. [Online]. Available: https://portal.3gpp.org/desktopmodules/Specifications/SpecificationDetails.aspx?specificationId=2991

[79] S. Jaeckel, L. Raschkowski, K. Börner, and L. Thiele, “QuaDRiGa: A 3-D Multi-Cell Channel Model With Time Evolution for Enabling Virtual Field Trials,” *IEEE Transactions on Antennas and Propagation*, vol. 62, no. 6, pp. 3242–3256, 2014.

[80] Fraunhofer HHI. QuaDRiGa: Quasi Deterministic Radio Channel Generator. [Online]. Available: https://quadriga-channel-model.de/

[81] S. Sun, G. R. MacCartney, and T. S. Rappaport, “A novel millimeter-wave channel simulator and applications for 5G wireless communications,” in *2017 IEEE International Conference on Communications (ICC)*, 2017, pp. 1–7.

[82] New York University. NYUSIM. [Online]. Available: https://wireless.engineering.nyu.edu/nyusim/

[83] M. S. Miah, D. Anin, A. Khatun, K. Haneda, L. Hentila, and E. T. Salonen, “On the Field Emulation Techniques in Over-the-Air Testing: Experimental Throughput Comparison,” *IEEE Antennas and Wireless Propagation Letters*, vol. 16, pp. 2224–2227, 2017.

[84] M. A. Garcia-Fernandez, J. D. Sanchez-Heredia, A. M. Martinez-Gonzalez, D. A. Sanchez-Hernandez, and J. F. Valenzuela-Valdes, “Advances in mode-stirred reverberation chambers for wireless communication performance evaluation,” *IEEE Communications Magazine*, vol. 49, no. 7, pp. 140–147, 2011.

[85] Y. Ji, W. Fan, G. F. Pedersen, and X. Wu, “On Channel Emulation Methods in Multiprobe Anechoic Chamber Setups for Over-the-Air Testing,” *IEEE Transactions on Vehicular Technology*, vol. 67, no. 8, pp. 6740–6751, 2018.

[86] W. Wang, R. Wang, H. Gao, and Y. Wu, “Implementation and Analysis of 3D Channel Emulation Method in Multi-Probe Anechoic Chamber Setups,” *IEEE Access*, vol. 7, pp. 108 571–108 580, 2019.

[87] H. Fielitz, K. A. Remley, C. L. Holloway, Q. Zhang, Q. Wu, and D. W. Matolak, “Reverberation-Chamber Test Environment for Outdoor Urban Wireless Propagation Studies,” *IEEE Antennas and Wireless Propagation Letters*, vol. 9, pp. 52–56, 2010.

[88] P. Kyösti, L. Hentilä, W. Fan, J. Lehtomäki, and M. Latva-Aho, “On Radiated Performance Evaluation of Massive MIMO Devices in Multiprobe Anechoic Chamber OTA Setups,” *IEEE Transactions on Antennas and Propagation*, vol. 66, no. 10, pp. 5485–5497, 2018.

[89] Y. Miao, W. Fan, J. Takada, R. He, X. Yin, M. Yang, J. Rodríguez-Piñeiro, A. A. Glazunov, W. Wang, and Y. Gong, “Comparing Channel Emulation Algorithms by Using Plane Waves and Spherical Vector Waves in Multiprobe Anechoic Chamber Setups,” *IEEE Transactions on Antennas and Propagation*, vol. 67, no. 6, pp. 4091–4103, 2019.

[90] C. L. Holloway, D. A. Hill, J. M. Ladbury, P. F. Wilson, G. Koepke, and J. Coder, “On the Use of Reverberation Chambers to Simulate a Rician Radio Environment for the Testing of Wireless Devices,” *IEEE Transactions on Antennas and Propagation*, vol. 54, no. 11, pp. 3167–3177, 2006.

[91] J. Frolik, T. M. Weller, S. DiStasi, and J. Cooper, “A Compact Reverberation Chamber for Hyper-Rayleigh Channel Emulation,” *IEEE Transactions on Antennas and Propagation*, vol. 57, no. 12, pp. 3962–3968, 2009.

[92] A. B. Kihero, M. Karabacak, and H. Arslan, "Emulation Techniques for Small Scale Fading Aspects by Using Reverberation Chamber," *IEEE Transactions on Antennas and Propagation*, vol. 67, no. 2, pp. 1246–1258, 2019.

[93] W. Shao and Y. Du, "Microwave Imaging by Deep Learning Network: Feasibility and Training Method," *IEEE Transactions on Antennas and Propagation*, vol. 68, no. 7, pp. 5626–5635, 2020.

[94] K. Xu, L. Wu, X. Ye, and X. Chen, "Deep Learning-Based Inversion Methods for Solving Inverse Scattering Problems With Phaseless Data," *IEEE Transactions on Antennas and Propagation*, vol. 68, no. 11, pp. 7457–7470, 2020.

[95] J. Thrane, D. Zibar, and H. L. Christiansen, "Model-Aided Deep Learning Method for Path Loss Prediction in Mobile Communication Systems at 2.6 GHz," *IEEE Access*, vol. 8, pp. 7925–7936, 2020.

[96] H. Cheng, S. Ma, and H. Lee, "CNN-Based mmWave Path Loss Modeling for Fixed Wireless Access in Suburban Scenarios," *IEEE Antennas and Wireless Propagation Letters*, vol. 19, no. 10, pp. 1694–1698, 2020.

[97] M. Bal, A. Marey, H. F. Ates, T. Baykas, and B. K. Gunturk, "Regression of Large-Scale Path Loss Parameters Using Deep Neural Networks," *IEEE Antennas and Wireless Propagation Letters*, vol. 21, no. 8, pp. 1562–1566, 2022.

[98] J. Zhang, L. Liu, Y. Fan, L. Zhuang, T. Zhou, and Z. Piao, "Wireless Channel Propagation Scenarios Identification: A Perspective of Machine Learning," *IEEE Access*, vol. 8, pp. 47 797–47 806, 2020.

[99] M. I. AlHajri, N. T. Ali, and R. M. Shubair, "Classification of Indoor Environments for IoT Applications: A Machine Learning Approach," *IEEE Antennas and Wireless Propagation Letters*, vol. 17, no. 12, pp. 2164–2168, 2018.

[100] M. Yang, B. Ai, R. He, C. Shen, M. Wen, C. Huang, J. Li, Z. Ma, L. Chen, X. Li, and Z. Zhong, "Machine-Learning-Based Scenario Identification Using Channel Characteristics in Intelligent Vehicular Communications," *IEEE Transactions on Intelligent Transportation Systems*, vol. 22, no. 7, pp. 3961–3974, 2021.

[101] T. Zhou, Y. Wang, C.-X. Wang, S. Salous, L. Liu, and C. Tao, "Multi-Feature Fusion Based Recognition and Relevance Analysis of Propagation Scenes for High-Speed Railway Channels," *IEEE Transactions on Vehicular Technology*, vol. 69, no. 8, pp. 8107–8118, 2020.

[102] I. Guvenc and C.-C. Chong, “A Survey on TOA Based Wireless Localization and NLOS Mitigation Techniques,” *IEEE Communications Surveys & Tutorials*, vol. 11, no. 3, pp. 107–124, 2009.

[103] S. Aditya, A. F. Molisch, and H. M. Behairy, “A Survey on the Impact of Multipath on Wideband Time-of-Arrival Based Localization,” *Proceedings of the IEEE*, vol. 106, no. 7, pp. 1183–1203, 2018.

[104] F. Zafari, A. Gkelias, and K. K. Leung, “A Survey of Indoor Localization Systems and Technologies,” *IEEE Communications Surveys & Tutorials*, vol. 21, no. 3, pp. 2568–2599, 2019.

[105] E. Gentilho, P. Scalassara, and T. Abrão, “Direction-of-Arrival Estimation Methods: A Performance-Complexity Tradeoff Perspective,” *Journal of Signal Processing Systems*, vol. 92, pp. 239–256, 2020.

[106] B. Van Veen and K. Buckley, “Beamforming: a versatile approach to spatial filtering,” *IEEE ASSP Magazine*, vol. 5, no. 2, pp. 4–24, 1988.

[107] J. Capon, “High-resolution frequency-wavenumber spectrum analysis,” *Proceedings of the IEEE*, vol. 57, no. 8, pp. 1408–1418, 1969.

[108] R. Schmidt, “Multiple emitter location and signal parameter estimation,” *IEEE Transactions on Antennas and Propagation*, vol. 34, no. 3, pp. 276–280, 1986.

[109] R. Roy and T. Kailath, “ESPRIT-estimation of signal parameters via rotational invariance techniques,” *IEEE Transactions on Acoustics, Speech, and Signal Processing*, vol. 37, no. 7, pp. 984–995, 1989.

[110] J. Fessler and A. Hero, “Space-alternating generalized expectation-maximization algorithm,” *IEEE Transactions on Signal Processing*, vol. 42, no. 10, pp. 2664–2677, 1994.

[111] B. Fleury, M. Tschudin, R. Heddergott, D. Dahlhaus, and K. Ingeman Pedersen, “Channel parameter estimation in mobile radio environments using the SAGE algorithm,” *IEEE Journal on Selected Areas in Communications*, vol. 17, no. 3, pp. 434–450, 1999.

[112] J. Bang, H. Chung, J. Hong, H. Seo, J. Choi, and S. Kim, “Millimeter-Wave Communications: Recent Developments and Challenges of Hardware and Beam Management Algorithms,” *IEEE Communications Magazine*, vol. 59, no. 8, pp. 86–92, 2021.

[113] 3GPP, “Study on new radio access technology Physical layer aspects,” 3rd Generation Partnership Project (3GPP), Technical Report (TR) 38.802, 2017, version 14.2.0. [Online]. Available: https://portal.3gpp.org/desktopmodules/Specifications/SpecificationDetails.aspx?specificationId=3066

[114] M. Giordani, M. Polese, A. Roy, D. Castor, and M. Zorzi, "A Tutorial on Beam Management for 3GPP NR at mmWave Frequencies," *IEEE Communications Surveys & Tutorials*, vol. 21, no. 1, pp. 173–196, 2019.

[115] C. Jeong, J. Park, and H. Yu, "Random access in millimeter-wave beamforming cellular networks: issues and approaches," *IEEE Communications Magazine*, vol. 53, no. 1, pp. 180–185, 2015.

[116] J. Choi, "Beam Selection in mm-Wave Multiuser MIMO Systems Using Compressive Sensing," *IEEE Transactions on Communications*, vol. 63, no. 8, pp. 2936–2947, 2015.

[117] A. Alkhateeb, Y.-H. Nam, M. S. Rahman, J. Zhang, and R. W. Heath, "Initial Beam Association in Millimeter Wave Cellular Systems: Analysis and Design Insights," *IEEE Transactions on Wireless Communications*, vol. 16, no. 5, pp. 2807–2821, 2017.

[118] S. Jayaprakasam, X. Ma, J. W. Choi, and S. Kim, "Robust Beam-Tracking for mmWave Mobile Communications," *IEEE Communications Letters*, vol. 21, no. 12, pp. 2654–2657, 2017.

[119] A. Bonfante, L. G. Giordano, I. Macaluso, and N. Marchetti, "Performance of Predictive Indoor mmWave Networks With Dynamic Blockers," *IEEE Transactions on Cognitive Communications and Networking*, vol. 8, no. 2, pp. 812–827, 2022.

[120] Q. Xu and Y. Huang, *Anechoic and Reverberation Chambers: Theory, Design, and Measurements.* Wiley-IEEE Press, 2019.

[121] W. Emerson, "Electromagnetic wave absorbers and anechoic chambers through the years," *IEEE Transactions on Antennas and Propagation*, vol. 21, no. 4, pp. 484–490, 1973.

[122] X. Chen, J. Tang, T. Li, S. Zhu, Y. Ren, Z. Zhang, and A. Zhang, "Reverberation Chambers for Over-the-Air Tests: An Overview of Two Decades of Research," *IEEE Access*, vol. 6, pp. 49 129–49 143, 2018.

[123] V. Rodriguez, "Basic Rules for Indoor Anechoic Chamber Design [Measurements Corner]," *IEEE Antennas and Propagation Magazine*, vol. 58, no. 6, pp. 82–93, 2016.

[124] P. Padilla, A. Muñoz-Acevedo, M. Sierra-Castañer, and M. Sierra-Pérez, "Electronically Reconfigurable Transmitarray at Ku Band for Microwave Applications," *IEEE Transactions on Antennas and Propagation*, vol. 58, no. 8, pp. 2571–2579, 2010.

[125] X. Chen, P.-S. Kildal, J. Carlsson, and J. Yang, "Comparison of Ergodic Capacities From Wideband MIMO Antenna Measurements in Reverberation Chamber and Anechoic Chamber," *IEEE Antennas and Wireless Propagation Letters*, vol. 10, pp. 446–449, 2011.

[126] X. Chen, P.-S. Kildal, J. Carlsson, and J. Yang, "MRC Diversity and MIMO Capacity Evaluations of Multi-Port Antennas Using Reverberation Chamber and Anechoic Chamber," *IEEE Transactions on Antennas and Propagation*, vol. 61, no. 2, pp. 917–926, 2013.

[127] C. Lemoine, P. Besnier, and M. Drissi, "Estimating the Effective Sample Size to Select Independent Measurements in a Reverberation Chamber," *IEEE Transactions on Electromagnetic Compatibility*, vol. 50, no. 2, pp. 227–236, 2008.

[128] F. Moglie and V. M. Primiani, "Analysis of the Independent Positions of Reverberation Chamber Stirrers as a Function of Their Operating Conditions," *IEEE Transactions on Electromagnetic Compatibility*, vol. 53, no. 2, pp. 288–295, 2011.

[129] J. D. Sanchez-Heredia, J. F. Valenzuela-Valdes, A. M. Martinez-Gonzalez, and D. A. Sanchez-Hernandez, "Emulation of MIMO Rician-Fading Environments With Mode-Stirred Reverberation Chambers," *IEEE Transactions on Antennas and Propagation*, vol. 59, no. 2, pp. 654–660, 2011.

[130] P.-S. Kildal, C. Orlenius, and J. Carlsson, "OTA Testing in Multipath of Antennas and Wireless Devices With MIMO and OFDM," *Proceedings of the IEEE*, vol. 100, no. 7, pp. 2145–2157, 2012.

[131] C. L. Holloway, H. A. Shah, R. J. Pirkl, W. F. Young, D. A. Hill, and J. Ladbury, "Reverberation Chamber Techniques for Determining the Radiation and Total Efficiency of Antennas," *IEEE Transactions on Antennas and Propagation*, vol. 60, no. 4, pp. 1758–1770, 2012.

[132] C. Lemoine, E. Amador, P. Besnier, J.-M. Floc'h, and A. Laisné, "Antenna Directivity Measurement in Reverberation Chamber From Rician K-Factor Estimation," *IEEE Transactions on Antennas and Propagation*, vol. 61, no. 10, pp. 5307–5310, 2013.

[133] X. Chen, P.-S. Kildal, and S.-H. Lai, "Estimation of Average Rician K-Factor and Average Mode Bandwidth in Loaded Reverberation Chamber," *IEEE Antennas and Wireless Propagation Letters*, vol. 10, pp. 1437–1440, 2011.

[134] J. F. Valenzuela-Valdés, A. Lozano-Guerrero, J. D. Sánchez-Heredia, A. Martínez-González, and P. Hallbjörner, "Measuring Distributed

MIMO System in Reverberation Chamber," *IEEE Antennas and Wireless Propagation Letters*, vol. 12, pp. 1586–1589, 2013.

[135] L. R. Arnaut and G. Gradoni, "Probability Distribution of the Coherence Bandwidth of a Reverberation Chamber," *IEEE Transactions on Antennas and Propagation*, vol. 63, no. 5, pp. 2286–2290, 2015.

[136] E. Zitzler, L. Thiele, M. Laumanns, C. Fonseca, and V. da Fonseca, "Performance assessment of multiobjective optimizers: an analysis and review," *IEEE Transactions on Evolutionary Computation*, vol. 7, no. 2, pp. 117–132, 2003.

[137] H. Ma, S. Shen, M. Yu, Z. Yang, M. Fei, and H. Zhou, "Multi-population techniques in nature inspired optimization algorithms: A comprehensive survey," *Swarm and Evolutionary Computation*, vol. 44, pp. 365–387, 2019.

[138] Z. Fei, B. Li, S. Yang, C. Xing, H. Chen, and L. Hanzo, "A Survey of Multi-Objective Optimization in Wireless Sensor Networks: Metrics, Algorithms, and Open Problems," *IEEE Communications Surveys & Tutorials*, vol. 19, no. 1, pp. 550–586, 2017.

[139] M. Srinivas and L. Patnaik, "Genetic algorithms: a survey," *Computer*, vol. 27, no. 6, pp. 17–26, 1994.

[140] K. Man, K. Tang, and S. Kwong, "Genetic algorithms: concepts and applications [in engineering design]," *IEEE Transactions on Industrial Electronics*, vol. 43, no. 5, pp. 519–534, 1996.

[141] M. Srinivas and L. Patnaik, "Adaptive probabilities of crossover and mutation in genetic algorithms," *IEEE Transactions on Systems, Man, and Cybernetics*, vol. 24, no. 4, pp. 656–667, 1994.

[142] K. Deb, A. Pratap, S. Agarwal, and T. Meyarivan, "A fast and elitist multiobjective genetic algorithm: NSGA-II," *IEEE Transactions on Evolutionary Computation*, vol. 6, no. 2, pp. 182–197, 2002.

[143] T. M. Shami, A. A. El-Saleh, M. Alswaitti, Q. Al-Tashi, M. A. Summakieh, and S. Mirjalili, "Particle Swarm Optimization: A Comprehensive Survey," *IEEE Access*, vol. 10, pp. 10 031–10 061, 2022.

[144] C. Coello, G. Pulido, and M. Lechuga, "Handling multiple objectives with particle swarm optimization," *IEEE Transactions on Evolutionary Computation*, vol. 8, no. 3, pp. 256–279, 2004.

[145] M. Clerc and J. Kennedy, "The particle swarm - explosion, stability, and convergence in a multidimensional complex space," *IEEE Transactions on Evolutionary Computation*, vol. 6, no. 1, pp. 58–73, 2002.

[146] J. Robinson and Y. Rahmat-Samii, “Particle swarm optimization in electromagnetics,” *IEEE Transactions on Antennas and Propagation*, vol. 52, no. 2, pp. 397–407, 2004.

[147] A. Nebro, J. Durillo, J. Garcia-Nieto, C. Coello Coello, F. Luna, and E. Alba, “SMPSO: A new PSO-based metaheuristic for multi-objective optimization,” in *2009 IEEE Symposium on Computational Intelligence in Multi-Criteria Decision-Making(MCDM)*, 2009, pp. 66–73.

[148] A. Gharamohammadi, F. Behnia, and R. Amiri, “Imaging Based on Correlation Function for Buried Objects Identification,” *IEEE Sensors Journal*, vol. 18, no. 18, pp. 7407–7413, 2018.

[149] M. Farina, A. Lucesoli, T. Pietrangelo, A. di Donato, S. Fabiani, G. Venanzoni, D. Mencarelli, T. Rozzi, and A. Morini, “Disentangling time in a near-field approach to scanning probe microscopy,” *Nanoscale*, vol. 3, pp. 3589–3593, 2011.

[150] M. Farina, F. Piacenza, F. De Angelis, D. Mencarelli, A. Morini, G. Venanzoni, T. Pietrangelo, M. Malavolta, A. Basso, M. Provinciali, J. C. M. Hwang, X. Jin, and A. Di Donato, “Investigation of Fullerene Exposure of Breast Cancer Cells by Time-Gated Scanning Microwave Microscopy,” *IEEE Transactions on Microwave Theory and Techniques*, vol. 64, no. 12, pp. 4823–4831, 2016.

[151] S. Gezici and H. V. Poor, “Position Estimation via Ultra-Wide-Band Signals,” *Proceedings of the IEEE*, vol. 97, no. 2, pp. 386–403, 2009.

[152] S. Loredo, M. Pino, F. Las-Heras, and T. Sarkar, “Echo identification and cancellation techniques for antenna measurement in non-anechoic test sites,” *IEEE Antennas and Propagation Magazine*, vol. 46, no. 1, pp. 100–107, 2004.

[153] J. Knapp and T. F. Eibert, “Near-Field Antenna Pattern Measurements in Highly Reflective Environments,” *IEEE Transactions on Antennas and Propagation*, vol. 67, no. 9, pp. 6159–6169, 2019.

[154] A. Soltane, G. Andrieu, E. Perrin, C. Decroze, and A. Reineix, “Antenna Radiation Pattern Measurement in a Reverberating Enclosure Using the Time-Gating Technique,” *IEEE Antennas and Wireless Propagation Letters*, vol. 19, no. 1, pp. 183–187, 2020.

[155] J. Wang, C. Jiang, H. Zhang, Y. Ren, K.-C. Chen, and L. Hanzo, “Thirty Years of Machine Learning: The Road to Pareto-Optimal Wireless Networks,” *IEEE Communications Surveys & Tutorials*, vol. 22, no. 3, pp. 1472–1514, 2020.

[156] P. Cunningham and S. J. Delany, “K-Nearest Neighbour Classifiers - A Tutorial,” *ACM Computing Surveys*, vol. 54, no. 6, jul 2021.

[157] S. B. Kotsiantis, “Decision trees: a recent overview,” *Artificial Intelligence Review*, vol. 39, pp. 261–283, 2011.

[158] A. McCallum and K. Nigam, “A comparison of event models for naive bayes text classification,” in *AAAI Conference on Artificial Intelligence*, 1998.

[159] T. Hastie, R. Tibshirani, and J. Friedman, *The Elements of Statistical Learning. Data Mining, Inference, and Prediction.* Springer New York, NY, 2009.

[160] S. Salcedo-Sanz, J. L. Rojo-Álvarez, M. Martínez-Ramón, and G. Camps-Valls, “Support vector machines in engineering: an overview,” *WIREs Data Mining and Knowledge Discovery*, vol. 4, no. 3, pp. 234–267, 2014.

[161] Y. Bengio, A. Courville, and P. Vincent, “Representation Learning: A Review and New Perspectives,” *IEEE Transactions on Pattern Analysis and Machine Intelligence*, vol. 35, no. 8, pp. 1798–1828, 2013.

[162] M. Usama, J. Qadir, A. Raza, H. Arif, K.-l. A. Yau, Y. Elkhatib, A. Hussain, and A. Al-Fuqaha, “Unsupervised Machine Learning for Networking: Techniques, Applications and Research Challenges,” *IEEE Access*, vol. 7, pp. 65 579–65 615, 2019.

[163] M. Espadoto, R. M. Martins, A. Kerren, N. S. T. Hirata, and A. C. Telea, “Toward a Quantitative Survey of Dimension Reduction Techniques,” *IEEE Transactions on Visualization and Computer Graphics*, vol. 27, no. 3, pp. 2153–2173, 2021.

[164] I. T. Jolliffe and J. Cadima, “Principal component analysis: a review and recent developments,” *Philosophical Transactions of the Royal Society A: Mathematical, Physical and Engineering Sciences*, vol. 374, no. 2065, p. 20150202, 2016.

[165] L. van der Maaten and G. Hinton, “Visualizing Data using t-SNE,” *Journal of Machine Learning Research*, vol. 9, no. 86, pp. 2579–2605, 2008.

[166] N. Pezzotti, B. P. F. Lelieveldt, L. v. d. Maaten, T. Höllt, E. Eisemann, and A. Vilanova, “Approximated and User Steerable tSNE for Progressive Visual Analytics,” *IEEE Transactions on Visualization and Computer Graphics*, vol. 23, no. 7, pp. 1739–1752, 2017.

[167] A. F. Molisch, “Ultra-Wide-Band Propagation Channels,” *Proceedings of the IEEE*, vol. 97, no. 2, pp. 353–371, 2009.

[168] Tuan-Do-Hong and P. Russer, “Signal processing for wideband smart antenna array applications,” *IEEE Microwave Magazine*, vol. 5, no. 1, pp. 57–67, 2004.

[169] L. C. Parra, “Steerable frequency-invariant beamforming for arbitrary arrays,” *The Journal of the Acoustical Society of America*, vol. 119, no. 6, pp. 3839–3847, 06 2006.

[170] W. Liu and S. Weiss, “Design of Frequency Invariant Beamformers for Broadband Arrays,” *IEEE Transactions on Signal Processing*, vol. 56, no. 2, pp. 855–860, 2008.

[171] W. Fan, I. Carton, J. O. Nielsen, K. Olesen, and G. F. Pedersen, “Measured wideband characteristics of indoor channels at centimetric and millimetric bands,” *EURASIP Journal on Wireless Communications and Networking*, vol. 2016, p. 58, 2016.

[172] S. Chan and C. Pun, “On the design of digital broadband beamformer for uniform circular array with frequency invariant characteristics,” in *2002 IEEE International Symposium on Circuits and Systems*, 2002, pp. 1–4.

[173] C. Gentile, A. J. Braga, and A. Kik, “A Comprehensive Evaluation of Joint Range and Angle Estimation in Ultra-Wideband Location Systems for Indoors,” in *2008 IEEE International Conference on Communications*, 2008, pp. 4219–4225.

[174] F. Zhang, W. Fan, and G. F. Pedersen, “Frequency-Invariant Uniform Circular Array for Wideband mm-Wave Channel Characterization,” *IEEE Antennas and Wireless Propagation Letters*, vol. 16, pp. 641–644, 2017.

[175] X. Cai and W. Fan, “A Complexity-Efficient High Resolution Propagation Parameter Estimation Algorithm for Ultra-Wideband Large-Scale Uniform Circular Array,” *IEEE Transactions on Communications*, vol. 67, no. 8, pp. 5862–5874, 2019.

[176] S. C. Chan and H. H. Chen, “Uniform Concentric Circular Arrays With Frequency-Invariant Characteristics—Theory, Design, Adaptive Beamforming and DOA Estimation,” *IEEE Transactions on Signal Processing*, vol. 55, no. 1, pp. 165–177, 2007.

[177] W. Wang, S. L. Capitaneanu, D. Marinca, and E.-S. Lohan, “Comparative Analysis of Channel Models for Industrial IoT Wireless Communication,” *IEEE Access*, vol. 7, pp. 91 627–91 640, 2019.

[178] G. Hampel, C. Li, and J. Li, “5G Ultra-Reliable Low-Latency Communications in Factory Automation Leveraging Licensed and Unlicensed Bands,” *IEEE Communications Magazine*, vol. 57, no. 5, pp. 117–123, 2019.

[179] I. Rodriguez, R. S. Mogensen, A. Schjørring, M. Razzaghpour, R. Maldonado, G. Berardinelli, R. Adeogun, P. H. Christensen, P. Mogensen, O. Madsen, C. Møller, G. Pocovi, T. Kolding, C. Rosa, B. Jørgensen, and S. Barbera, “5G Swarm Production: Advanced Industrial Manufacturing Concepts Enabled by Wireless Automation,” *IEEE Communications Magazine*, vol. 59, no. 1, pp. 48–54, 2021.

[180] I. Rodriguez, R. S. Mogensen, A. Fink, T. Raunholt, S. Markussen, P. H. Christensen, G. Berardinelli, P. Mogensen, C. Schou, and O. Madsen, “An Experimental Framework for 5G Wireless System Integration into Industry 4.0 Applications,” *Energies*, vol. 14, no. 15, 2021.

[181] M. Cheffena, “Propagation Channel Characteristics of Industrial Wireless Sensor Networks [Wireless Corner],” *IEEE Antennas and Propagation Magazine*, vol. 58, no. 1, pp. 66–73, 2016.

[182] E. Tanghe, D. P. Gaillot, M. Liénard, L. Martens, and W. Joseph, “Experimental Analysis of Dense Multipath Components in an Industrial Environment,” *IEEE Transactions on Antennas and Propagation*, vol. 62, no. 7, pp. 3797–3805, 2014.

[183] Y. Ai, J. B. Andersen, and M. Cheffena, “Path-Loss Prediction for an Industrial Indoor Environment Based on Room Electromagnetics,” *IEEE Transactions on Antennas and Propagation*, vol. 65, no. 7, pp. 3664–3674, 2017.

[184] G. G. Messier, M. W. Wasson, and M. J. Herrmann, “Petroleum Refinery Mesh Network Propagation Measurements,” *IEEE Transactions on Antennas and Propagation*, vol. 65, no. 10, pp. 5645–5648, 2017.

[185] V. Semkin, E. M. Vitucci, F. Fuschini, M. Barbiroli, V. Degli-Esposti, and C. Oestges, “Characterizing the UAV-to-Machine UWB Radio Channel in Smart Factories,” *IEEE Access*, vol. 9, pp. 76 542–76 550, 2021.

[186] D. Chizhik, J. Du, R. A. Valenzuela, D. Samardzija, S. Kucera, D. Kozlov, R. Fuchs, J. Otterbach, J. Koppenborg, P. Baracca, M. Doll, I. Rodriguez, R. Feick, and M. Rodriguez, “Directional Measurements and Propagation Models at 28 GHz for Reliable Factory Coverage,” *IEEE Transactions on Antennas and Propagation*, vol. 70, no. 10, pp. 9596–9606, 2022.

[187] H. Elayan, O. Amin, B. Shihada, R. M. Shubair, and M.-S. Alouini, "Terahertz Band: The Last Piece of RF Spectrum Puzzle for Communication Systems," *IEEE Open Journal of the Communications Society*, vol. 1, pp. 1–32, 2020.

Appendices

Appendix A

Introducción y conclusiones

Con el objetivo de cumplir con la normativa de la Universidad de Granada (UGR) referente a la elaboración de la tesis doctoral en un idioma diferente al español, este apéndice expone los Capítulos de Introducción (Sección 1.1) y Conclusiones (Sección 3.1) en español, presentándose así el presente documento en los idiomas español e inglés.

Introducción

Las comunicaciones móviles han cambiado el mundo. Desde finales del siglo XIX y principios del siglo XX, la humanidad ha mostrado gran interés por utilizar las ondas electromagnéticas como una herramienta para transmitir información. Esto quedó reflejado en estudios pioneros en el marco teórico, como los presentados por James Clerk Maxwell y Heinrich Rudolf Hertz, y en el marco práctico, como la transmisión de ondas de radio a través del océano Atlántico por Guillermo Marconi. Dado el creciente interés alentado por el uso de las ondas de radio como medio de transmisión de información, la investigación llevada a cabo durante el siglo XX condujo a la implementación de la tecnología de Primera Generación (1G) para redes móviles en la década de 1980 [1]. Estas comunicaciones primitivas, basadas en comunicaciones de voz mediante tecnología analógica, fueron evolucionando hasta la generación actual, la Quinta Generación (5G) para redes móviles, basada íntegramente en tecnología digital y comunicaciones de datos [2]. Actualmente, el Proyecto de Asociación de Tercera Generación (*3rd Generation Partnership Project*, 3GPP) ha propuesto tres casos de uso: banda ancha móvil mejorada (*Enhanced Mobile BroadBand*, eMBB), comunicación ultra confiable y de baja latencia (*Ultra Reliable Low Latency Communication*, URLLC) y comunicaciones masivas máquina-a-máquina (*Massive Machine Type Communications*, mMTC) para el despliegue de redes 5G [3]. Estos casos de uso aparecen como consecuencia de los requisitos cada vez más exigentes de los usuarios finales que emplean las redes. Dichos requisitos aparecen reflejados en los indicadores clave de rendimiento (*Key Performance Indicators*, KPI), como la velocidad de datos, la eficiencia espectral, la eficiencia energética, la fiabilidad o el consumo de energía en la red [4]. Mejorar simultáneamente todos estos KPI es el principal reto tecnológico para la comunidad científica, con el fin de proporcionar comunicaciones eficientes a las generaciones móviles actuales (5G) y futuras generaciones (6G).

Con el fin de mejorar los KPI, la comunidad investigadora está realizando múltiples esfuerzos desde la perspectiva de la capa física [5, 6]. Varios campos de estudio, como el diseño de antenas [7], el modelado de canal [8], los sistemas de múltiples entradas y múltiples salidas (*Multiple-Input Multiple-Output*, MIMO) [9], la gestión de haces [10] o la precodificación de canal [11] participan actualmente en el desarrollo de tecnologías habilitadoras. Todos los campos anteriores tienen un punto en común: un aumento en frecuencia hacia la banda de ondas milimétricas (mmWaves). La banda de ondas milimétricas incluye aquellas frecuencias en el rango 30 GHz - 300 GHz, cuya longitud de onda es inferior a 1 cm. Hasta hace pocos años, las ondas milimétricas no se tenían en cuenta para despliegues comerciales porque se consideraban tecnológicamente inviables. Por ello, las comunicaciones se han realizado tradicionalmente en la banda inferior a 6 GHz (sub-6 GHz) [12]. Sin embargo, el limitado ancho de banda disponible en la banda sub-6 GHz y los estudios realizados en la última década han convertido la banda de ondas milimétricas en una oportunidad para el desarrollo tecnológico de los sistemas de comunicaciones [13, 14, 15, 16, 17]. Aunque esta banda ya se propuso como solución tecnológica desde el siglo pasado [18, 19, 20], no fue hasta hace apenas 10 años cuando los primeros despliegues demostraron su viabilidad en entornos de comunicación reales. Por ejemplo, en 2013, trabajo de campo basado en campañas de medida fue realizado en las bandas de frecuencia de 28 GHz y 38 GHz en entornos exteriores e interiores en Manhattan [21]. Este trabajo demostró que, a través del uso de antenas altamente directivas, es posible compensar el fenómeno de atenuación sufrido en entornos altamente densos como Manhattan, alcanzando radios de celda de 200 m. Estos resultados prometedores llevaron a la comunidad científica de radiopropagación a poner todos sus esfuerzos en el análisis de estas bandas de frecuencias, extendiendo el trabajo experimental a lo largo de la última década [22, 23, 24]. De manera simultánea, los organismos de estandarización como 3GPP comenzaron a estandarizar tecnología de acceso radio, conocida como 5G New Radio (5G NR), a partir de la versión 15 del estándar en adelante. Así, una nueva banda de frecuencias estandarizada, y conocida como rango de frecuencias 2 (Frequency Range 2, FR2), entre 24.25 GHz y 71 GHz fue incluida al ya existente rango de frecuencias 1 (Frequency Range 1, FR1) entre 410 MHz y 7125 MHz, denotando la confianza de las grandes compañías de telecomunicaciones en la banda de ondas milimétricas [25, 26]. En solo 10 años, los despliegues comerciales de redes 5G NR en la banda de ondas milimétricas se están convirtiendo en una realidad [27, 28].

Desde la perspectiva de la investigación en radiopropagación, la transición a ondas milimétricas no solo supone un punto de inflexión, sino que en paralelo también están aumentando los escenarios de propagación en los que pueden tener lugar las comunicaciones. De este modo, el concepto de redes heterogéneas (HetNet) propone mejorar la distribución de los recursos radioeléctricos dividiendo la red en celdas de cobertura de distintos tamaños [29]. Mientras que los despliegues tradicionales han tenido en cuenta modelos de propagación urbanos para tamaños de macroceldas en la banda FR1 (por ejemplo, el modelo Okumura-Hata [30]), hoy en día están surgiendo escenarios de comunicaciones de distinta naturaleza, como los vehiculares [31], vehículos aéreos no tripulados (UAV) [32, 33], ferroviarios [34, 35, 36] o en interiores [37, 38, 39]. Además, actualmente se analizan entornos que antes no contaban con una infraestructura dedicada a soportar una red de comunicaciones, como centros comerciales [40, 41], fábricas [42, 43] o estadios [44]. Por último, incluso los escenarios típicos de macroceldas basados en comunicaciones urbanas [45, 46, 47] y comunicaciones rurales [48] deben investigarse de nuevo para tener en cuenta las características de estas bandas de frecuencias más altas.

Tanto la aparición de las ondas milimétricas como el desarrollo de nuevos escenarios de comunicaciones surgen como una oportunidad para mejorar las comunicaciones móviles proporcionando una mejor calidad de servicio, basada en un mayor ancho de banda, menos interferencias y una mayor resolución espacial, lo que implica un alto rendimiento y una gran fiabilidad en la red móvil. Sin embargo, estos avances también plantean varios problemas, lo que da lugar a nuevos desafíos pendientes. El reto principal está directamente relacionado con las características de propagación de las ondas milimétricas. La menor longitud de onda a estas frecuencias implica un cambio de paradigma en los mecanismos de propagación. La fórmula de transmisión de Friis [49], que expresa la pérdida de trayecto por atenuación (*Path Loss*, PL) en el espacio libre, aumenta cuadráticamente con la frecuencia, lo que implica una mayor atenuación del canal en la banda de ondas milimétricas. Además, las señales en esta banda son muy susceptibles al desvanecimiento y hay que tener en cuenta otros factores, no tan relevantes en sub-6 GHz. Esto tiene implicaciones como la atenuación por lluvia —ya que la longitud de onda tiene un tamaño equivalente al de las gotas de lluvia [50, 51]— o incluso la atenuación atmosférica, provocada por la presencia de moléculas de gas en la atmósfera [52]. Por ello, la presencia de vegetación [53, 54], el bloqueo humano [55, 56, 57] y la penetración de materiales [58] se convierten en importantes fuentes de bloqueo. Por último, los fenómenos de propagación por reflexión, dispersión y difracción varían con respecto a la banda sub-6 GHz. En ondas milimétricas, las superficies con una rugosidad comparable a la longitud de onda favorecerán la propagación por dispersión difusa, en detrimento de la reflexión especular [59, 60]. Además, debido a la corta longitud de onda, los fenómenos de pérdida por difracción son más pronunciados porque los objetos son grandes en términos de longitud de onda, lo que propicia el bloqueo de la señal [61].

Dado el gran número de fuentes de atenuación, es esencial garantizar la condición de línea de visión directa (*Line-of-Sight*, LoS) en el canal de comunicación o habilitar mecanismos que garanticen un nivel de señal adecuado, incluso en condiciones sin línea de visión directa (*Non Line-of-Sight*, NLoS). Para ello, la caracterización física del canal de propagación, es decir, el modelado del canal [8, 62, 63], es fundamental tanto desde el punto de vista temporal como espacial y angular. Por un lado, las características temporales se reflejan en la respuesta al impulso del canal (*Channel Impulse Response*, CIR), o perfil de retardo de potencia (*Power Delay Profile*, PDP), que expresan la amplitud/potencia de las componentes multitrayecto (*Multipath Components*, MPCs) en función de su instante de llegada (*Time-of-Arrival*, ToA) [64]. A partir del PDP medido de un canal de propagación, se extraen características temporales como la dispersión del retardo, el número de rayos o el ToA de cada componente [19, 65]. Por otro lado, las características espaciales se definen en el perfil de potencia angular (*Power Angular Profile*, PAP), que calcula la potencia recibida de los MPCs en función del ángulo [66, 67]. De este modo, para una caracterización espacial 3D, se deben tener en cuenta los ángulos de azimut y de elevación, y se pueden extraer características como la dirección de llegada (*Direction-of-Arrival*, DoA) o la dirección de salida (*Direction-of-Departure*, DoD) para cada uno de los MPCs [68, 69]. Cabe señalar que los perfiles anteriores pueden combinarse para producir una caracterización angular y temporal conjunta del canal de comunicación [64, 69, 70].

El principal problema de las campañas de medida es su elevado coste debido a la complejidad y logística asociada [21, 27]. Para solucionar este problema, se proponen modelos de canal teóricos para reducir la complejidad de las campañas [71]. Estos se dividen principalmente en modelos deterministas, como los propuestos por las técnicas de trazado de rayos [72, 73, 74, 75], y modelos estocásticos, que se basan en modelos probabilísticos de las características del canal, como los propuestos por Saleh-Valenzuela [76], Zwick [77] o los modelos estandarizados por 3GPP [26, 78]. Estos modelos de canal se extienden finalmente a simuladores de canal, que calculan eficientemente las características del canal mediante simulaciones, siendo algunos de los más conocidos QuaDRiGa [79, 80] o NYUSIM [81, 82]. Por lo tanto, estos simuladores son especialmente útiles en las primeras fases de despliegue de las redes móviles.

Una solución intermedia entre las extensas campañas de medida y los modelos teóricos de canal surge con el concepto de emulación de canal [83, 84]. Este consiste en la emulación de características específicas del canal, ya sea del perfil espacial o temporal, a partir de mediciones realizadas en entornos controlados como cámaras anecoicas [85, 86] y cámaras reverberantes [87]. De este modo, se reduce significativamente la complejidad del proceso de medida. Esta opción ha cobrado especial relevancia con el desarrollo de los sistemas MIMO, que son más complejos en términos de análisis radioeléctrico al tener múltiples transmisores y receptores operando simultáneamente [88, 89]. Por lo tanto, la validación de nuevos dispositivos 5G con pruebas *Over-The-Air* (OTA) permite evaluar el análisis radioeléctrico en el laboratorio. Otros ejemplos de este tipo de técnicas son la emulación de canales de propagación con distribuciones Rician o Hyper-Rayleigh [90, 91], o la emulación de efectos de desvanecimiento a pequeña escala [92].

Otro de los campos basado en el estudio del modelado de canal para mejorar la caracterización del canal de comunicación se basa en la Inteligencia Artificial (*Artificial Intelligence*, AI), el aprendizaje automático (*Machine Learning*, ML) y el aprendizaje profundo (*Deep Learning*, DL). Se han propuesto varias técnicas basadas en AI para la investigación 5G [93, 94], siendo el canal de comunicación una de las principales áreas de interés. En concreto, se han empleado redes neuronales para el procesamiento de imágenes de satélite, permitiendo la inferencia de modelos de pérdida de trayecto por atenuación tanto en bandas sub-6 GHz como de ondas milimétricas [95, 96, 97]. Otro enfoque se basa en el uso de algoritmos de aprendizaje supervisado para la clasificación e identificación de entornos de propagación. Clasificar correctamente los escenarios permite adaptar los modelos de canal a las características específicas de un entorno determinado, mejorando así la fiabilidad y el rendimiento de las comunicaciones [98]. En la literatura se pueden encontrar varios casos prácticos de identificación de escenarios de distinta naturaleza, como escenarios en interiores [99], vehiculares [100] o ferroviarios de alta velocidad [101].

En relación con los perfiles espaciales y temporales previamente abordados, la localización de fuentes u objetos mediante estos perfiles ha sido uno de los campos más estudiados debido a su potencial interés en la caracterización de canales [102, 103, 104]. Por ello, a lo largo del tiempo se han desarrollado múltiples métodos para estimar y caracterizar el DoA en canales multitrayecto [105]. Generalmente, estos métodos aprovechan la diversidad espacial de un conjunto de sensores utilizando teoría de procesado de señales de arrays para extraer los ángulos de incidencia de una onda. Algunos de ellos, como las técnicas *Delay-and-Sum* (DAS) [106] y *Minimum Variance Distortionless Response* (MVDR) [107], se basan en el escaneo espacial de haces. Otras, como *MUltiple SIgnal Classification* (MUSIC) [108], explotan la ortogonalidad de la señal con respecto al subespacio de ruido en la matriz de covarianza espacial. Posteriormente, aparecieron nuevos enfoques basados en técnicas de desplazamiento de matrices, como *Estimation Signal Parameters Via Rotational Invariance Techniques* (ESPRIT) [109], o basados en técnicas de esperanza-maximización, como *Space-Alternating Generalized Expectation-maximization* (SAGE) [110, 111], que evitan efectuar una búsqueda exhaustiva de los DoAs desconocidos. Estos métodos han sido muy utilizados durante el desarrollo de campañas de medida para la caracterización óptima del perfil espacial del canal de comunicación. Además, tanto los mecanismos de localización como la identificación del canal adquieren especial relevancia en el despliegue de redes 5G en la banda de ondas milimétricas debido a la necesidad de garantizar enlaces de comunicación seguros, fiables y robustos. Esto se debe principalmente a la necesidad de compensar las pérdidas por atenuación en estas frecuencias mediante el diseño de antenas altamente direccionales. Es aquí donde interviene el concepto de gestión de haces, basado en el diseño inteligente de arquitecturas de sistemas que operen en la banda de ondas milimétricas y gestionen las cadenas de radiofrecuencia (RF) con el fin de garantizar un rendimiento óptimo del enlace de comunicaciones [10, 112, 113]. Por lo tanto, el concepto de gestión del haz se trata de una serie de mecanismos que sirven para facilitar esta gestión [114]. Por ejemplo, el barrido del haz es capaz de proporcionar cobertura espacial en una región específica y evalúa el haz adecuado para cada usuario basándose en la medida, la determinación y el reporte del haz óptimo [115, 116, 117, 118]. Además, como las ondas milimétricas son propensas al bloqueo, se establecen mecanismos de recuperación de haces para recuperar un enlace bloqueado mediante la identificación de un haz candidato [119]. Por todo ello, la estandarización de estos mecanismos, junto con el desarrollo de modelos teóricos de canales y técnicas de caracterización de canales, así como la realización de campañas de medida, son clave para el desarrollo de las futuras comunicaciones móviles.

Esta tesis tiene como objetivo fundamental contribuir a la caracterización y medida de canales de comunicaciones en la banda de ondas milimétricas, para facilitar y mejorar el despliegue de tecnologías de futura generación para comunicaciones móviles. Este documento de tesis está organizado de la siguiente manera. En el Capítulo 1, y más concretamente en la sección 1.1, se introduce la importancia de las ondas milimétricas para los sistemas 5G, exponiendo los principales retos asociados a la capa física en esta banda y los estudios y soluciones propuestos basados en el estado del arte actual. Las secciones 1.1.1 - 1.1.6 profundizan en algunas de las cuestiones presentadas en la sección 1.1, que serán aspectos clave para esta tesis y se abordarán con más detalle en capítulos posteriores. Las secciones 1.2 y 1.3 proponen los principales objetivos desarrollados y la metodología seguida a lo largo de la tesis, respectivamente. El apartado 1.4 muestra los principales resultados obtenidos a lo largo de la tesis. En el Capítulo 2 se encuentran los trabajos y publicaciones, que recogen las principales aportaciones realizadas a lo largo de la tesis. Éstas van precedidas de una introducción a cada trabajo. Este capítulo se divide en cuatro secciones. La sección 2.1 muestra la simulación de canales de propagación mediante simuladores de canal y su optimización mediante algoritmos genéticos y de enjambre de partículas. La sección 2.2 trata de la emulación y clasificación de canales de propagación, proponiendo técnicas de post-procesado y algoritmos de identificación basados en aprendizaje automático. La sección 2.3 plantea técnicas basadas en *beamformers* invariantes en frecuencia para caracterizar conjuntamente DoA y ToA en canales de comunicación. La sección 2.4 presenta una campaña de medidas realizada en un escenario industrial en condiciones operativas para una red 5G NR, centrándose en los procedimientos de gestión del haz. Finalmente, el Capítulo 3 resume las principales contribuciones desarrolladas durante la tesis y esboza posibles líneas de investigación futuras basadas en el trabajo de la presente tesis.

Conclusiones

Esta tesis se ha centrado principalmente en la caracterización y medida del canal de comunicación para la banda de ondas milimétricas. A lo largo de este documento se han presentado diversas propuestas, métodos y técnicas para el estudio del canal de propagación en esta banda de frecuencias, que se resumen en la simulación, optimización, emulación, clasificación, caracterización y medida de canales de comunicaciones.

A continuación, se presentan las principales conclusiones extraídas de cada uno de los estudios propuestos en esta tesis:

- En lo que respecta a [J1], se presenta la simulación y optimización de un despliegue heterogeneo de red. Los resultados muestran que la optimización de la potencia de transmisión de las estaciones base desplegadas mejora el rendimiento de la red desde un punto de vista multicapa. De este modo, se maximiza simultáneamente el rendimiento de los usuarios de la red y se reducen el consumo energético y los costes de señalización asociados a los saltos entre celdas. Para la optimización se han hecho uso de dos familias de algoritmos de optimización, los algoritmos genéticos y la optimización por enjambre de partículas, siendo esta última la que obtiene los mejores resultados en función de las métricas propuestas.

- En cuanto a [J2], se analiza el rendimiento de los sistemas MIMO distribuidos en varios entornos y bandas de frecuencia. Para ello, se realiza un estudio de la eficiencia espectral del canal mediante simulaciones y medidas de laboratorio. Los resultados muestran la importancia de la diversidad espacial del canal reflejada en la correlación del canal en sistemas D-MIMO, aumentando significativamente la eficiencia espectral para canales poco correlados, es decir, con alta diversidad espacial. Además, la distribución uniforme de la potencia recibida en el usuario entre los distintos canales disponibles garantiza una óptima eficiencia espectral del sistema de comunicaciones. Por lo tanto, el diseño de dichos sistemas debe tratar de cumplir ambas condiciones para un despliegue óptimo de estas redes móviles basadas en D-MIMO.

- En el caso de [J3], se propone la técnica de time-gating para la emulación de canales de propagación. Mediante el uso de funciones de enventanado en el dominio del tiempo, las señales de banda ultraancha sufren modificaciones a través del desplazamiento temporal y la atenuación o amplificación de las componentes multitrayecto. El análisis de parámetros de canal como la eficiencia espectral o la correlación entre señales demuestra que existe una buena concordancia entre los canales emulados y los canales objetivo. Estos resultados experimentales, realizados tanto en entornos anecoicos como reverberantes, validan la técnica de emulación de canales como método para recrear y caracterizar canales de propagación a partir de medidas de laboratorio, simplificando así la complejidad de realizar medidas *in situ* en escenarios reales.

- En [J4], se presentan técnicas de reducción de la dimensionalidad como método para la clasificación visual de diversos escenarios de propagación. Se contemplan varios parámetros del canal de propagación como el espacio de alta dimensión formado por un conjunto de datos que abarca hasta cinco entornos de propagación diferentes. La aplicación de un algoritmo no lineal de reducción de la dimensionalidad permite clasificar los escenarios en el espacio de baja dimensión y, al mismo tiempo, distinguirlos en función del ángulo de apuntamiento. Los resultados de este algoritmo mejoran a técnicas como PCA o Isomap. La clasificación de espacios de baja dimensión mediante algoritmos de aprendizaje supervisado muestra que, a pesar de la reducción de la dimensionalidad, la información se preserva respecto al espacio original de alta dimensionalidad, con una precisión de clasificación similar tanto en los espacios de alta dimensión como en los de baja dimensión. Por último, se demuestra que el uso de time-gating es capaz de modificar un escenario determinado para que se asemeje a un escenario objetivo en la clasificación visual, validando así esta última técnica.

- En relación con [J5], el trabajo propone el uso de *beamformers* invariantes en frecuencia para la estimación conjunta del DoA y ToA basados en geometrías de arrays elípticos. Esta técnica supone la generalización de la estimación con arrays circulares, ya que las formas elípticas incluyen intrínsecamente al círculo, así como a los arrays pseudolineales. Esto se debe a los grados de libertad añadidos por la excentricidad y el ángulo de rotación de la geometría elíptica. Además, se demuestra que una configuración aleatoria suficientemente densa de sensores puede aproximarse mediante arrays elípticas concéntricos, lo que supone la posibilidad de realizar estimaciones conjuntas a partir de arrays pseudoaleatorios con la técnica propuesta. Finalmente, el marco teórico queda validado gracias a las medidas experimentales realizadas en una cámara anecoica en la que se emulan entornos multitrayecto. Los resultados muestran una excelente concordancia entre las simulaciones y las medidas experimentales.

- En lo que concierne a [J6], basado en el marco de los *beamformers* invariantes en frecuencia presentados en el trabajo previo, se propone el uso de arrays tóricos para extender la caracterización conjunta del DoA y ToA a escenarios 3D. La geometría del toro permite la definición de círculos en múltiples planos, lo que permite múltiples estimaciones 2D en distintos planos del espacio 3D. La combinación inteligente de estas estimaciones permite la caracterización 3D del canal de propagación —es decir, los ángulos de azimut y de elevación— y el ToA. Esta técnica se ha validado mediante simulaciones que muestran resultados con buena precisión en entornos multitrayecto en la banda de ondas milimétricas.

- En relación con [J7], se llevan a cabo dos campañas de medición en un entorno industrial con una red FR2 5G en condiciones operativas. Utilizando un robot móvil autónomo capaz de recorrer la fábrica de forma autónoma, se realizan medidas de la potencia recibida en todo el escenario, generando así mapas de cobertura. El análisis posterior de estas medidas permite el desarrollo de análisis de pérdidas de trayecto por atenuación en función de la distancia y el estudio del tamaño óptimo de celda. Por último, la comparación entre ambas campañas realizadas con diferentes configuraciones del módulo transmisor permite estudiar los procedimientos de gestión del haz implicados en la red, tales como la recuperación, el barrido y la conmutación del haz. De este modo, se espera que estos resultados sean de utilidad para las tareas de planificación radioeléctrica en despliegues de antenas direccionales en entornos industriales.